Emerging Technology for RF and Millimeter-wave Circuits based on Carbone Nanotubes

Phi Long Doan

Université Grenoble Alpes

THÈSE

Pour obtenir le grade de

DOCTEUR DE L'UNIVERSITE GRENOBLE ALPES

Spécialité : **Optique et Radiofréquence**

Arrêté ministériel : 25 mai 2016

Présentée par

Phi Long DOAN

Thèse dirigée par **Florence PODEVIN, Maître de conférence, Université Grenoble-Alpes-Grenoble INP**, et
codirigée par **Emmanuel PISTONO, Maître de conférence, Université Grenoble-Alpes**

préparée au sein du **Laboratoire RFIC-Lab**
dans **l'École Doctorale E.E.A.T.S**

Technologie émergente pour le développement de circuits RF et millimétriques à base de nanotubes de carbone

Thèse soutenue publiquement le **17 Décembre 2020**,
devant le jury composé de :

M. Didier VINCENT
Professeur à l'Université Jean Monnet de Saint-Etienne, Président
M. Frédéric ANIEL
Professeur à l'Université de Paris-Saclay, Rapporteur
M. Anthony GHIOTTO
Maître de conférence à Bordeaux-INP, Rapporteur
Mme. Marjorie GRZESKOWIAK
Maître de conférence à l'ISAE-Supaero, Examinatrice
M. Dominique BAILLARGEAT
Professeur à l'Université de Limoges, Examinateur
M. Philippe COQUET
Professeur à l'Université de Lille, Examinateur
Mme. Florence PODEVIN
Maître de conférence à l'Université Grenoble-Alpes--Grenoble-INP, Directrice de thèse
M. Emmanuel PISTONO
Maître de conférence à l'Université Grenoble-Alpes, Co-directeur de thèse

Acknowledgments

First and foremost, I would like to express my appreciation and sincere gratitude to my supervisor, Mrs. Florence PODEVIN and my co-supervisor, Mr. Emmanuel PISTONO for their unconditional help, support and guidance that have instructed me all along my work in this PhD thesis. Without their precious advices and valuable comments, this thesis would not be achieved. I would also like to express my thanks to Prof. Philippe FERRARI for giving the opportunity to commence this 3-year interesting and unforgettable journey. During these years, I have learnt from many people not only how to work in a scientific way, but also how to improve myself day by day.

Besides my advisors, I would like to thank the rest of my thesis committee: Prof. Frédéric ANIEL from University of Paris-Saclay, and Mr. Anthony GHIOTTO from Bordeaux-INP for having accepted to review this thesis; Mrs. Marjorie GRZESKOWIAK from ISAE-Supaero, Prof. Philippe COQUET from University of Lille and Prof. Dominique BAILLARGEAT from University of Limoges for examining this work and Prof. Didier VINCENT from University of Saint-Etienne for being the president of my thesis jury.

I would also like to acknowledge the ANR TRICOT project for financing me during this thesis period. In the same framework, I would express my sincerest thanks to our collaborators in this project: Prof. Dominique BAILLARGEAT, Mr. Kamel FRIGUI, Mr. Stéphane BILA, Mr. Philippe ROUX-LEVY and Mr. Joseph DE-SAXCE from XLIM laboratory, Limoges, France for their sharing experiences in carbon nanotubes modelling; Prof. Philippe COQUET, Mr. Jianxiong WANG, Mr. Siah CHUN FEI, Mr. Simon GOH CHUN KIAT from CINTRA laboratory, Singapore; Mr. Stéphane PIOTROWICZ from III-V Laboratory, Paris, France for their helps in sample preparations and fabrications that was performed in this thesis. Especially, I would like to thank the XLIM laboratory for accommodating me during my research period at University of Limoges, France.

I wish to extend my special thanks to the technical team, Mr. Nicolas CORRAO and Mr. Loïc VINCENT for their useful guideline and their endurance patience when helping me to carry out hundreds measurements with always a smile on their faces.

I would alsos like to show my deep appreciation to the administrative and technical office of RFIC-Lab, Mr. Frédéric CHEVROT, Mr. Ahmed KHALID, Mr. Youness RAJAB, Mrs. Anne-Laure FOURNERET and Mrs. Laurence BEN-TITO for their valuable help and support during this thesis.

A very special gratitude goes to my fellow labmates and friends in RFIC-Lab: Marc, Jordan, Giuseppe, Anh Tu, Julio, Leonardo, Mohamad, Imadeddine and so on. I am very grateful to work with you all.

Last but not least, nobody has been more important to me in this tough adventure than the members of my family. I would like to thank my parents Phi Phong DOAN and Thi Hoa BUI, my younger sister Bui Thao Ngan DOAN, whose unlimited love, guidance and support always are with me in whatever I pursue. More importantly, I would like to thank my loving and supportive wife, Nhu Quynh, who always stays beside me to share the difficulties of life and boosts me up when I was exhausted during this thesis. Without you, this hard work could not be completed at all.

Abstract

The fifth-generation (5G) technology is known as the new generation of mobile data connectivity and wireless communication systems. Specifically, the underemployed spectrum in the millimeter-wave frequency band might be seen as a potentially profitable solution for achieving speed of delivery (10-100 Gbit/s) and low-latency response (1-10 ms). However, the development of mm-wave high performance circuits and systems is requiring low-cost fabrication process, small area, low consumption and 3D integration. In this context, carbon nanotubes (CNT) based technology has attracted a lot of attention and could be considered as an interesting candidate for designing the mm-wave circuits due to the CNT outstanding characteristics as compared to the other materials. Therefore, in this thesis, in the framework of the ANR project TRICOT, CNT will be considered as particular materials to design and develop a new 3D integration technology dedicated to mm-waves.

After presenting the context of 5G, and the interest for Butler matrices based on substrate integrated waveguide (SIW) topology, as beam forming networks, a special focus is provided onto the CNT manufacturing and modeling backgrounds as the latter technology which is very innovative for RF and mm-wave designers. Then the work achieved in this PhD thesis is principally concentrated in two directions. The first one involves in the utilization of CNT technology to design air-filled SIW (AF-SIW) circuits for mm-wave applications in E-band (71-86 GHz). The second direction concerns the utilization of the slow-wave (SW) concept for the miniaturization of AF-SIW circuits designed at 28 GHz and based on both conventional PCB and CNT technologies. Two technologies are challenged: slow-wave effects provided by a CNT forest transferred in an advanced PCB technology (AF-SW-SIW) vs slow-wave effect provided by regular blind vias in the same technology (Partially AF-SW-SIW). For the three topics, AF-SIW in E-band, AF-SW-SIW and PAF-SW-SIW at 28 GHz, the proposed structures were detailed, then theoretical analyses were developed, and simulation and first measurement results were presented. The retro-simulations were also realized when needed, which permitted to validate the proposed concepts by waveguides that should present losses below 0.05 dB/mm. Each times two elementary blocks of the Butler matrix were designed: the 3-dB and 0-dB couplers. Extremely low-loss, well isolated and well balanced devices for both E-band and 28-GHz are expected, with in addition high compactness with about 68% of saved surface at 28 GHz.

Résumé

La cinquième génération de téléphonie mobile (5G) se concentre sur le spectre sous-utilisé des ondes millimétriques. Elle est considérée comme la solution potentiellement valable pour permettre à la fois des flux de données extrêmement rapides (10-100 Gbit/s) et de faibles temps de latence (1-10 ms). Cependant, le développement de circuits et de systèmes haute performance aux ondes millimétriques requière un procédé de fabrication faible coût, des surfaces petites, une faible consommation et une intégration 3D. Dans ce contexte, la technologie CNT, à base de nanotubes de carbone, a attiré beaucoup d'attention et pourrait être considérée comme une candidate intéressée pour la conception de circuits millimétriques en raison de ses caractéristiques exceptionnelles par rapport aux autres matériaux. Ainsi, dans cette thèse, menée dans le cadre du projet ANR TRICOT, une attention particulière sera portée au matériau CNT pour concevoir et développer une nouvelle technologie d'intégration 3D dédiés aux applications millimétriques.

Après avoir rappelé le contexte de la 5G et présenté une solution intéressante pour réaliser des réseaux de formation de faisceaux, à savoir la matrice de Butler basée sur une topologie de guides d'ondes intégrés dans le substrat (SIW), une attention particulière est portée sur l'état des connaissances en termes de fabrication et de modélisation des CNTs. En effet il s'agit là d'un domaine méconnu des concepteurs RF et millimétriques. Dans un deuxième temps, les travaux réalisés dans le cadre de cette thèse de doctorat sont abordés sous deux angles différents. Le premier concerne l'utilisation de la technologie CNT pour concevoir des circuits AF-SIW (air-filled SIW) pour les applications en bande E (71-86 GHz). La seconde direction concerne l'utilisation du concept d'onde lente (SW pour slow-wave) pour la miniaturisation de circuits AF-SIW conçus pour des applications à 28 GHz. Les deux approches suivantes sont mises en compétition: effet d'ondes lentes amené par une forêt de CNT transférée au sein d'une technologie PCB avancée (AF-SW-SIW) et effet d'ondes lentes sur la base de vias borgnes classiques au sein de cette même technologie PCB (Partially AF-SW-SIW). Dans les trois cas, AF-SIW en bande E, AF-SW-SIW et PAF-SW-SIW à 28 GHz, les structures proposées ont été détaillées, puis des analyses théoriques ont été développées, des résultats de simulation et des premiers résultats de mesure ont été présentés. Les rétro-simulations ont également été réalisées en cas de besoin, ce qui a permis de valider nos nouveaux concepts de guides d'onde faible perte avec des pertes inférieures à 0,05 dB/mm. Pour chaque cas, deux blocs élémentaires de la matrice de Butler ont été conçus : les coupleurs 3-dB et 0-dB. Quelle que soit la bande considérée des dispositifs extrêmement faible perte, équilibrés et isolés sont attendus. De plus, une forte compacité avec environ 68% de surface réduite est observée à 28 GHz.

General Introduction

Since the first generation (1G) of mobile telecommunication introduced in the years of 1980s when it was used to deliver the analog voice, the development of wireless cellular technology has been increased rapidly over the past two decades. Up to now, the fifth generation (5G) is known as the new generation of mobile data connectivity and wireless communication systems. Indeed, 5G and even more future generations, are expected to provide significantly broadband speeds, lower latency than previous generations while also improving the capacity to perform the full potential of wireless applications.

However, the available bands for 5G wireless communication have become gradually restricted. This is mainly due to the demand for data transfer that has increased faster than predicted leading to bandwidth enlargement. The shortage of free channels in the radiofrequency and microwave bands forced the industrial companies to develop new systems at higher frequencies with larger bandwidths, especially at millimeter-waves (30 GHz to 300 GHz). In particular, 28 GHz and E-band (71-86 GHz) are attractive candidates. However, the development of next generation of mm-wave high performance circuits and systems is requiring low-cost fabrication process, small area, low consumption and 3D integration. Among various alternative and innovative technologies, carbon nanotubes (CNTs) could be considered as an interesting technology for designing the mm-wave circuits due to their outstanding characteristics as compared to the other materials.

Theoretically, increasing the working frequency leads to an increase in transmission loss due to the substantial degradation of the signal-to-interference-plus-noise ratio, which is also due to the losses in free space increasing when the frequency raises up. In this context, high gain switched-beam antenna system is an interesting solution that can generate several directive beams with a high gain to cover a sufficient predefined angular range, leading to an increase in the capacity of data trans/receiver for wireless communication systems.

In the meantime, beam forming has become the core technique in the rapid development of this antenna system. Compared to the other beam-forming solutions, the Butler matrix (BM) has received a great interest and has been used in a variety of applications. This is mainly due to the advantages of BM as compared to the other counterparts such as perfect matching, isolation and equal power division that can be obtained at the same time. In addition, BM has larger bandwidth, structural simplicity and lower loss than the other techniques. That explains why BM was chosen as the targeted device to be designed in a carbon nanotubes technology in the framework of the French ANR project TRICOT (Technologie émergente pour le développement de circuits RF et millimétriques à base de nanotubes de carbone).

During my PhD thesis, funded by the TRICOT project, elementary blocks of BM such as waveguides, couplers and crossovers will be designed in both RF (28 GHz) and mm-wave (E-band 71-86 GHz) frequency bands. Thanks to its attractive features such as high Q factor, high power capability, low-loss, reduced weight that have been demonstrated in literature, substrate integrated waveguide (SIW) was selected as a guided

transmission medium for our circuits in both band and reorganized in CNTs, CNTs with PCB or PCB depending on the RF or mm-wave band.

Based on the previous considerations, the work achieved in this PhD thesis was mainly concentrated in two directions. The first one involves in the utilization of CNT technology to design air-filled SIW (AF-SIW) circuits for mm-wave applications in E-band. The second direction concerns the utilization of the slow-wave concept for the miniaturization of AF-SIW circuits designed for the RF applications based on both conventional PCB and CNT technologies. In both subjects, the proposed structures were detailed, with theoretical analyses and simulations. Then, first measurement results were presented and compared to retro-simulations allowing validating the proposed concepts. Based on this plan, the outline of this PhD thesis can be introduced in the following paragraphs.

In the first chapter of this thesis, the context and an overview concerning the techniques utilized to design and fabricate BM will be introduced in both RF and mm-wave frequency bands. State-of-the-art miniaturization techniques and low-loss air-filled waveguides will be also presented in this chapter.

Based on state-of-the-art results, the second chapter will introduce in detail the physical properties of carbon nanotubes. CNTs could be considered as a potential material for next-generation electronics applications in order to replace classical metal-based structures. The analytical and electromagnetic modeling of CNTs developed at XLIM laboratory, Limoges, France, and CINTRA laboratory, Singapore, will be also presented in this chapter. This electromagnetic bulk equivalent model will be considered for the design of the CNT-based devices developed during this PhD thesis and presented in Chapter 3 and 4.

In the third chapter, a detailed description of AF-SIW waveguide based on CNT technology will be presented. By replacing the lateral metallic wall of rectangular waveguide by CNTs wall, the CNT-based AF-SIW can be obtained. Furthermore, the CNT technology used to design the AF-SIW waveguide will be also applied to the design of 0-dB and 3-dB couplers based on the short-slot topology with the same concept.

In the fourth chapter, an air-filled slow-wave SIW (AF-SW-SIW) based on CNT technology designed at 28 GHz for RF applications will be investigated and presented. In this concept, the slow-wave effect is performed thanks to a forest of CNTs, which separates the electric and magnetic fields distributed inside the waveguide. Three different thicknesses of CNTs forest were considered to obtain different slow wave factors. The elementary blocks of BM such as coupler and crossover will be also presented by using this structure.

The last chapter will be dedicated to the detailed description of partially AF-SW-SIW (PAF-SW-SIW) design blocks based on conventional PCB technology designed at 28 GHz for RF applications. In order to challenge this technology with the one presented in Chapter 4, a comparison between this PCB-based PAF-SW-SIW and the CNT-based AF-SW-SIW will be carried out. An equivalent model for PCB-based PAF-SW-SIW, which allows reducing significantly simulation time, will be also detailed in this chapter.

Finally, a general conclusion that summarizes the main results achieved in this PhD thesis will be presented.

“Không quan trọng bạn đi chậm như thế nào, miễn là đừng bao giờ dừng lại”

Khổng Tử

Table of content

Chapter 1. Introduction

My PhD thesis takes part of the French ANR TRICOT project dedicated to analyze the potentialities of metallic carbon nanotubes technology for rectangular waveguides and slow-wave rectangular waveguides. The use-case concerns beam-forming networks based on Butler matrices in the framework of 5G frequency range, i.e. at millimeter waves where low-loss devices are essential. As a matter of fact, after presenting the context of 5G (section 1.1) and picturing an overview on beam forming networks (section 1.2), we will explain the Butler matrices (BM) working principle and will address various technologies used for BM (section 1.3). In particular, it will be shown that the Substrate Integrated Waveguide (SIW) is a good candidate for low-loss (section 1.4). Carbon Nanotubes (CNT) technology will be explained in detail in Chapter 2 and applied to E-band air-filled SIW in Chapter 3 and 28-GHz air-filled slow-wave SIW in Chapter 4, to be compared with 28-GHz partially-air-filled slow-wave SIW in printed-circuit-board (PCB) technology in Chapter 5, where CNTs have been replaced by internal metallic blind vias. It is important to note that the technological innovative aspects and research efforts to develop millimeter wave integrated waveguides with CNTs or internal blind vias will be mostly demonstrated in this manuscript on the basis of waveguides and/or stand-alone blocks constituting the BM itself, excluding the realization of a complete BM.

1.1 Context

The fifth-generation (5G) technology is known as the new generation of mobile data connectivity and wireless communication systems. On the basis of actual usage and demand in terms of data, it provides breakneck broad-band speeds and has enough capacity to perform every function without a decrease in connection speed, no matter how many people is connecting into the network at the same time. One of the main benefits of 5G technology over the fourth-generation (4G) technology is not only its speed of delivery, between 10 Gbps and 100 Gbps, but also the latency. Latency refers to the delay occurring before a connection establishment (every time a data packet is sent). From a low-latency of 40 ms to 60 ms for 4G, which is not enough to provide real-time response, an ultra-low-latency can range between 1 ms and 10 ms for 5G [1]. That means the data can be transmitted in real-time.

Due to 5G wireless communication foreseen success and the unprecedented vast market that it addresses and should continue to address during next years, the available bands have become step-by-step restricted. This issue is mainly due to the demand for data transfer that has increased faster than predicted leading to bandwidth enlargement, as predicted in [2]. The shortage of free channels in the radiofrequency and microwave bands forced and obliged the industrial companies to develop new systems at higher frequencies with larger bandwidths, especially at millimeter-waves (30 GHz to 300 GHz).

Actually, 5G addresses frequencies up to 100 GHz, which is the range this PhD work focuses on. Even if industrial microelectronics companies are already anticipating frequencies above 100 GHz (sixth generation or 6G), there is still room for research in 5G circuits improvements. In particular, 28 GHz and E-band (71-86 GHz) are attractive candidates [3]. As a primary concern, E-band is called “Next Generation Wireless

Backhaul Spectrum" [4]. Practically, it is divided into four sub-bands 71-76 GHz and 81-86 GHz for the 5G backhaul, 76-77 GHz for the long-range radar systems, and 77-81 GHz for the short-range radar systems.

However, increasing the working frequency leads to an increase in transmission loss due to the substantial degradation of the signal-to-interference-plus-noise ratio (SINR) which is also due to the losses in free space increasing when the frequency raises up [2]. Therefore, high gain antenna systems with a directional beam could be considered to solve this problem due to its line-of-sight (LoS) link in long-range mm-wave point-to-point communications [5]. For non-line-of-sight (NLoS) communications, the single-directional beam needs to be driven to find a relevant link. To overcome this drawback, a multi-beam antenna system is considered as an excellent candidate which can generate a number of simultaneous but independent directive beams with a high gain to cover a sufficient predefined angular range [6]. Beam-forming technique, which has the ability to provide unique patterns for beam switching or steering, has become the core technology in the rapid development of this antenna system. Therefore, in the next section, an overview of the beam-forming networks (BFNs) will be presented.

1.2 Beam-forming network overview

As mentioned previously, the BFNs could be considered as the heart of multi-beam antenna system due to its ability to direct the main beam of the antenna pattern towards different directions based on the signal created by itself. Since the early 1960s, a large number of well-known multiple-input-multiple-output (MIMO) ports solutions providing multi-beams by alternatively choosing the input excitation port have been proposed. These solutions can be categorized basically in two classes: matrices and lenses. We briefly consider here the most common ones, namely the Rotman Lens [7], the Blass [8]–[10], Nolen [11], [12], and Butler [13] matrices. The schematics of these techniques are illustrated in Figure 1-1.

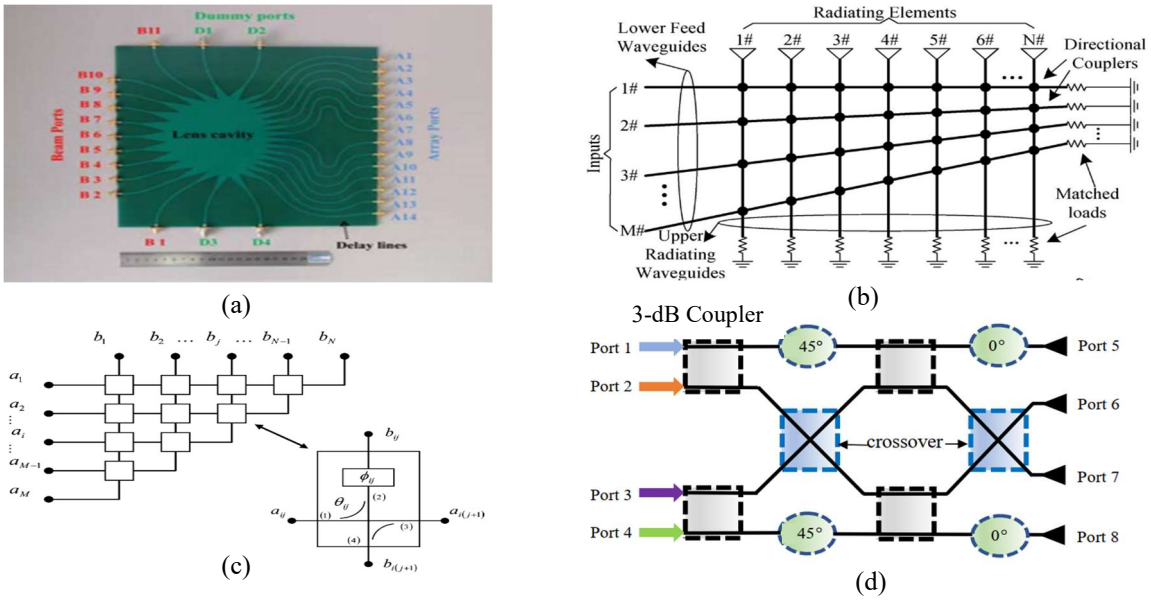

Figure 1-1. (a) Rotman lens [14]*, (b) Blass matrix* [10]*, (c) Nolen matrix* [12] *and (d) Butler matrix* [15].

The Rotman lens was introduced by Rotman and Turner in the 1960s [7]. It is an RF beam-former with N inputs and M outputs. The RF signals from the input ports (beam ports) propagate through the lens cavity and are received by the output ports (antenna ports) before transmitting to the antenna array. The positions of the beam and antenna ports as well as the transmission line lengths are calculated by using the equations of optical path-length equality so that desired phase and amplitude distributions can be obtained [7]. An example of Rotman lens is reported in [14], consisting of a lens cavity, 14 antenna ports, 11 beam ports and 4 dummy ports. The lens cavity is used to focus the incident waves on the beam ports. The antenna ports are connected to antenna array, meanwhile the beam ports are for receiving the signal from the lens cavity. The dummy ports are terminated with loads for absorbing inter-cavity reflections. The delay lines are designed to compensate for the phases of the incoming waves from different angles [14]. Due to the multi-beam formation functionality, numerous researchers have lately found that Rotman lens is a promising candidate for real-time microwave or millimeter-wave imaging applications [16]. However, they are typically limited to far-field imaging, because their parallel multi-beam formation is based on the condition that the scattered waves arriving at the array are plane waves. In the near field, the non-plane waves scattered from a near-field target will spread across several beam ports of the Rotman lens. As a result, out-of-focus blurs appear in the near-field images. In addition, they usually suffer from low efficiency due to spillover losses and high coupling between adjacent ports, which make them less suitable for high power applications [16].

According to the feeding method, the matrix-based BFNs could be divided into two main categories: corporate and series feeds [17]. Whereas the Nolen matrix and the Blass matrix utilize the series feed method, the BM, on the other hand, is a corporate multi-beam feed. While BM is usually designed with an equal number of input (beam) and output (antenna) ports (N×N), Blass and Nolen matrices can be designed with an unequal number of inputs and outputs (M×N). In the Blass matrix, the two sets of transmission lines referred to as row and columns of the matrix are interconnected at each crossover by a directional coupler. At each crossover, a small portion of the signal is coupled to each column, ultimately exciting the corresponding arbitrary number of radiating elements. The signal applied at any input port propagates along the corresponding feed line. Each line is terminated with a matched load to absorb the residual signal. By feeding each input port, a different phase distribution is produced along the array, hence providing a different radiated beam orientation, depending on the various electrical path [8]. The Nolen matrix can be seen as a modified Blass matrix in which the diagonal couplers are replaced by simple bent transmission lines. Accordingly, the termination loads at the end of each feeding line in a standard Blass matrix are suppressed, resulting in theoretically lossless operation [12].

However, the lack of symmetry between input and output ports makes these matrices more complicated to design as the path to the outputs. Besides, the efficiency of Blass matrix and Nolen matrix are quite low due to high losses associated with the structures. Moreover, the magnitude and phase shift mismatches at the antenna ports also make these matrices less attractive. Compared to the Blass matrix and Nolen matrix, the BM has received a great interest with a vast amount of research efforts, and has been used

in a variety of applications. This is mainly due to the advantages of BM as compared to the other counterparts such as perfect matching, isolation and equal power division that can be obtained at the same time [18], [19]. In addition, BM has larger bandwidth, structural simplicity and lower loss than the other Blass or Nolen matrices. That explains why BM was chosen as the targeted device to be investigated in TRICOT project. Its working principle is detailed in the next section.

1.3 Butler Matrix overview

1.3.1 Principle

BM is certainly the most extensively investigated beam-forming network developed to feed multi-beam antenna systems due to its outstanding properties. A typical $(N \times N)$ BM has N input (signal) ports to which power is applied, and N output (antenna) ports to which N antenna elements are connected, where N is a power of 2. RF power is fed to the antenna elements with a progressive phase difference between antenna elements so that the main beam of multi-beam antenna system can be in the desired direction. The progressive output phases are obtained thanks to an attachment of 3-dB, 90° couplers, crossovers and fixed phase shifters. The beam direction is controlled by switching the input power to the desired input port, via a single-pole N-through, SPNT or switch.

The principle of a common (4×4) BM leading to four different phase states and thus to four beam directions θ_i at the output port, is illustrated in Figure 1-2, where the antenna radiation patterns are in the xOy plane, x being the axis in which the antenna elements are placed. Practically, the antenna elements are spaced by $\lambda_0/2$ between each other, λ_0 being the free-space wavelength. The beam direction θ_i corresponds to an input signal entering through port *i*. If port 1 is excited, the progressive output phase between consecutive antenna elements $\Delta\varphi$ is equal to 45°, which orients the main beam at $\theta_1 = +14.5°$. If port 3 is excited, the progressive output phase $\Delta\varphi$ is equal to $-135°$ and the main beam is directed to $\theta_3 = +48.6°$. Due to symmetry around the yOz plane, when port 2 or 4 is fed, we have the same absolute value of the phase of output signal and the beam direction but sign is inverted (+ or -) [20].

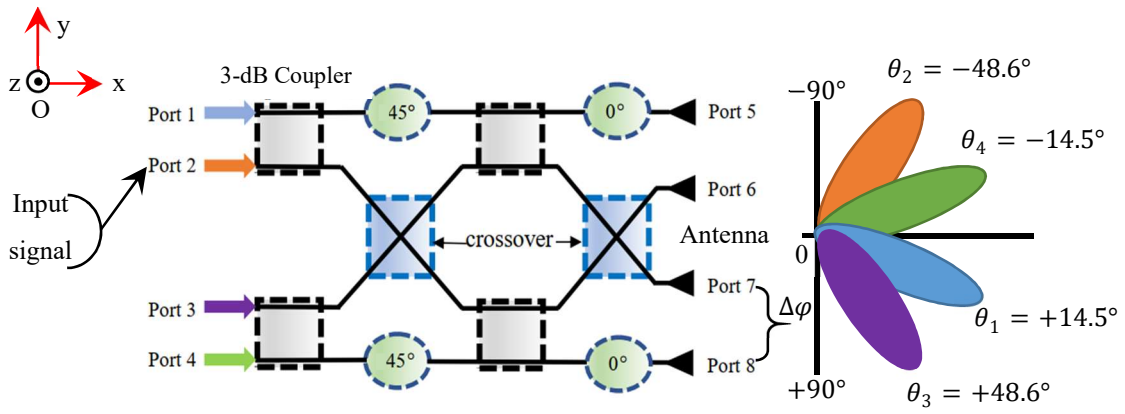

Figure 1-2. Working principle of conventional 4x4 BM.

Over the last decades, a huge number of different topologies have been studied and developed not only to facilitate the design and fabrication of BM but also to improve the BM performance. Therefore, in the next sections, an overview of these techniques will be introduced as well as the state-of-the-art of BM in both RF and mm-wave designs.

1.3.2 State-of-the-art of BM design technique

The most important thing when designing a BM is the ability to obtain the compromise between complexity and performance. Thus, numerous design techniques for simplification and improvement of BMs have been investigated with different transmission lines topologies:

- planar transmission lines: micro-strip line (MS-line) ([17], [18], [19], [20]–[26], [27]–[36], [37]–[42]), coplanar waveguide (CPW): [47], [48]. Some designed were also developed in CMOS technology: [49]–[54].
- Substrate Integrated Waveguide (SIW) technology: [51], [52], [53], [54]–[60], [61]–[70], [71]–[76].

Actually, the MS-line technology is the most commonly used for BM design in both single-layered and multi-layered substrate, especially for RF and microwave applications. Indeed, multi-layered transmission line technologies can be applied to avoid using crossovers [21], [22], [33], [40]. The avoidance of crossovers was also investigated to broaden the bandwidth in [22] and [40] by using multi-section coupled-line directional couplers in micro-strip multi-layer technology for both 4×4 and 8×8 BMs, respectively. For similar purpose, multi-layered CPW technology was also implemented in a 4×4 BM [48]. Furthermore, some non-2^N BMs, such as 3×3 BM [25], quasi 6×6 BM [26] and 4×6 BM [39] designed in MS technology were also studied and developed to enrich the options of beam numbers and thus, improve the configuration flexibility.

As we know, in order to have more directional beams for better transmission performance, higher-order BMs are required. However, the number of elementary blocks exponentially increases with the order of the BMs [48]. Therefore, many researchers have studied on miniaturization of the effective size of the structure as for example in [44], [45]. Particularly, if the BMs are implemented in silicon-based technology, the increase of elementary blocks leads to the increase of the design complexity and chip area. Thus, the circuit miniaturization becomes crucial for single-chip CMOS realization. Several works have been done to solve this issue by using the multi-layer bifilar transformer [49], the subsector technique [50], or lumped elements [52].

In parallel, SIW technology [81] have drawn a lot of attention over the two last decades thanks to the its attractive features such as high Q factor, high power capability, low-loss, reduced weight, and no susceptibility to electromagnetic interference or wide instantaneous bandwidth features. A large number of investigated devices such as filters, mixers, couplers, antenna has been developed, as for example in [82]–[88]. Thus, the use of SIW technology appears to be a good candidate for the implementation of Butler Matrix as well as the smart antenna systems when compared to micro-strip or planar waveguide technologies. Based on the system requirements, the structure of SIW BM can be formed by considering single-layered [58], [60], [61], [75], [76], [80], or multi-layered substrate, [57], [59], [62], [63], [65], [70], [72], [73], [78], [79]. One of the main advantages of multi-

layered substrate over the single-layered one is obviously the size reduction thanks to the decrease of the number of crossovers. Nevertheless, another important factor when dealing with SIW is the simplicity in the design. In fact, single-layered appears to be facilitate the design, and this is the reason why many authors preferred dealing with single-layered structures.

Next, the sub-section 1.3.3 will provide a detailed description of the BM design technique in both MS-line and SIW technology for RF applications meanwhile in 1.3.4, these two techniques will be presented for mm-wave applications.

1.3.3 Butler Matrix design overview for RF applications in MS-line and SIW technology

1.3.3.1 MS-line technology

As discussed previously, the MS-line technology is the most commonly used for BM design, especially for RF and microwave applications. Indeed, numerous researches have been done by using this technology either in single-layered or multi-layered substrate. Therefore, in this section, a detailed state-of-the-art of MS-line-based BM in RF will be introduced.

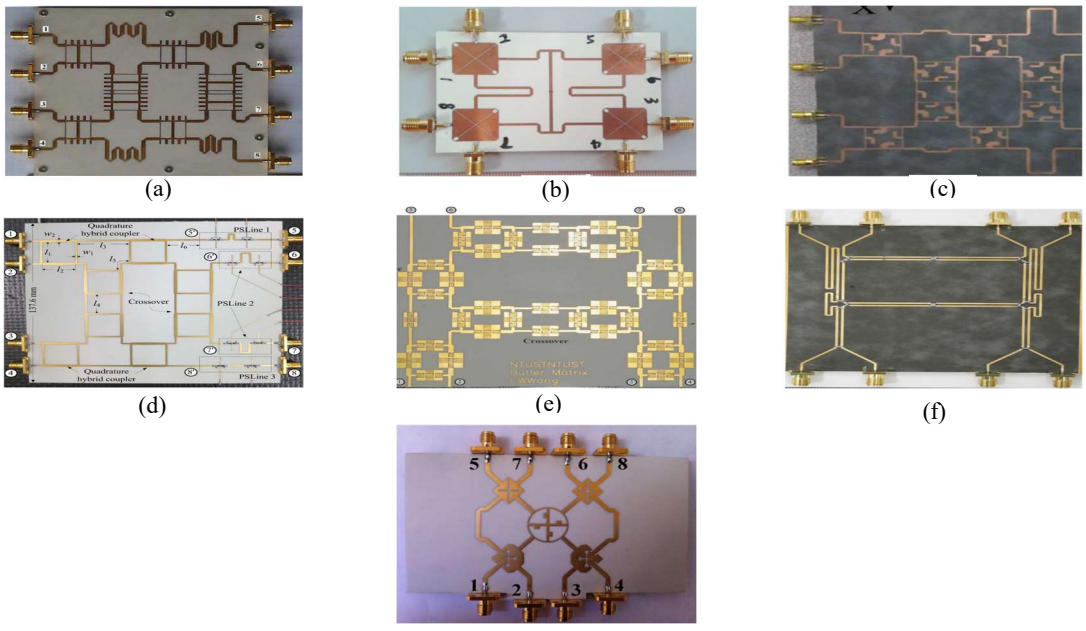

Figure 1-3. Butler matrixes based on single-layered microstrip in RF frequency band: (a) [31]*, (b)* [32]*, (c)* [35]*, (d)* [37]*, (e)* [44]*, (f)* [45]*, (g)* [46].

In Figure 1-3, several 4×4 MS single-layered BMs with different design methods are presented. Figure 1-3 (a) illustrates a BM using eight 3-branch-line couplers designed with lumped distributed elements to reduce the BM dimension. Multi-U-shaped coupled-line Schiffman phase shifters are also selected to achieve a good transmission and phase performance [31]. In Figure 1-3 (b), a miniaturized BM using 3-dB cross-slotted patch hybrid couplers is introduced [32] leading to an area reduction of 56% while maintaining a similar performance in comparison with that based on traditional patch hybrids. Another miniaturized BM is introduced in [35] (see Figure 1-3 (c)), the proposed BM is

implemented with couplers and crossovers considering stub-loaded transmission lines in order to obtain an area reduction of 55% as compared to the traditional one while maintaining the performance within the design frequency range.

A miniaturized BM based on a planar artificial transmission line is illustrated in Figure 1-3 (e) for application in ultra-high-frequency radio-frequency identification systems [44]. This planar artificial transmission line is based of micro-strip quasi-lumped elements and is capable of synthesizing micro-strip lines with various characteristic impedances and electrical lengths. By using this planar artificial transmission line, the circuit size of BM can be reduced 21% compared to the conventional one. Figure 1-3 (f) shows another size reduction technique for designing a BM by using a particular type of coupler which has swapped port characteristic wherein the locations of the isolation and coupled ports are switched, allowing obtaining a low 10% area reduction as compared to a conventional Butler matrix [45]. Finally, in Figure 1-3 (g), a compact BM is proposed using only one crossover. The second crossover and the output phase shifters are removed to avoid the interconnecting mismatch loss and imbalanced amplitude introduced by these phase shifters compared with the conventional one [46].

In Figure 1-3 (d), phase reconfigurable synthesized transmission lines are used to connect to the output of conventional BM to form an extended 4×4 BM [37]. This new design aims to provide a low-complexity solution to expand the beam controllability as well as spatial coverage of a conventional beam-switching system.

As an alternative to single-layered BMs, multi-layered MS technology can be used to design especially high-ordered MBs in order to reduce the structure complexity and circuit dimension, which extensively increases due to the escalation of elementary blocks. Several multi-layered MS based BM are presented in Figure 1-4.

A double-layer structure wide-band 8×8 BM is presented in [21], Figure 1-4 (a). The double layer structure is adopted to place components on the up and down layers without crossover, thus reducing the loss and size and is easy for producing. A three-branch line coupler is employed as a wideband bridge, and two-section stepped coupling microstrip Schiffman phase shifters are used to realize wideband phase shift. Figure 1-4 (b), a two-octave 4×4 BM was proposed in multi-layer microstrip asymmetric coupled-line technology [22]. To achieve two-octave frequency band in terms of amplitude and phase responses, multi-section coupled-line directional couplers and Schiffman C-sections are considered. A high performance three-section coupled-line 3-dB microstrip directional coupler is utilized as a basic element of the BM and compensated MS-line Schiffman C-sections are considered to provide appropriate differential phase characteristics. In [24], the use of coupled-line 3-dB/90° directional couplers and Schiffman phase shifters is also considered to ensure the broad-band amplitude and phase characteristics of the 8x8 BM (see Figure 1-4 (c)). In Figure 1-4 (d), a compact broad-band 8×8 Butler matrix integrated with tunable phase shifters is proposed to provide full beam switching/steering capability [28]. The strip-line tunable phase shifter is designed based on the asymmetric reflection-type configuration, where a Chebyshev matching network is utilized to convert the port impedance from 50 Ω to 25 Ω so that a phase tuning range in excess of 120° can be obtained. A 80% size reduction compared with a conventional BM was also achieved. In Figure 1-4 (e), a broad-band BM is proposed by combining a broad-band forward-wave

directional coupler and a broad-band middle network to obtain a large 47% relative bandwidth and a 67% size reduction as compared with the original size [34]. Meanwhile in Figure 1-4 (f) a slow-wave structure with high slow-wave factor is proposed. The structure is composed of meandered lines, low impedance transmission lines and interdigital structures and, for these reasons, is capable of reducing the circuit size significantly due to its good slow-wave property [36]. Another broad-band planar fully integrated 8×8 BM using coupled-line directional couplers is shown in [40], Figure 1-4 (g). A particular arrangement of the network allows the creation of an entirely planar design having two metallization layers and no interconnections between these layers. Four selected crossovers are realized as a tandem connection of two 3-dB/90 coupled-line directional couplers, which, together with reference transmission lines having appropriate electrical lengths, perform simultaneously crossovers of signal lines, and all needed broad-band constant value phase shifters. Moreover, two of the needed 3-dB/90 directional couplers are designed as tandem connections of two 8.34-dB directional couplers, acting as 3-dB/90 directional couplers having crossed outputs. Finally, a low-loss wideband flat-topped 8×8 BM is presented in Figure 1-4 (h). This BM is composed of double-side coupler loaded with open stubs and Schiffman phase shifter to get desired phase performance in a wide relative bandwidth of 60% [42].

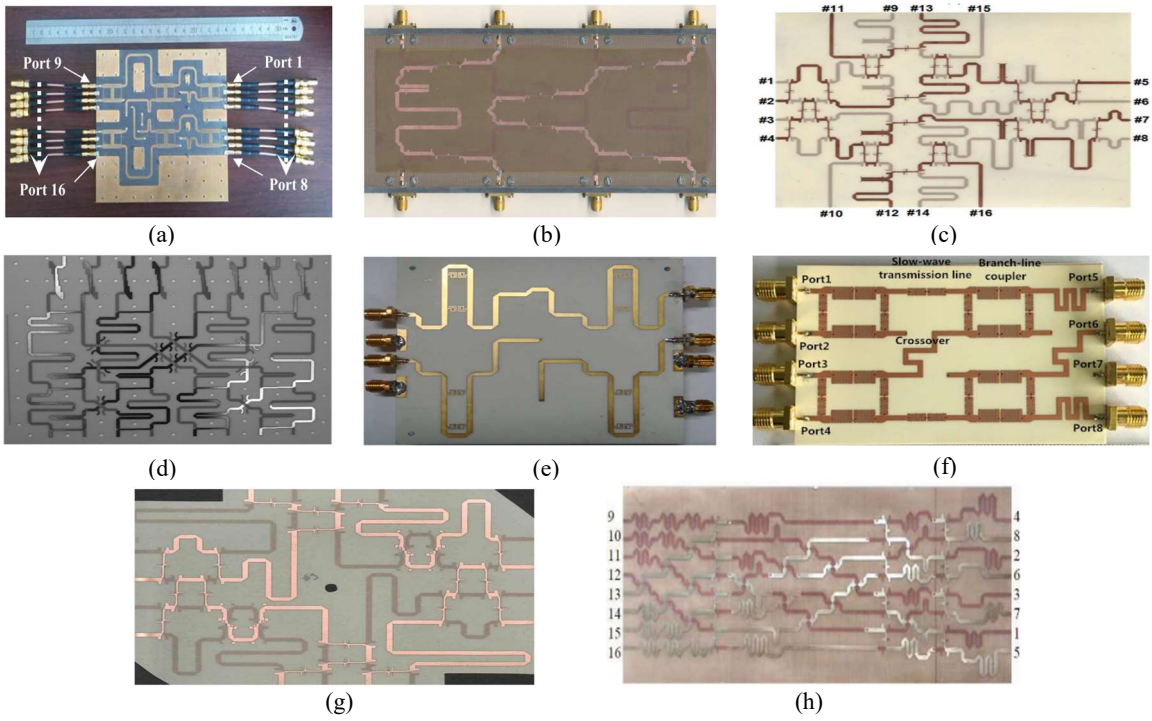

Figure 1-4. Butler matrixes based on multi-layered microstrip in RF frequency band: (a) [21]*, (b)* [22]*, (c)* [24]*, (d)* [28]*, (e)* [34]*, (f)* [36]*, (g)* [40]*, (h)* [42].

Table 1-1 compares state-of-the-art MS-line based BMs in both single-layered and multi-layered substrate for RF electronic applications. The reference, year/type, central frequency, size, BW, average transmission coefficient, maximum amplitude imbalance and phase imbalance at the central frequency, are listed. The BW is considered for an input impedance matching equal or better than 10 dB. Let us notice that ideally (without losses),

the average transmission coefficient should equal to -6 dB for a 4×4 BM, and -9dB for a 8×8 BM. It can be noticed from this state-of-art overview that one of the major claims is miniaturization of blocks, essentially couplers and phase shifters in multi-layered MS technology as crossovers may benefit from the multiple metallic layers opportunities. In the meantime this may be an issue for crossover isolation, as outlined in [89].

REF	Year /Type	Frequency (GHz)	Size (mm×mm) ($\lambda \times \lambda$)	BW (%) (GHz)	Avg. Trans.Coeff (dB)	Max Amp.Imb (dB)	Max Phase.Imb (°)	Layers
[44]	2007 (4x4)	0.915	99x108 (0.49x0.54)	10.7 (0.89-0.99)	-8.6	±1.1	±7.5	single
[45]	2010 (4x4)	1	70x70 (0.35x0.35)	NA	-8.3	±0.9	±8	single
[28]	2010 (8x8)	2.2	160x100 (2.16x1.35)	56 (1.6-2.8)	-10.1	±2.2	±20.7	multi
[22]	2010 (4x4)	3	NA	113 (1.12-4.5)	-7.1	±0.9	±10	multi
[31]	2011 (4x4)	5	86.5x95.3 (2.65x2.92)	20 (4.5-5.5)	-7.5	±1.5	±10	single
[40]	2011 (8x8)	3	130x100 (2.39x1.83)	33 (2.5-3.5)	-7.2	±0.45	±7.5	multi
[21]	2013 (8x8)	5	150x150 (4x4)	10 (4.7-5.2)	-13.2	±1.5	±12	multi
[32]	2013 (4x4)	2.4	85x75 (1.3x1.15)	14 (2.2-2.5)	-7.3	±0.7	±5	single
[34]	2013 (4x4)	2.5	81.65x71.56 (1.17x1.02)	47 (1.96-3.15)	-7.1	±1	±6	multi
[33]	2014 (8x8)	4.3	150x150 (4x4)	23.2 (3.7-4.7)	-14.2	±2	±15	multi
[46]	2014 (4x4)	6	NA	20.1 (5.4-6.6)	-7.24	±0.4	±0.9	single
[35]	2014 (4x4)	2.4	NA	16.7 (2.2-2.6)	-8.2	±1.5	±2.1	single
[24]	2016 (8x8)	3	170x145 (1.4x1.2)	33 (2-4)	-10.1	±0.5	±10	multi
[36]	2017 (4x4)	0.97	76x39 (0.42x0.22)	14.4 (0.92-1.06)	-7.31	±1.2	±6.85	multi
[37]	2018 (4x4)	2.4	137.6x140 (2.07x2.11)	16.7 (2.2-2.6)	-7.7	±1.2	±9.3	single
[42]	2020 (4x4)	9	NA	60(5-12)	-9.1	±1.5	±8	multi

Table 1-1. Summary of State-of-the-art MS-based BM in RF frequency band.

1.3.3.2 SIW technology

Contrary to the large amount of research work for MS-line based BM in RF applications, a limited number of publications concerning the design of SIW-based BM has been found in literature. Figure 1-5 shows several kinds of BM based on SIW technology for RF applications.

In Figure 1-5 (a), a 4×4 single-layered BM designed in Ku-band is presented [76]. Thanks to improved cross-couplers, a 24% relative frequency bandwidth is obtained. Figure 1-5 (b) illustrates a multi-layered SIW BM beam-forming network designed for 24-GHz automotive radar systems [79]. In this structure, a SIW H-plane coupler is optimized

with an H-plane slit to provide the required phase shift. A class of SIW E-plane 3-dB couplers in doubled layer substrate is considered as the fundamental building blocks to avoid crossovers. Meanwhile, a particular technique to design a compact wideband 4×4 BM for Ku-band applications is presented in [78], see Figure 1-5 (c). In this article, a two-layer SIW BM is designed through a two-fold enhancement approach leading to a significant size reduction of about 50% with respect to the traditional one. In Figure 1-5 (d), a BM-fed two-dimensional scan linearly polarized 2×2 microstrip ring antenna array which is designed in low-cost SIW technology for Ka-band applications is introduced [57]. The highly efficient, compact and passive BM is designed with SIW cruciform couplers and its special topology is well adapted for feeding antenna arrays. Finally, in Figure 1-5 (e), a broad-band 4×4 SIW multi-layered BM operated at central frequency of 9.5 GHz is presented. The proposed Butler matrix consists of two 90° couplers and a broad-band phase shifter that allows to obtain a broad-band operated frequency range and achieve a compact BM thanks to the absence of crossovers [59].

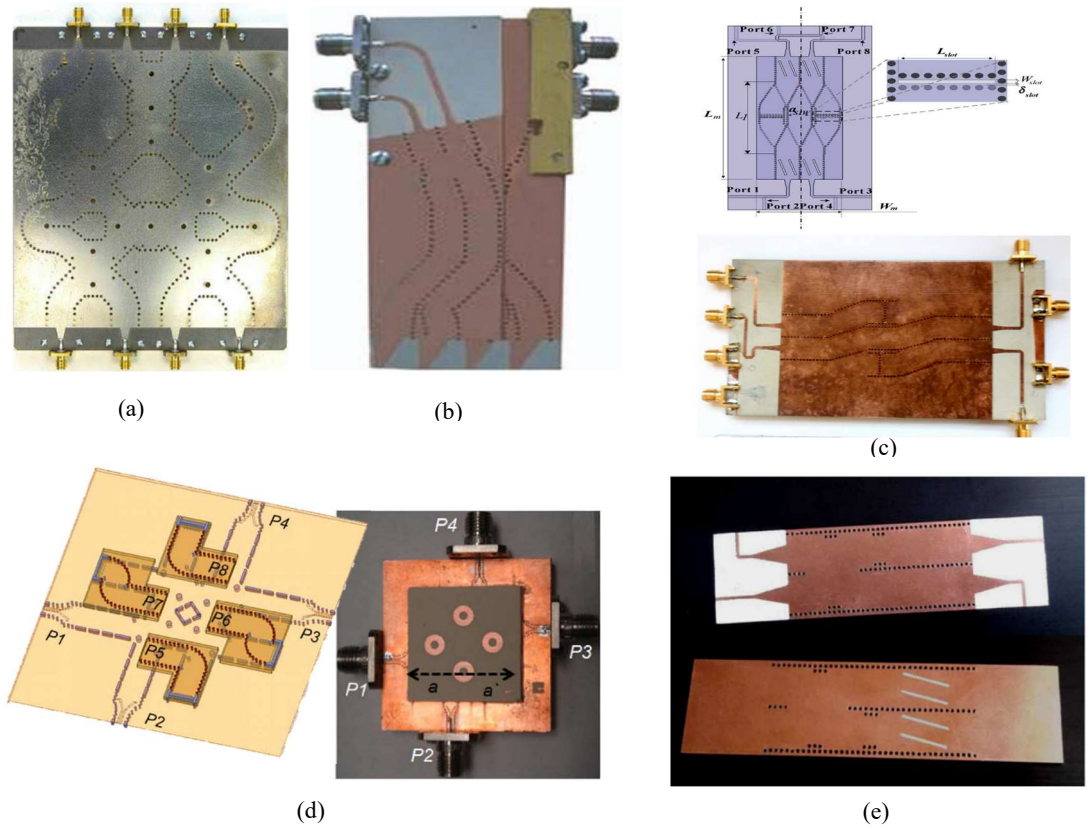

Figure 1-5. Butler matrixes based on SIW technology in RF frequency band: (a) [76]*, (b)* [79]*, (c)* [78]*, (d)* [57]*, (e)* [59].

The performance of these BMs is presented in Table 1-2. Let us notice that due to large lateral dimensions of the SIWs, only frequencies above about 10 GHz are addressed in this technology.

REF	Year /Type	Frequency (GHz)	Size (mm×mm) ($\lambda \times \lambda$)	BW (%) (GHz)	Avg. Trans.Coeff (dB)	Max Amp.Imb (dB)	Max Phase.Imb (°)	Layers
[76]	2010 (4x4)	12.5	144x146 (6x6.08)	24 (11-14)	-7.5	±1	±15	single
[78]	2011 (4x4)	12.5	36.25x83.18 (1.51x3.46)	24 (11-14)	-6.7	±0.6	±7	multi
[79]*	2012 (4x4)	24	51x28 (4.08x2.24)	16.67 (22-26)	-6.35	±0.11	±5	multi
[57]*	2014 (4x4)	26.5	NA	10.71 (25-28)	-7.3	±0.75	±12	multi
[59]	2015 (4x4)	9.5	55x34 (1.74x1.07)	42.1 (7.5-11.5)	-6.2	±0.6	±5	multi

Table 1-2. Summary of the State-of-the-art SIW-based BM in RF frequency band.

(*) the results of the BM are simulated but the entire antenna system was fabricated and measured

1.3.4 Butler Matrix design overview for mm-wave applications in MS-line and SIW technology

1.3.4.1 MS-line technology

In contrast to the huge number of MS-line-based BMs in RF band, only a few works have been done to design the MS-line-based BM for mm-wave applications. It is mainly due to the design and fabrication tolerances in high frequency PCB technology as well as the radiation losses, which increase at higher frequency. However, because of its low cost, the use of microstrip technology for BM realization in mm-wave stays interesting, especially for mm-wave on-chip radio. Three examples of 4×4 BM designed for mm-wave applications are presented in Figure 1-6.

Figure 1-6 (a) shows a 60-GHz two-dimensionally scanning array employing wide band planar switched beam network which is composed of two 4×4 MS-line based BM and four hybrid couplers designed in low cost PCB technology [27]. The network has eight I/O ports, each producing a different beam. The first four ports span one BM and the last four ports span the other. The selection of the Butler matrix (left or right) determines the E-plane scan angle, and the selection of port within the matrix determines the H-plane scan angle. The measured results show that this network causes approximately 2 dB of loss in the band of interest and the peak realized gain of the array is achieved at 12.3 dBi. Another 60-GHz switched-beam patch antenna array with 4×4 BM network is also illustrated in Figure 1-6 (b) [30]. By using this network, a return loss greater than 9.6 dB can be obtained over the frequency range of 59.7-65 GHz, meanwhile the maximum insertion loss is found to be around 1.7 dB. Finally, in Figure 1-6 (c), a 4×4 BM with millimeter microstrip is designed at around 40 GHz without any crossing on single-layered substrate. However, the parasitic radiations of the feeding network (which is the Butler matrix) slightly affect the antenna radiating patterns by an increase of the side-lobes levels in the H-plane and thus narrower beams [29].

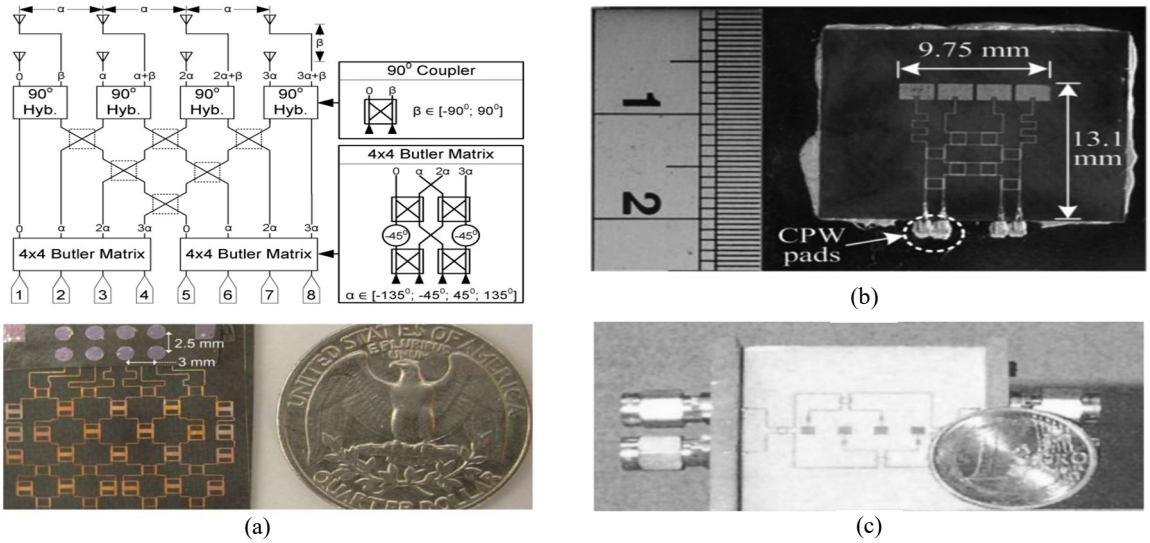

Figure 1-6. Butler matrixes based on microstrip in mm-wave frequency band: (a) [27]*, (b)* [30]*, (c)* [29].

1.3.4.2 SIW technology

For mm-wave applications, MS-line technology has not attracted many interests to design the BM, whereas the use of SIW technology is much more preferred for this issue. It is mainly due to its characteristics to reduce insertion losses compared to other planar technologies while maintaining most advantages of such technology such as high *Q*-factor, high power capability, high integration, manufacturing simplicity, low weight, etc. Thus, in this section, a detailed description of SIW-based BMs designed for mm-wave application is presented. Several kinds of mm-wave SIW-based BMs are illustrated in Figure 1-7.

In Figure 1-7 (a), a single-layered SIW multi-beam slot array operating at about 30 GHz for future 5G mobile terminal application is presented [60]. The multi-beam forming network is realized with a Butler matrix that is composed of hybrid couplers, crossovers, and phase shifters (135° and 0°). By using this BM, the transmission coefficients of port 1 and port 2 (as input ports) could be found respectively at -7.0±0.8 dB and -7.0±2.8 dB while the maximum phase error is only approximately 6°. Another single-layered SIW multi-beam slot array operating from 28 to 32 GHz also used for 5G applications is illustrated in [61], Figure 1-7 (b). This particular BM is designed by using a modified hybrid coupler followed by a -45° compensating phase shifter. The modified hybrid coupler is capable of outputting 45°/135° phase differences and exhibits excellent performance with wideband and flat phase balance, 135° ± 1.8° and 45° ± 1.8° in the completely operating band. This enables phase dispersions of the designed Butler matrix with peak-to-peak error of 13°, for both port 1 or port 2 excitations; coupling to the output ports is well equalized at −6.3 dB with 1.2 dB dispersion across the entire operating bandwidth of interest from 28 GHz to 32 GHz.

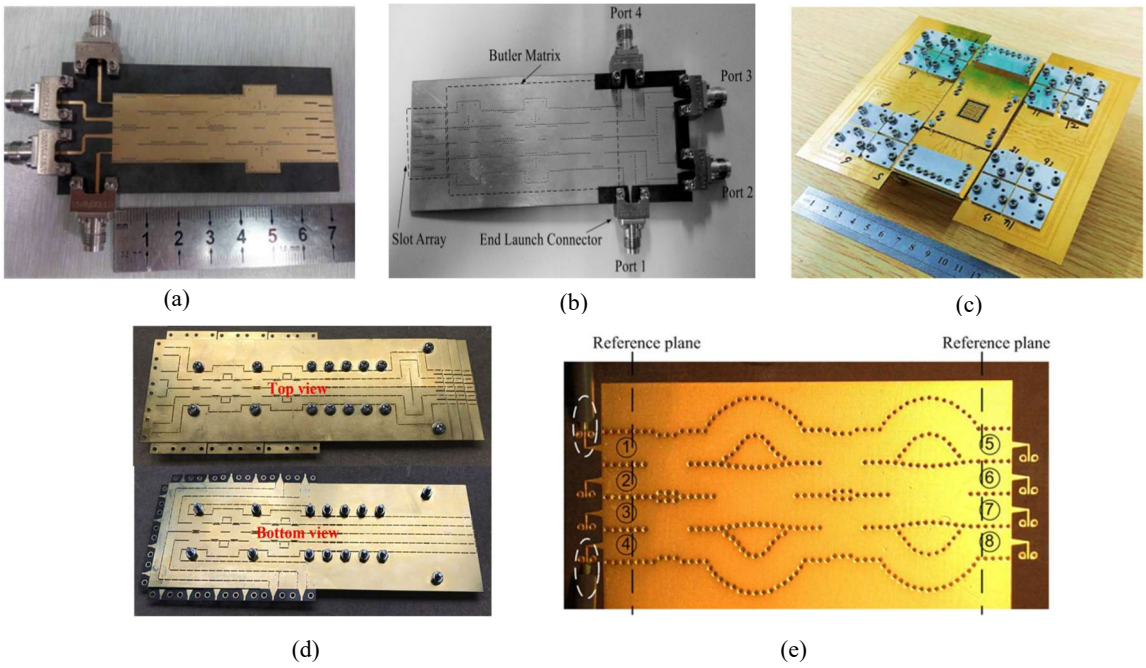

Figure 1-7. Butler Matrixes based on SIW in mm-wave frequency band: (a) [60]*, (b)* [61]*, (c)* [72]*, (d)* [73]*, (e)* [75].

Figure 1-7 (c) presents a millimeter-wave 2-D multi-beam aperture-coupled magneto-electric dipole antenna array operating at 60-GHz band [72]. This antenna array is fed by two sets of 4x4 SIW BM arranged in orthogonal directions. The simulated S-parameters show that the impedance bandwidth is wider than 22.6% for reflection coefficients of less than −10 dB from 54.2 to 68 GHz. Besides, the insertion loss of the Butler matrix is less than 1.5 dB, the difference in power between different output ports is less than 1.4 dB, the isolation between any two output ports is larger than 14 dB and finally, the maximum phase error is less than ±9° over the operating band from 56 to 65 GHz. Another millimeter-wave 2-D beam-scanning multi-beam array antenna fed by multi-layered SIW BFN is illustrated in Figure 1-7 (d) [73]. The BFN is formed by connecting two stacks of sub-BFNs, the E-plane sub-BFN and the H-plane sub-BFN. The H-plane sub-BFN is realized by a traditional H-plane 4×4 BM. The key point of this design is to propose an E-plane 4x4 BM which realizes a planar E-plane sub-BFN. These two sets of sub-BFNs can joint directly without resorting to any connectors or connecting networks to form such a compact 16-way BFN with a reduced area. For the E-plane BM, from 28 to 32 GHz, the return loss and isolation coefficients between distinguished output ports are better than 18 dB. At the center frequency (30 GHz), the phase and amplitude errors are lower than ±3° and ±0.8 dB, respectively. The biggest errors are observed at 28 GHz with ±18° for phase error and ±2 dB for amplitude error. The average insertion loss of the total E-plane BM is about 0.97 dB. Meanwhile for the H-plane BM, from 28 to 32 GHz, the phase peak-to-peak errors are less than ±15°. The average insertion loss of the H-plane BM is about 0.47 dB. Finally, a 60-GHz SIW BM which is designed and fabricated by a standard single-layer PCB process is illustrated in Figure 1-7 (e) [75]. As the measured results of the proposed BM show, for the operating bandwidth from 58 to 62 GHz, the reflections and isolations are lower than -13.5 dB and the insertion losses are below 2.5 dB meanwhile the phase peak-to-peak errors are less than ±17°.

In order to have an overview of the development of mm-wave SIW-based BMs, a performance summary of the state-of-the-art of these BMs during the last decade will be introduced in Table 1-3.

REF	Year /Type	Freq. (GHz)	Size (mm×mm) ($\lambda \times \lambda$)	BW (%) (GHz)	Avg. Trans.Coeff (dB)	Max Amp.Imb (dB)	Max Phase.Imb (°)	Layers
[75]	2010 (4x4)	60	27.1x17.8 (5.42x3.56)	31.7 (48-67)	-8.2	±1.5	±17	single
[80]*	2012 (4x4)	77	31.5x28.5 (8.09x7.31)	12.3 (72-81.5)	-6.7	±0.3	±4	single
[58]*	2015 (4x4)	60	14.98x17.75 (3x3.55)	11.67 (57-64)	-7	±1.5	±14	single
[60]*	2016 (4x4)	30	61.9x27.4 (6.19x2.74)	13.3 (28-32)	-6.8	±1	±10	single
[61]*	2016 (4x4)	30	110x42.5 (11.03x4.25)**	13.3 (28-32)	-6.75	±0.7	±7	single
[63]*	2017 (4x8)	38	NA	10.5 (36-40)	-10.8	±0.8	±5	multi
[65]*	2017 (8x8)	29.5	101.7x40.68 (10.4x4.6)	10.17 (28-31)	-11	NA	±15	multi
[62]*	2017 (4x4)	60	NA	33.3 (50-70)	-8.2	±1	±5	multi
[70]*	2017 (4x4)	94	NA	2.13 (93-95)	-7.2	±0.3	±5	multi
[72]*	2017 (4x4)	60	150x150 (30x30)	23.33 (54.68)	-7.5	±1.4	±9	multi
[73]*	2018 (4x4)	30	165x45 (16.5x4.5)	14.29 (28-32)	-7	±2	±18	multi

Table 1-3. Summary of the State-of-the-art SIW-based BM in mm-wave frequency band.

(*) the results of the BM are simulated but the entire antenna system was fabricated and measured
(**) area including access lines and antennas

1.3.5 Pros and Cons

As mentioned previously, over the two last decades, the BM have attracted a lot of attention compared to the others beam-forming networks due to its outstanding characteristics such as perfect matching, isolation and equal power division that can be obtained at the same time. In addition, BM has realizable large bandwidth, its structural simplicity and very low power consumption. By combining with SIW technology, the SIW-based BMs step-by-step have become an unbeatable candidate for designing smart antenna system that is an essential component for future communication networks.

However, some drawbacks are still existing that require to be further studied and dealt with. The first problem is the structure dimension. Even when the multi-layered substrate was used to avoid using the crossovers, the total area of investigated SIW BMs remains large. Therefore, a necessary method is required to miniaturize theses SIW-based BMs. Thus, in this thesis, a slow-wave effect will be considered as a solution for the miniaturization of SIW-based BMs, especially at 28 GHz in PCB technology. This method will be detailed in Chapter 4 and Chapter 5.

Another drawback needs to be considered when designing a SIW-based BM: that is the sensitivity of elementary blocks such as couplers, crossovers and phase shifters,

which has a high impact on the BM performance, especially the sensitivity in transmission path isolation of the crossover. Indeed, as indicated in [89], when the crossover transmission path isolation (S_{21}) varies from 35 dB down to 15 dB, the output amplitude imbalance goes from 0.33 dB to 3.6 dB and the output phase imbalance goes from 1.5° to about 18°. Therefore, a good transmission path isolation (at least better than 25 dB) needs to be achieved when designing the crossover in order to maintain a good BM performance.

1.4 Low-loss and compact Substrate Integrated Waveguides

In this thesis, elementary blocks of BM will be designed in both RF and mm-wave frequency band. Thanks to its attractive features such as high Q factor, high power capability, low-loss, reduced weight that have been demonstrated in literature, SIW technology will be considered as a selection for guided transmission topology for our circuits in RF frequency band. Nevertheless, SIW is a substrate-based structure and hence it still suffers from dielectric losses increasing at high frequency. Therefore, in this thesis, three topologies of SIW will be studied.

First, in Chapter 3, an Air-Filled SIW (AF-SIW) will be studied for mm-wave applications in a particular interposer technology based on Carbon-Nanotubes (CNT). Then, in order to obtain a compact Air-Filled SIW, two topologies of slow-wave SIW (SW-SIW) will be studied. Based on CNT technology, an AF-SW-SIW will be designed in Chapter 4 and finally, a proof-of-concept will be proposed in PCB technology at 28 GHz for 5G applications and will be presented in Chapter 5. In that case, a Partially Air-Filled Slow-Wave SIW (PAF-SW-SIW) will be considered. Hence, a compromise between low-loss and compactness will be addressed by using respectively, air-filled technology and slow-wave effect. Finally, in order to evaluate the proof-of-concept performance, the two topologies of AF-SW-SIW and PAF-SW-SIW will be compared.

Hence, before presenting the considered waveguide topologies (in Chapter 3, Chapter 4, and Chapter 5), a general description of SIWs, miniaturization techniques and air-filled structures will be introduced in this section.

1.4.1 SIW structure

Whereas the classical metallic rectangular waveguide (RWG) is an extremely low-loss structure, it suffers of heavy weight, low integration capability and high cost of fabrication. On the other hand, the planar transmission lines although have lower Q-factors, they possess lightweight structure and especially a cheap fabrication process. Therefore, the Substrate Integrated Waveguide (SIW), which possesses the advantages of both aforementioned technologies, has been extensively studied in the past 20 years and has become an outstanding candidate for RF systems. Generally, SIW is a rectangular waveguide-based structure realized in low-profile technology such as printed circuit board (PCB) technology with two metallized layers [81]. The upper and lower substrate metallization are used as the top and bottom walls of the waveguide structure whereas the lateral walls are synthesized in the form of two rows of conducting metallic vias embedded in the dielectric substrate (see Figure 1-8). As for RWG, the main geometrical parameters of a SIW are its width W and height h. Two other parameters are introduced, the via-holes diameter d and their longitudinal spacing s.

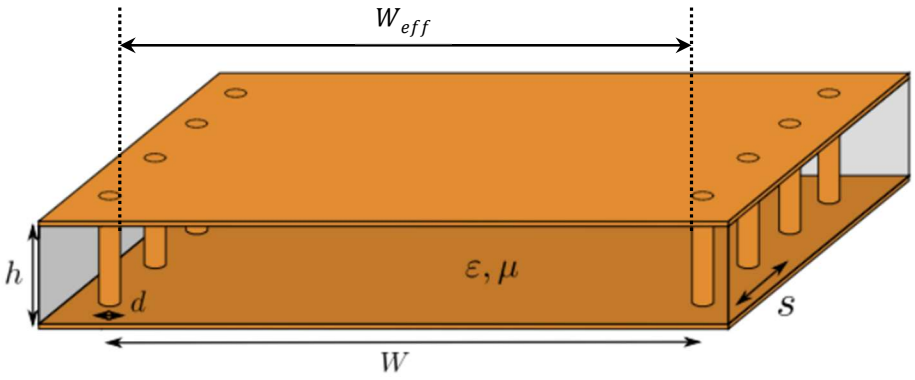

Figure 1-8. SIW geometry [90].

Because the electric side walls of SIW structure are constructed by two parallel via arrays, the associated longitudinal currents cannot travel along the lateral walls, thus only TE mode can be propagated inside SIW with the vertical electric current density on the side walls [91]. The cut-off frequency corresponding to TE_{m0} modes can be described via the equivalent RWG width W_{eff}, as shown in (1-1), where W_{eff} corresponds to the width of a classical RWG having the same electrical characteristics as the SIW structure with its real width W, ε_r being the dielectric constant of the substrate [81].

$$f_{c_{m0}} = \frac{c_0 \times m}{2 \times W_{eff} \times \sqrt{\varepsilon_r}} \tag{1-1}$$

The first mode also called fundamental mode is the TE_{10} mode is calculated in (1-2)

$$f_{c_{10}} = \frac{c_0}{2 \times W_{eff} \times \sqrt{\varepsilon_r}} \tag{1-2}$$

The second mode called TE_{20} appears at $2f_{c_{10}}$. Hence, the first-mode bandwidth is limited by $f_{c_{10}}$ and $2f_{c_{10}}$. In a practical manner, the operating frequency band of the TE_{10} mode is then considered between $1.2f_{c_{10}}$ and $1.8f_{c_{10}}$ [92].

Over the last decade, many publications aimed to study, analyze and develop the design rules for SIW circuit design. These design rules are based on three different principles [90] summarized as follow:

- Minimize the leakage between the via holes
- Avoid the presence of bandgaps within the operating frequency band
- Limit the mechanical impact of drilling by avoiding very high densities of via-holes

The fundamental design rules for the proper operation of SIW were investigated in [93] and were more detailed in [81]. First, the condition $s > d$ should be followed for obvious practical reasons. Then by combining all consideration, the two following rules were given:

$$0.05 < \frac{s}{\lambda_c} < 0.25 \tag{1-3}$$

$$s \leq 2d \tag{1-4}$$

where λ_c is the cut-off wavelength related to the cut-off frequency f_c by $f_c = 1/(\lambda_c \sqrt{\epsilon\mu})$

The equation (1-3) is related to bandgap consideration, while the equation (1-4) reflects an arbitrary mechanical consideration that aims at avoiding unnecessary drilling.

Moreover, the equation (1-4) presents a sufficient condition for negligible leakage losses. By using the dispersion properties extracted from the Boundary Integral-Resonant Mode Expansion (BI-RME) method combined with the Floquet's theorem [94], an empirical equation was extracted to link the effective width W_{eff} of a conventional RWG and the real width W of SIW structure which has the same characteristics. This equation is shown in (1-5):

$$W_{eff} = W - \frac{d^2}{0.95s} \tag{1-5}$$

An accurate formula of the equivalent width W_{eff} is introduced in [91] by studying the leakage characteristics of SIW based on a numerical multimode calibration procedure. This new equation takes the dispersion effect generated by the ratio d/W_{eff} into account. Thus, the SIW propagation constant can match this from a RWG as depicted in [91]. This equation is given in (1-6):

$$W_{eff} = W - 1.08\frac{d^2}{s} + 0.1\frac{d^2}{W} \tag{1-6}$$

After having some physical parameters of the SIW waveguide, full-mode analysis can be carried out by electromagnetic simulation software.

1.4.2 SIW miniaturization techniques

Thanks to its outstanding performance as compared to planar transmission lines, SIW structures have still drawn a lot of attention for the research activities in recent years. As mentioned previously, one intrinsic and major drawback of the SIW is its huge lateral dimension as compared to classical planar transmission lines (e.g. microstrip, CPW). Therefore, the dimension miniaturization became one of the critical issues of performance improvement of SIW-based structures. Thus, in this section, some techniques to reduce the SIW-based structure dimension are presented.

As illustrated in Figure 1-9, the ridge SIW is known as a first solution to reduce the large dimension of a well-known classical metallic waveguide. The structure of the ridge waveguide is quite similar to the rectangular waveguide with one or two ridges inserted in the center of the waveguide. This principle was first published in 1947 by S. B. Cohn [95]. In this publication, it was found that a lower cut-off frequency can be achieved into the ridge waveguide at the same dimension of the hollow metallic waveguide.

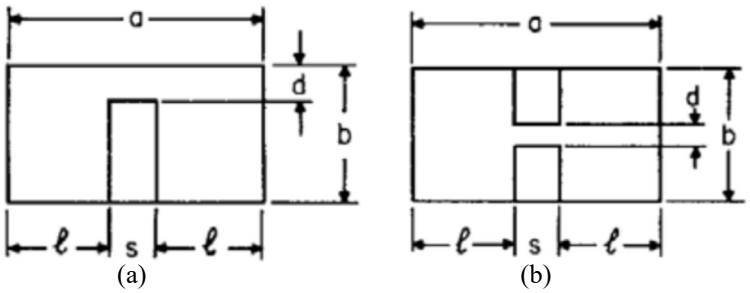

Figure 1-9. (a) Single and (b) double ridge rectangular waveguide cross-section [95].

Thanks to the possibility of multi-layer configuration in PCB technology, the ridge concept has been adapted in 2007 for broad-band transitions from microstrip to SIW [96], as presented in Figure 1-10 (a). With the development of SIW technology, the ridge SIW could be easily implemented into a dielectric substrate by using the conductive vias array

to form the lateral walls and the blind vias for ridge support [97], as depicted in Figure 1-10 (b). In this article, the authors demonstrated that a metal strip connecting all blind vias could be used to remove the bandgap effect related to the periodicity and improve the bandwidth to three times that of the usual SIW.

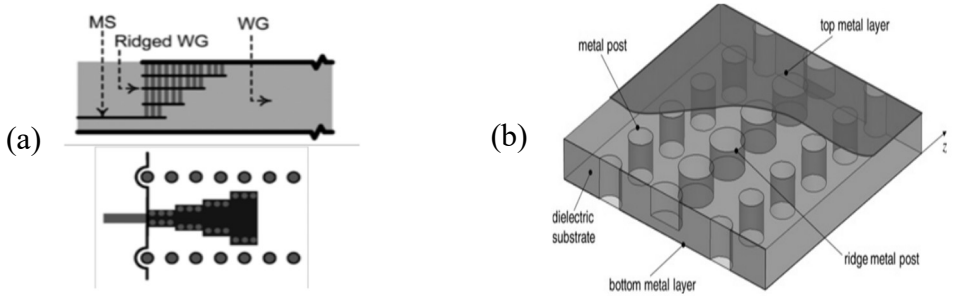

Figure 1-10. (a) Transition from microstrip to SIW based on Ridge SIW [96] *and (b) Ridge waveguide with the connection of the blind via holes for band-gap removal* [97].

It was also demonstrated that an interesting 37% expansion of mono-mode bandwidth [98], as well as lateral miniaturization up to 40% [99] could be achieved. Recently, a novel ridge-SIW-based humidity sensor combined with quarter-mode technique was studied and developed in [100], where the occupied surface is only 20% of the whole surface of the classical SIW sensor.

The second technique to reduce the SIW-based circuits size is so-called "folded SIW". It also relies on a multi-layer configuration. The idea is to bend the waveguide in order to reduce its lateral dimension. It was first introduced by W. L. Barrow in 1941 [101], see Figure 1-11 (a). By folding the wave path inside the waveguide, a very low cut-off frequency can be obtained for the same width of a standard waveguide. In this waveguide, the miniaturization is directly related to the number of bends.

The folded waveguide was first adapted in SIW technology in 2004 [102], and later applied to the design of several passive components. Depending on the way they are bent, the transversely folded SIW can be classified into two main categories: "C-" or "T-shape", respectively presented in Figure 1-11 (b) and (c). From the technology point-of-view, the T-shape configuration has the advantage of presenting a vertical symmetric electric field distribution over the C-shape, facilitating the excitation. However, both structures must be realized in a multi-layered substrate, thus increasing the fabrication cost. A "L-shape" was also introduced in [103] for the feeding of folded tapered slot antenna.

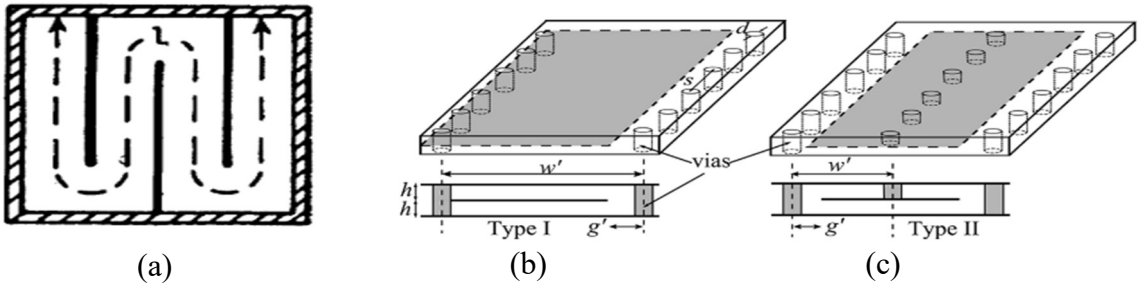

Figure 1-11. (a) Folded rectangular waveguide as introduced by W. L. Barrow [101]*, (b) Folded SIW in C shape and (c) in T shape* [104].

After the first publication in 2004 [105], the C-shape configuration has attracted much more attention as compared to the T-shape geometry. It is mainly because the "C-

shape" folded SIW could provide very similar propagation characteristics as the conventional SIW [106], [107]. Interesting theoretical derivations have also been performed based on a variation analysis recently [104].

In practice, several realizations of folded SIW have been done in PCB technology and for different passive components such as filters [105], [108], [109], antennas [110], couplers [111], etc. But it is worth mentioning that this miniaturization technique has been also recently chosen for the fabrication of SIW in the IBM 130-nm CMOS technology around 200 GHz [112]. It has also drawn attention for the design of compact filters in LTCC technology, which offers the possibility of stacking an important number of layers [113]–[115].

Another miniaturization technique for SIW-based circuits based on symmetry consideration by regarding the distribution of electromagnetic fields inside SIW, which is called "partial-mode waveguides" [116]. Theoretically, the fundamental mode in RWG with a symmetry plane along the propagation direction is equivalent to the presence of a magnetic wall. As illustrated in Figure 1-12 (a), this vertical magnetic symmetry can be replaced by an open-circuit condition without introducing a significant difference in the propagation characteristics [116]. The propagating mode in this open structure is thus called half-mode (HM). The dominant mode in the HM waveguide is like one half of the TE_{10} mode of the full SIW, leading to the same cut-off frequency. However, the latter HM structure involves electromagnetic coupling with the other circuits in a complete integrated system. Indeed, while the full SIW provides an excellent electromagnetic shielding, a strong radiation loss is observed in HM-SIW mainly due to leakage loss in one side of the waveguide. The concept of HM-SIW was first introduced by Hong in 2006 [117] and then rapidly developed and applied to the design of power dividers [116], [118], couplers [119], [120], filters [121], [122], [123] and antenna applications [124], [125].

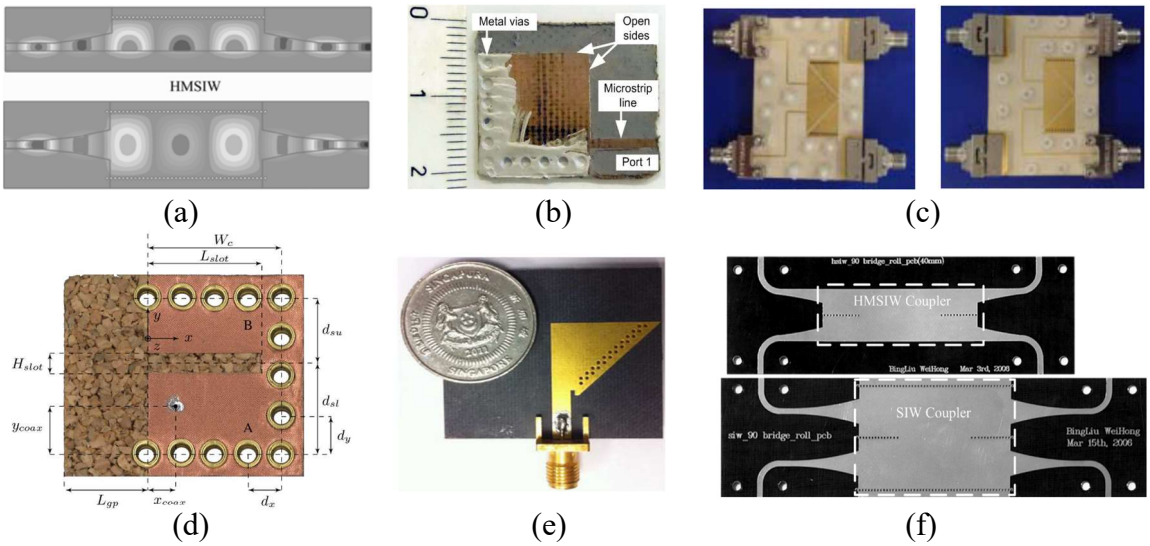

Figure 1-12. (a) Electric field distributed in HMSIW and SIW [116]*, (b) Quarter-mode resonant cavity filter* [121]*, (c) Quarter- and height-mode filter* [122]*, (d) HMSIW cavity-backed slot antenna on cork substrate* [124]*, (e) Quarter-mode SIW antenna* [125] *and (f) HMSIW 3-dB coupler* [119].

Another approach for miniaturization of SIW-based circuits is the use of slow-wave concept. Generally, a slow wave factor (swf) can be defined as the ratio between the free-space velocity in vacuum c_0 and actual phase velocity in the considered waveguide v_p, as described in (1-7) [90]. It can also be expressed as the ratio of free-space and guided wavelength λ_0 and λ, or phase constant β_0 and β. In this definition, an effective relative permittivity ε_{reff} containing the contribution of material properties, as well as any additional slow-wave mechanism is introduced.

$$swf = \frac{c_0}{v_p} = \frac{\lambda_0}{\lambda} = \frac{\beta}{\beta_0} = \sqrt{\varepsilon_{reff}} \tag{1-7}$$

From the equation (1-7), each waveguide structure realized in dielectric material with permittivity greater than 1 would be considered as a slow-wave structure. Therefore, a second formula (1-8) is preferred to define the slow-wave factor [90]. It is defined as the ratio between the phase velocity in the conventional waveguide v_p^{ref} and the phase velocity v_p of the slow-wave structure achieved through geometry and material modifications.

$$SWF = \frac{v_p^{ref}}{v_p} = \frac{\lambda_{ref}}{\lambda} = \frac{\beta}{\beta_{ref}} \tag{1-8}$$

Consequently, this slow-wave factor SWF can be simplified as given in (1-9):

$$SWF = \frac{v_p^{ref}}{v_p} = \frac{\sqrt{\varepsilon_{sw\_ref}}}{\sqrt{\varepsilon_{ref}}} \tag{1-9}$$

$$\varepsilon_{sw\_ref} = \varepsilon_{ref} \times SFW^2 \tag{1-10}$$

Based on this slow-wave concept, A. Niembro published a first slow-wave SIW (SW-SIW) structure in 2014 [126], the schematic of this SW-SIW being illustrated in Figure 1-13 (a). In this structure, the slow-wave phenomenon is achieved by adding inside an SIW waveguide a blind via hole array connected only to the lower metallized layer. Hence, it allows concentrating the electric filed in between the upper metallized and the top of the blind vias whereas the magnetic field flows around the blind vias and remains present in the whole volume of SIW. This spatial separation of electric and magnetic fields is a typical phenomenon for slow-wave transmission lines, leading to a slowdown in the phase velocity.

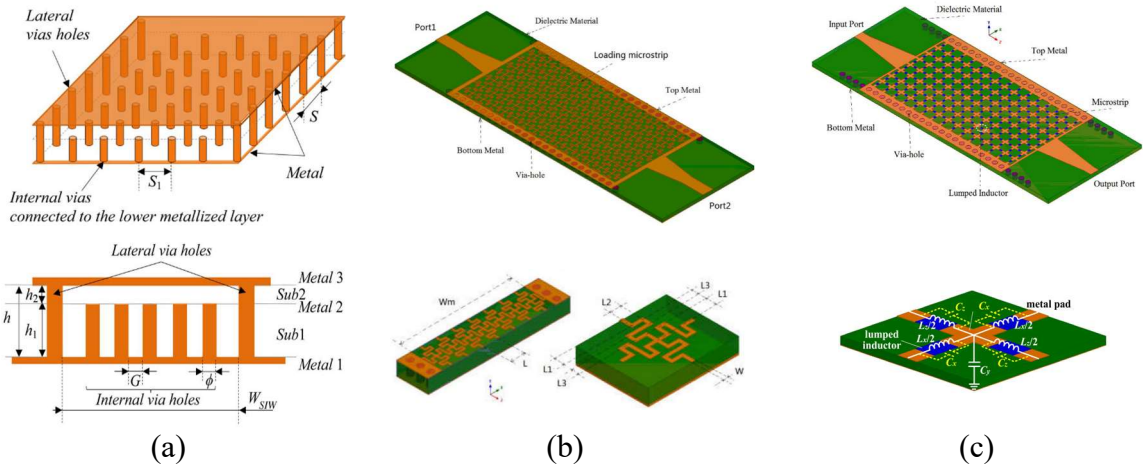

Figure 1-13. (a) Slow-wave SIW with blind via insertion [126]*, (b) Slow-wave SIW with partially polyline loading* [127] *and (c) Slow-wave SIW based on anisotropic artificial materials* [128].

Two other topologies based on the same idea were also investigated for SIW miniaturization with slow-wave concept, which is that of loading the top cover of the SIW either with polylines [127] or lumped inductors [128] to create an additional inductive effect. These both techniques are presented in Figure 1-13 (b) and (c), respectively. These potential techniques provide a miniaturization of surface dimension of about 65 %.

Another technique, which is called Spoof Surface Plasmon Polariton (SSPP), have been also studied and investigated recently for SIW-based circuit miniaturization [129]. The SSPP is a kind of artificial periodic structure to imitate the capability of the natural SPP, which can confine the electromagnetic wave with miniaturized circuit size. The SSPP along with the conversion structure, which converses the electromagnetic mode from the SSPP to spatial mode, can perform a broad passband feature [130], [131]. A slow-wave half-mode SIW using SSPP structure is presented in [132], Figure 1-14. The measured results show that an insertion loss of 1.02 dB is obtained at 12 GHz meanwhile a wideband relative bandwidth of 66.67 % (return loss greater than 10 dB) can be found (from 8 to 16 GHz). A significant reduction of 50 % in both longitudinal and lateral dimensions is also achieved as compared to the SIW one providing an excellent slow-wave effect.

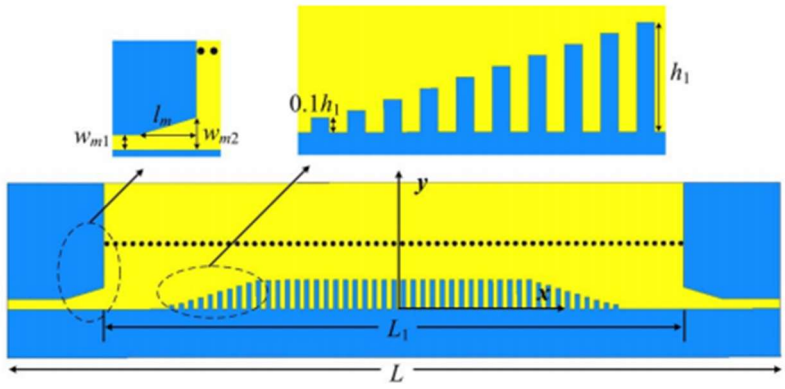

Figure 1-14. Configuration of HMSIW-SPP [132].

In this thesis, as mentioned previously, the slow-wave concept will be considered to reduce the circuit dimension and will be presented more in details in Chapter 4 and Chapter 5.

1.4.3 Air-Filled SIW overview

As the operating frequency of dielectric-based circuits is on the rise, the existence of the dielectric material in the propagating medium causes undesirable high dielectric losses. Also, the dielectric filling inside the waveguide reduces the average power handling capability of the conventional SIW in comparison with the corresponding air-filled waveguides [133]. Therefore, the possibility to reduce the SIW dielectric losses become one of the hot topics for performance improvement of SIW-based circuits, especially in PCB technology.

A considered solution to reduce the SIW dielectric losses is to provide the air propagation medium for the SIW waveguide to create an AF-SIW, in which the dielectric material between the lateral walls must be engraved. This technique is not possible for single-layered SIW but realizable in multi-layered SIW structure. In 2014, a multi-layer PCB-based SIW structure containing an air cut in the middle section has been introduced

for the first time by Belenguer et al. [134] with only computational analysis of the attenuation constant and a cut-off frequency of the AF-SIW. This structure is illustrated in Figure 1-15.

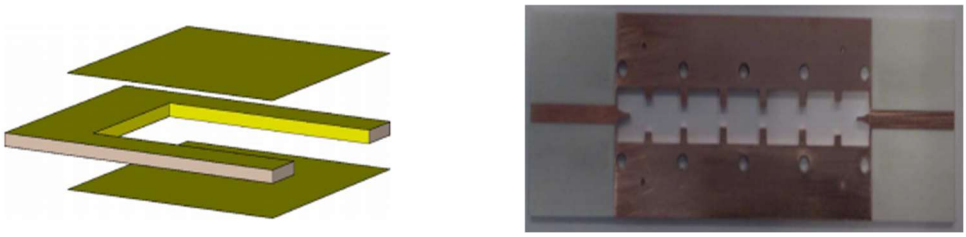

Figure 1-15. Air-filled SIW structure and its application on 19-GHz filter [134].

After this first publication, numerous works have been reported for the development of AF-SIW, which can be used for different applications such as power divider [135], [136], couplers [137], phase shifters [138], [139], filters [140]–[143], antennas [144]–[146], and humidity sensors [147], [148], etc.

The AF-SIW concept was also used for this thesis as mentioned previously. A detailed description of this technique will be introduced in Chapter 3, Chapter 4 and Chapter 5 for mm-wave applications in E-band or at 28 GHz.

1.5 In mm-wave frequency band: towards a platform choice

It is worth mentioning that the mm-wave frequency spectrum has recently become the crucial concern of many research and development projects due to its potential characteristics for mobile communication networks and 5G applications. In this context, the use of PCB technologies to fabricate the mm-wave circuits is restricted due to its insufficient manufacturing accuracy and reliability [149]. On the other hand, when a complete integration of the systems on chip is required, the possibility of current integrated technologies is limited. This limitation is not only due to the relatively poor performance of the passive circuits in integrated technologies but also due to the large surface area occupied for these passive circuits, leading to prohibitive costs [89]. Thus, intermediate platforms need to be considered essentially. These ones called interposers allow realizing high-quality passive devices thanks to more appropriate dimensions (such as high-thickness and low-loss substrates) and more flexibility in the design as compared to other integrated technologies. Moreover, it makes possible the 3D connection of active chips such as CMOS/BiCMOS, GaAS dies through interposer vias and solder bumps from chip to PCB technology [89]. Generally, 3D integration for microelectronic systems reduces the interconnect length, wiring delay, and system size, while enhancing functionality by heterogeneous integration, and passive electrical performance.

Over the last decades, numerous types of interposers have been studied and developed for mm-wave 3D integration such as silicon [150], [151], glass [152]–[154] organic interposers [155], [156], metallic nanowire membrane (MnM) interposers [157]–[161], benzocyclobutene (BCB) interposers [162] and carbon nanotube (CNT) interposers [15], [163]–[166]. Due to its outstanding characteristics compared to the other interposers such as excellent electrical and thermal conductivity, CNT has recently attracted a lot of attention and has become an interesting candidate for designing the mm-wave circuits.

Therefore, in this thesis, in the framework of the ANR project TRICOT, CNT will

be considered as particular materials to design and develop a new 3D integration technology and concept dedicated to future applications in mm-wave interconnects and circuits, especially E-band. In the meantime, efforts will be put also to expand the possibilities offered by more conventional PCB multi-layered technologies at the limits of mm-waves, at 28 GHz.

1.6 Conclusion

The context for this thesis was introduced in the beginning, which emphasizes the important role of multi-beam antenna systems for mm-wave applications, especially for 5G mobile communication networks. The beam-forming technique, which has the ability of providing unique patterns for beam switching or steering, has become the core technology in the rapidly development of this antenna system. Therefore, an overview of four common categories of BFNs was also presented. Among them, BM has a fundamental role because of its outstanding characteristics that makes it the first choice to realize this work. An overview concerning the techniques utilized to design and fabricate BM was also introduced, in RF and mm-wave frequency bands. In fact, the SIW technology has demonstrated its possibility to become a pertinent choice for BM design due to its attractive features such as high Q factor, high power capability, low-loss, reduced weight, and no susceptibility to electromagnetic interference or wide instantaneous bandwidth features. Hence, in this thesis, SIW technology is considered as the core technology to design our circuits and systems in both 28-GHz and E-band.

A short description of SIW technology, as well as miniaturization techniques and low-loss air-filled technology were also introduced in this chapter. These techniques will be considered in this thesis. In Chapter 3, for mm-wave E-band, an AF extremely low-loss SIW with the use of CNT as metallic walls will be studied. Then, at 28 GHz, an AF extremely low-loss SIW using slow-wave effect created by CNT forest for size miniaturization will be detailed in Chapter 4. Finally, a PAF low-loss SIW using slow-wave effect created by blind via holes will be presented in Chapter 5.

Before that, it is important to understand the CNT technology that will be introduced comprehensively in Chapter 2.

REFERENCES

[1] S. Hill and P. Beaton, "5G vs. 4G: How will the next generation improve on the last?," 2020. [Online]. Available: https://www.digitaltrends.com/mobile/5g-vs-4g/.

[2] J. G. Andrews *et al.*, "What will 5G be?," *IEEE J. Sel. Areas Commun.*, vol. 32, no. 6, pp. 1065–1082, 2014.

[3] Z. Haisong, "Second-generation E-Band for LTE backhaul," *SoftMobile*, pp. 27–28.

[4] S. Peleg, "The Advantages of E-Band Wireless Systems in Mobile Backhaul Applications," *Siklu Inc, Petach-Tikva*, vol. 44, no. March, 2009.

[5] M. Ando, J. Hirokawa, T. Yamamoto, and S. Member, "Novel Single-Layer Waveguides for High-Efficiency Millimeter-Wave Arrays," vol. 46, no. 6, pp. 792–799, 1998.

[6] T. E. Bogale and L. B. Le, "Massive MIMO and mmWave for 5G Wireless HetNet: Potential Benefits and Challenges," *IEEE Veh. Technol. Mag.*, vol. 11, no. 1, pp. 64–75, 2016.

[7] W. Rotman and R. Turner, "Wide-angle microwave lens for line source applications," *IEEE Trans. Antennas Propag.*, vol. 11, no. 6, pp. 623–632, 1963.

[8] J. Blass, "The Multidirectional antenna: A new approach to stacked beams," *IRE Int. Conv. Rec.*, vol. 8, no. 7, pp. 48–50, 1960.

[9] F. Casini, R. V. Gatti, L. Marcaccioli, and R. Sorrentino, "A novel design method for Blass matrix beam-forming networks," *2007 Eur. Radar Conf. EURAD*, no. October, pp. 232–235, 2007.

[10] P. Chen, W. Hong, Z. Kuai, and J. Xu, "A double layer substrate integrated waveguide blass matrix for beamforming applications," *IEEE Microw. Wirel. Components Lett.*, vol. 19, no. 6, pp. 374–376, 2009.

[11] N. J. G. Fonseca, "Printed S-band 4 × 4 nolen matrix for multiple beam antenna applications," *IEEE Trans. Antennas Propag.*, vol. 57, no. 6, pp. 1673–1678, 2009.

[12] T. Djerafi, N. J. G. Fonseca, and K. Wu, "Broadband substrate integrated waveguide 4x4 Nolen matrix based on coupler delay compensation," *IEEE Trans. Microw. Theory Tech.*, vol. 59, no. 7, pp. 1740–1745, 2011.

[13] J. Butler and R. Lowe, "Beam forming matrix simplifies design of electronically scanned antennas," *Electron. Des.*, vol. 9, pp. 170 – 173, 1961.

[14] M. Yu, D. Zhao, Y. Jin, and B. Z. Wang, "Near-Field Image Restoration for Rotman Lens by Localized Angle-Time Spread Function-Based Filtering Method," *IEEE Trans. Antennas Propag.*, vol. 63, no. 5, pp. 2353–2358, 2015.

[15] P. Doan, F. Podevin, E. Pistono, P. Ferrari, P. Coquet, and D. Baillargeat, "Potentialités d ' une matrice de Butler en technologie guide d ' onde à base de Nanotubes de Carbone pour des applications 5G en bande E," *XXIèmes Journées Natl. Microondes 14-17 mai 2019 – Caen Potentialités*, 2019.

[16] S. Clark, C. Martin, V. Kolinko, J. Lovberg, and P. J. Costianes, "A real-time wide field of view passive millimeter-wave imaging camera," *Proc. - Appl. Imag. Pattern Recognit. Work.*, vol. 2003-Janua, pp. 250–254, 2004.

[17] F. E. Fakoukakis and G. A. Kyriacou, "Novel nolen matrix based beamforming networks for series-fed low SLL multibeam antennas," *Prog. Electromagn. Res. B*, no. 51, pp. 33–64, 2013.

[18] D. Tarek, J. G. F. Nelson, and W. Ke, "Design and Implementation of a Planar 4×4 Butler Matrix in SIW Technology for Wideband Applications," *Eur. Microw. Conf.*, vol. 24, no. September, 2010.

[19] M. Nedil, T. A. Denidni, S. Member, L. Talbi, and S. Member, "Novel Butler

Matrix Using CPW Multilayer Technology," vol. 54, no. 1, pp. 499–507, 2006.
[20] S. . Z. Ibrahim, M.K.A.Rahim, T Masri, M.N.A.Karim, and M.Z.A.AbdulAziz, "Multibeam antenna array with Butler Matrix for WLAN applications," *Second Eur. Conf. Antennas Propag.*, pp. 1–5, 2007.
[21] J. Guan, K. Ding, F. He, and X. Ying, "A Compact 8×8 Butler Matrix Based on Double-layer Double-layer Structure," 2013.
[22] K. Wincza and K. Sachse, "Broadband 4×4 Butler matrix in microstrip multilayer technology designed with the use of three-section directional couplers and phase correction Networks," *4th Microw. Radar Week, MRW-2010 - 18th Int. Conf. Microwaves, Radar Wirel. Commun. MIKON 2010 - Conf. Proc.*, pp. 4–7, 2010.
[23] M. Koubeissi, C. Decroze, T. Monediere, and B. Jecko, "A New Method To Design A Butler Matrix With Broadside Beam: Application To A Multibeam Antenna," *Microw. Opt. Technol. Lett.*, vol. 48, no. 1, pp. 35–40, 2006.
[24] K. Wincza and S. Gruszczynski, "Broadband Integrated 8 × 8 Butler Matrix Utilizing Quadrature Couplers and Schiffman Phase Shifters for Multibeam Antennas With Broadside Beam," *IEEE Trans. Microw. Theory Tech.*, vol. 64, no. 8, pp. 2596–2604, 2016.
[25] K. Ding, X. Fang, Y. Wang, and A. Chen, "Printed dual-layer three-way directional coupler utilized as 3× 3 beamforming network for orthogonal three-beam antenna array," *IEEE Antennas Wirel. Propag. Lett.*, vol. 13, pp. 911–914, 2014.
[26] K. Ding, J. Bai, and A. Kishk, "A quasi butler matrix with 6×6 beam-forming capacity using 3×3 hybrid couplers," *2017 32nd Gen. Assem. Sci. Symp. Int. Union Radio Sci. URSI GASS 2017*, vol. 2017-Janua, no. August, pp. 1–4, 2017.
[27] W. F. Moulder, W. Khalil, and J. L. Volakis, "60-GHz two-dimensionally scanning array employing wideband planar switched beam network," *IEEE Antennas Wirel. Propag. Lett.*, vol. 9, pp. 818–821, 2010.
[28] C. C. Chang, R. H. Lee, and T. Y. Shih, "Design of a beam switching/steering butler matrix for phased array system," *IEEE Trans. Antennas Propag.*, vol. 58, no. 2, pp. 367–374, 2010.
[29] C. Dall'Omo, T. Monediere, B. Jecko, F. Lamour, I. Wolk, and M. Elkael, "Design and realization of a 4 × 4 microstrip butler matrix without any crossing in millimeter waves," *Microw. Opt. Technol. Lett.*, vol. 38, no. 6, pp. 462–465, 2003.
[30] C. Tseng, C. Chen, and T. Chu, "A Low-Cost 60-GHz Switched-Beam Patch Antenna Array With Butler Matrix Network," *IEEE Antennas Wirel. Propag. Lett.*, vol. 7, pp. 432–435, 2008.
[31] C. Chen, H. Wu, and W. Wu, "Design And Implementation Of A Compact Planar 4 × 4 Microstrip Butler Matrix For Wideband Application," *Prog. Electromagn. Res. C*, vol. 24, pp. 43–55, 2011.
[32] Y. L. Li, Q. S. Liu, S. Sun, and S. S. Gao, "A miniaturised Butler matrix based on patch hybrid couplers with cross slots," *IEEE Antennas Propag. Soc. AP-S Int. Symp.*, pp. 2145–2146, 2013.
[33] Y. Zhai, X. Fang, K. Ding, and F. He, "Miniaturization design for 8 × 8 butler matrix based on back-to-back bilayer microstrip," *Int. J. Antennas Propag.*, vol. 2014, 2014.
[34] T. H. Lin, S. K. Hsu, and T. L. Wu, "Bandwidth enhancement of butler matrix using broadband forward-wave directional coupler and phase difference compensation," *IEEE Trans. Microw. Theory Tech.*, vol. 61, no. 12, pp. 4099–4109, 2013.
[35] W. Nie, Y. Fan, S. Luo, and Y. Guo, "A switched-beam microstrip antenna array with miniaturized butler matrix network," *Microwave and Optical Technology Letters*, vol. 57, no. 4. pp. 841–845, 2015.

[36] F. Wu and L. Sun, “Miniaturization of 4×4 Butler matrix using high slow-wave factor structure,” *Proc. 2017 IEEE 2nd Adv. Inf. Technol. Electron. Autom. Control Conf. IAEAC 2017*, vol. 3, pp. 1772–1775, 2017.
[37] H. N. Chu and T. G. Ma, “An Extended 4 \times 4 Butler Matrix with Enhanced Beam Controllability and Widened Spatial Coverage,” *IEEE Trans. Microw. Theory Tech.*, vol. 66, no. 3, pp. 1301–1311, 2018.
[38] A. Tajik, A. Shafiei Alavijeh, and M. Fakharzadeh, “Asymmetrical 4×4 butler matrix and its application for single layer 8×8 butler matrix,” *IEEE Trans. Antennas Propag.*, vol. 67, no. 8, pp. 5372–5379, 2019.
[39] Q. Shao, F.-C. Chen, Y. Wang, Q.-X. Chu, and M. J. Lancaster, “Design of Modified 4x6 Filtering Butler Matrix Based on All-Resonator Structures,” *IEEE Trans. Microw. Theory Tech.*, vol. 67, no. 9, pp. 3617–3627, 2019.
[40] K. Wincza, S. Gruszczynski, and K. Sachse, “Broadband planar fully integrated 8×8 butler matrix using coupled-line directional couplers,” *IEEE Trans. Microw. Theory Tech.*, vol. 59, no. 10 PART 1, pp. 2441–2446, 2011.
[41] K. Wincza and S. Gruszczynski, “A broadband 4×4 butler matrix for modern-day antennas,” *35th Eur. Microw. Conf. 2005 - Conf. Proc.*, vol. 2, pp. 1331–1334, 2005.
[42] C.-H. Chen, X.-P. Zhang, and J. Xu, “Implementation of a low-loss wide-band flat-topped beam-forming network based on Butler martix,” 2020.
[43] G. Tudosie, R. Vahldieck, and A. Lu, “A novel modularized folded highly compact LTCC Butler matrix,” *IEEE MTT-S Int. Microw. Symp. Dig.*, pp. 691–694, 2008.
[44] C. W. Wang, T. G. Ma, and C. F. Yang, “A new planar artificial transmission line and its applications to a Miniaturized Butler Matrix,” *IEEE Trans. Microw. Theory Tech.*, vol. 55, no. 12, pp. 2792–2801, 2007.
[45] Y. S. Jeong and Tae Wook Kim, “Design and analysis of swapped port coupler and its application in a miniaturized butler matrix,” *IEEE Trans. Microw. Theory Tech.*, vol. 58, no. 4, pp. 764–770, 2010.
[46] G. Tian, J. P. Yang, and W. Wu, “A novel compact Butler Matrix without phase shifter,” *IEEE Microw. Wirel. Components Lett.*, vol. 24, no. 5, pp. 306–308, 2014.
[47] W. Y. Chen, Y. R. Hsieh, C. C. Tsai, Y. M. Chen, C. C. Chang, and S. F. Chang, “A compact two-dimensional phased array using grounded coplanar-waveguides butler matrices,” *Eur. Microw. Week 2012 “sp. Microwaves”, EuMW 2012, Conf. Proc. - 42nd Eur. Microw. Conf. EuMC 2012*, pp. 747–750, 2012.
[48] M. Ben Kilani, M. Nedil, N. Kandil, and T. A. Denidni, “Novel wideband multilayer Butler matrix using CPW technology,” *IEEE Antennas Propag. Soc. AP-S Int. Symp.*, vol. 54, no. 1, pp. 499–507, 2012.
[49] T. Y. Chin, S. F. Chang, C. C. Chang, and J. C. Wu, “A 24-GHz CMOS butler matrix MMIC for multi-beam smart antenna systems,” *Dig. Pap. - IEEE Radio Freq. Integr. Circuits Symp.*, pp. 633–636, 2008.
[50] T. Y. Chin, S. F. Chang, J. C. Wu, and C. C. Chang, “A 25-GHz compact low-power phased-array receiver with continuous beam steering in CMOS technology,” *IEEE J. Solid-State Circuits*, vol. 45, no. 11, pp. 2273–2282, 2010.
[51] T. Y. Chin, J. C. Wu, S. F. Chang, and C. C. Chang, “A V-band 8 × 8 CMOS butler matrix MMIC,” *IEEE Trans. Microw. Theory Tech.*, vol. 58, no. 12 PART 1, pp. 3538–3546, 2010.
[52] B. Cetinoneri, Y. A. Atesal, and G. M. Rebeiz, “An 8 × 8 Butler matrix in 0.13-µm CMOS for 5-6-GHz multibeam applications,” *IEEE Transactions on Microwave Theory and Techniques*, vol. 59, no. 2. pp. 295–301, 2011.
[53] B. Cetinoneri *et al.*, “CMOS 4x4 and 8x8 Butler Matrices,” vol. 4, pp. 69–72, 2010.

[54] C. C. Chang, T. Y. Chin, J. C. Wu, and S. F. Chang, "Novel design of a 2.5-GHz fully integrated CMOS butler matrix for smart-antenna systems," *IEEE Trans. Microw. Theory Tech.*, vol. 56, no. 8, pp. 1757–1763, 2008.
[55] S. I. Yamamoto, J. Hirokawa, and M. Ando, "A Beam Switching Slot Array with a 4-Way Butler Matrix Installed in Single Layer Post-Wall Waveguides," *IEICE Trans. Commun.*, vol. E86-B, no. 5, pp. 1653–1659, 2003.
[56] A. Ali, N. Fonseca, F. Coccetti, and H. Aubert, "Novel two-layer broadband 4 x 4 butler matrix in SIW technology for Ku-band applications," *Proc. 2008 Asia Pacific Microw. Conf. APMC 2008*, pp. 25–28, 2008.
[57] A. B. Guntupalli, T. Djerafi, and K. Wu, "Two-Dimensional scanning antenna array driven by integrated waveguide phase shifter," *IEEE Trans. Antennas Propag.*, vol. 62, no. 3, pp. 1117–1124, 2014.
[58] N. Tiwari and T. R. Rao, "A switched beam antenna array with butler matrix network using substrate integrated waveguide technology for 60 GHz wireless communications," *AEU - Int. J. Electron. Commun.*, vol. 70, no. 6, pp. 850–856, 2016.
[59] S. Karamzadeh, V. Rafii, M. Kartal, and B. S. Virdee, "Compact and Broadband 4 x 4 SIW Butler Matrix with Phase and Magnitude Error Reduction," *IEEE Microw. Wirel. Components Lett.*, vol. 25, no. 12, pp. 772–774, 2015.
[60] Q. L. Yang, Y. L. Ban, K. Kang, C. Y. D. Sim, and G. Wu, "SIW Multibeam Array for 5G Mobile Devices," *IEEE Access*, vol. 4, pp. 2788–2796, 2016.
[61] Q. L. Yang, Y. L. Ban, J. W. Lian, Z. F. Yu, and B. Wu, "SIW Butler Matrix with Modified Hybrid Coupler for Slot Antenna Array," *IEEE Access*, vol. 4, pp. 9561–9569, 2016.
[62] Y. Li and K. M. Luk, "60-GHz Dual-Polarized Two-Dimensional Switch-Beam Wideband Antenna Array of Aperture-Coupled Magneto-Electric Dipoles," *IEEE Trans. Antennas Propag.*, vol. 64, no. 2, pp. 554–563, 2016.
[63] Y. Cao, K. S. Chin, W. Che, W. Yang, and E. S. Li, "A Compact 38 GHz Multibeam Antenna Array with Multifolded Butler Matrix for 5G Applications," *IEEE Antennas Wirel. Propag. Lett.*, vol. 16, pp. 2996–2999, 2017.
[64] Y. J. Cheng and Z. J. Xuan, "Two-dimensional beam scanning antenna array with 90-degree SIW twist," *2017 Int. Work. Antenna Technol. Small Antennas, Innov. Struct. Appl. iWAT 2017*, pp. 264–266, 2017.
[65] L. H. Zhong, Y. L. Ban, J. W. Lian, Q. L. Yang, J. Guo, and Z. F. Yu, "Miniaturized SIW Multibeam Antenna Array Fed by Dual-Layer 8 × 8 Butler Matrix," *IEEE Antennas Wirel. Propag. Lett.*, vol. 16, pp. 3018–3021, 2017.
[66] F. Ren, W. Hong, and K. Wu, "W-band series-connected patches antenna for multibeam application based on SIW Butler matrix," *2017 11th Eur. Conf. Antennas Propagation, EUCAP 2017*, pp. 198–201, 2017.
[67] Y. J. Cheng, W. Hong, and K. Wu, "A two-dimensional multibeam array antenna based on substrate integrated waveguide technology," *Proc. 2008 Asia Pacific Microw. Conf. APMC 2008*, pp. 1–4, 2008.
[68] Z. Chen, X. Wu, and F. Yang, "A Compact SIW Butler Matrix with Straight Delay Lines at 60 GHz," pp. 2141–2142, 2017.
[69] X. Li, M. Cai, H. Shen, and G. Yang, "A compact two-dimensional multi beam antenna fed by two-layer SIW butler matrix," *2017 IEEE Antennas Propag. Soc. Int. Symp. Proc.*, vol. 2017-Janua, pp. 305–306, 2017.
[70] and Q. X. Wanchen Yang, Yayang Yang, Wenquan Che, Chong Fan, "94-GHz Compact 2-DMultibeam LTCC Antenna Based on Multifolded SIW Beam-Forming Network," vol. 65, no. 8, pp. 4328–4333, 2017.

[71] M. K. Khattak *et al.*, "A Flat, Broadband and High Gain Beam-steering Antenna for 5G Communication M.," pp. 5–6, 2017.
[72] Y. Li, J. Wang, and K. M. Luk, "Millimeter-Wave MultiBeam Aperture-Coupled Magnetoelectric Dipole Array With Planar Substrate Integrated Beamforming Network for 5G Applications," *IEEE Trans. Antennas Propag.*, vol. 65, no. 12, pp. 6422–6431, 2017.
[73] J. W. Lian, Y. L. Ban, Q. L. Yang, B. Fu, Z. F. Yu, and L. K. Sun, "Planar Millimeter-Wave 2-D Beam-Scanning Multibeam Array Antenna Fed by Compact SIW Beam-Forming Network," *IEEE Trans. Antennas Propag.*, vol. 66, no. 3, pp. 1299–1310, 2018.
[74] P. Chen *et al.*, "A multibeam antenna based on substrate integrated waveguide technology for MIMO wireless communications," *IEEE Trans. Antennas Propag.*, vol. 57, no. 6, pp. 1813–1821, 2009.
[75] C. J. Chen and T. H. Chu, "Design of a 60-GHz substrate integrated waveguide Butler matrix-a systematic approach," *IEEE Trans. Microw. Theory Tech.*, vol. 58, no. 7 PART 1, pp. 1724–1733, 2010.
[76] T. Djerafi, N. J. G. Fonseca, and K. Wu, "Design and implementation of a planar 4 × 4 butler matrix in SIW technology for wide band high power applications," *40th Eur. Microw. Conf.*, no. 35, pp. 910–913, 2010.
[77] T. Djerafi, N. J. G. Fonseca, and K. Wu, "Design And Implementation Of A Planar 4 × 4 Butler Matrix In Siw Technology For Wide Band High Power Applications," *Prog. Electromagn. Res. B*, vol. 35, no. September, pp. 29–51, 2011.
[78] A. A. M. Ali, N. J. G. Fonseca, F. Coccetti, and H. Aubert, "Design and implementation of two-layer compact wideband butler matrices in siw technology for ku-band applications," *IEEE Trans. Antennas Propag.*, vol. 59, no. 2, pp. 503–512, 2011.
[79] T. Djerafi and K. Wu, "Multilayered Substrate Integrated Waveguide 4 x 4 Butler Matrix," *Wiley Period. Inc.*, pp. 210–224, 2011.
[80] T. Djerafi and K. Wu, "A low-cost wideband 77-ghz planar butler matrix in siw technology," *IEEE Trans. Antennas Propag.*, vol. 60, no. 10, pp. 4949–4954, 2012.
[81] D. Deslandes and W. Ke, "Accurate modeling, wave mechanisms, and design considerations of a substrate integrated waveguide," *IEEE Trans. Microw. Theory Tech.*, vol. 54, no. 6, pp. 2516–2526, 2006.
[82] M. Bozzi, "Substrate integrated waveguide (SIW) technology: New research trends for low-cost and eco-friendly wireless systems," pp. 1–1, 2012.
[83] S. Sirci *et al.*, "Design and Multiphysics Analysis of Direct and Cross-Coupled SIW Combline Filters Using Electric and Magnetic Couplings," *IEEE Trans. Microw. Theory Tech.*, vol. 63, no. 12, pp. 4341–4354, 2015.
[84] Y. Shen, H. Wang, W. Kang, and W. Wu, "Dual-band SIW differential bandpass filter with improved common-mode suppression," *IEEE Microw. Wirel. Components Lett.*, vol. 25, no. 2, pp. 100–102, 2015.
[85] D. F. Guan, Z. P. Qian, Y. S. Zhang, and Y. Cai, "A hybrid SIW and GCPW guided-wave structure coupler," *IEEE Microw. Wirel. Components Lett.*, vol. 24, no. 8, pp. 518–520, 2014.
[86] J. X. Chen, W. Hong, Z. C. Hao, H. Li, and K. Wu, "Development of a low cost microwave mixer using a broad-band Substrate Integrated Waveguide (SIW) coupler," *IEEE Microw. Wirel. Components Lett.*, vol. 16, no. 2, pp. 84–86, 2006.
[87] D. Chaturvedi, A. Kumar, and S. Raghavan, "An Integrated SIW Cavity-Backed Slot Antenna-Triplexer," *IEEE Antennas Wirel. Propag. Lett.*, vol. 17, no. 8, pp. 1557–1560, 2018.

[88] Z. Zhang, X. Cao, J. Gao, S. Li, and J. Han, "Broadband SIW Cavity-Backed Slot Antenna for Endfire Applications," *IEEE Antennas Wirel. Propag. Lett.*, vol. 17, no. 7, pp. 1271–1275, 2018.
[89] G. Acri, "Sensibilité à la technologie et accordabilité des matrices de Butler en guide intégré dans le substrat , déclinées sur substrat PCB à 28 GHz et sur interposer above-IC benzocyclobutène aux fréquences millimétriques," 2020.
[90] M. BERTRAND, "Guides à ondes lentes intégrés dans le substrat pour les applications en bandes RF et millimétriques," 2017.
[91] F. Xu and K. Wu, "Guided-wave and leakage characteristics of substrate integrated waveguide," *IEEE Trans. Microw. Theory Tech.*, vol. 53, no. 1, pp. 66–72, 2005.
[92] A. T. HO, "Contribution of the slow-wave effect for antenna miniaturization and humidity sensor applications."
[93] D. Deslandes, "Etude et développement du guide d'ondes intégré au substrat pour la conception de systèmes en ondes millimétriques."
[94] Y. Cassivi, L. Perregrini, P. Arcioni, M. Bressan, K. Wu, and G. Conciauro, "Dispersion characteristics of substrate integrated rectangular waveguide," *IEEE Microw. Wirel. Components Lett.*, vol. 12, no. 9, pp. 333–335, 2002.
[95] S. B. Cohn, "Properties of Ridge Wave Guide," *Proc. IRE*, vol. 35, no. 8, pp. 783–788, 1947.
[96] Y. Ding and K. Wu, "Substrate integrated waveguide-to-microstrip transition in multilayer substrate," *IEEE Trans. Microw. Theory Tech.*, vol. 55, no. 12, pp. 2839–2844, 2007.
[97] M. Bozzi, S. A. Winkler, and K. Wu, "Broadband and compact ridge substrate-integrated waveguides," *IET Microwaves, Antennas Propag.*, vol. 4, no. 11, pp. 1965–1973, 2010.
[98] W. Che, C. Li, P. Russer, and Y. L. Chow, "Propagation and band broadening effect of planar integrated ridged waveguide in multilayer dielectric substrates," *IEEE MTT-S Int. Microw. Symp. Dig.*, pp. 217–220, 2008.
[99] Y. L. Chow and W. Che, "Successive SIW (substrate integrated waveguides) types for width reductions by physical reasoning and formulas by analytical (use of) MoM," *2008 Int. Conf. Microw. Millim. Wave Technol. Proceedings, ICMMT*, vol. 4, pp. 1746–1749, 2008.
[100] T. R. Jones, M. H. Zarifi, and M. Daneshmand, "Miniaturized Quarter-Mode Substrate Integrated Cavity Resonators for Humidity Sensing," *IEEE Microw. Wirel. Components Lett.*, vol. 27, no. 7, pp. 612–614, 2017.
[101] W. L. Barrow and H. Schaevitz, "Hollow pipes of relatively small dimensions," vol. 60, no. March, pp. 119–122, 1941.
[102] N. Grigoropoulos and P. R. Young, "Compact folded waveguides," *Conf. Proceedings- Eur. Microw. Conf.*, vol. 2, pp. 973–976, 2004.
[103] A. Doghri, A. Ghiotto, T. Djerafi, and K. Wu, "Corrugated SIW L-folded antipodal parabolic tapered slot antenna," *Asia-Pacific Microw. Conf. Proceedings, APMC*, pp. 893–895, 2012.
[104] N. Nguyen-Trong, T. Kaufmann, L. Hall, and C. Fumeaux, "Variational Analysis of Folded Substrate-Integrated Waveguides," *IEEE Microw. Wirel. Components Lett.*, vol. 25, no. 6, pp. 352–354, 2015.
[105] D. W. Kim and J. H. Lee, "A partial h-plane waveguide as a new type of compact waveguide," *Microwave and Optical Technology Letters*, vol. 43, no. 5. pp. 426–428, 2004.
[106] W. Che, L. Geng, K. Wu, and Y. L. Chow, "Theoretical investigation and experimental verification of compact folded substrate integrated waveguide," *Proc.*

37th Eur. Microw. Conf. EUMC, no. October, pp. 380–383, 2007.
[107] W. Che, L. Geng, K. Deng, and Y. L. Chow, "Analysis and experiments of compact folded substrate-integrated waveguide," *IEEE Trans. Microw. Theory Tech.*, vol. 56, no. 1, pp. 88–93, 2008.
[108] W. Shen, W. Y. Yin, and X. W. Sun, "Miniaturized dual-band substrate integrated waveguide filter with controllable bandwidths," *IEEE Microw. Wirel. Components Lett.*, vol. 21, no. 8, pp. 418–420, 2011.
[109] L. Huang and S. Zhang, "Ultra-Wideband Ridged Half-Mode Folded Substrate-Integrated Waveguide Filters," *IEEE Microw. Wirel. COMPONENTS Lett.*, vol. 28, no. 7, pp. 579–581, 2018.
[110] B. Sanz Izquierdo, P. R. Young, N. Grigoropoulos, J. C. Batchelor, and R. J. Langley, "Slot antenna on C type compact substrate integrated waveguide," *35th Eur. Microw. Conf. 2005 - Conf. Proc.*, vol. 1, pp. 469–472, 2005.
[111] Y. Ding and K. Wu, "Miniaturized hybrid ring circuits using T-Type Folded Substrate Integrated Waveguide (TFSIW)," *IEEE MTT-S Int. Microw. Symp. Dig.*, pp. 705–708, 2009.
[112] M. S. Mahani and G. W. Roberts, "A mmWave Folded Substrate Integrated Waveguide in a 130-nm CMOS Process," *IEEE Trans. Microw. Theory Tech.*, vol. 65, no. 8, pp. 2775–2788, 2017.
[113] H. Y. Chien, T. M. Shen, T. Y. Huang, W. H. Wang, and R. B. Wu, "Miniaturized bandpass filters with double-folded substrate integrated waveguide resonators in LTCC," *IEEE Trans. Microw. Theory Tech.*, vol. 57, no. 1, pp. 1774–1782, 2009.
[114] R. Zhang, Z. Wang, B. Yan, and R. Xu, "FSIW cavity filter and derivative FSIW cavity and its filters with LTCC technology," *APMC 2009 - Asia Pacific Microw. Conf. 2009*, pp. 1360–1363, 2009.
[115] L. S. Wu, X. L. Zhou, and W. Y. Yin, "A novel multilayer partial h-plane filter implemented with folded substrate integrated waveguide (FSIW)," *IEEE Microw. Wirel. Components Lett.*, vol. 19, no. 8, pp. 494–496, 2009.
[116] B. Liu, W. Hong, L. Tian, H. B. Zhu, W. Jiang, and K. Wu, "Half Mode Substrate Integrated Waveguide (HMSIW) multi-way power divider," *Asia-Pacific Microw. Conf. Proceedings, APMC*, vol. 2, pp. 917–920, 2006.
[117] W. Hong *et al.*, "Half mode substrate integrated waveguide: A new guided wave structure for microwave and millimeter wave application," *IRMMW-THz 2006 - 31st Int. Conf. Infrared Millim. Waves 14th Int. Conf. Terahertz Electron.*, p. 219, 2006.
[118] J. Chen, W. Hong, P. Yan, B. Liu, Y. Wang, and K. Wu, "Design of a six-port junction using half-mode substrate integrated waveguide," *Asia-Pacific Microw. Conf. Proceedings, APMC*, pp. 12–15, 2007.
[119] B. Liu, W. Hong, Y.-Q. Wang, Q.-H. Lai, and K. Wu, "Half Mode Substrate Integrated Waveguide (HMSIW) 3-dB Coupler," *IEEE Microw. Wirel. COMPONENTS Lett.*, vol. 17, no. 1, pp. 22–24, 2007.
[120] B. Liu, W. Hong, Y. Zhang, J. X. Chen, and K. Wu, "Half-mode substrate integrated waveguide (HMSIW) double-slot coupler," *Electron. Lett.*, vol. 43, no. 2, pp. 113–114, 2007.
[121] S. Moscato, C. Tomassoni, M. Bozzi, and L. Perregrini, "Quarter-Mode Cavity Filters in Substrate Integrated Waveguide Technology," *IEEE Trans. Microw. Theory Tech.*, vol. 64, no. 8, pp. 2538–2547, 2016.
[122] P. Li, H. Chu, and R. S. Chen, "Design of compact bandpass filters using quarter-mode and eighth-mode SIW cavities," *IEEE Trans. Components, Packag. Manuf. Technol.*, vol. 7, no. 6, pp. 956–963, 2017.

[123] K. Gong, W. Hong, J. Chen, H. Tang, D. Hou, and Y. Zhang, "Novel Compact Bandpass Filter Based on Folded Half Mode Substrate Integrated Waveguide Cavities," *J. Electromagn. Eng. Sci.*, vol. 10, no. 3, pp. 179–182, 2010.
[124] O. Caytan *et al.*, "Half-Mode Substrate-Integrated-Waveguide Cavity-Backed Slot Antenna on Cork Substrate," *IEEE Antennas Wirel. Propag. Lett.*, vol. 15, pp. 162–165, 2016.
[125] C. Jin, R. Li, A. Alphones, and X. Bao, "Quarter-mode substrate integrated waveguide and its application to antennas design," *IEEE Trans. Antennas Propag.*, vol. 61, no. 6, pp. 2921–2928, 2013.
[126] A. Niembro-Martín *et al.*, "Slow-wave substrate integrated waveguide," *IEEE Trans. Microw. Theory Tech.*, vol. 62, no. 8, pp. 1625–1633, 2014.
[127] H. Jin, K. Wang, J. Guo, S. Ding, and K. Wu, "Slow-Wave Effect of Substrate Integrated Waveguide Patterned with Microstrip Polyline," *IEEE Trans. Microw. Theory Tech.*, vol. 64, no. 6, pp. 1717–1726, 2016.
[128] H. Jin, Y. Zhou, Y. M. Huang, and K. Wu, "Slow-wave propagation properties of substrate integrated waveguide based on anisotropic artificial material," *IEEE Trans. Antennas Propag.*, vol. 65, no. 9, pp. 4676–4683, 2017.
[129] X. Shen, T. Jun, D. Martin-cano, and F. J. Garcia-vidal, "Conformal surface plasmons propagating on ultrathin and flexible films," pp. 1–6, 2012.
[130] P. P. Structure, L. Ji, X. Li, and J. Mao, "Half-Mode Substrate Integrated Waveguide Dispersion Tailoring Using 2 . 5-D Spoof Surface," vol. 68, no. 7, pp. 2539–2550, 2020.
[131] P. Chen, L. Li, K. Yang, Q. Chen, and S. Member, "Hybrid Spoof Surface Plasmon Polariton and Substrate Integrated Waveguide Broadband Bandpass Filter With Wide Out-of-Band Rejection," vol. 28, no. 11, pp. 2018–2020, 2018.
[132] P. P. Structure *et al.*, "Slow-Wave Half-Mode Substrate Integrated Waveguide Using Spoof Surface," vol. 66, no. 6, pp. 2946–2952, 2018.
[133] N. Bayat-makou and A. A. Kishk, "Contactless Air-Filled Substrate Integrated Waveguide," vol. 66, no. 6, pp. 2928–2935, 2018.
[134] A. Belenguer, H. Esteban, and V. E. Boria, "Novel empty substrate integrated waveguide for high-performance microwave integrated circuits," *IEEE Trans. Microw. Theory Tech.*, vol. 62, no. 4, pp. 832–839, 2014.
[135] F. Parment, A. Ghiotto, T. P. Vuong, J. M. Duchamp, and K. Wu, "Air-filled substrate integrated waveguide for low-loss and high power-handling millimeter-wave substrate integrated circuits," *IEEE Trans. Microw. Theory Tech.*, vol. 63, no. 4, pp. 1228–1238, 2015.
[136] F. Parment, S. Member, A. Ghiotto, and S. Member, "Air-to-Dielectric-Filled Two-Hole Substrate- Integrated Waveguide Directional Coupler," vol. 27, no. 7, pp. 621–623, 2017.
[137] F. Parment, A. Ghiotto, T. P. Vuong, J. M. Duchamp, and K. Wu, "Broadband directional Moreno coupler for high-performance air-filled SIW-based Substrate Integrated Systems," *IEEE MTT-S Int. Microw. Symp. Dig.*, vol. 2016-August, pp. 15–17, 2016.
[138] N. Nguyen, A. Ghiotto, T. Vuong, A. Vilcot, F. Parment, and K. Wu, "Slab Air-Filled Substrate Integrated Waveguide," no. 5, pp. 2018–2021, 2018.
[139] F. Parment, A. Ghiotto, T. P. Vuong, J. M. Duchamp, and K. Wu, "Double Dielectric Slab-Loaded Air-Filled SIW Phase Shifters for High-Performance Millimeter-Wave Integration," *IEEE Trans. Microw. Theory Tech.*, vol. 64, no. 9, pp. 2833–2842, 2016.
[140] T. Martin, A. Ghiotto, T. P. Vuong, F. Lotz, and P. Monteil, "High performance

air-filled substrate integrated waveguide filter post-process tuning using capacitive post," *IEEE MTT-S Int. Microw. Symp. Dig.*, pp. 196–199, 2017.
[141] F. Parment, A. Ghiotto, T. P. Vuong, J. M. Duchamp, and K. Wu, "Low-loss air-filled Substrate Integrated Waveguide (SIW) band-pass filter with inductive posts," *Eur. Microw. Week 2015 "Freedom Through Microwaves", EuMW 2015 - Conf. Proceedings; 2015 45th Eur. Microw. Conf. Proceedings, EuMC*, pp. 761–764, 2015.
[142] T. Martin, A. Ghiotto, T. P. Vuong, and F. Lotz, "Self-temperature-compensated air-filled substrate-integrated waveguide cavities and filters," *IEEE Trans. Microw. Theory Tech.*, vol. 66, no. 8, pp. 3611–3621, 2018.
[143] C. Tomassoni, L. Silvestri, M. Bozzi, L. Perregrini, and A. Ghiotto, "A novel filter based on a dual-mode air-filled substrate integrated waveguide cavity resonator," *2017 IEEE MTT-S Int. Conf. Numer. Electromagn. Multiphysics Model. Optim. RF, Microwave, Terahertz Appl. NEMO 2017*, pp. 290–292, 2017.
[144] Q. Van Den Brande, S. Lemey, J. Vanfleteren, and H. Rogier, "Highly Efficient Impulse-Radio Ultra-Wideband Cavity-Backed Slot Antenna in Stacked Air-Filled Substrate Integrated Waveguide Technology," *IEEE Trans. Antennas Propag.*, vol. 66, no. 5, pp. 2199–2209, 2018.
[145] A. Ghiotto, F. Parment, T. P. Vuong, and K. Wu, "Millimeter-Wave Air-Filled SIW Antipodal Linearly Tapered Slot Antenna," *IEEE Antennas Wirel. Propag. Lett.*, vol. 16, pp. 768–771, 2017.
[146] F. Parment, A. Ghiotto, T.-P. Vuong, J.-M. Duchamp, and K. Wu, "Millimetre-wave air-filled substrate integrated waveguide slot array antenna," *Electron. Lett.*, vol. 53, no. 11, pp. 704–706, 2017.
[147] M. Ndoye, I. Kerroum, D. Deslandes, and F. Domingue, "Air-filled substrate integrated cavity resonator for humidity sensing," *Sensors Actuators, B Chem.*, vol. 252, pp. 951–955, 2017.
[148] A. Tuho, M. Ndoye, P. Ferrari, F. Domingue, and E. Pistono, "Miniaturized Humidity Sensor Based on a Partially Air-Filled Slow-Wave SIW Resonator," *2018 48th Eur. Microw. Conf. EuMC 2018*, pp. 640–643, 2018.
[149] J. Coonrod and R. Corporation, "Understanding Circuit Material Performance Concerns for PCBs at Millimeter- Wave Frequencies."
[150] M. Sunohara, H. Sakaguchi, A. Takano, R. Arai, K. Murayama, and M. Higashi, "Studies on electrical performance and thermal stress of a silicon interposer with TSVs," *Proc. - Electron. Components Technol. Conf.*, pp. 1088–1093, 2010.
[151] S. W. Ho, S. W. Yoon, Q. Zhou, K. Pasad, V. Kripesh, and J. H. Lau, "High RF performance TSV silicon carrier for high frequency application," *Proc. - Electron. Components Technol. Conf.*, pp. 1946–1952, 2008.
[152] V. Sukumaran, T. Bandyopadhyay, V. Sundaram, and T. Rao, "Low-cost thin glass interposers as a superior alternative to silicon and organic interposers for packaging of 3-D ICs," *IEEE Trans. Components, Packag. Manuf. Technol.*, vol. 2, no. 9, pp. 1426–1433, 2012.
[153] S. Cho, V. Sundaram, R. R. Tummala, and Y. K. Joshi, "Impact of Copper Through-Package Vias on Thermal Performance of Glass Interposers," *IEEE Trans. Components, Packag. Manuf. Technol.*, vol. 5, no. 8, pp. 1075–1084, 2015.
[154] L. Brusberg, H. Schröder, M. Töpper, and H. Reichl, "Photonic system-in-package technologies using thin glass substrates," *Proc. Electron. Packag. Technol. Conf. EPTC*, pp. 930–935, 2009.
[155] A. Usman *et al.*, "Interposer Technologies for High-Performance Applications," *IEEE Trans. Components, Packag. Manuf. Technol.*, vol. 7, no. 6, pp. 819–828,

2017.
[156] K. Oi *et al.*, “Development of new 2.5D package with novel integrated organic interposer substrate with ultra-fine wiring and high density bumps,” *Proc. - Electron. Components Technol. Conf.*, pp. 348–353, 2014.
[157] M. V. Pelegrini *et al.*, “Interposer based on metallic-nanowire-membrane (MnM) for mm-wave applications,” *Eur. Microw. Week 2016 “Microwaves Everywhere”, EuMW 2016 - Conf. Proceedings; 46th Eur. Microw. Conf. EuMC 2016*, pp. 1461–1464, 2016.
[158] H. Masuda and K. Fukuda, “Ordered metal nanohole arrays made by a two-step replication of honeycomb structures of anodic alumina,” *Science*, vol. 268, no. 5216. pp. 1466–1468, 1995.
[159] J. M. Pinheiro *et al.*, “110-GHz Through-Substrate-Via Transition Based on Copper Nanowires in Alumina Membrane,” *IEEE Trans. Microw. Theory Tech.*, vol. 66, no. 2, pp. 784–790, 2018.
[160] A. L. C. Serrano *et al.*, “Modeling and characterization of slow-wave microstrip lines on metallic-nanowire- filled-membrane substrate,” *IEEE Trans. Microw. Theory Tech.*, vol. 62, no. 12, pp. 3249–3254, 2014.
[161] A. L. C. Serrano *et al.*, “Slow-wave microstrip line on nanowire-based alumina membrane,” *IEEE MTT-S Int. Microw. Symp. Dig.*, pp. 8–11, 2014.
[162] A. S. Grimault-Jacquin *et al.*, “Characteristics of Coplanar Waveguide of Small Cross Section on BCB with Coplanar Ground to Conductor-Backed Plane Interconnection,” *J. Infrared, Millimeter, Terahertz Waves*, vol. 40, no. 10, pp. 1010–1020, 2019.
[163] P. Franck, D. Baillargeat, and B. K. Tay, “A bulk equivalent model of carbon-nanotube arrays : Application to the design of novel antennas,” *2014 Int. Conf. Numer. Electromagn. Model. Optim. RF, Microwave, Terahertz Appl. NEMO 2014*, pp. 3–6, 2014.
[164] C. Brun, “Carbon nanotubes based nanopackaging dedicated to innovative high frequency interconnections,” Limoges, 2013.
[165] M. Cometto *et al.*, “Theoretical study of CNT based waveguide,” *2018 IEEE MTT-S Int. Conf. Numer. Electromagn. Multiphysics Model. Optim. NEMO 2018*, pp. 18–20, 2018.
[166] Philippe ROUX-LEVY, “Nanostructures de carbone dédiées aux interconnexions hautes fréquences,” 2018.

Chapter 2. Carbon nanotube overview

Carbon nanotubes (CNTs) have been known as the most researched and studied material in 20th century. Whereas the first observation of CNTs was made in 1952 by two Soviet scientists L.V. Radushkevich and V.M. Lukyanovich [1], CNTs were officially discovered 39 years after by S. Iijima when synthesizing fullerenes by using arc discharge technique in 1991 [2]. Since that, CNTs have been researched in various fields, for examples in display technology [3], solar energy harvesting [4], [5], or even in drug delivery [6]. Besides, CNTs are considered as a concurrent material to metal on many applications in micro-/nano-electronics, spintronics, optics as well as material science, mechanical and biological fields due to their high conductivity, physical strength, high aspect ratio and lightness [7], [8].

Therefore, in this chapter, a summary of essential background of CNTs in the scope of the thesis will be given. In section 2.1, some CNT properties are briefly presented. The growth techniques employed by the laboratory CINTRA-Singapore, who is in charge of the device fabrication in the framework of the French ANR TRICOT project, are described in section 2.2. Then, CNT electromagnetic modeling for full-wave simulation is introduced in section 2.3. Finally, some electronic applications using CNTs are detailed in section 2.4.

2.1 Carbon nanotube properties

2.1.1 Physics of carbon nanotubes

Carbon nanotubes can be categorized into two types: single-wall carbon nanotubes (SWCNTs) and multi-wall carbon nanotubes (MWCNTs) [7].

2.1.1.1 Single-wall carbon nanotubes

SWCNTs can be scrutinized as a monolayer hexagonal lattice of carbon atoms composed of a single long wrapped graphene sheet, with a diameter ranging from 1 to several nm depending on the growth mechanism [9]. They can be illustrated by a chiral vector $\overrightarrow{C_h}$ corresponding to the direction to which the graphene sheet is rolled up. A couple of indices (n and m which are integers) defines the chiral vector $\overrightarrow{C_h} = n\overrightarrow{a_1} + \overrightarrow{ma_2}$ which along two directions ($\overrightarrow{a_1}$ and $\overrightarrow{a_2}$, respectively) in the honeycomb crystal lattice of graphene (Figure 2-1). The smallest theoretical SWCNT identified so far has a 0.47-nm diameter [10] (chirality of (n, m)=(6,0)), and the SWCNT diameter is calculated by [7]:

$$D = \frac{\sqrt{3}}{\pi} \times b \times \sqrt{m^2 + m \cdot n + n^2} \tag{2-1}$$

with b=0.142 nm is the distance between two consecutive carbon atoms.

Depending on the relationship between n and m, three configurations of the CNT can be defined leading to two particular behaviors (metallic or semiconductor):

- If $m = n$, the nanotube has a “armchair” type structure: metallic
- If $m = 0$, the nanotube has a “zig-zag” type structure: semiconductor
- In all other cases, the nanotube is “chiral”: semiconductor

Theoretically, by controlling the chirality of CNTs, the nature of CNTs can be defined [11]–[13]. However, currently, this chirality is not perfect controlled due to the growth mechanisms.

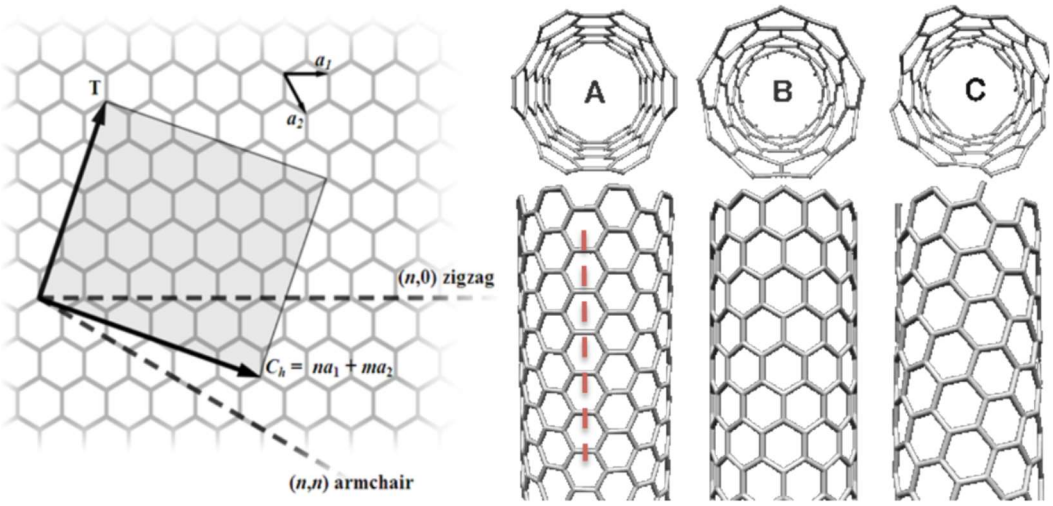

Figure 2-1. (a) Definition of the chirality vector $\overrightarrow{C_h}$ on a graphene sheet structure. (b) Three different configurations of CNTs: "A" conductive armchair, "B" semi-conductive zig-zag, and "C" semi-conductive random chiral [14].

2.1.1.2 Multi-wall carbon nanotubes

The multi-wall carbon nanotube (MWCNT) consists of several imbricated rolled up sheets of graphene (shells) which interweave one inside the other like a Russian doll (Figure 2-2) [15]. The diameter of these CNTs usually ranges between 10 and 100 nm with an interspace between the adjacent shells equal to the Van der Waals length ($d = 0.34\ nm$). It must be noted that the internal carbon nanotubes have not only different sizes but also their own chirality.

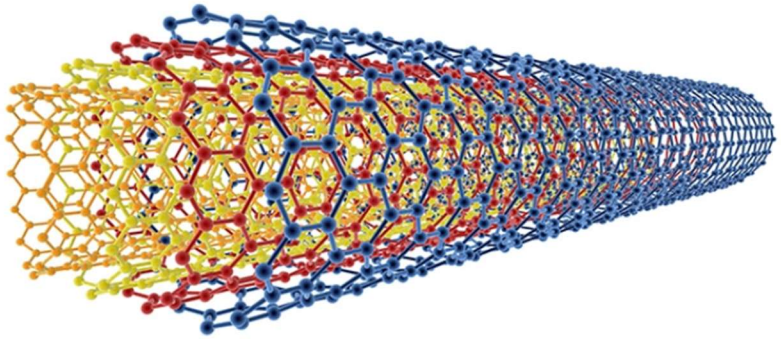

Figure 2-2. A multi-wall carbon nanotube [16].

In a MWCNT, the inner tube diameter is about half the outer one [7], (i.e. $D_{max}/2$ and D_{max},) and the number of shells p can be obtained for a minimum outer diameter of 3 nm by:

$$p = 1 + int\left(\frac{D_{max} - \frac{D_{max}}{2}}{2d}\right) \quad (2\text{-}2)$$

For example, 15 shells are obtained for a 20-nm diameter.

Besides, a MWCNT, which has more than three walls, has a high possibility to be conductive. Indeed, it was proven that if only one wall in a MWCNT is metallic, the entire MWCNT is metallic [7],[17]. Moreover, among the three categories of chirality: "zig-zag", "armchair" and "chiral", the "armchair" configuration is always metallic. Hence, if these three configurations appear equally in a MWCNT, then each wall has a possibility to be metallic of 1/3.

2.1.2 Intrinsic properties of carbon nanotubes

2.1.2.1 Electrical properties

As described in [7], the CNT conduction is quantized, leading to electron moves through discrete conduction channels. Depending on the value of mean free path (MFP) and the length of the conductor, this conduction is either ballistic or diffusive. The MFP is the average distance, which is travelled by a moving particle before successive colliding to another particle. When the length of a conductor is smaller than the value of MFP, the electron transport is ballistic, otherwise it is diffusive [7].

In CNTs, the electrons move at a speed that is almost equal to the speed of light (3.10^8 m/s), leading to the MFP determined in [18]:

$$MFP = \frac{2\sqrt{3}\pi V^2 r}{2\sigma_E^2 + 9\sigma_t^2} \quad (2\text{-}3)$$

with σ_E and σ_t are the variances of the on-site energy E and V is the nearest-neighbor tight-binding parameter (V= -2.7 eV [19]), and r is the CNT radius.

The MFP can be considered approximately as proportional to the radius r of CNT and therefore to its diameter D. For a CNT of diameter 1 nm, the MFP is 1 µm, leading to the following equation:

$$MFP \approx 1000D \quad (2\text{-}4)$$

As described in [20], a long MFP ranging from 1 to 25 µm could be found in CNTs. Meanwhile in bulk material, the electron transport is diffusive (Figure 2-3), thus the electron is able to propagate in all directions and consequently MFP is extremely low (about 38 nm in gold and about 40 nm in copper) as compared to the case of CNTs.

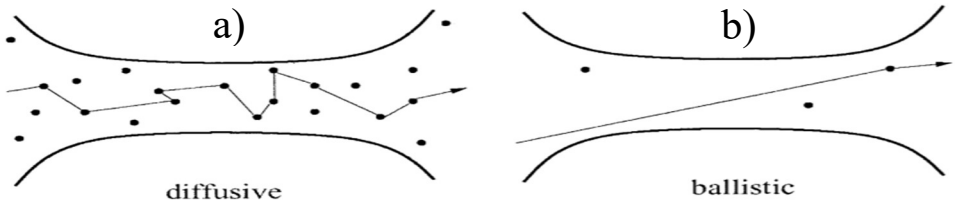

Figure 2-3. a) Diffusive electron conduction in a 3-D material and b) Anisotropic ballistic transport of the electron in 1-D material as CNT [21].

The MFP value is bigger for MWCNT than for SWCNT due to the relationship between MFP and tube diameter as shown in (2-4). In [20], for a MWCNT, a 25-µm MFP was found.

Due to the high value of MFP in carbon nanotubes compared to bulk materials, the usual electrical conductivity of SWCNT is $10^8\ S.m^{-1}$ and can reach up to $10^{10}\ S.m^{-1}$ for MWCNT, which is much higher than copper and gold [22]. Moreover, a maximum current density greater than 10^9 A/cm² can be obtained in carbon nanotubes [23]. Table

2-1 presents the main CNTs properties versus copper, showing that CNTs could be a very promising conductive material for next generation of electronics applications.

	Copper	SWCNT	MWCNT
Max. current density (A/cm^2)	10^5	10^9 [23]	10^9 [23]
Thermal conductivity (W/mK)	385	5800 [24]	3000 [25]
Mean free path (nm) @ 300 K	40	>1000	>25000
Max. electrical conductivity ($S.m^{-1}$)	$5{,}96.10^7$	10^8 [26]	$10^8 \sim 10^{10}$
Young's modulus (GPa)	128	1500	1500

Table 2-1. Comparison of general properties between carbon nanotubes and gold [27].

2.1.2.2 Thermal properties

Carbon-based materials (diamonds and graphite) possess an excellent thermal conductivity compared to any known material at moderate temperature [7], which is the case too, for carbon nanotubes. While thermal conductivity depends on the movement of electrons to conduct heat in metals, the CNTs thermal conduction is provided thanks to the vibration of the covalent bonds holding the carbon atoms together [28]; the atoms themselves are wiggling around and transmitting the heat through the CNTs. The excellent strength of the carbon bond helps transmit this vibration throughout the nanotube, leading to an excellent thermal conductivity. A very high room-temperature thermal conductivity in carbon nanotubes ranging from 1750 to 5800 W/mK [25], [29], [30] was obtained, as compared to other materials such as silicon (84 W/mK), gold (318 W/mK) and copper (400 W/mK), leading to high potentialities in terms of heat dissipation [31].

2.1.2.3 Mechanical properties

As discussed previously, CNTs are based on rolled-up sheets of a monolayer hexagonal lattice of carbon atoms, in which each atom is connected to the others through a strong chemical covalent sp^2 bond [7]. Hence, as shown in [32], CNTs are the strongest and toughest materials yet discovered in term of tensile strength and elastic modulus due to this strong bond. This bond is even stronger than the sp^3 bond found in diamond, one of the hardest materials. In [33], a tensile strength of 63 GPa was obtained for a MWCNT. Although the strength of individual CNT shells is extremely high, weak shear interactions between adjacent shells, tubes, bundles, and matrix material lead to a significant reduction in the effective strength of multiwall carbon nanotubes and carbon nanotube bundles down to only a few GPa [34]. This limitation has been recently addressed and effectively increases the strength of these materials to ≈ 60 GPa for multiwall carbon nanotube and ≈17 GPa for double-walled carbon nanotube bundles [34].

Besides, CNT possesses a good property of elasticity: it returns to its original structure without damaging after taking an external force [35], [36]. A CNT is able to be bended up to an angle greater than 45° [35], [37] without breaking (Figure 2-4). A MWCNT has a capacity to bend up to an angle of 110° without permanent damage [38]. Nevertheless, they can buckle under very high compressive, torsional, or bending stress [39]. It must be noted that the electrical performance of CNTs is affected by bending them.

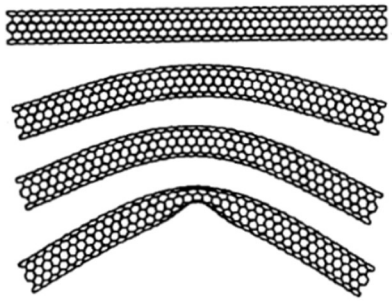

Figure 2-4. Structure of bending nanotubes calculated by Rochefort et al.[40]

From top to bottom: CNT bended at 0, 30, 45 and 60°.

2.2 Carbon nanotubes fabrication

Three main methods to realize the CNT synthesis can be found in the literature.

Firstly, the arc discharge method was used in 1991. It is the most used for CNTs production due to its simplicity to launch [2].

Secondly, the laser ablation (or laser vaporization) was discovered in 1995 [41], where a high power pulsed laser was use to vaporize a target of metal-graphite composite under high temperature and controlled pressure.

Thirdly, the chemical vapor deposition (CVD) was developed for CNTs growth. Due to a better control in growth and good understanding of the CVD process, the catalyst CVD has been widely considered in research groups to synthesize CNTs. Since 1993 [42], a lot of methods have been proposed to improve the purity and the direction, size, diameter control of the CNTs: thermal CVD (TCVD) [43], plasma enhanced CVD (PECVD) oxygen assisted [44], water assisted [45], microwave plasma-enhanced (MPECVD) [46], radio frequency plasma-enhanced (RF-CVD) [47], or hot-filament CVD (HFCVD) [48].
In Table 2-2, arc discharge, laser ablation, TCVD and PECVD techniques are compared with their pros and cons.

Method	Process difficulty	Process temperature	Quality of growth	CNT homogeneity and its parameters
Arc discharge	Easy and repeatable High temperature	3700 °C	CNT purity > 90 %	• Random length • Random diameter • No vertically aligned CNTs • No possible patterned
Laser ablation	Easy and repeatable Medium temperature	1300 °C	CNT purity > 90 %	• Random length • Random diameter • No vertically aligned CNTs • No possible patterned
TCVD	Numerous sensitive processing parameters (temperature, pressure, time, gas flow rate, catalyst, etc)	700-900 °C	Good quality (>75% of purity)	• SWCNTs and MWCNTs • Very dense bundle • Long CNTs (up to mm) • CNT verticality by the VDW forces • Quite homogeneous CNTs (length and diameter)
PECVD	Numerous sensitive processing parameters (temperature, pressure, time, gas flow rate, catalyst, etc) + plasma requirement	550-700 °C	Low quality	• Only MWCNTs • Low dense bundle • Short CNTs (up to 50 µm) • Very good vertically aligned CNTs due to plasma • Quite homogeneous CNTs (length and diameter)

Table 2-2. Summary of CNT growth techniques [27].

From this table, it can be noted that a higher CNT purity can be obtained by arc discharge or laser ablation as compared to CVD techniques. Nevertheless, those methods do not allow obtaining a vertical alignment. Hence, due to several reasons (lower process temperature, high production availability for equipment tools in microelectronics, lower cost and ease of scale-up), and since vertically aligned CNTs are expected in the framework of this ANR project, the CVD methods will be considered. This technique allows a good growth flexibility in terms of parameters control, various usable substrates, CNTs forms and direction [27]. This technique also enables the realization of the various patterns that we require. Prior to our collaboration with CINTRA/NTU, TCVD and PECVD had been compared in terms of CNT growth characteristics, by the team that is composed by Yap Chin Chong, Li Hong, Dunlin Tan and Chow Wei Leong, and directed by Prof. Tay Beng Kang. Advantages and drawbacks observed by this group are

summarized in Table 2-3 [27]. Due to the purity of CNTs in acceptable or even high quality, repeatable CNT growth via thermal CVD was proposed. The detailed method could be found in the thesis of C. Brun [27].

	SWCNTs	MWCNTs
Thermal CVD	• High CNTs quality • Dense CNT bundle (up to $10^{14-15}m^{-2}$) • Long CNTs (up to mm with super growth and up to 350 µm with normal growth) • Small patterns (5 µm) 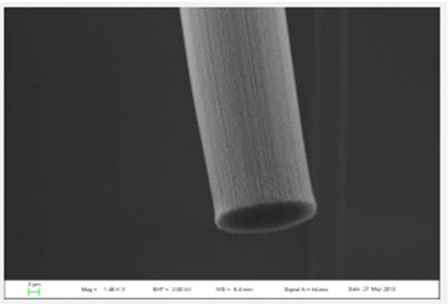	• Acceptable quality of CNTs • Lower CNT density (up to $10^{13}m^{-2}$) • Long CNTs (up to 1,7 mm with super growth and up to 350 µm with normal growth) • Big diameters (from 50 to 350 nm) • Small patterns (5 µm) 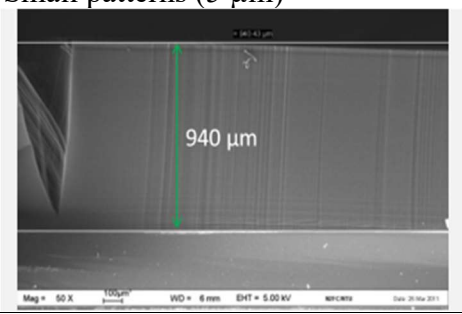
Plasma enhanced CVD	Under investigation by other groups	• Low CNTs quality • Low CNTs density (up to $10^{10}m^{-2}$) • Short CNTs (up to 30 µm) • Big diameters (from 50 to 350 nm) • Small patterns (5 µm) 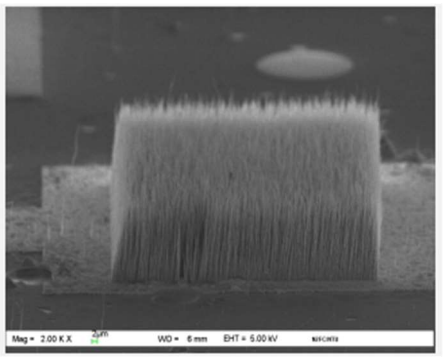

Table 2-3. CNT growth capabilities achieved at CINTRA/NTU [27].

In the next part of this chapter, an explanation of CNT modeling used for DC and high frequency electronics application will be described. Two main concepts will be considered: analytical and electromagnetic modeling.

2.3 Carbon nanotube modeling for electronics applications

In this section, analytical and electromagnetic models of carbon nanotubes for millimeter-wave electronics applications proposed in [27] are presented. In the first part, the analytical model of carbon nanotubes in DC and RF will be introduced, allowing to develop a circuit model that can be integrated for example in ADS in order to design CNT-

based RF components. The second part will present the electromagnetic model of CNTs that can be considered as an equivalent 3D bulk material in HFSS Ansys Simulation. This equivalent material developed in [8], which allows designing complicated CNT-based passive devices in HFSS such as waveguides, couplers, phase shifters, Butler matrix, etc. Particularly, in this PhD work, this model is very helpful to demonstrate the possibility of using CNTs to perform slow-wave effect that will be introduced in the Chapter 4.

2.3.1 Analytical modeling of CNTs for DC applications

In DC, both SWCNTs and MWCNTs can be modeled by an electrical resistance composed of three resistances in series that contribute to the total resistance: the contact resistance R_C, the quantum resistance R_Q and the distributed nanotube resistance R_{CNT}. The DC circuit schematic of carbon nanotube is shown in Figure 2-5.

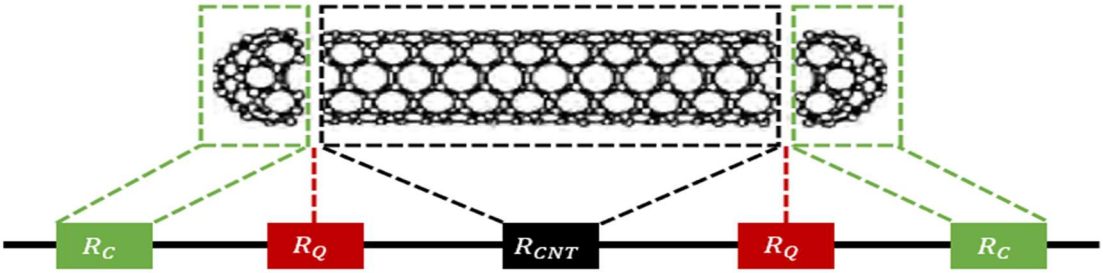

Figure 2-5. Schematic circuit in DC of a carbon nanotube [27].

2.3.1.1 Contact resistance R_C

The contact resistance R_C is the resistance between the CNTs and materials in contact with them. Generally, this contact occurs between the metal layer and carbon nanotube, leading to a contact resistance R_C ranging from tenths of kΩ and few MΩ [49]–[54]. In [55], the strongly dependence of the contact resistance on the contact surface and the diameter of the carbon nanotube was demonstrated. As shown in Figure 2-6, the greater the CNT diameter, the lower contact resistance.

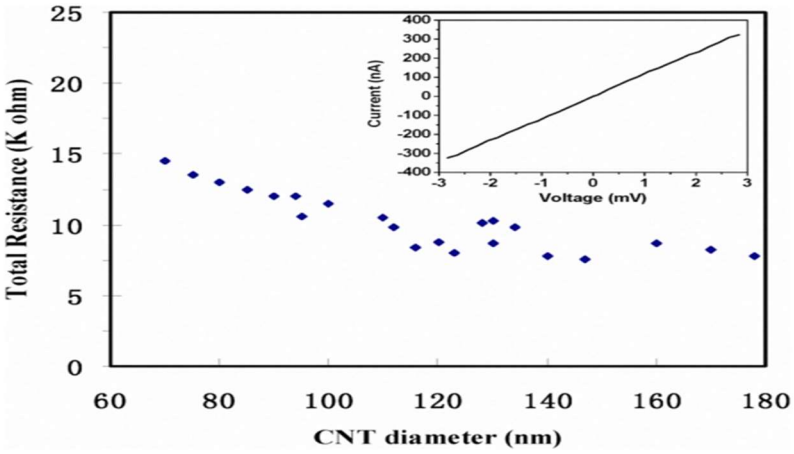

Figure 2-6. Contact resistance in function of the CNT diameter [55].

Besides, the catalyst materials and its thickness also play an important role in the change of contact resistance value [27]. Finally, depending on the choice of metals (such as copper, silver, gold) which connect to the CNTs, the contact resistance between carbon nanotubes and metal is modified [35].

2.3.1.2 Quantum resistance R_Q

As discussed previously, the electron propagation in CNTs is quantized [7], leading to a limited number of discrete conducting channels for the electron conduction. Each channel only accepts one electron travelling at the same time, hence the quantum resistance R_Q appears from this particular 1-D structure [27]. Besides, the electron conduction along the nanotubes is ballistic and for this kind of transport, the Landauer formula can be applied in order to estimate the current in the carbon nanotube channel [56]. By assuming no scattering and ideal contacts, the conductance of the 1-D structure can be given by $G = G_0 NT$, where T is the probability that an electron could be transmitted along the channel, N is the number of the channels available for transport and G_0 is the conductance quantum ($G_0 = 2e^2/h$). With perfect contacts, when the reflection equals zero and no back scattering along the channel result in transmission probability $T = 1$ [56], the conductance of the system becomes $G = \left(\frac{2e^2}{h}\right) N$. In a SWCNT, there is only one shell with only two channels of conduction per shell. Thus $N = 2$ and the conductance is $G = \left(\frac{4e^2}{h}\right)$ leading to the quantum resistance R_Q equals to $\frac{1}{G} = 6.45\ k\Omega$. More generally, the quantum resistance of a SWCNT shell is given by [27]:

$$R_{Q-SWC} = \frac{h}{N_{chann\ /she}\ \cdot 2e^2} \tag{2-5}$$

where h is the Planck's constant; e is the elementary electron charge; $N_{channel/shell} = 2$ is the number of channels in the selected shell.

In the case of MWCNTs, the number of conducting channels for each MWCNT shell must be calculated [7], [17]. Thus, by summing up all the possible conducting channels, the value of R_Q can be calculated for a MWCNT. Generally, this quantum resistance is given by [27]:

$$R_{Q-MWCNT} = \frac{h}{N_{channels/MWCNT} \cdot 2e^2} \tag{2-6}$$

where $N_{channels/MWCNT} = \sum_{i=1}^{p} N_{i-channel/shell}$ and p is the number of shells calculated with equation (2-2).

In the case of a MWCNT having a diameter of 10 nm and 8 shells, a R_Q equal to 0.8 kΩ is obtained. This quantum resistance is much lower than the one of a SWCNT. Nevertheless, the density of SWCNTs (up to $10^{14-15} m^{-2}$) is much higher (10 and 100 times) than the density of MWCNTs (up to $10^{13} m^{-2}$), which may compensate the difference in terms of total $N_{channels}$ larger for MWCNTs than for SWCNTs and leads to an approximate value of quantum resistance. Finally, it must be reminded that for SWCNTs, tunneling effects between shells does not exist, that is also an advantage for the vertical resistance of the CNT [27].

2.3.1.3 Carbon nanotube resistance R_{CNT}

Theoretically, the electron transport inside a carbon nanotube becomes diffusive when the length of the CNT is greater than its mean free path MFP (approximately 1 µm in SWCNTs and 25 µm in MWCNTs), thus leading to a resistance R_{CNT} defined as follow [57]:

$$R_{CNT-SWCNT}(L_{CNT} > MFP) = R_{Q-SWC} \times \frac{L_{CNT}}{MFP} \quad (2\text{-}7)$$

$$R_{CNT-MWCNT}(L_{CNT} > MFP) = R_{Q-MWCNT} \times \frac{L_{CNT}}{MFP} \quad (2\text{-}8)$$

where L_{CNT} is the length of CNT and MFP is the CNT mean free path. Typically, for a 20-µm SWCNT, the R_{CNT} can be calculated as 129 kΩ [57].

From (2-7) and (2-8), and since the MFP depends on the purity of the CNT, the presence of defects in the CNT increases its distributed resistance R_{CNT}.

Different results from the literature have been summarized in [58], as illustrated in Figure 2-7.

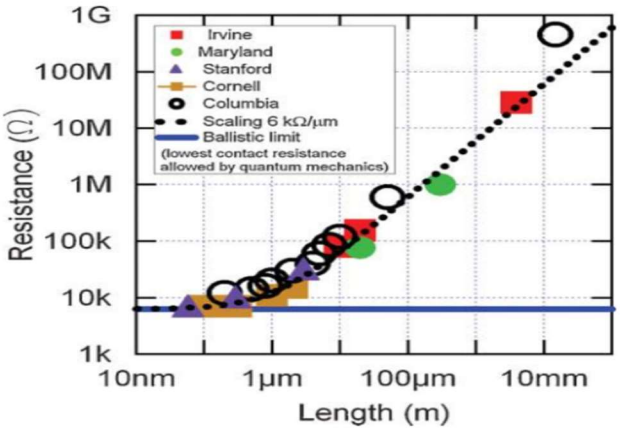

Figure 2-7. Resistance at room temperature of a SWCNT as a function of its length measured by several laboratories [58].

2.3.2 Analytical modeling of CNTs for RF applications

2.3.2.1 Modeling of single-wall carbon nanotube

As demonstrated in [59], a metallic SWCNT can be described as a micro-strip line composed of a single tube above a ground plane. Hence, a transmission line electrical model can be considered to model the propagation in a carbon nanotube, as shown in Figure 2-8. This circuit is composed by one lumped component (the quantum resistance R_Q) and five distributed components (the scattering-induced resistance or distributed CNT resistance R_{CNT}, the kinetic and magnetic inductances L_K and L_M and the quantum and electrostatic capacitances C_Q and C_{ES}) [17], [59]:

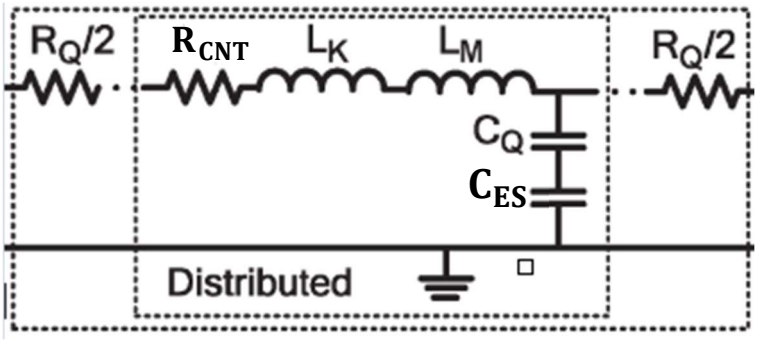

Figure 2-8. Equivalent distributed circuit model of a metallic SWCNT [17].

- The value of magnetic inductance L_M and electrostatic capacitance C_{ES} can be calculated by the following equations:

$$L_M = \frac{\mu_0 L_{CNT}}{2\pi} arcosh\left(\frac{d}{a}\right) = \frac{\mu_0 L_{CNT}}{2\pi} \ln\left(\frac{d}{a} + \sqrt{\frac{d^2}{a^2} - 1}\right) \quad (2\text{-}9)$$

$$C_{ES} = \frac{2\pi\varepsilon_0 L_{CNT}}{arcos\ (\frac{d}{a})} = \frac{2\pi\varepsilon_0 L_{CNT}}{\ln(\frac{d}{a} + \sqrt{\frac{d^2}{a^2} - 1})} \quad (2\text{-}10)$$

where a is the CNT radius, d is the distance between the CNT and the ground plane ($d > a$), L_{CNT} is the CNT length, ε_0 is the vacuum permittivity and μ_0 is the vacuum permeability.

- The distributed CNT resistance R_{CNT} and the quantum resistance R_Q have been already detailed on the DC model section (section 2.3.1). For this equivalent distributed circuit model, the equations for R_{CNT} and R_Q remain the same.
- The kinetic inductance L_K and the quantum capacitances C_Q have been studied in [59]–[62], leading to the following equations for one channel of conduction:

$$C_{Q/cha} = \frac{1}{2} e^2 D(\mu) = \frac{4e^2}{h v_F} \approx 193\ aF/\mu m \quad (2\text{-}11)$$

$$L_{K/channe} = \frac{h}{4e^2 v_F} \approx 8\ nH/\mu m \quad (2\text{-}12)$$

where h is the Planck's constant; e is the elementary electron charge; v_F is the Fermi's velocity (9.10^5 m/s) and $D(\mu)$ is the density of states at the Fermi energy of metallic CNTs.

Since two conducting channels exist in a SWCNT, the $L_{K/chann}$ inductance must be multiplied by 1/2 to obtain the total kinetic inductance per unit length and the $C_{Q/chann}$ capacitance must be multiplied by 2 [7] to obtain the total quantum capacitance per unit length, as:

$$C_{Q/SWCNT} = \frac{8e^2}{h v_F} \approx 319\ aF/\mu m \quad (2\text{-}13)$$

$$L_{K/SWCNT} = \frac{h}{8e^2 v_F} \approx 3.3\ nH/\mu m \quad (2\text{-}14)$$

2.3.2.2 Modeling of multi-wall carbon nanotube

Based on several rolled up sheets of graphene, a MWCNT can be modeled as multiple SWCNT transmission lines in parallel. Each shell shield its adjacent shells from each other so there is coupling effect only between adjacent shells [17]. Therefore, on the MWCNT circuit modeling, shells are connected at the MWCNT terminus and the MWCNT can be modeled by the schematic illustrated on Figure 2-9 [17].

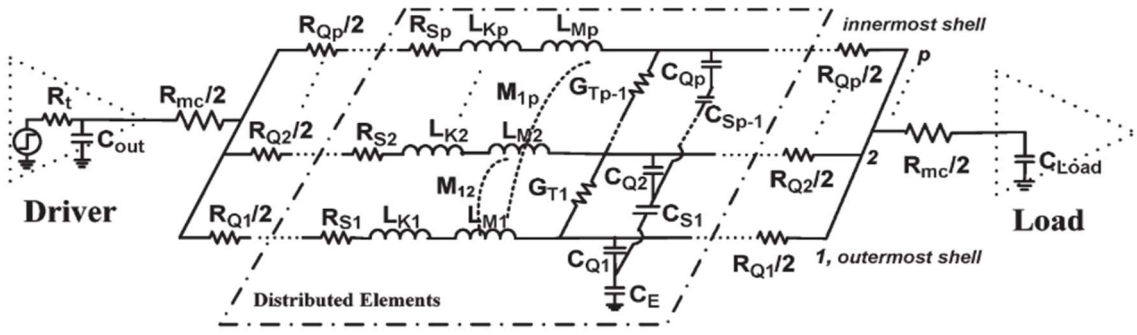

Figure 2-9. Equivalent distributed circuit model of an MWCNT with p shells based on RLC transmission line model. R_{mc} is the imperfect contact resistance between the MWCNT and the material in contact [17]*. Only the outermost shell has electrostatic capacitance C_E with the ground.*

As shown in Figure 2-9, each shell of the MWCNT was modeled by one transmission line. Since each shell has a different diameter, the value of each component of the model is different for all shells. Finally, two "coupling" effects between adjacent shells i and $i+1$ (the coupling capacitance C_S and the tunneling conductance G_T) and a mutual inductance M_{ij} between adjacent shells i and j can be calculated as [17], [17]:

$$C_S = \frac{2\pi\varepsilon_0}{\ln(\frac{D_{i+1}}{D_{i+1} - 2*d})} \times L_{CNT} \quad (2\text{-}15)$$

$$G_T = \sigma \times \pi \times D_i \quad (2\text{-}16)$$

$$M_{ij} = \frac{\mu_0}{2\pi}(ln\frac{4L_{CNT}}{D_j} - 1 + \frac{D_j + D_i}{\pi L_{CNT}}) \quad (2\text{-}17)$$

where σ is the tunneling conductivity ranging from no tunneling effect ($\sigma = 0$) to the measurement value of 0.3 $(\mu\Omega.cm^2)^{-1}$ [17], ε_0 is the vacuum permittivity, μ_0 is the vacuum permeability, L_{CNT} is the CNT shell length, D_i and D_j are the diameters of shells i and j, respectively and d is the distance between two adjacent shells (0.34 nm).

2.3.2.3 Modeling of a bundle of CNTs

In this PhD work, carbon nanotubes are always considered in a bundle structure (both SWCNTs and MWCNTs). Thus, to facilitate the modeling process of CNT bundle, all CNTs are considered as identical (same length and diameter). This assumption is not exact in realty, as illustrated in Figure 2-10 showing a SEM picture of a MWCNT bundle grown by PECVD process at CINTRA. Nevertheless, in a first approximation, and for modeling simplicity, the length and distance between carbon nanotubes can be considered approximately identical.

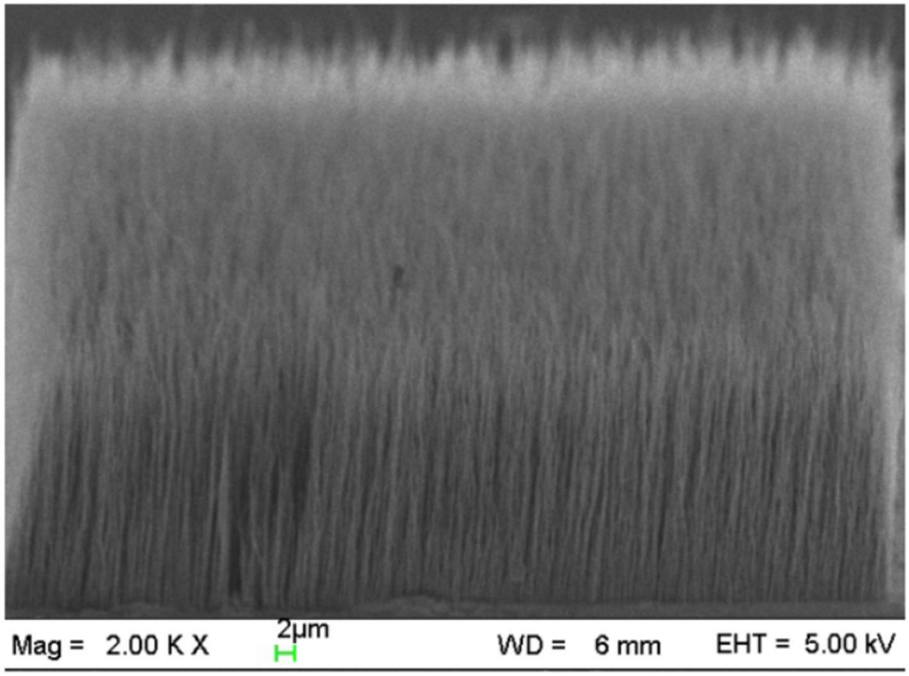

Figure 2-10. MWCNT bundle grown by PECVD technique et CINTRA [27].

Based on this assumptions (identical length and diameter), the electrical components of CNT bundle can be calculated as follow: the series elements in the transmission line circuit such as the resistances and inductances are divided by the number

of CNTs whereas the parallel components such as the capacitances are multiplied by the number of CNTs. From (2-5) to (2-14), the value of each component of CNT bundle is calculated by the following equations:

$$R_{Q-bundle} = \frac{h}{2e^2} \times \frac{1}{N_{channels} \times N_{CNT}} \quad (2\text{-}18)$$

$$R_{CNT-bundl} = R_{Q-bundle} \times \frac{L_{CNT}}{MFP} = \frac{h}{2e^2} \times \frac{1}{N_{channels} \times N_{CNT}} \times \frac{L_{CNT}}{MFP} \quad (2\text{-}19)$$

$$L_{K-bundle} = \frac{h}{4e^2 v_F} \times L_{CNT} \times \frac{1}{N_{channels} \times N_{CNT}} \quad (2\text{-}20)$$

$$C_{Q-bundle} = \frac{4e^2}{h v_F} \times L_{CNT} \times N_{channels} \times N_{CNT} \quad (2\text{-}21)$$

$$C_{ES-bundle} = \frac{2\pi\varepsilon_0}{\ln(\frac{d}{a} + \sqrt{\frac{d^2}{a^2} - 1})} \times L_{CNT} \times N_C \quad (2\text{-}22)$$

For a SWCNT bundle, two conducting channels exist ($N_{channels} = 2$). For a MWCNT bundle, the number of conducting channels for each MWCNT is obtained by:

$$N_{channels/MWCNT} = \sum_{i=1}^{p} N_{i-channel/shell} \quad (2\text{-}23)$$

In order to simply the model of MWCNT bundle, the coupling effects between shells are neglected [63]–[65]. To calculate the number of CNTs in a bundle, we use the following equation [66]:

$$N_{CNT} = n_F \times n_G \times (\frac{d_{bundle}}{d_{CNT}})^2 \quad (2\text{-}23)$$

where:

- n_F is the filling factor of the original bundle shape ranging between 0 and 1;
- n_G is the CNT density factor calculated by dividing the space area occupied by a defined number of CNTs (using the surface of CNTs) by the total area, this value also ranges from 0 to 1;
- d_{bundle} is the bundle diameter and d_{CNT} is the average carbon nanotube diameter in the bundle.

2.3.2.4 Discussion about analytical modeling

The analytical model presented above was developed by XLIM laboratory (Limoges, France) [27]. It was based on numerous worldwide experimental measurements and was built from the physical behaviors of CNTs: quantum paths, inductive and capacitive coupling, contact resistance… This theoretical analysis served to recent researches (essentially performed at XLIM laboratory, Limoges, France) as an element of comparison to validate the electromagnetic modeling that is presented in the next section.

2.3.3 Electromagnetic modeling of CNTs RF applications

In order to predict the electromagnetic behavior of CNTs, a 3-D model was developed by XLIM [8] for electromagnetic analysis on software such as Ansys HFSS or CST Microwave Studio. This model aimed to obtain in particular an equivalent material with the behavior of an artificial material containing the CNT properties.

2.3.3.1 Single wall carbon nanotube electromagnetic modeling

Based on [67], a metallic SWCNT with radius a less than 3.39 nm was modeled by considering an empty tube with an infinitely thin wall provided with a complex surface

conductivity similar to a Drude conductivity (see Figure 2-11). This complex surface conductivity is frequency dependent:

$$\sigma_{SWCNT,surf}(\omega) \cong -j\frac{2e^2 v_F}{\pi^2 \bar{h} a(\omega - j\nu)} \quad (2\text{-}24)$$

where $\bar{h}$ is the reduced Planck's constant ($1{,}06.10^{-34}$ m^2.kg/s), e is the elementary electron charge, v_F is the Fermi's velocity ($9{,}71.10^5$ m/s), $\nu = 1/\tau$ is the frequency of relaxation ($(3.10^{-12})^{-1}$ Hz) and ω is the angular frequency.

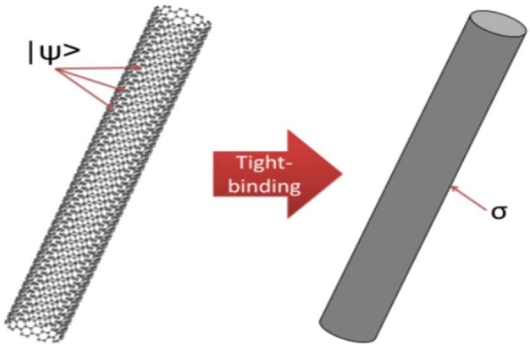

Figure 2-11. Using the tight-binding theory, a SWCNT can be approximated as a hollow cylinder with the complex conductivity σ [68].

By considering this surface conductivity on the CNT surface as an impedance boundary, simulations of a SWCNT were performed at XLIM laboratory by C. Brun [26] by using the HFSS software and compared to the analytical model. Figure 2-12 shows the HFSS configuration with a carbon nanotube placed in parallel above a ground plane at the distance of h' in order to obtain a transmission line structure.

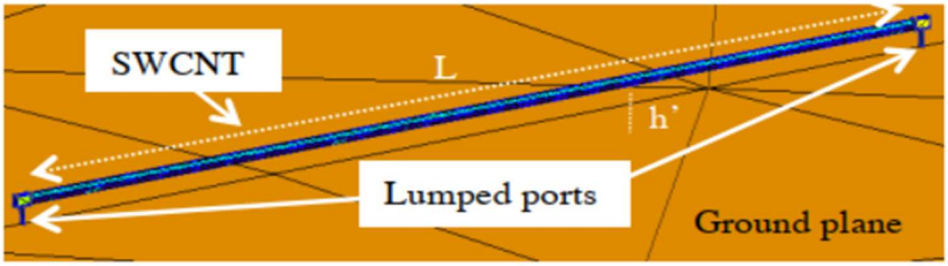

Figure 2-12. Circular CNT in a transmission line configuration for HFSS simulation [27].

Two SWCNT were simulated and compared with the analytical and with the EM model, leading to a very good agreement up to 300 GHz as shown in Figure 2-13.

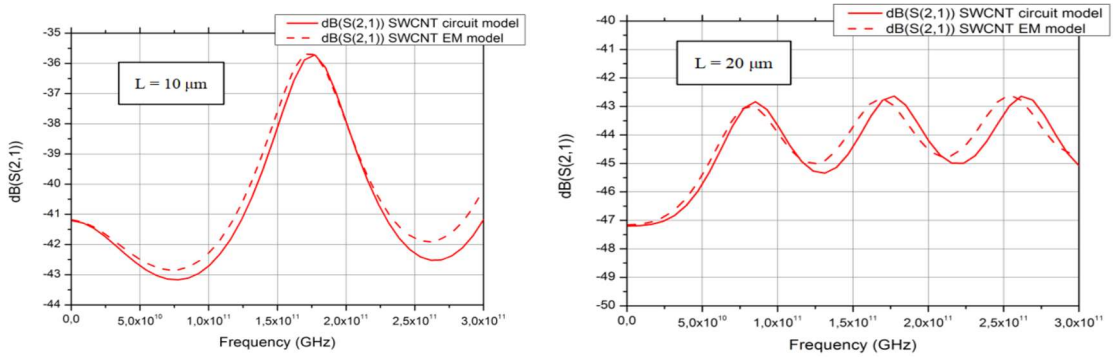

Figure 2-13. S-parameters of a 10-µm and 20-µm length of SWCNT in transmission line configuration simulated by C. Brun [27].

2.3.3.2 *Bundle of single wall carbon nanotubes electromagnetic modeling*

Bundle of CNTs have already been considered at high frequency to overcome issues such as high impedance and poor efficiency [7], [59], [67], [69]–[77]. Several types of bundle modeling were introduced in the Ph.D. thesis of C. Brun [27]. However, we will only detail in this manuscript the one that was finally chosen for our designs. Therefore, in this section, only the bundle with an unlimited number of SWCNTs will be introduced. This kind of bundle can be considered as a bulk equivalent model that is very helpful to design complicated passive circuits at high frequency such as waveguides, couplers, phase-shifters, Butler matrices, etc. Besides, with the help of this equivalent model, the possibility of using CNTs to perform slow-wave effect will be introduced in the next chapters.

This bulk equivalent model was developed in the PhD thesis of P. Franck (PhD at XLIM laboratory, University of Limoges in collaboration with the UMI CINTRA, NTU Singapore) [68]. The purpose of this model is to reduce the exponential computing time during a complete 3-D electromagnetic simulation, on software similar to HFSS, of an unlimited number of SWCNTs in parallel. We recall here the principle as well as the formulas linked to this equivalent model. This model is the main model used during this thesis to perform HFSS simulations as we said previously. The principle of this bulk equivalent model is illustrated in Figure 2-14.

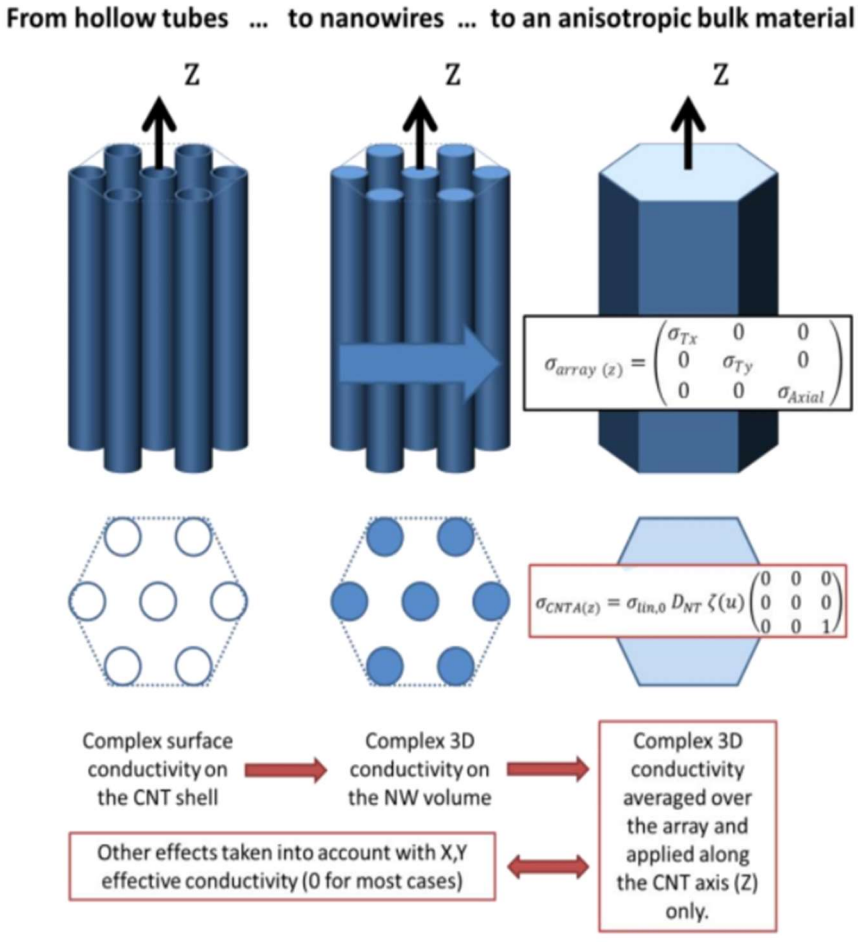

Figure 2-14. Schematic illustration of the bulk equivalent model [78].

In this model, a bundle of SWCNTs having the same dimension in term of diameter and length was considered. These SWCNTs were vertically aligned and equally spaced by considering the model presented in [67], [79] for each of these nanotubes. Hence, the CNTs were assimilated as hollow cylinders with complex conductivity $\sigma_{SWCNT,surf}(\omega) \cong -j\frac{2e^2 v_F}{\pi^2 \hbar a(\omega - jv)}$ as already mentioned in the section 2.3.3.1.

Then, an equivalent model of bulk nanowire (NW) was derived from the empty SWCNT by assuming that the NW has the same size as the empty cylinder and respecting the same distributed Ohm's law, leading to the following equation linking the conductivities of both structures:

$$\sigma_{NW,bulk}(z,\omega) = \sigma_{SWCNT,surf}(z,\omega) \times \frac{P_{SWCNT}}{S_{SWCNT}} \tag{2-25}$$

where P_{SWCNT} and S_{SWCNT} are the perimeter and the area of the cross-section of the SWCNT, respectively.

Finally, an equivalent bulk model from a bundle of several equivalent bulk nanowires was derived by assuming a homogeneous distribution of the NWs in the bundle as shown in Figure 2-15.

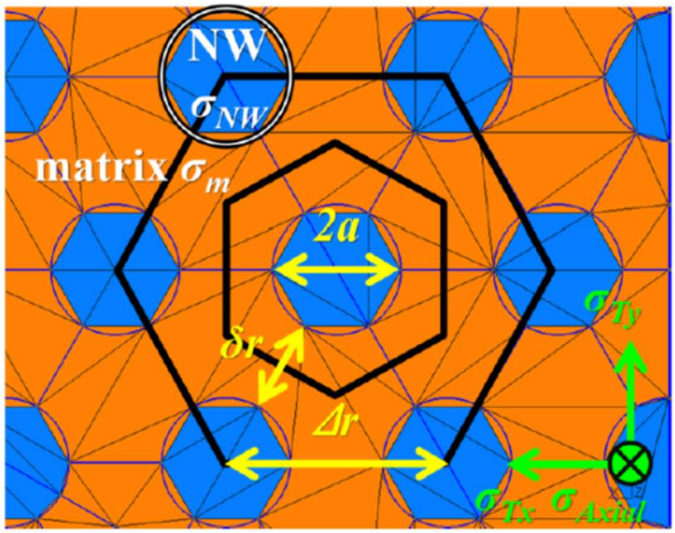

Figure 2-15. Cross-sectional cut of a hexagonal array of NWs [68].

This equivalent bulk material was modeled by an anisotropic effective bulk conductivity σ_{array} of the bundle of equivalent bulk NWs:

$$\sigma_{array(z)} = \begin{pmatrix} \sigma_{Tx} & 0 & 0 \\ 0 & \sigma_{Tx} & 0 \\ 0 & 0 & \sigma_{Axial} \end{pmatrix} \tag{2-26}$$

where σ_{Tx} and σ_{Ty} are the transverse conductivities of the equivalent material that can be neglected and σ_{Axial} is the anisotropic conductivity along the axis of NWs, here the z-axis.

Finally, in the particular case of a bundle of CNTs in the air, it was demonstrated that the anisotropic effective bulk conductivity σ_{array} can be given by:

$$\sigma_{array(z)} = \sigma_{lin,0} D_{CNT} \zeta(u) \begin{pmatrix} 0 & 0 & 0 \\ 0 & 0 & 0 \\ 0 & 0 & 1 \end{pmatrix} \tag{2-27}$$

where $\sigma_{lin,0} = \frac{8e^2 v_F}{h\nu}$ is the linear conductivity over a single SWCNT; D_{CNT} corresponds to $2 * 10^{15}$ NW/m^2; $\zeta(u) = \frac{1-ju}{1+u^2}$ and $u = \omega\tau = \frac{\omega}{\nu} = \frac{f}{F_v}$.

The main advantage of this method is low computing resource requirement necessary to model a bundle of thousands (or much more) SWCNTs. However, there are also some limitations: only homogeneous bundle of CNTs can be modeled, meaning all carbon nanotubes have the same diameter and length; only single-wall are modeled; and CNTs need to be aligned [68].

In order to integrate this model into HFSS to design CNT-based electronic structures, the anisotropic complex conductivity must be transformed into a combination of a relative permittivity $\varepsilon_r = \frac{\varepsilon}{\varepsilon_0}$ and a loss tangent $tan\delta_E = \frac{\varepsilon_r^{"}}{\varepsilon_r'}$. To process, several equations must be used as follow:

$$\varepsilon = \varepsilon' + j\varepsilon^{"} = K\varepsilon_0 - j\frac{\sigma}{\omega} \quad (2\text{-}28)$$

$$\sigma = \sigma' + j\sigma^{"} \quad (2\text{-}29)$$

Hence,

$$\varepsilon = \left(K\varepsilon_0 + \frac{\sigma^{"}}{\omega}\right) + j\left(-\frac{\sigma'}{\omega}\right) \quad (2\text{-}30)$$

And therefore

$$\varepsilon_r' = \frac{\varepsilon'}{\varepsilon_0} = K + \frac{\sigma^{"}}{\omega\varepsilon_0} \quad (2\text{-}31)$$

$$tan\delta_E = \frac{-\sigma'}{K\omega\varepsilon_0 + \sigma^{"}} \quad (2\text{-}32)$$

For metallic SWCNTs, applying equation (2-27), we obtain:

$$\varepsilon_r' = K - \frac{\sigma_{lin,0} D_{CNT} u}{\omega\varepsilon_0(1+u^2)} \quad (2\text{-}33)$$

$$tan\delta_E = -\frac{1}{u\left(\frac{K\varepsilon_0(1+u^2)}{\sigma_{lin,0} D_{CNT}\tau} - 1\right)} \quad (2\text{-}34)$$

2.3.4 Discussion about electromagnetic modeling and choice for CNT topology

In section 2.3, the CNT modeling developed by XLIM with two approaches, analytical and electromagnetic, was presented to model SWCNTs, MWCNTs and bundle of CNTs. A good agreement between the two models was demonstrated for a SWCNT. A specific approach for bundles was presented and validated on bundles of SWCNTs. Electromagnetic modeling of single MWCNTs, and of bundles of MWCNTs, is still under investigation at CINTRA, Singapore; the lack of accuracy is certainly due to the difficulty of modeling tunneling effect between the numerous shells of the MWCNTs.

Moreover, as mentioned in the technological fabrication part, section 2.2, bundles, or forest, of SWCNTs are denser than bundles, or forest, of MWCNTs, which may compensate for the higher resistance of SWCNTs.

For both reasons (fabrication and modeling), the choice was made between the partners of the TRICOT project, to focus on SWCNTs. The available electromagnetic model of SWCNTs bundle, or forest, paves the way to design the CNT-based devices for various high frequency applications. Particularly, this equivalent bulk model plays an

important role for designing the slow-wave passive circuits at high frequency, as the purpose of this PhD thesis that will be presented more in detail in the next chapters.

Before presenting in depth the main core of this PhD design work, in Chapter 3, Chapter 4 and Chapter 5, some state-of-the-art applications based on CNTs are presented in the last section.

2.4 Examples of application of CNTs in electronics

Since the first discovery of CNTs by S. Iijima in 1991, the carbon nanotubes have been considered in many applications for low and high frequency electronics such as in transistors, gas sensors, waveguides, antennas, interconnection, etc. On the next paragraphs, some applications will be introduced in order to illustrate various possibilities of using the CNT as an electronic material.

2.4.1 Transistors

Based on Moore's law predicting the transistors miniaturization, and since semi-conductive properties can exist for CNTs, numerous studies have been proposed to achieve CNT-based transistors [80]. Among them, the researches have widely focused on the field effect transistor based on CNTs (CNTFETs) [81]–[85]. An ON current exhibited by CNTFETs has been demonstrated that it is 20-30 times higher than the one exhibited by Si MOSFETs [86]–[88].

2.4.2 Gas sensors

Recently, the gas sensors based on carbon nanotubes have been widely developed. Compared to existing technologies, the CNT-based gas sensors allow obtaining ultra-compact devices, which are effective at room temperature, with a low power consumption, a very fast response time, a low recovery time (few seconds) and a good stability [89]. They also show a good versatility (i.e., they can be used for several gases such as NO2 and NH3) and finally, relatively low fabrication costs can be reached [90], [91].

2.4.3 Waveguides

The first CNT-based waveguide was designed and developed by M. Cometto [92] based on the concept of substrate integrated waveguide (SIW). This considered air-filled waveguide is composed of lateral walls made of CNT bundle instead of metallic vias and assembled with top and bottom metallic plates. In order to excite this waveguide, a CNT bump was placed at the extremity of the two signal lines of the CPW in/out accesses. The waveguide structure is described in Figure 2-16.

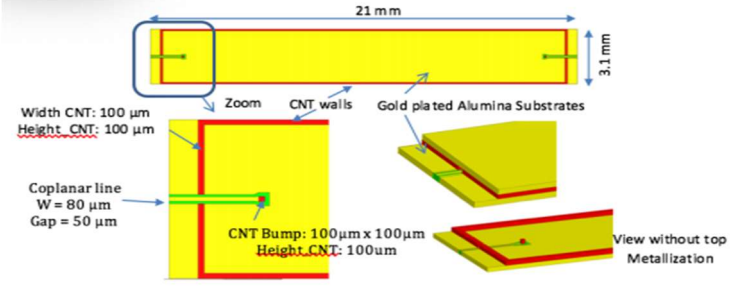

Figure 2-16. CNT-based waveguide with CNT walls are in red [92].

Based on these first results, new CNT-based waveguides have been designed in the framework of TRICOT ANR project. In particular, CNT-based waveguides considering coupling slots and CPW access lines will be presented in this PhD manuscript. A detailed study will be proposed in Chapter 3.

2.4.4 Antennas

During the last decade, many researches involved in developing antennas based on carbon nanotubes have been proposed. For example, an innovative patch antenna was designed by using the CNT inks to replace the metal [93], [94]. In [95], in order to form the antenna, a vertically aligned bundle of CNTs grown on a flexible substrate and included it in a composite polymer was considered. CNTs were also used in antenna as loads or conductors as CNTs can be metallic [96]–[98]. Other applications relying on the ink-jet printing of CNT-loaded conductive ink were done to fabricate diverse RF circuits [99], [100]. Some more work was done on CNT antennas at higher frequencies, making use of the quantum effects of the CNTs to design millimeter wave resonant antennas [101].

2.4.5 Interconnections

As defined in Figure 2-17, two main levels of interconnections are defined in integrated circuits regarding to their size, their length and their purpose. The level 1 consists of all "chip-to-chip packaging" interconnects such as wire bonding, flip-chips or via holes which are used to connect the chip to its package. Meanwhile, the level 0 is the back-end-of-line interconnections, which is composed of all smaller interconnections than the first level. They are usually located into the integrated circuits themselves. In addition, in literature, numerous researches have been studied to demonstrate the possibility of using CNTs for both levels of interconnections, such as [22], [102], [103] for level 0 or [104]–[106] for level 1.

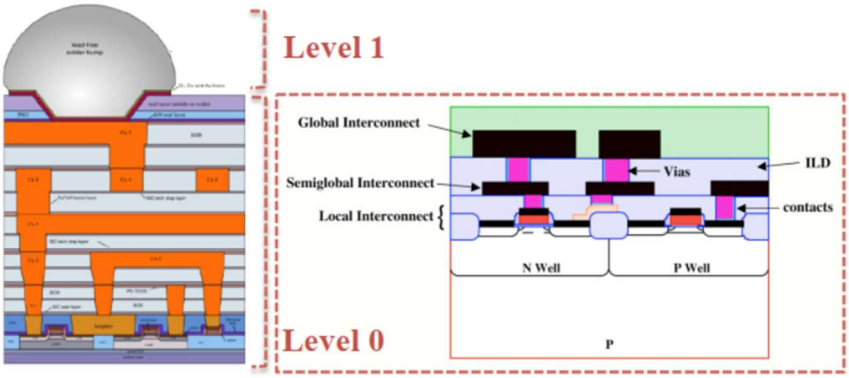

Figure 2-17. Level 1 and level 0 of interconnection in integrated circuits [107].

2.4.6 Other applications

As indicated previously, due to their high thermal conductivity, CNTs can be considered as a good candidate to replace metal-based coolers in thermal management. Indeed, by using a thick layer of carbon nanotubes, a lighter cooler than copper-based one can be achieved with a better performance [108].

CNTs were recently used to fabricate an on-chip random number generator, which is useful to many cryptography and communication processes [109].

The use of CNTs for demodulation and narrow-band amplifiers was also demonstrated in [110], [111].

Finally, MWCNTs were employed as an electromechanical switch NEMS [112]. The advantage of using CNT-based switch is the low switching time (few nanoseconds) compared to other classical approaches. Moreover, a lower switch capacitance can be reached, and consequently decrease the switch response. However, most of the devices showed failures with high power tests. Thus, reliability of the CNT-based switches needs to be much more investigated [112].

2.5 Conclusion

In this second chapter, we have presented the physical properties of carbon nanotubes. Due to their outstanding properties as compared to other materials, CNTs could be considered as a potential material for next-generation electronics applications in order to replace classical metal-based structures. A wide number of electronics applications based on CNTs has been reported: field effect transistors, antennas, interconnections or promising low-loss waveguides as studied in the framework of this PhD thesis.

Four main methods to grow CNTs for electronics applications were also described in this chapter: arc discharge, laser ablation, and thermal CVD and PECVD method. Thermal CVD and PECVD are the only methods enabling vertical alignments. Thus, thermal CVD was chosen in the framework of the TRICOT ANR Project due to several main reasons: low process temperature, repeatability, excellent knowledge by the laboratory in charge of the fabrication (CINTRA, Singapore) and ease of scale-up. Even if a lower CNT purity is obtained by CVD method than by arc discharge or laser ablation, the values for CNT purity are superior to 75% that is totally acceptable. Also, bundles of SWCNTs grown through thermal CVD present interestingly high densities up to $10^{14-15}m^{-2}$.

Two analytical and electromagnetic modeling of CNTs performed at XLIM laboratory, Limoges, France, were also described in this chapter. Since a very good agreement between the analytical model of a bundle of SWCNTs and a bulk model of the same bundle was obtained, it was decided to consider this bulk model to design and optimize the microwave structures developed in the next chapters in electromagnetic simulations.

REFERENCES

[1] L. V. Radushkevich and V. . Lukyanovich, "The Structure of Carbon Forming in Thermal Decomposition of Carbon Monoxide on an Iron Catalyst," *Russ. J. Phys. Chem. 26, 88-95*, 1952.

[2] S. Iijima, "Helical microtubules of graphitic carbon," *Nature*, vol. 354, pp. 56–57, 1991.

[3] W. B. Choi *et al.*, "Fully sealed, high-brightness carbon- nanotube field-emission display," vol. 3129, no. November 1999, pp. 73–76, 1999.

[4] J. Wei *et al.*, "Double-walled carbon nanotube solar cells," *Nano Lett.*, vol. 7, no. 8, pp. 2317–2321, 2007.

[5] I. R. Bruce, P. V. Kamat, and A. Bunker, "Single-Walled Carbon Nanotube–CdS Nanocomposites as Light-Harvesting Assemblies : Photoinduced Charge-Transfer Interactions." pp. 2458–2463, 2005.

[6] A. Bianco, K. Kostarelos, and M. Prato, "Applications of carbon nanotubes in drug delivery," *Curr. Opin. Chem. Biol.*, vol. 9, no. 6, pp. 674–679, 2005.

[7] H. Li, C. Xu, N. Srivastava, and K. Banerjee, "Carbon Nanomaterials for Next-Generation Interconnects and Passives: Physics, Status, and Prospects," *IEEE Trans. Electron Devices*, vol. 56, no. 9, pp. 1799–1821, 2009.

[8] P. Franck, D. Baillargeat, and B. K. Tay, "Mesoscopic model for the electromagnetic properties of arrays of nanotubes and nanowires: A bulk equivalent approach," *IEEE Trans. Nanotechnol.*, vol. 11, no. 5, pp. 964–974, 2012.

[9] A. Aqel, K. M. M. A. El-nour, R. A. A. Ammar, and A. Al-warthan, "Carbon nanotubes , science and technology part (I) structure , synthesis and characterisation," *Arab. J. Chem.*, vol. 5, no. 1, pp. 1–23, 2012.

[10] H. Li, N. Srivastava, J. F. Mao, W. Y. Yin, and K. Banerjee, "Carbon nanotube vias: Does ballistic electron-phonon transport imply improved performance and reliability?," *IEEE Trans. Electron Devices*, vol. 58, no. 8, pp. 2689–2701, 2011.

[11] M. F. C. Fiawoo, A. M. Bonnot, H. Amara, C. Bichara, J. Thibault-Pénisson, and A. Loiseau, "Evidence of correlation between catalyst particles and the single-wall carbon nanotube diameter: A first step towards chirality control," *Phys. Rev. Lett.*, vol. 108, no. 19, pp. 1–5, 2012.

[12] F. Yang *et al.*, "Chirality-specific growth of single-walled carbon nanotubes on solid alloy catalysts," *Nature*, vol. 510, no. 7506, pp. 522–524, 2014.

[13] J. R. Sanchez-Valencia *et al.*, "Controlled synthesis of single-chirality carbon nanotubes," *Nature*, vol. 512, no. 1, pp. 61–64, 2014.

[14] T. Wang, "Towards Carbon Nanotube-based on-chip Interconnection." 1999.

[15] J. M. A. Alsharef, M. R. Taha, and T. A. Khan, "Physical Dispersion of Nanocarbons in Composites-A review," *Technol. J.*, no. June, 2017.

[16] Azonano, "Multi-walled carbon nanotubes: production, ananysis and application," 2013. [Online]. Available: https://www.azonano.com/article.aspx?ArticleID=3469.

[17] H. Li, W. Y. Yin, K. Banerjee, and J. F. Mao, "Circuit modeling and performance analysis of multi-walled carbon nanotube interconnects," *IEEE Trans. Electron Devices*, vol. 55, no. 6, pp. 1328–1337, 2008.

[18] C. T. White and T. N. Todorov, "Carbon nanotubes as long ballistic conductors," *Nature*, vol. 393, no. 6682, pp. 240–241, 1998.

[19] J. W.G.Wildoer, A. G. Rinzler, L. C. Venema, C. Dekker, and R. E. Smalley, "Electronic structureof atomically resolved carbonnanotubes," vol. 584, no. 10, pp. 1996–1999, 1998.

[20] H. J. Li, W. G. Lu, J. J. Li, X. D. Bai, and C. Z. Gu, "Multichannel ballistic transport in multiwall carbon nanotubes," *Phys. Rev. Lett.*, vol. 95, no. 8, pp. 1–4, 2005.

[21] R. A. Coutu, J. R. Reid, R. Cortez, R. E. Strawser, and P. E. Kladitis, "Microswitches with Sputtered Au , AuPd , Au-on-AuPt, and AuPtCu Alloy Electric Contacts," *IEEE Trans. COMPONENTS Packag. Technol.*, vol. 29, no. 2, pp. 341–349, 2006.
[22] K. Banerjee, H. Li, and N. Srivastava, "Current status and future perspectives of carbon nanotube interconnects," *2008 8th IEEE Conf. Nanotechnology, IEEE-NANO*, no. c, pp. 432–436, 2008.
[23] B. Q. Wei, R. Vajtai, and P. M. Ajayan, "Reliability and current carrying capacity of carbon nanotubes," *Appl. Phys. Lett.*, vol. 79, no. 8, pp. 1172–1174, 2001.
[24] J. Hone, M. Whitney, C. Piskoti, and A. Zettl, "Thermal conductivity of single-walled carbon nanotubes," *Phys. Rev. B*, vol. 59, no. 4, 1999.
[25] P. Kim, L. Shi, A. Majumdar, and P. L. McEuen, "Thermal transport measurements of individual multiwalled nanotubes," *Phys. Rev. Lett.*, vol. 87, no. 21, pp. 215502-1-215502–4, 2001.
[26] T. W. Ebbesen, H. J. Lezec, H. Hiura, J. W. Bennett, H. F. Ghaemi, and T. Thio, "Electrical conductivity of individual carbon nanotubes," *Nature*, vol. 382, no. 6586, pp. 54–56, 1996.
[27] C. Brun, "Carbon nanotubes based nanopackaging dedicated to innovative high frequency interconnections," Limoges, 2013.
[28] R. Booker and E. Boysen, "Scanning the properties of nanotubes." [Online]. Available: https://www.understandingnano.com/nanotubes-carbon-properties.html.
[29] C. Ren, W. Zhang, Z. Xu, Z. Zhu, and P. Huai, "Thermal conductivity of single-walled carbon nanotubes under axial stress," *J. Phys. Chem. C*, vol. 114, no. 13, pp. 5786–5791, 2010.
[30] E. Pop, D. Mann, Q. Wang, K. Goodson, and H. Dai, "Thermal conductance of an individual single-wall carbon nanotube above room temperature," *Nano Lett.*, vol. 6, no. 1, pp. 96–100, 2006.
[31] T. Iwai *et al.*, "Thermal and source bumps utilizing carbon nanotubes for flip-chip high power amplifiers," *Tech. Dig. - Int. Electron Devices Meet. IEDM*, vol. 2005, no. c, pp. 257–260, 2005.
[32] "Mechanical properties of carbon nanotubes." .
[33] M. F. Yu, O. Lourie, M. J. Dyer, K. Moloni, T. F. Kelly, and R. S. Ruoff, "Strength and breaking mechanism of multiwalled carbon nanotubes under tensile load," *Science (80-.).*, vol. 287, no. 5453, pp. 637–640, 2000.
[34] T. Filleter, R. Bernal, S. Li, and H. D. Espinosa, "Ultrahigh strength and stiffness in cross-linked hierarchical carbon nanotube bundles," *Adv. Mater.*, vol. 23, no. 25, pp. 2855–2860, 2011.
[35] J. Bernholc, D. Brenner, M. Buongiorno Nardelli, V. Meunier, and C. Roland, "Mechanical and electrical properties of nanotubes," *Annu. Rev. Mater. Sci.*, vol. 32, pp. 347–375, 2002.
[36] B. Ruelle, "Functionalization of carbon nanotubes via plasma post-discharge surface treatment: implication as nanofiller in polymeric matrices," *Ph. D. Thesis*, no. December 2014, pp. 4–6, 2009.
[37] Y. Saito, "Preparation and Properties of Carbon Nanopeapods," *Int. Symp. MICROMECHATRONICS Hum. Sci.*, pp. 43–49, 1999.
[38] A. L. Kalamkarov, A. V Georgiades, S. K. Rokkam, V. P. Veedu, and M. N. Ghasemi-Nejhad, "Analytical and numerical techniques to predict carbon nanotubes properties," *Int. J. Solids Struct. 43*, vol. 43, pp. 6832–6854, 2006.
[39] K. Jensen, W. Mickelson, A. Kis, and A. Zettl, "Buckling and kinking force

measurements on individual multiwalled carbon nanotubes," *Phys. Rev. B - Condens. Matter Mater. Phys.*, vol. 76, no. 19, pp. 1–5, 2007.
[40] A. Rochefort, P. Avouris, F. Lesage, and D. R. Salahub, "Electrical and mechanical properties of distorted carbon nanotubes," *Phys. Rev. B - Condens. Matter Mater. Phys.*, vol. 60, no. 19, pp. 13824–13830, 1999.
[41] T. Guo, P. Nikolaev, A. Thess, D. T. Colbert, and R. E. Smalley, "Catalytic growth of single-walled manotubes by laser vaporization," *Chem. Phys. Lett.*, vol. 243, no. 1–2, pp. 49–54, 1995.
[42] M. José-Yacamán, M. Miki-Yoshida, L. Rendón, and J. G. Santiesteban, "Catalytic growth of carbon microtubules with fullerene structure," *Appl. Phys. Lett.*, vol. 62, no. 6, pp. 657–659, 1993.
[43] C. J. Lee *et al.*, "Synthesis of aligned carbon nanotubes by thermal chemical vapor deposition," *Chem. Phys. Lett.*, vol. 312, no. 1, pp. 461–468, 1999.
[44] M. H. Rümmeli *et al.*, "Oxide-driven carbon nanotube growth in supported catalyst CVD," *J. Am. Chem. Soc.*, vol. 129, no. 51, pp. 15772–15773, 2007.
[45] T. Yamada *et al.*, "Revealing the secret of water-assisted carbon nanotube synthesis by microscopic observation of the interaction of water on the catalysts," *Nano Lett.*, vol. 8, no. 12, pp. 4288–4292, 2008.
[46] L. C. Qin, D. Zhou, A. R. Krauss, and D. M. Gruen, "Growing carbon nanotubes by microwave plasma-enhanced chemical vapor deposition," *Appl. Phys. Lett.*, vol. 72, no. 26, pp. 3437–3439, 1998.
[47] G. W. Ho, A. T. S. Wee, J. Lin, and W. C. Tjiu, "Synthesis of well-aligned multiwalled carbon nanotubes on Ni catalyst using radio frequency plasma-enhanced chemical vapor deposition," *Thin Solid Films*, vol. 388, no. 1–2, pp. 73–77, 2001.
[48] Z. P. Huang, J. W. Xu, Z. F. Ren, J. H. Wang, M. P. Siegal, and P. N. Provencio, "Growth of highly oriented carbon nanotubes by plasma-enhanced hot filament chemical vapor deposition," *Appl. Phys. Lett.*, vol. 73, no. 26, pp. 3845–3847, 1998.
[49] F. Wakaya, K. Katayama, and K. Gamo, "Contact resistance of multiwall carbon nanotubes," *Microelectron. Eng.*, vol. 67–68, pp. 853–857, 2003.
[50] C. Lan, P. Srisungsitthisunti, P. B. Amama, T. S. Fisher, X. Xu, and R. G. Reifenberger, "Measurement of metal/carbon nanotube contact resistance by adjusting contact length using laser ablation," *Nanotechnology*, vol. 19, no. 12, 2008.
[51] S. C. Lim *et al.*, "Contact resistance between metal and carbon nanotube interconnects: Effect of work function and wettability," *Appl. Phys. Lett.*, vol. 95, no. 26, pp. 1–4, 2009.
[52] A. I. Vorob'eva, "Fabrication techniques of electrode arrays for carbon nanotubes," *Physics-Uspekhi*, vol. 52, no. 3, pp. 225–234, 2009.
[53] X. Sun, K. Li, R. Wu, P. Wilhite, and C. Y. Yang, "Contact resistances of carbon nanotubes grown under various conditions," *2010 IEEE Nanotechnol. Mater. Devices Conf. NMDC2010*, pp. 332–333, 2010.
[54] K. Asaka, M. Karita, and Y. Saito, "Modification of interface structure and contact resistance between a carbon nanotube and a gold electrode by local melting," *Appl. Surf. Sci.*, vol. 257, no. 7, pp. 2850–2853, 2011.
[55] X. Sun, K. Li, W. Wu, P. Wilhite, T. Saito, and C. Y. Yang, "Contact resistances of carbon nanotube via interconnects," *2009 IEEE Int. Conf. Electron Devices Solid-State Circuits, EDSSC 2009*, pp. 131–135, 2009.
[56] P. L. McEuen, M. S. Fuhrer, and H. Park, "Single-Walled Carbon Nanotube Electronics," *IEEE Trans. Nanotechnol.*, vol. 1, no. 1, pp. 78–84, 2002.

[57] J.-Y. Park *et al.*, “Electron−Phonon Scattering in Metallic Single-Walled Carbon Nanotubes,” *Nano Lett.*, vol. 4, no. 3, pp. 517–520, 2004.
[58] C. Rutherglen and P. Burke, “Nanoelectromagnetics: Circuit and electromagnetic properties of carbon nanotubes,” *Small*, vol. 5, no. 8, pp. 884–906, 2009.
[59] P. J. Burke, “Luttinger liquid theory as a model of the gigahertz electrical properties of carbon nanotubes,” *Nanotechnology, IEEE Trans.*, vol. 1, no. 3, pp. 129–144, 2002.
[60] M. P. Anantram and F. Léonard, “Physics of carbon nanotube electronic devices,” *Reports Prog. Phys.*, vol. 69, no. 3, pp. 507–561, 2006.
[61] S. Salahuddin, M. Lundstrom, and S. Datta, “Transport effects on signal propagation in quantum wires,” *IEEE Trans. Electron Devices*, vol. 52, no. 8, pp. 1734–1742, 2005.
[62] H. Li and K. Banerjee, “High-frequency analysis of Carbon Nanotube interconnects and implications for on-chip inductor design,” *IEEE Trans. Electron Devices*, vol. 56, no. 10, pp. 2202–2214, 2009.
[63] P. G. Collins and P. Avouris, “Multishell conduction in multiwalled carbon nanotubes,” *Appl. Phys. A Mater. Sci. Process.*, vol. 74, no. 3, pp. 329–332, 2002.
[64] Y. G. Yoon, P. Delaney, and S. G. Louie, “Quantum conductance of multiwall carbon nanotubes,” *Phys. Rev. B - Condens. Matter Mater. Phys.*, vol. 66, no. 7, pp. 734071–734074, 2002.
[65] B. Bourlon, C. Miko, L. Forró, D. C. Glattli, and A. Bachtold, “Determination of the intershell conductance in multiwalled carbon nanotubes,” *Phys. Rev. Lett.*, vol. 93, no. 17, pp. 1–4, 2004.
[66] W. T. Chee and M. Jianmin, “Transmission line characteristics of a CNT-based vertical interconnect scheme,” *Proc. - Electron. Components Technol. Conf.*, no. I, pp. 1936–1941, 2007.
[67] G. W. Hanson and S. Member, “Fundamental transmitting properties of carbon nanotube antennas,” *IEEE Trans. Antennas Propag.*, vol. 53, no. 11, pp. 3426–3435, 2005.
[68] P. Franck, “Mesoscopic electromagnetic model of carbon-nanotube arrays and scalable technological processes: application to the fabrication of novel antennas,” 2013.
[69] V. Parkash and A. K. Goel, “Electrostatic capacitances for carbon nanotube interconnects,” *Microw. Opt. Technol. Lett.*, vol. 51, no. 10, pp. 2374–2378, 2009.
[70] P. J. Burke, S. Li, and Z. Yu, “Quantitative theory of nanowire and nanotube antenna performance,” *IEEE Trans. Nanotechnol.*, vol. 5, no. 4, pp. 314–334, 2006.
[71] M. V. Shuba, G. Y. Slepyan, S. A. Maksimenko, C. Thomsen, and A. Lakhtakia, “Theory of multiwall carbon nanotubes as waveguides and antennas in the infrared and the visible regimes,” *Phys. Rev. B - Condens. Matter Mater. Phys.*, vol. 79, no. 15, pp. 1–17, 2009.
[72] A. Naeemi and J. D. Meindl, “Design and performance modeling for single-walled carbon nanotubes as local, semiglobal, and global interconnects in gigascale integrated systems,” *IEEE Trans. Electron Devices*, vol. 54, no. 1, pp. 26–37, 2007.
[73] C. Rutherglen, D. Jain, and P. Burke, “Rf resistance and inductance of massively parallel single walled carbon nanotubes: Direct, broadband measurements and near perfect 50 impedance matching,” *Applied Physics Letters*, vol. 93, no. 8. 2008.
[74] M. Zhang, X. Huo, P. C. H. Chan, Q. Liang, and Z. K. Tang, “Radio-frequency characterization for the single-walled carbon nanotubes,” *Appl. Phys. Lett.*, vol. 88, no. 16, 2006.
[75] J. J. Plombon, K. P. O’Brien, F. Gstrein, V. M. Dubin, and Y. Jiao, “High-frequency

electrical properties of individual and bundled carbon nanotubes," *Appl. Phys. Lett.*, vol. 90, no. 6, pp. 1–4, 2007.
[76] A. Tselev, M. Woodson, C. Qian, and J. Liu, "Microwave impedance spectroscopy of dense carbon nanotube bundles," *Nano Lett.*, vol. 8, no. 1, pp. 152–156, 2008.
[77] Y. A. Kim, T. Hayashi, M. Endo, Y. Gotoh, N. Wada, and J. Seiyama, "Fabrication of aligned carbon nanotube-filled rubber composite," *Scr. Mater.*, vol. 54, no. 1, pp. 31–35, 2006.
[78] P. Franck, D. Baillargeat, and B. K. Tay, "A bulk equivalent model of carbon-nanotube arrays : Application to the design of novel antennas," *2014 Int. Conf. Numer. Electromagn. Model. Optim. RF, Microwave, Terahertz Appl. NEMO 2014*, pp. 3–6, 2014.
[79] G. Y. Slepyan, S. a. Maksimenko, A. Lakhtakia, O. Yevtushenko, and A. V. Gusakov, "Electrodynamics of carbon nanotubes: Dynamic conductivity, impedance boundary conditions, and surface wave propagation," *Phys. Rev. B*, vol. 60, no. 24, pp. 17136–17149, 1999.
[80] M. M. Shulaker *et al.*, "Carbon nanotube computer," *Nature*, vol. 501, no. 7468, pp. 526–530, 2013.
[81] E. Shahrom and S. A. Hosseini, "A new low power multiplexer based ternary multiplier using CNTFETs," *Int. J. Electron. Commun.*, vol. 93, no. June, pp. 191–207, 2018.
[82] A. Fediai *et al.*, "Towards an optimal contact metal for CNTFETs," *R. Soc. Chem.*, pp. 10240–10251, 2016.
[83] S. Mothes, M. Claus, and M. Schröter, "Toward Linearity in Schottky Barrier CNTFETs," *IEEE Trans. Nanotechnol.*, vol. 14, no. 2, pp. 372–378, 2015.
[84] G. Gelao, R. Marani, R. Diana, and A. G. Perri, "A Semiempirical SPICE Model for n-Type Conventional CNTFETs," *IEEE Trans. Nanotechnol.*, vol. 10, no. 3, pp. 506–512, 2011.
[85] S. Lin, Y. Kim, and F. Lombardi, "Design of a Ternary Memory Cell Using CNTFETs," *IEEE Trans. Nanotechnol.*, vol. 11, no. 5, pp. 1019–1025, 2012.
[86] J. A., G. J., W. Q., L. M., and D. H., "Ballistic Carbon Nanotube field-effect transistors," *Nature*, vol. 424, no. August, p. 654, 2003.
[87] H. Li and Q. Zhang, "Tunable ambipolar Coulomb blockade characteristics in carbon nanotubes-gated carbon nanotube field-effect transistors," *Appl. Phys. Lett.*, vol. 94, no. 2, 2009.
[88] A. D. Franklin *et al.*, "Sub-10 nm carbon nanotube transistor," *Nano Lett.*, vol. 12, no. 2, pp. 758–762, 2012.
[89] P. Bondavalli, P. Legagneux, and D. Pribat, "Carbon nanotubes based transistors as gas sensors : State of the art and critical review," *Sensors Actuators, B Chem.*, vol. 140, pp. 304–318, 2009.
[90] J. T. W. Yeow and Y. Wang, "A review of carbon nanotubes-based gas sensors," *J. Sensors*, vol. 2009, 2009.
[91] P. Bondavalli, P. Legagneux, and D. Pribat, "Carbon nanotubes based transistors as gas sensors: State of the art and critical review," *Sensors Actuators, B Chem.*, vol. 140, no. 1, pp. 304–318, 2009.
[92] M. Cometto *et al.*, "Theoretical study of CNT based waveguide," *2018 IEEE MTT-S Int. Conf. Numer. Electromagn. Multiphysics Model. Optim. NEMO 2018*, pp. 18–20, 2018.
[93] A. C. Patel, M. P. Vaghela, H. Bajwa, and H. Seddik, "Conformable patch antenna design for remote health monitoring," *2010 Long Isl. Syst. Appl. Technol. Conf. LISAT 10*, pp. 1–6, 2010.

[94] H. Bajwa, P. Patra, A. A. Ikram, and J. Mirza, "Nanostructured conformable patch antenna array," *2010 Int. Conf. Inf. Emerg. Technol. ICIET 2010*, pp. 1–4, 2010.
[95] Y. Zhou, Y. Bayram, F. Du, L. Dai, and J. L. Volakis, "Polymer-carbon nanotube sheets for conformal load bearing antennas," *IEEE Trans. Antennas Propag.*, vol. 58, no. 7, pp. 2169–2175, 2010.
[96] A. Mehdipour, I. D. Rosca, A. R. Sebak, C. W. Trueman, and S. V. Hoa, "Carbon nanotube composites for wideband millimeter-wave antenna applications," *IEEE Trans. Antennas Propag.*, vol. 59, no. 10, pp. 3572–3578, 2011.
[97] A. Mehdipour, I. D. Rosca, A. R. Sebak, C. W. Trueman, and S. V. Hoa, "Full-composite fractal antenna using carbon nanotubes for multiband wireless applications," *IEEE Antennas Wirel. Propag. Lett.*, vol. 9, pp. 891–894, 2010.
[98] E. Amram Bengio *et al.*, "High efficiency carbon nanotube thread antennas," *Appl. Phys. Lett.*, vol. 111, no. 16, 2017.
[99] L. Yang, R. Zhang, D. Staiculescu, C. P. Wong, and M. M. Tentzeris, "A novel conformal RFID-enabled module utilizing inkjet-printed antennas and carbon nanotubes for gas-detection applications," *IEEE Antennas Wirel. Propag. Lett.*, vol. 8, pp. 653–656, 2009.
[100] S. Pacchini *et al.*, "Inkjet-printing of hybrid Ag/conductive polymer towards strechable microwave devices," *Eur. Microw. Week 2015 "Freedom Through Microwaves", EuMW 2015 - Conf. Proceedings; 2015 45th Eur. Microw. Conf. Proceedings, EuMC*, pp. 865–868, 2015.
[101] P. Franck, D. Baillargeat, and B. K. Tay, "Carbon-nanotube-based electrically-short resonant antennas," *Int. J. Microw. Wirel. Technol.*, vol. 6, no. 1, pp. 57–62, 2014.
[102] A. Naeemi and J. D. Meindl, "Performance modeling for single- and multiwall carbon nanotubes as signal and power interconnects in gigascale systems," *IEEE Trans. Electron Devices*, vol. 55, no. 10, pp. 2574–2582, 2008.
[103] Y. Awano, S. Sato, M. Nihei, T. Sakai, Y. Ohno, and T. Mizutani, "Carbon nanotubes for VLSI: Interconnect and transistor applications," *Int. Symp. VLSI Technol. Syst. Appl. Proc.*, vol. 98, no. 12, pp. 10–11, 2011.
[104] Z. Liu, L. Ci, S. Kar, P. M. Ajayan, and J. Q. Lu, "Fabrication and electrical characterization of densified carbon nanotube micropillars for IC interconnection," *IEEE Trans. Nanotechnol.*, vol. 8, no. 2, pp. 196–203, 2009.
[105] A. Ceyhan and A. Naeemi, "Cu interconnect limitations and opportunities for SWNT interconnects at the end of the roadmap," *IEEE Trans. Electron Devices*, vol. 60, no. 1, pp. 374–382, 2013.
[106] D. Jiang, T. Wang, S. Chen, L. Ye, and J. Liu, "Paper-mediated controlled densification and low temperature transfer of carbon nanotube forests for electronic interconnect application," *Microelectron. Eng.*, vol. 103, pp. 177–180, 2013.
[107] Wikipedia, "Back end of line." [Online]. Available: https://en.wikipedia.org/wiki/Back_end_of_line.
[108] K. Kordás *et al.*, "Chip cooling with integrated carbon nanotube microfin architectures," *Appl. Phys. Lett.*, vol. 90, no. 12, 2007.
[109] W. A. Gaviria Rojas *et al.*, "Solution-processed carbon nanotube true random number generator," *Nano Lett.*, vol. 17, no. 8, pp. 4976–4981, 2017.
[110] K. Jensen, J. Weldon, H. Garcia, and A. Zettl, "Nanotube radio," *Nano Lett.*, vol. 7, no. 11, pp. 3508–3511, 2007.
[111] C. Rutherglen and P. Burke, "Carbon nanotube radio," *Nano Lett.*, vol. 7, no. 11, pp. 3296–3299, 2007.
[112] S. Demoustie, "Review of two microwave applications of carbon nanotubes: nano-antennas and nano-switches," *Comptes Rendus Phys.*, vol. 9, no. 1, pp. 53–66, 2008.

Chapter 3. Potentialities of CNT as metallic walls for Air-Filled SIW (AF-SIW) in E-band (71-86GHz)

In the previous chapter, we considered some characteristics of CNT as well as its applications in electronic systems. Therefore, in this chapter, an Air-Filled SIW (AF-SIW) based on CNT technology used to design the elementary blocks of a Butler Matrix (BM) in band E (71-86 GHz) will be investigated and introduced. As we know, the SIW concept is based on the realization of a waveguide embedded inside a substrate by using for instance a standard PCB technology. This is achieved by using double-faced metallized substrates, and vias arranged in two parallel lines to define the lateral walls of the waveguide. Based on this basic concept, to obtain CNT-based AF-SIW, the lateral metallic-via walls of rectangular waveguides will be replaced by CNTs walls transferred to the top or bottom metallic layer by flip-chip technique. The design rules as well as the fabrication process of these structures will be detailed in this chapter.

3.1 Review on the electromagnetic model for CNT simulation

Considering CNTs in vacuum or in air, the model developed by XLIM/CINTRA, our collaborators in the TRICOT ANR project, and presented in detail so far in Chapter 2, is reminded in equation (3-1):

$$\sigma_{CNTA}(z) = \begin{pmatrix} 0 & 0 & 0 \\ 0 & 0 & 0 \\ 0 & 0 & \sigma_{Axial}(q,\omega) \end{pmatrix} \quad (3\text{-}1)$$

with

$$\sigma_{Axial}(q,\omega) = D_{NT} * \frac{8*e^2*v_F}{h*(\nu+j\omega)} \quad (3\text{-}2)$$

This EM model represents an artificial material having vertical conductivity $\sigma_{Axial}(q,\omega)$ aligned along z-axis, which can be created by using Ansoft HFSS in order to perform simulations.

Fixed parameters are $e \approx 1.602 * 10^{-19}\ C$, the elementary charge; $h \approx 6.626 * 10^{-34}\ J.s$, the Plank constant; $v_F = 9.71 * 10^5\ m/s$, the Fermi velocity in CNTs; $\nu = \tau^{-1}$, the relaxation frequency with $\tau \approx 3 * 10^{-12} s$.

Variable parameters are ω, the angular frequency, and the density of CNTs, that may fluctuate depending on the process used for the CNTs growth. On the basis of CINTRA experience, $D_{NT} = 2 * 10^{15}$ per m^2 has been chosen for simulation. At 78.5 GHz, mid-E-band frequency, this leads to $\sigma_{Axial}(q,\omega)$ = 1.01*10^6 S/m.

3.2 CNT-based AF-SIW waveguide

3.2.1 General view of the proposed AF-SIW

The choice was made to feed this CNT-based AF-SIW through CPW-to-SIW transitions. Due to energy transfer conditions through this transition, silicon-based wafer for CNT was not an accurate choice, so that a PCB-based substrate was considered. As a matter of fact, an exploded view of investigated CNT-based AF-SIW waveguide structure, together with its access lines, is presented in Figure 3-1. This waveguide consists of three

layers: (i) a bottom metallic layer etched on a dielectric substrate ROGERS RT Duroid 5880 (with a thickness of 0.127 mm and a relative dielectric permittivity of 2.2) where the feeding lines and matching slots are defined, (ii) the CNT walls transferred on the bottom metallic layer by using flip-chip process to form the lateral wall of the waveguide, and (iii) the top metallic cover layer. Notice that to avoid the appearance of substrate modes [1], [2] within the E-band, a thin bottom substrate thickness (0.127 mm) is considered.

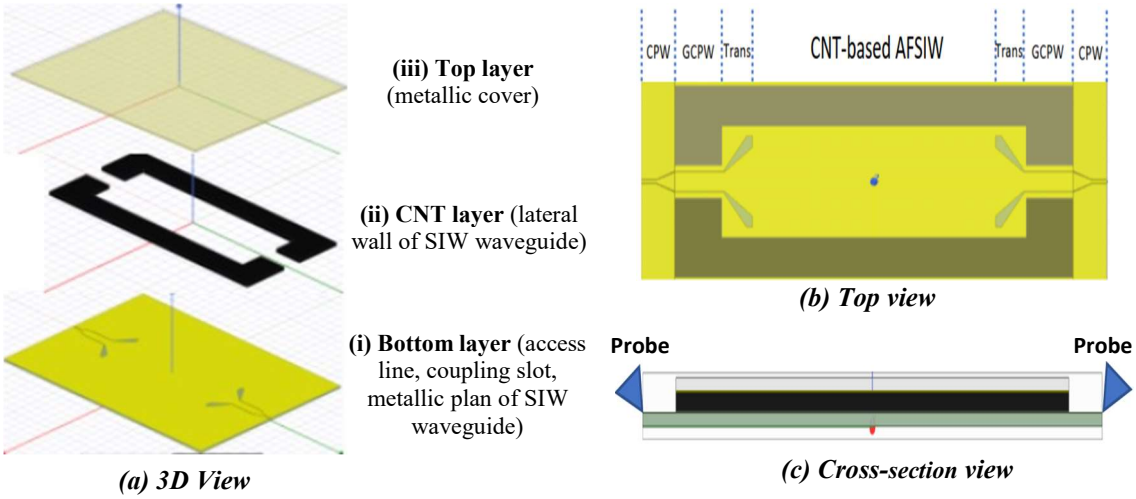

Figure 3-1. Exploded 3D-view of CNT-based AF-SIW with its transitions and access lines.

In order to feed this waveguide, an optimized and developed transition was designed and simulated based on the coplanar waveguide (CPW) transition design in [3]. It should be noticed that, for this SIW waveguide, the electrical energy is contained in the air inside the waveguide, therefore a direct transition from a CPW access line on Duroid substrate (in which the electrical energy is essentially contained inside the substrate) to the waveguide is tricky. An intermediate path, via a grounded-CPW (GCPW) in the air, is therefore needed to ensure a smoother transition. The top metallic cover will also serve as a ground plan for the GCPW access line. A detailed description of the transition used for our waveguide will be presented in the next section and in order to compare the performance, the state-of-the-art of transitions from transmission line to SIW will be also introduced.

3.2.2 Transmission line-to-SIW transitions - state of the art

High performance transition between planar transmission lines and SIW is the key circuit building element for the integrated applications of SIW. Several transitions from transmission line to SIW were investigated over the last years. They can be roughly divided into single-layered substrate or multi-layered substrate applications. Multi-layered connections can be typically used in circuits involving a multi-layered fabrication process such as LTCC [4]. Dual-layered SIW transitions to microstrip [5] or CPW technology [6] have been also successfully proposed, but multi-layered SIW circuit implementations often experience alignment issues.

Therefore, the vast majority of recently published transitions from transmission line to SIW have been investigated as single-layered circuits including connection to microstrip [7], [8], grounded CPW [3], [9]–[13], regular CPW [14]–[17], and coplanar

strip-line [18]. A transition involving a slot-line was also presented within a SIW magic-T structure for mixer application [19]. Figure 3-2 and Figure 3-3 illustrate some different types of transitions.

Figure 3-2 (a) illustrates a SIW-based bandpass filter based on LTCC technology and this filter operates around 35 GHz [4]. By using the multilayered microstrip-to-SIW transition for coupling the first resonator, the filter size and losses could be reduced additionally compared to a classical shunt-inductance-coupled filter in MS technology. Another multilayered ultra-wideband CPW-to-SIW transition using an elevated-CPW section is presented in Figure 3-2 (b) [6]. The elevated-CPW is used to attain a gradual mode matching and to achieve the consequent wide bandwidth. The measurement results show 70% fractional bandwidth at 10 dB return loss and 0.9 dB insertion loss from 19 to 40 GHz (the operating frequency is 30 GHz).

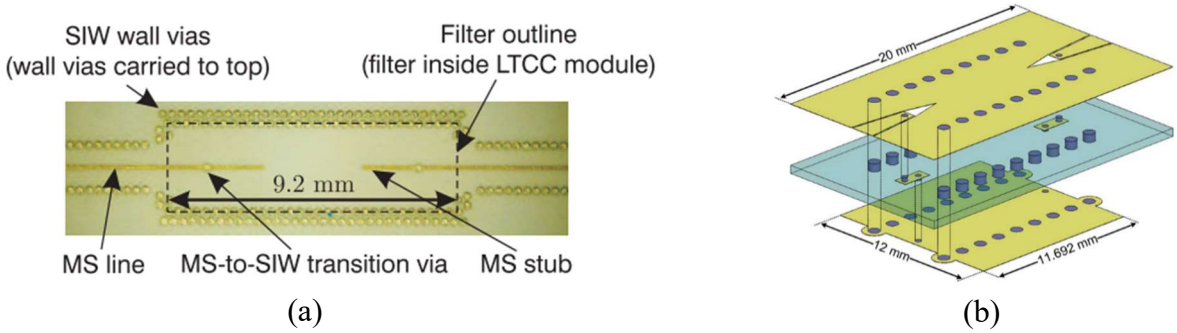

Figure 3-2. Multi-layered connections between planar transmission lines and SIW as given in: (a) [4] *; (b)* [6].

Several kinds of single-layered connections between planar transmission lines and SIW are introduced in Figure 3-3. A transition from microstrip to SIW within the same dielectric substrate is presented in Figure 3-3 (a). The experiments at 28 GHz show that a relative bandwidth of 12% with a 20-dB return loss can be obtained with an in-band insertion loss better than 0.3 dB [7]. The first back-to-back transition structure from CPW to SIW integrated on the same substrate layer was proposed by Dominic Deslandes and Ke Wu in 2001 [14] as illustrated in Figure 3-3 (b). This transition is based on the 90° bend coupling slot in the terminal of CPW. The length of each CPW bend slot is approximately $\lambda/4$ and ended with a short circuit. With this kind of transition, a 7%-bandwidth was obtained with a 15-dB return loss and a measured insertion loss better than 3.2 dB in the entire band. After this first study of CPW-to-SIW transition, numerous works were developed to improve the performance of this kind of transition. For example, in [3] and in [15], by using the triangular-shaped coupling slot, a very large relative bandwidth of 80% for 20-dB return loss is obtained, with a maximum insertion loss of only 0.4 dB and 0.3 dB, respectively. These two transitions are illustrated in Figure 3-3 (f) and Figure 3-3 (c), respectively. Another kind of transition from planar transmission line to SIW is presented in Figure 3-3 (e). This transition is based on a current probe used to transfer power between two dissimilar transmission lines [9]. The experiments at 28 GHz show that a relative bandwidth of 10% for 20-dB return loss can be easily obtained with an insertion loss lower than 0.73 dB over the bandwidth of interest.

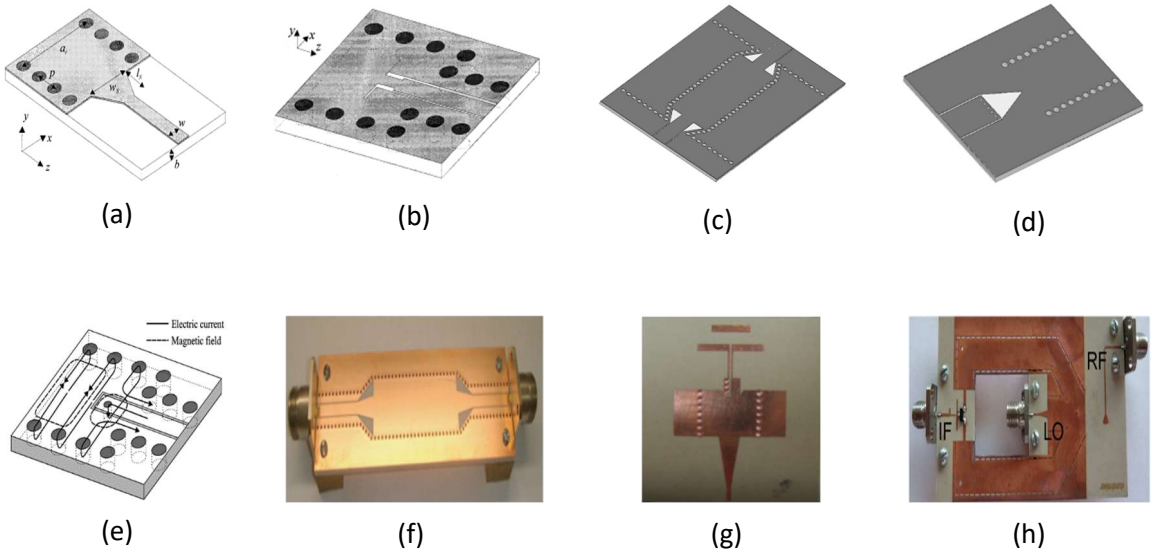

Figure 3-3. Single-layered connection between planar transmission lines and SIW: (a) Microstrip tapered transition in [7]*, (b) Coplanar slot transition in* [14]*, (c) Back-to-back CPW-to-SIW transition in* [15]*, (d) Inverted CPW-to-SIW interconnect in* [16]*, (e) GCPW-to-SIW current probe in* [9]*, (f) GCPW-to-SIW triangle coupling slot in* [3]*, (g) Coplanar Strip-line to SIW transition in* [18]*, (h) Slot-line to SIW transition in* [19].

In order to compare the performance of difference types of TLine-to-SIW transition, a summary in terms of operating frequency, bandwidth and maximum insertion loss is presented in Table 3-1.

Ref	Type of transition	Layer	Operating Frequency (GHz)	Relative Bandwidth regarding matching	Maximum Insertion Loss (dB)
[6]	CPW-to-SIW	Multi	30	70% at 10-dB	0.9
[7]	Microstrip-to-SIW	Single	28	12% at 20-dB	0.3
[9]	GCPW-to-SIW current probe	Single	28	10% at 20-dB	0.73
[12]	GCPW-to-SIW coupling slot	Single	50	30% at 20-dB	0.5
[3]	GCPW-to-SIW triangle slot	Single	13	80% at 20-dB	0.4
[14]	CPW-to-SIW coupling slot	Single	28	7% at 15-dB	3.2
[15]	CPW-to-SIW triangle slot	Single	23	80% at 20-dB	0.3
Our work (3.2.3)	CPW-to-GCPW-to-SIW triangle slot	Multi	78.5	35% at 15-dB	0.5

Table 3-1. Performance comparison of different types of TLine-to-SIW transitions.

As shown in Table 3-1, the transitions in form of triangle coupling slot exhibit a wider bandwidth (about 80%) than the other ones and achieved a significantly low insertion loss of less than 0.4 dB. Thus, this kind of coupling slot was chosen for our CNT-based AF-SIW, which will be presented more in details in the next section.

3.2.3 Proposed CNT-based AF-SIW transition

As mentioned previously, a CPW-to-GCPW-to-SIW transition is considered for our CNT-based AF-SIW as presented in Figure 3-1. This transition is mainly based on the

quarter-wavelength triangle coupling slot introduced in [3], but a slightly more complex geometry was adopted in order to achieve better results for the whole E-band frequency. The detailed view of this transition is illustrated in Figure 3-4.

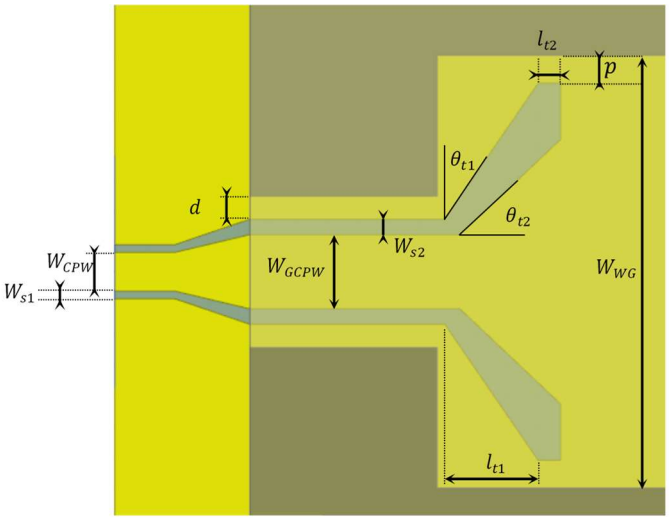

Figure 3-4. Schematic view of broadband transition for CNT-based AF-SIW.

The broadband transition geometry is established by two angles θ_{t1} and θ_{t2} as well as the taper lengths l_{t1} and l_{t2}. These dimensions are crucial factors to achieve a very good matching. Also, the distance p between the end of the transition and the CNT lateral wall is defined. The physical dimensions of the CPW and GCPW are also given: W_{CPW}, W_{s1}, d, W_{GCPW}, W_{s2}.

For the starting point, l_{t1} should be equal to a quarter-wavelength at the center frequency of the E-band (0.95 mm at 78.5 Hz). Numerous parametric analysis perform with full-wave simulations concluded to an outer angle θ_{t1} around 35°, meanwhile the typical value for θ_{t2} is around 40°. The optimized dimensions of the transitions are as follows: $l_{t1} = 0.62$ mm, $l_{t2} = 0.15$ mm, $\theta_{t1} = 35°$, $\theta_{t2} = 38°$, $p = 0.25$ mm.

Concerning the CPW and GCPW dimensions, a 50-Ω characteristic impedance needs to be obtained. Let us notice that these dimensions were also optimized in compliance with the standard 100-um pitch for measurements with GSG pads. Thus, the optimized dimensions are as follows: $W_{CPW} = 78$ um, $W_{s1} = 10$ um, $d = 150$ um, $W_{GCPW} = 480$ um, $W_{s2} = 25$ um.

By using this transition, the simulated return loss is better than 15 dB in the entire E-band. Meanwhile, the maximum simulated insertion loss is better than 0.5 dB over the E-band and occurs at 86 GHz. These results allow us to believe in a suitable access line for our circuits. The detailed simulation results will be introduced in the next part.

3.2.4 Design and simulation results of the CNT-based AF-SIW

In order to achieve a first cut-off frequency of 52 GHz for the E-band operation, the waveguide width W_{WG} is calculated as 2.8 mm by using the following equation:

$$f_{c_{10}} = \frac{c_0}{2 \times W_{WG} \times \sqrt{\varepsilon_r}} \tag{3-4}$$

where $f_{c_{10}}$ is the first cut-off frequency, c_0 is the light velocity in vacuum, and ε_r is the relative permittivity of waveguide dielectric, in this case $\varepsilon_r = 1$ because the waveguide is

filled with air. The height of the CNT walls h_{CNT} is chosen at 200 µm, that is an easily reachable height at CINTRA, Singapore for future realization.

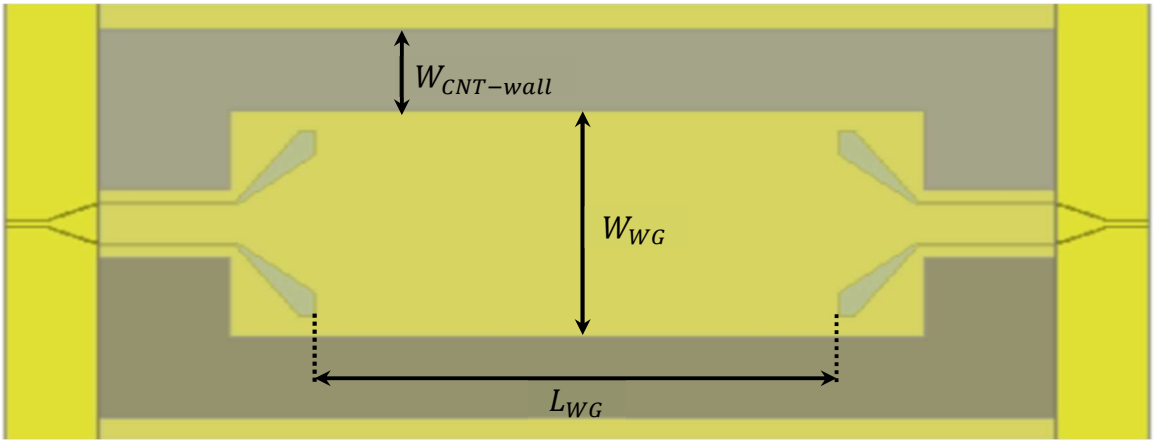

Figure 3-5. Top view of investigated CNT-based AF-SIW.

First simulations were carried out by focusing on the width of the CNT walls. In order to evaluate the impact of the CNT lateral walls width ($W_{CNT-wall}$) on the waveguide performance, a variation of the width between 0.1 mm and 1 mm was applied in simulation. The simulation results which are obtained with a 9-mm long air-filled waveguide including access lines (L_{WG}), 0.2-mm height (h_{CNT}) and 2.8-mm width (W_{WG}), are shown in Figure 3-6.

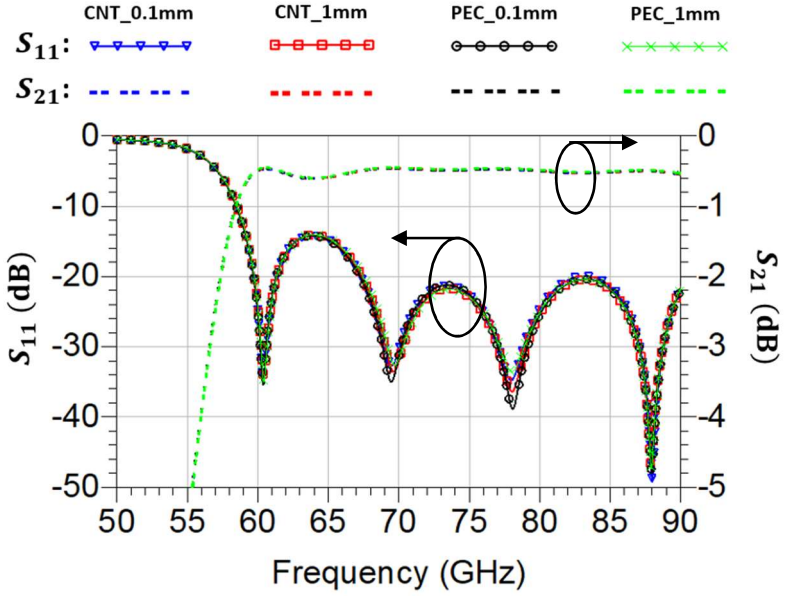

Figure 3-6. Performance comparison in term of S-parameters of investigated CNT-based AF-SIW with two different values of CNT-wall width ($W_{CNT-wall} = 0.1\ mm$ and $W_{CNT-wall} = 1\ mm$).

As shown in Figure 3-6, the width of the lateral wall has a very small impact on the insertion loss, even for a small wall thickness (0.1 mm). The results are also comparable with the ones obtained with a perfect electrically conducting wall (PEC) Hence, CNTs can be used instead of metallic walls for the realization of waveguides without affecting the transmission even if $\sigma_{Axial}(q,\omega) = 1.01*10^6$ S/m. This is due to the preferential axial conduction in CNTs while transversal conduction has been neglected.

This will have to be confirmed further by measurements. In addition, it allows us to select the value of CNT-wall width, which is compatible with the fabrication process requirements without any constraint regarding its impact.

The extraction of the propagation constant will be performed through a de-embedding algorithm [20] requiring sets of S-parameters for different lengths of waveguides. Ideally, the extraction should be done using two different waveguides whose electrical length differs from 90 degrees at the center frequency [21]. However, for losses estimation a longer phase difference should be necessary to raise the power loss level way above the measurement uncertainty. For these reasons, five different lengths of the investigated waveguide were implemented following the rule given by (3-5), where L_0 = 1.4 mm stands for the waveguide length of the shorter feature ("Thru") and ΔL = 0.9 mm is close to a quarter of guided wavelength at center frequency. The simulated results obtained for different lengths of investigated waveguides are illustrated in Figure 3-7.

$$L_i = L_0 + i * \Delta L \qquad , 0 \leq i \leq 4 \tag{3-5}$$

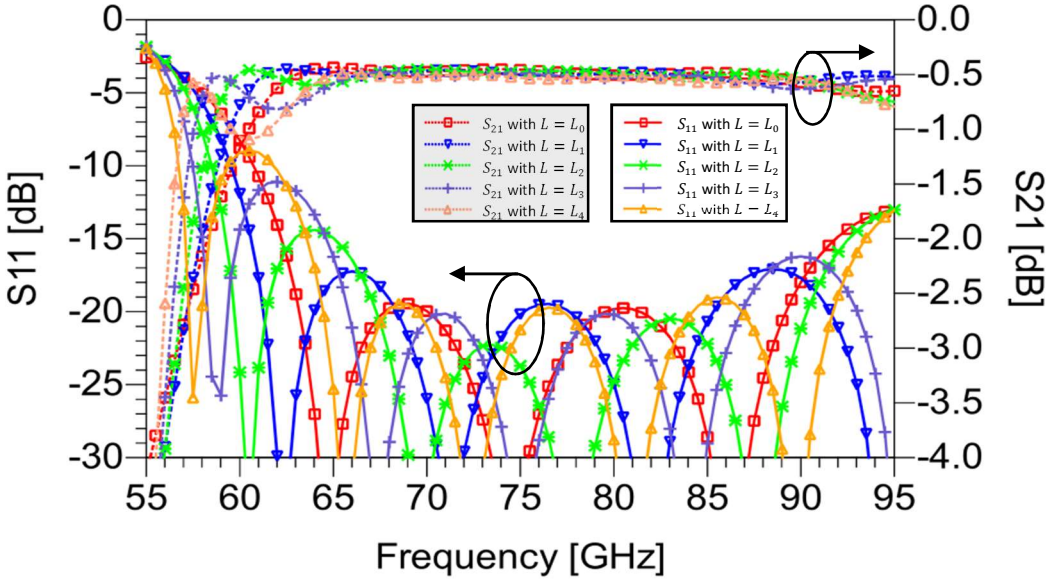

Figure 3-7. Simulated S-parameters of the different waveguides with transitions and CPW/GCPW access line fabricated for E-band.

As presented in Figure 3-7, the simulated return loss is better than 15 dB in the entire E-band for all structures. Meanwhile, the maximum simulated insertion loss is better than 0.6 dB over the E-band and occurs at 86 GHz.

In order to validate the de-embedding algorithm used to extract the attenuation constant as well as the quality factor of the investigated waveguides [20], simulated results with MATLAB code are presented in Figure 3-8, where two different lengths of waveguides ("L_0=Thru" and "L_4") were chosen for this extraction. The quality factor at 1.5*f_{c10} = 80 GHz is about 400, meanwhile the maximum attenuation constant is around 0.015 dB/mm over the entire E-band.

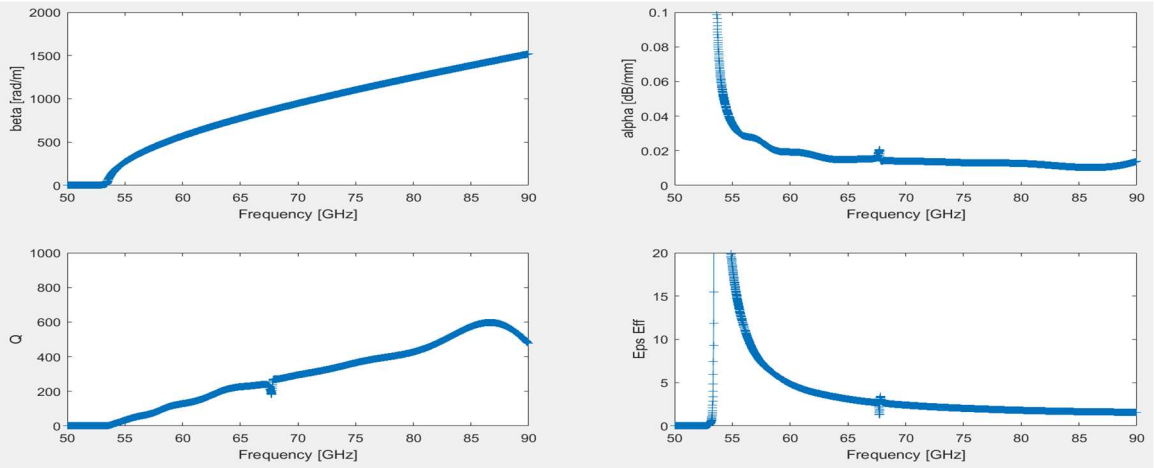

Figure 3-8. Waveguide performance vs. frequency: a) phase constant, (b) attenuation constant, (c) Q-factor and d) effective permittivity after de-embedding technique from MATLAB (L_4 - L_0).

3.3 Fabrication process

In this section, the description of the fabrication process considered by CINTRA laboratory in Singapore to manufacture the CNT-based AF-SIW waveguides is introduced, following their recommendations. This fabrication process is composed of three steps: bottom layer definition, top layer definition and waveguide definition by flip-chip bonding from top layer toward the bottom layer. The general layout overview is firstly introduced.

3.3.1 Layout overview

Top view of layout for all fabricated structures including waveguides and calibration kits, to be fabricated on a wafer of 4-inches diameter, are illustrated in Figure 3-9. Two different values of the width of CNT walls will be considered: 1 mm and 1.5 mm in order to adapt the fabrication process requirements and also to compare the waveguide performance. The waveguides having CNT lateral wall of 1 mm are placed on the left side of this wafer, whereas the waveguides of 1.5-mm-CNT wall are placed on the right side. Those two widths are for mechanical stability comparison.

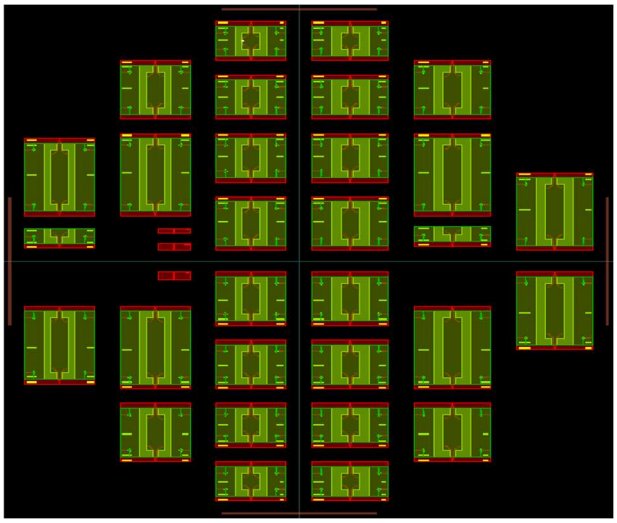

Figure 3-9. Layout of the CNT-based AF-SIW waveguides and calibration kits.

3.3.2 Bottom layer

3.3.2.1 CNTs preparation

The CNTs will be fully grown on a Silicon wafer and after the growth, a gold layer of 120 nm by using E-beam evaporation will be deposited on top of the CNTs. The geometry of this structure is illustrated on Figure 3-10.

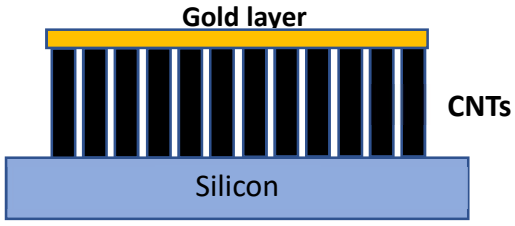

Figure 3-10. CNTs preparation.

3.3.2.2 Bottom layer definition

After the growth of CNTs, the next step is the preparation of the bottom layer. This layer could be fabricated by the following stages:

- A cleaned ROGERS substrate (RT Duroid 5880 with a thickness of 0.127 mm and a relative dielectric permittivity of 2.2) is used to prepare the bottom part of AF-SIW.
- Negative photoresist is spun onto the wafer and the wafer is put into oven and soft-baked afterwards.
- The wafer is inserted into mask aligner and aligned regarding the Bottom mask.
- After using UV light to polymerize resist, mask is removed and resist is developed.
- After development, gold is deposition through e-beam evaporation with a thickness of 1000 nm.
- Negative resist is removed and bottom is defined.

The whole process of the bottom layer definition is illustrated in Figure 3-11 and Figure 3-12 presents the mask used during the photolithography process.

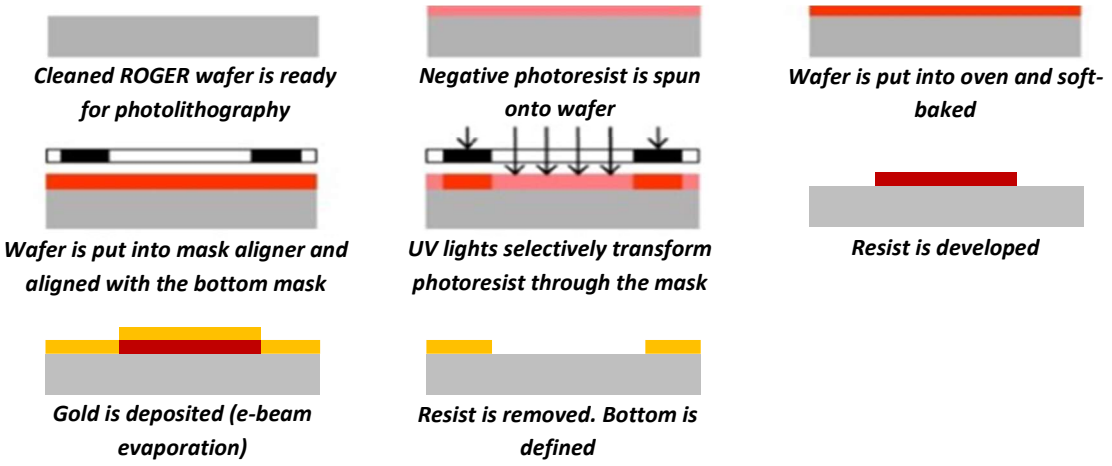

Figure 3-11. Bottom layer definition.

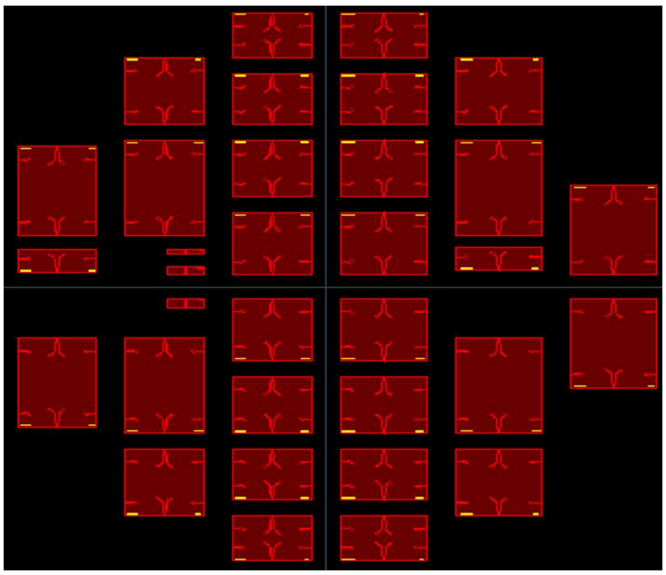

Figure 3-12. The photolithography Bottom mask.

3.3.2.3 CNT transfer on bottom layer

After the fabrication of bottom layer, the next step consists in transferring the CNTs, which were already prepared (see Figure 3-10), on the bottom layer by using flip-chip bonding. In order to carry out this step, a particular adhesive material called SAC305 is considered to efficiently stick the CNT on the bottom layer. A summary of this step is presented below:

- The photolithography CNT mask (as illustrated in Figure 3-13) is used to deposit the SAC305 on the bottom layer through e-beam evaporation with a thickness of 1000 nm. This step will be done in one shot on the whole bottom with a process similar to the one on Figure 3-11. This step is usually performed by evaporating SAC305 through a simple shadow mask but a photolithography mask guarantees more uniformity in the process than a shadow one.
- CNTs transferring is carried out by flip-chip bonding process by using "the principle of the sandwich", which means that the SAC305 will make contact between two gold layers instead of one gold layer and the CNTs. This principle will be presented in Figure 3-14 and Figure 3-15.
- During the flip-chip bonding process, the bottom will be heated at 260° for 2min30s as the melting point of SAC305 is around 217°. The force applied on the whole wafer is around 60 N.
- After the flip-chip bonding process, the silicon wafer will be pulled away the CNT and the CNT transferring process is finished.
- After CNT transfer, the bottom wafer will be diced into unit devices.
- Finally, a thin layer of gold (120 nm) will be sputtered on top of the CNTs to protect it from potential damage (see Figure 3-16), by using a shadow mask similar to the CNT mask. The mask is necessary as it prevents gold from deposition inside the CPW gap and waveguide slots of the bottom layer. Also a shadow mask is mandatory instead of the photolithography CNT mask as CNTs cannot be put in contact with any material.

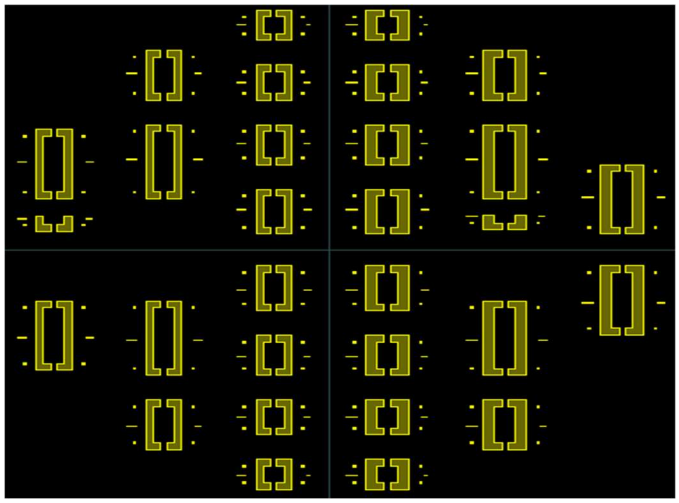

Figure 3-13. The photolithography CNT mask.

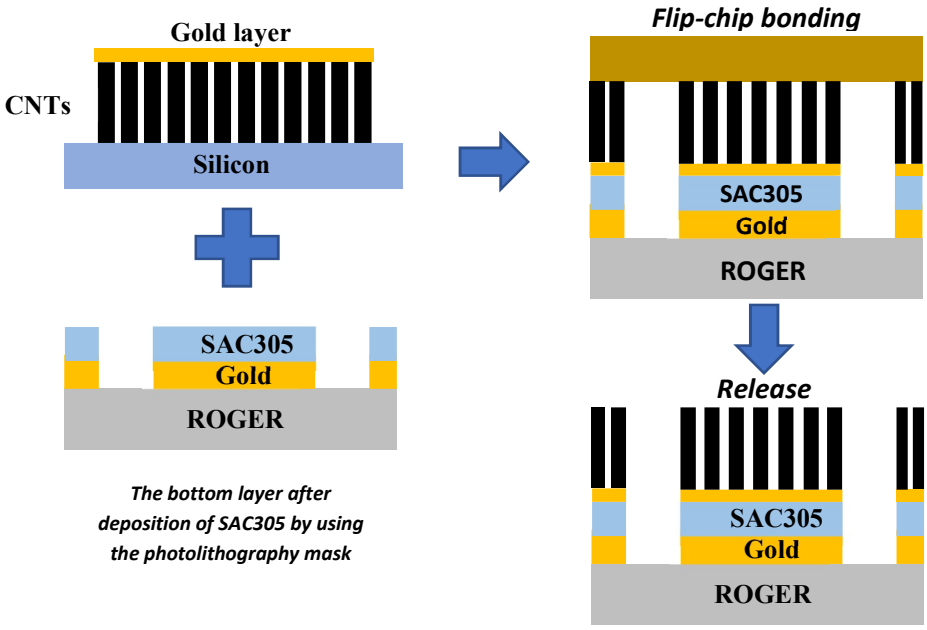

Figure 3-14. Diagram of CNT transferring on ROGER substrate.

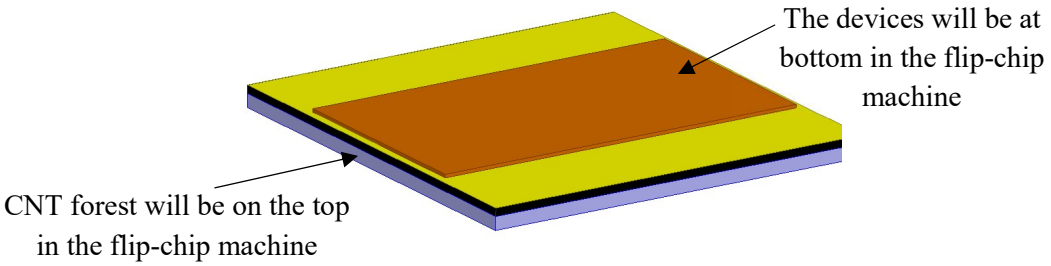

Figure 3-15. Flip-chip bonding process.

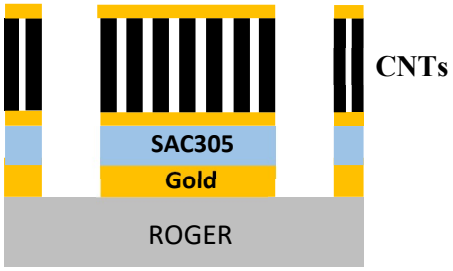

Figure 3-16. Sputtering of gold through a shadow mask to cover the CNT.

3.3.3 Top/cover layer definition

The process to define the top layer is similar to the one used for the bottom layer as illustrated in Figure 3-17. However, the wafer used for top layer is made of silicon instead of ROGER substrate. The photolithography Cover mask is also presented in Figure 3-18.

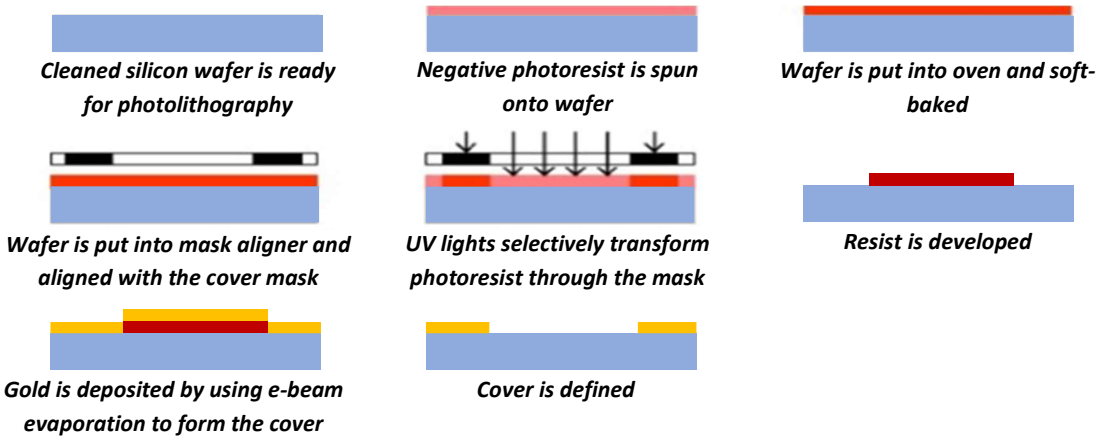

Figure 3-17. Top/cover layer definition .

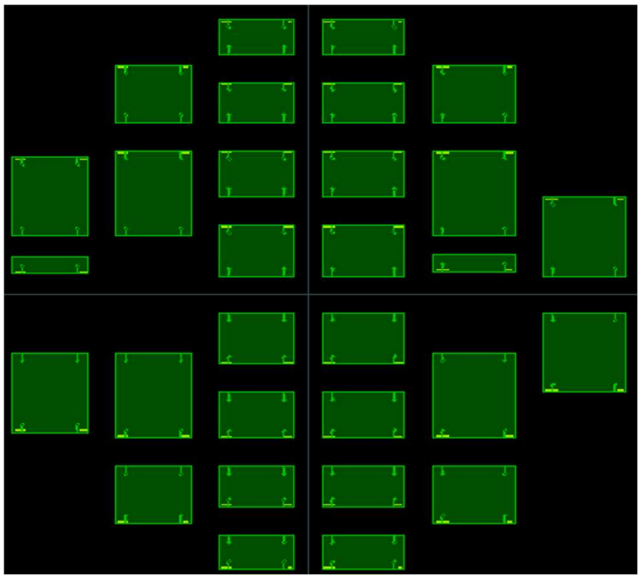

Figure 3-18. The photolithography Cover mask.

After definition, the cover wafer will be diced into unit devices in order to process the final step.

3.3.4 Waveguide definition by flip-chip process from cover towards bottom layer

Finally, the CNT-based AF-SIW waveguide manufacturing is completed by flip-chip bonding process from the cover layer towards the bottom layer. This step could be detailed as follows:

- On the cover layer of unit device, SAC305 with thickness of 1000 nm will be evaporated through the photolithography CNT mask (see Figure 3-19). This is possible as the latter is symmetrical as long as only one device is considered. Using the photolithography method with CNT mask instead its shadow mask counterpart enables better precision in the process.
- Flip-chip bonding from cover towards bottom layer (see Figure 3-20), in presence of spacers not to crash CNTs.
- Once again, the device will be heated at 260° for 2min30s. This is the same SAC305 with a melting point around 217°. The force applied on the unit device is around 40 N.

Figure 3-19. Cover layer after SAC305 deposition.

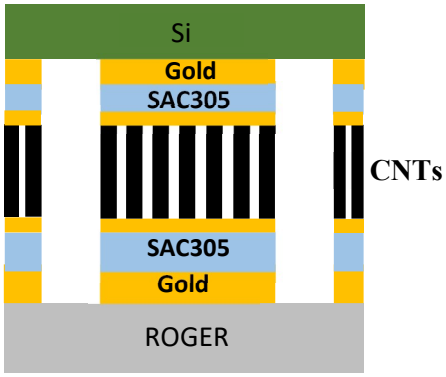

Figure 3-20. Waveguide definition.

3.4 Measurement results

The first measurement process was carried on at CINTRA laboratory-Singapore for the CNT-based AF-SIW named "L2". Figure 3-21 illustrates the general view of the investigated waveguide after CNTs transfer on bottom layer.

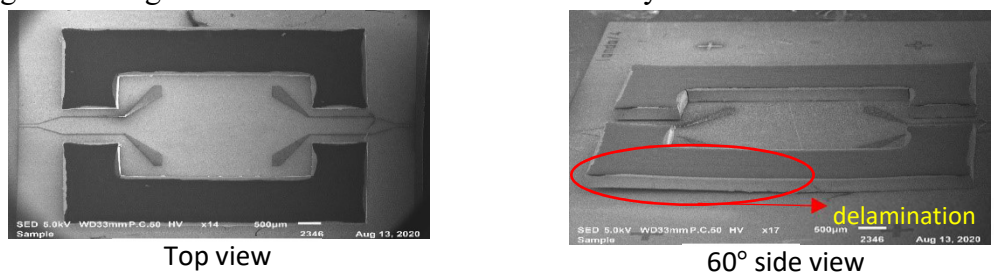

Figure 3-21. General view of CNT-based AF-SIW after CNTs transfer on bottom layer.

As shown in Figure 3-21, it is obvious that a delamination is observed between the CNT wall and the bottom layer, which can lead to a bad behavior of this waveguide with much bottom leakage. In order to check the waveguide performance and investigate where unexpected results could come from, three measurement configurations were taken into account:

- Measurement with the presence of CNT wall (the one delaminated) and with the top cover: **w/CNT w/cover**
- Measurement with the presence of CNT wall (the one delaminated) and without the top cover: **w/CNT wo/cover**
- Measurement without the CNT and without the top cover, on another L_2 device, just before the CNT transfer. That means that only the 1000 nm of SAC305 act as a "wall": **wo/CNT wo/cover**

The relevant measurement results of these configurations are presented in Figure 3-22. The simulation results of the second configuration was also convened for comparison purpose (no delamination has been considered during simulation).

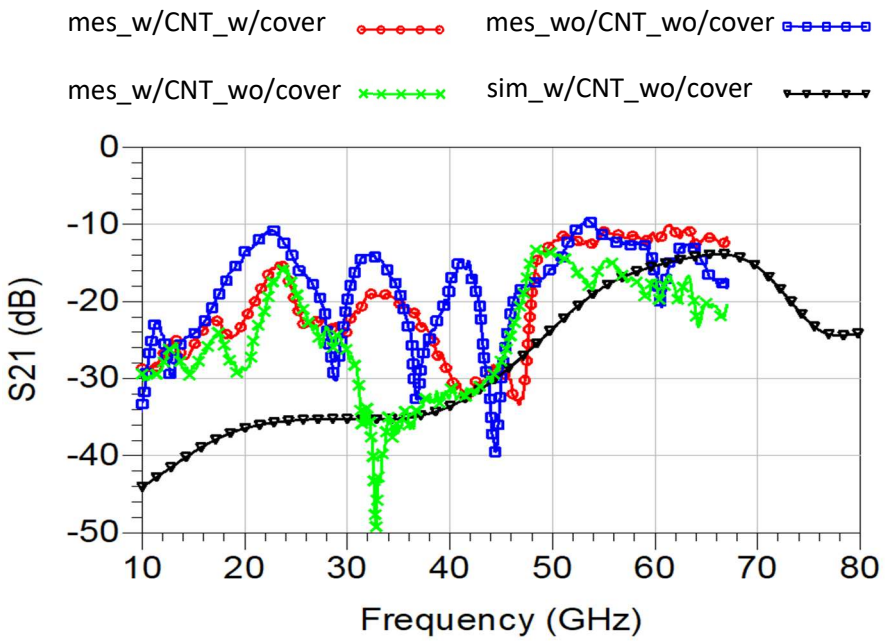

Figure 3-22. Measurement results for three measurement configurations.

The measurement results illustrated in Figure 3-22 demonstrates, at first sight, an opened waveguide structure behavior. Nevertheless, a deep insight leads to the following observations: the results are not so much different between waveguides 'w/CNT w/cover' and 'w/CNT wo/cover' (red and green curves). In both cases, a cut-off frequency of ~50 GHz may be observed. In parallel, no cut-off frequency is visible in the framework of 'wo/CNT wo/cover' measurements: this proves that the CNT wall acts as a metallic wall.

For the two cases with CNTs, it can be observed that the presence of cover has some influence regarding loss. In the "waveguide bandwidth", losses are increasing with frequency when no cover is present, that is not the case in the presence of cover that prevent from top leakage if cover contact with CNT wall is perfect. By the way, it seems

difficult to explain if the encountered losses come from delamination part at the bottom or from a bad contact with the cover on top, or both.

To better clarify, a simulation 'w/CNT wo/cover' was also performed to be compared with measurements in almost similar conditions (leading to a comparison between black and green curves, green curve with delamination, black curve without delamination). Increasing loss with frequencies, but without a clear cut-off frequency this time, was observed in simulation. Having the cut-off frequency observation apart, this let us think that during the 'w/CNT w/cover' measurements there exist some contacts between the CNT walls and the top cover even if this contact is not perfect everywhere.

As a conclusion, there exist bad contacts between the CNT wall and the bottom layer because of delamination part, which obviously provides huge bottom leakage during propagation. There certainly exist some contacts between CNTs and cover but nothing can be proven concerning the quality of this contact: some top leakage may also come from this part. Hence, it is important to improve techniques to transfer CNTs in order to have a better contact between CNT walls and metalized substrate and cover. Further simulations considering delamination should be provided to better investigate the behavior.

3.5 CNT-based AF-SIW 3-dB coupler

Recently, the couplers have been recognized as essential building blocks in microwave and mm-wave circuits which can operate different functions depending on the application [22]–[25]. In some cases, they can be used to split an input signal into two waves with a certain power ratio between them while affecting one of the two by a certain amount of phase shift. This function is particularly effective for realizing mixers [26], [27], phase shifters [28], [29] and antenna feeding networks [21], [24], [29], [30]. In addition, the couplers are also used to extract a small fraction of a travelling signal along a waveguide, thus providing information about its amplitude and phase [32]. It is important that this extraction could be directional, in the sense that the coupler will be able to differentiate between two opposite travelling directions. The main application of such a component is the measurement of scattering parameters. Couplers are therefore a critical component of any vector network analyzer (VNA) [32].

As the SIW technology provides a good platform for carrying relatively high-power signals while avoiding parasitic coupling, it has been extensively studied to design the couplers and to improve its performance. Indeed, several kinds of SIW couplers used for antenna feeding network were surreptitiously introduced in Chapter 1, section 1.3.4, when dealing with Butler matrices. They will be detailed in this section in order to compare with the proposed couplers in terms of performance.

Generally, most of SIW couplers are based on one of two different topologies: the slot-based and the ring-shaped couplers. As illustrated in Figure 3-23, the slot-based couplers are based on coupled modes travelling in adjacent waveguides through apertures, either performed in the waveguide broad [33], [34] or side [35] walls. The ring-shaped couplers are based on the well-known ring shaped (or rat-race) couplers and it was first applied in SIW in 2006 [36] but was introduced as early as in 1947 by Tyrrell [37] in conventional rectangular waveguide. The power distribution in this case is caused by a specific standing-wave pattern along the ring.

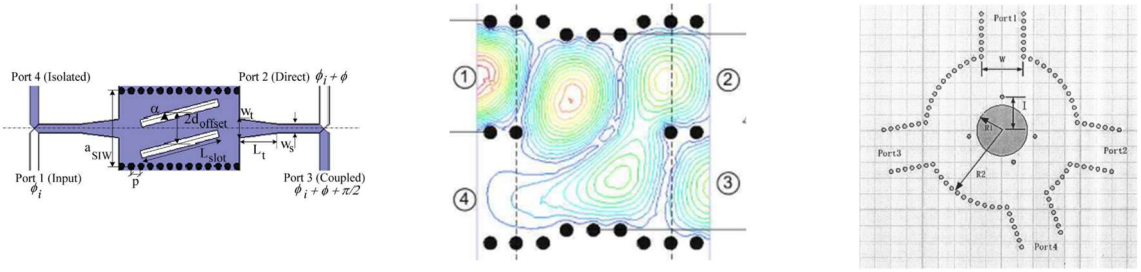

(a) (b) (c)

Figure 3-23. Three examples of existing SIW coupling topologies for coupler design: (a) broad-wall aperture [34]*, (b) side-wall aperture (short-slot)* [35] *and (c) ring-shaped* [36].

Thanks to its simple formulation and wide use in antenna feeding networks, the short-slot topology was selected in this PhD to design the SIW-based couplers. The detailed description of this topology will be introduced in the next section.

3.5.1 Short-slot coupler principle of operation and theory

The short-slot coupler topology was first demonstrated by Riblet based on the waveguide technology in 1952 [38] along with its theoretical description and then it was widely used in a lot of different rectangular waveguide based applications. Since 2005, this topology of coupler has been extensively designed. For instance, SIW 90° hybrid couplers based short-slot structure are reported in [35], [24], [25], [39]–[43].

Basically, the operation principle of short-slot coupler depends on the interference of two propagating modes: TE_{10} and TE_{20}. The schematic of this topology in SIW implementation form is illustrated in Figure 3-24 [32]. In order to provide the required interference, a larger waveguide is inserted between four waveguide accesses. For practical reasons, the access waveguides are operating in their mono-mode frequency band, carrying only a propagating TE_{10}. However, both TE_{10} and TE_{20} modes can propagate in the enlarged middle zone and provide the power division functionality. Therefore, equal power division, and 90° of phase difference between the output ports at the central frequency is required, along with low return loss and high isolation for the largest relative bandwidth.

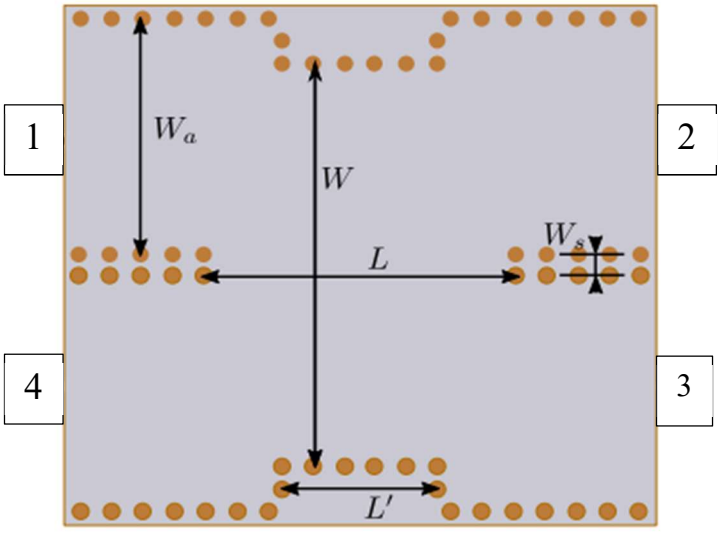

Figure 3-24. Topology of short-slot coupler in SIW technology [32].

The geometric parameters defining this device are denoted as W_a, W_s, W, L and L'. The frequency of operation defines the access waveguide width W_a for mono-mode operation. The waveguide separation wall defined by W_s is not a critical parameter, an arrangement of one or two via holes is sufficient to avoid unwanted coupling. The fundamental parameters responsible for the interference phenomenon are those defining the center region size, namely L and W. An analysis of the scattering matrix based on even-odd mode analysis is presented in [35]. By considering both the interference pattern required for the power division and the minimization of return loss, they obtained design equations for W and L, given by (3-6) and (3-7), respectively. In these equations, $|S_{31}|$ refers to the coupled power to the opposite port, k is the free space wavenumber at the operating frequency and n is a positive integer. The secondary parameter L' is tuned by full-wave simulation in HFSS in order to obtain the best results.

$$W = \frac{\pi}{k}\sqrt{\frac{[\pi(2n+1)+4sin^{-1}|S_{31}|][3\pi(2n+1)-4sin^{-1}|S_{31}|]}{8sin^{-1}|S_{31}|[\pi(2n+1)-2sin^{-1}|S_{31}|]}} \quad (3\text{-}6)$$

$$L = \frac{\pi(2n+1)}{2\sqrt{k^2-\left(\frac{\pi}{W}\right)^2}} \quad (3\text{-}7)$$

3.5.2 Coupler design

In this part, a CNT-based AF-SIW 3-dB coupler based on the short-slot topology is introduced. As we discussed previously, in order to obtain CNT-based AF-SIW, the lateral metallic-via walls of rectangular waveguides will be replaced by CNT walls which could be transferred to the top or bottom metallic layer by flip-chip technique. The implementation form of this coupler is illustrated in Figure 3-25, the geometric parameters defining this device are W_a, W, L and L' which have the same function as presented in Figure 3-24. The width of the CNT-lateral walls W_{CNT} was chosen at least 1 mm for the fabrication process and measurement.

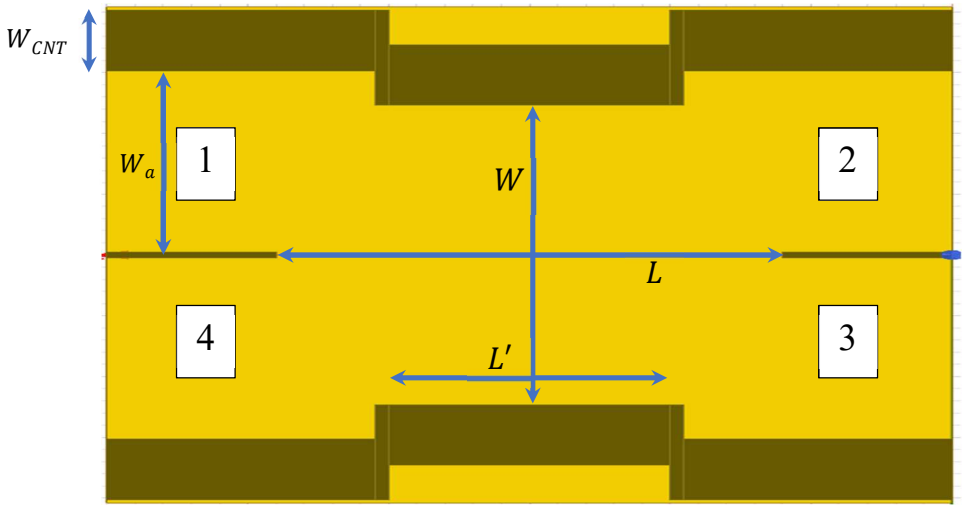

Figure 3-25. Topology of short-slot AFSIW coupler based on CNT technology.

By considering the case where $|S_{31}| = 1/\sqrt{2}$, design equations (3-6) and (3-7) reduce to (3-8) and (3-9), where λ_0 is the free-space wavelength at 78.5 GHz considering the substrate dielectric constant ε_r. In our case $\varepsilon_r = 1$ because the waveguide is filled with air.

$$W = \lambda_0 \sqrt{\frac{(n+1)(3n+1)}{(4n+1)\varepsilon_r}} \quad (3\text{-}8)$$

$$L = \lambda_0 \sqrt{\frac{(n+1)(3n+1)}{12\varepsilon_r}} \quad (3\text{-}9)$$

The numerical values obtained for $n = 1, 2, 3$ are shown in Table 3-2. In fact, n should be as small as possible for area reduction, since W and L are increasing with n. For $n \geq 2$ the width W is greater than 5.87 mm, which leads to the possible propagation of TE_{30} mode at the operating frequency, therefore $n = 1$ was selected.

n	1	2	3
***W* (mm)**	4.86	5.87	6.75
***L* (mm)**	3.14	5.09	7.02

Table 3-2. Theoretical dimensions of the interference region in AF-SIW technology for a CNT-based 3-dB coupler.

In order to locate approximately in the center of the mono-mode, W_a was calculated as 2.8 mm for a cut-off frequency $f_{c10} = 52$ GHz, as the waveguides of section 3.2.4. Thus, the second mode starts to propagate above 100 GHz.

3.5.3 Simulation results

After optimization by implementing the coupler in HFSS with full-wave simulation, the final geometric parameters obtained for 3-dB coupler are $W_a = 2.8\ mm$, $W = 4.92\ mm, L = 3.6\ mm$ and $L' = 2\ mm$. The value of W is relatively close to the theory value, but L is much larger than its initial value. This is mainly related to the non-negligible influence of the evanescent TE_{30} mode for short-slot topology as mentioned in [35], [44]. The optimized responses are illustrated in Figure 3-26 and the E-field distributed inside this coupler is also presented in Figure 3-27.

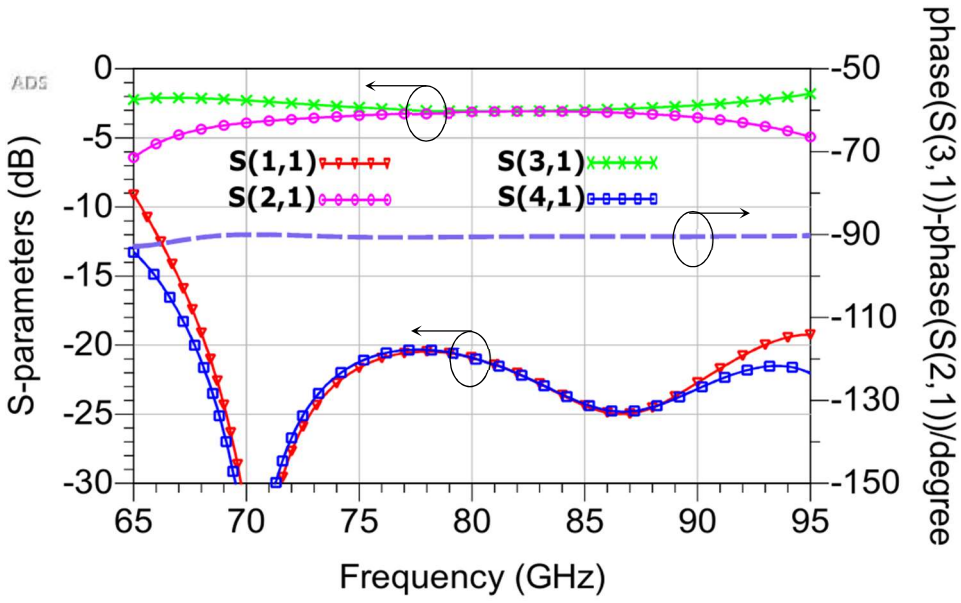

Figure 3-26. Simulated S-parameters of the optimized CNT-based 3-dB coupler in AF-SIW technology.

Generally, the simulated return loss as well as isolation are greater than 20 dB over the entire E-band (71-86 GHz). At the center frequency of 78.5 GHz, the insertion loss is about 0.1 dB justifying the interest for this low-loss technology. In terms of unbalance between the through port and coupled port, it is less than 0.63° in phase over the entire E-band and remains less than 1 dB between 73 and 86 GHz in amplitude (1.4 dB at 71 GHz).

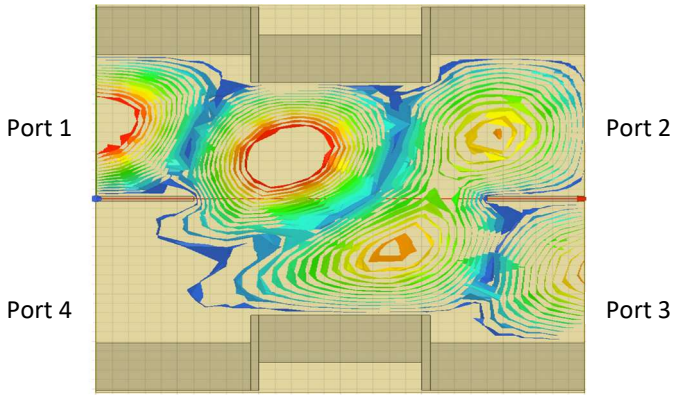

Figure 3-27. E-field distribution inside the investigated 3-dB coupler.

In order to evaluate our coupler, a performance comparison is proposed in Table 3-3 between this investigated coupler and the existing couplers in literature designed for mm-wave applications. The reference, year/type, central frequency, bandwidth, insertion loss, amplitude imbalance and phase imbalance at the central frequency, are listed.

REF	Year/Type	Freq. (GHz)	BW (%) (GHz)	Insertion Loss (dB)	Amplitude Imbalance (dB)	Phase Imbalance (°)
[35]	2010 (short-slot)	60	34.5 (46.3-67)	0.3	0.4	11
[45]	2012 (narrow-wall)	77	11.7 (72-81)	0.2	0.1	0.5
[46]	2015 (short-slot)	60	11.7 (57-64)	0.3	0.2	5
[47]	2016 (short-slot)	30	13.3 (28-32)	0.1	0.2	0.5
[48]	2017 (short-slot)	30	13.3 (28-32)	0.1	0.2	0.4
[49]	2016 (short-slot)	60	27.6 (53-70)	0.5	0.4	2
Our work [50]	2020 (short-slot)	78.5	19.1 (71-86)	0.1	0.5	0.63

Table 3-3. Performance summary of SIW-based couplers for mm-wave applications.

3.6 CNT-based AF-SIW crossover

The crossover, or also called 0-dB coupler, is used to convey all input power to the diametrically opposite port (coupled port). The short-slot topology presented in section 3.5.1 could be also used to design the crossover. The geometric parameters as well as the

simulation results of CNT-based AF-SIW crossover will be introduced in the next sections.

3.6.1 Design

As we said previously, the short-slot topology can be used to design the crossover, therefore the same design equations will be used to set the initial geometric dimension for this crossover, but in this time the amplitude of the transmission coefficient S_{31} must be equal to 1 (instead of $1/\sqrt{2}$ for the 3dB-coupler). In that case, design equations can be reduced to (3-10) and (3-11).

$$W = 0.5\lambda_0\sqrt{\frac{(2n+3)(6n+1)}{8n*\varepsilon_r}} \quad (3\text{-}10)$$

$$L = 0.5\lambda_0\sqrt{\frac{(2n+3)(6n+1)}{12*\varepsilon_r}} \quad (3\text{-}11)$$

The calculated dimensions for $n = 1, 2, 3$ are given in Table 3-4. Once again both W and L are increasing with n. In this case, $n = 3$ was chosen as starting point for the optimization because these devices were first dedicated to be an elementary block of a Butler Matrix, in which longer crossover makes the design and realization of the phase shifter easier (as explained in [35]). Moreover, the access waveguide width W_a was fixed at the same value as the 3-dB coupler.

n	1	2	3
***W* (mm)**	4.02	4.59	5.13
***L* (mm)**	3.28	5.29	7.26

Table 3-4. Theoretical dimensions of the interference region in AFSIW technology for a CNT-based crossover.

3.6.2 Simulation results

After optimization by implementing the coupler in HFSS with full-wave simulation, the final geometric parameters obtained for crossover are $W = 5.19\ mm, L = 7.69\ mm$ and the optimized value for the narrower region L' was found at 5.19 mm. An illustration of the simulated crossover is given in Figure 3-28 and the E-field distributed inside this coupler is presented in Figure 3-29.

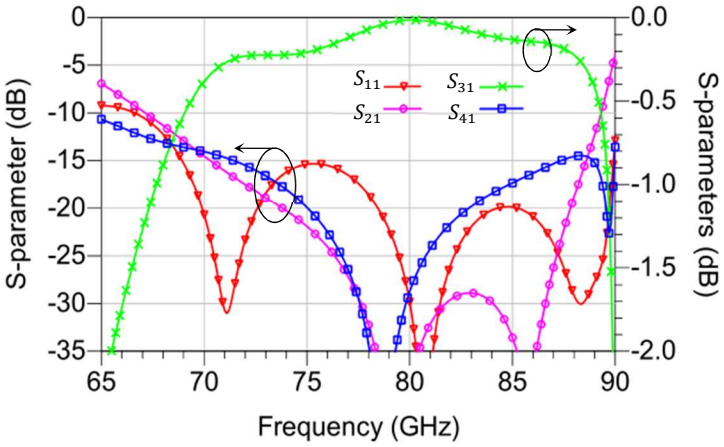

Figure 3-28. Simulated S-parameters of the optimized AF-SIW crossover in CNT technology.

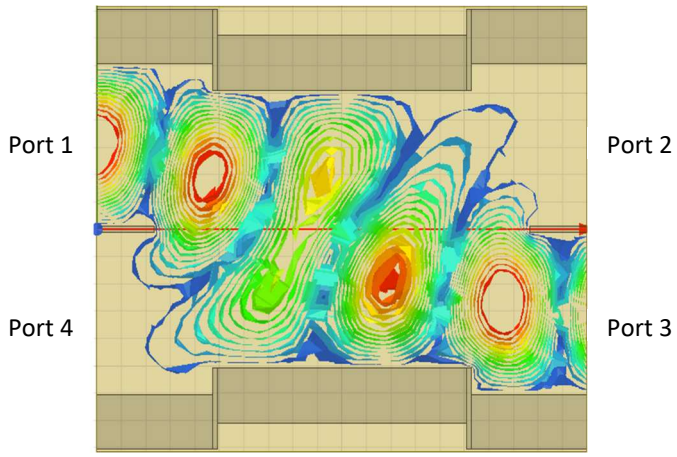

Figure 3-29. E-field distribution inside the investigated 3-dB crossover.

At the center frequency of 78.5 GHz, an insertion loss of 0.05 dB is predicted while return loss remains higher than 15 dB over the entire band from 71 to 86 GHz. Finally, isolation of both ports 2 and 4 is better than 15 dB between 70 and 88 GHz, and better than 35 at 78.5 GHz.

Once again, a performance comparison with the mm-wave crossovers of the literature is proposed in Table 3-5.

REF	Year/Type	Freq. (GHz)	BW (%) (GHz)	Insertion Loss (dB)	Direct Transmission Isolation (dB)	Isolation (dB)
[35]	2010 (short-slot)	60	26.7 (51-67)	0.35	28	20
[46]	2015 (short-slot)	60	11.7 (57-64)	0.3	18	27
[47]	2016 (short-slot)	30	13.3 (28-32)	0.1	40	35
[51]	2009 (central-junction)	60	15 (55-64)	0.15	35	40
Our work [50]	2020 (short-slot)	78.5	19.1 (71-86)	0.05	40	40

Table 3-5. Performance summary of SIW-based crossover for mm-wave applications.

3.7 CNT-based AF-SIW Butler matrix

3.7.1 Design

By combining the previous results of coupler and crossover on Keysight ADS and optimizing the electrical length of the phase shifters, a first simulation schematic for the BM is established and illustrated in Figure 3-30. In this experiment, the phase shifter physical length was considered as the same value of crossovers, only the electrical lengths of phase shifters were optimized in order to obtain 45° or 0° differences as compared with the output phase of crossover. The full-wave simulation of this Butler matrix was not

carried out in HFSS due to the enormous simulation time. Moreover, in this time of preparing this manuscript, we have not yet had the accurate measurement results for these investigated waveguides to compare with the simulation one due to the fabrication process, so it is not worth realizing a full-wave simulation of this Butler matrix. However, the ADS simulation results of this Butler matrix allows us to observe and analyze its performance. These results are presented in the next section (see Figure 3-31).

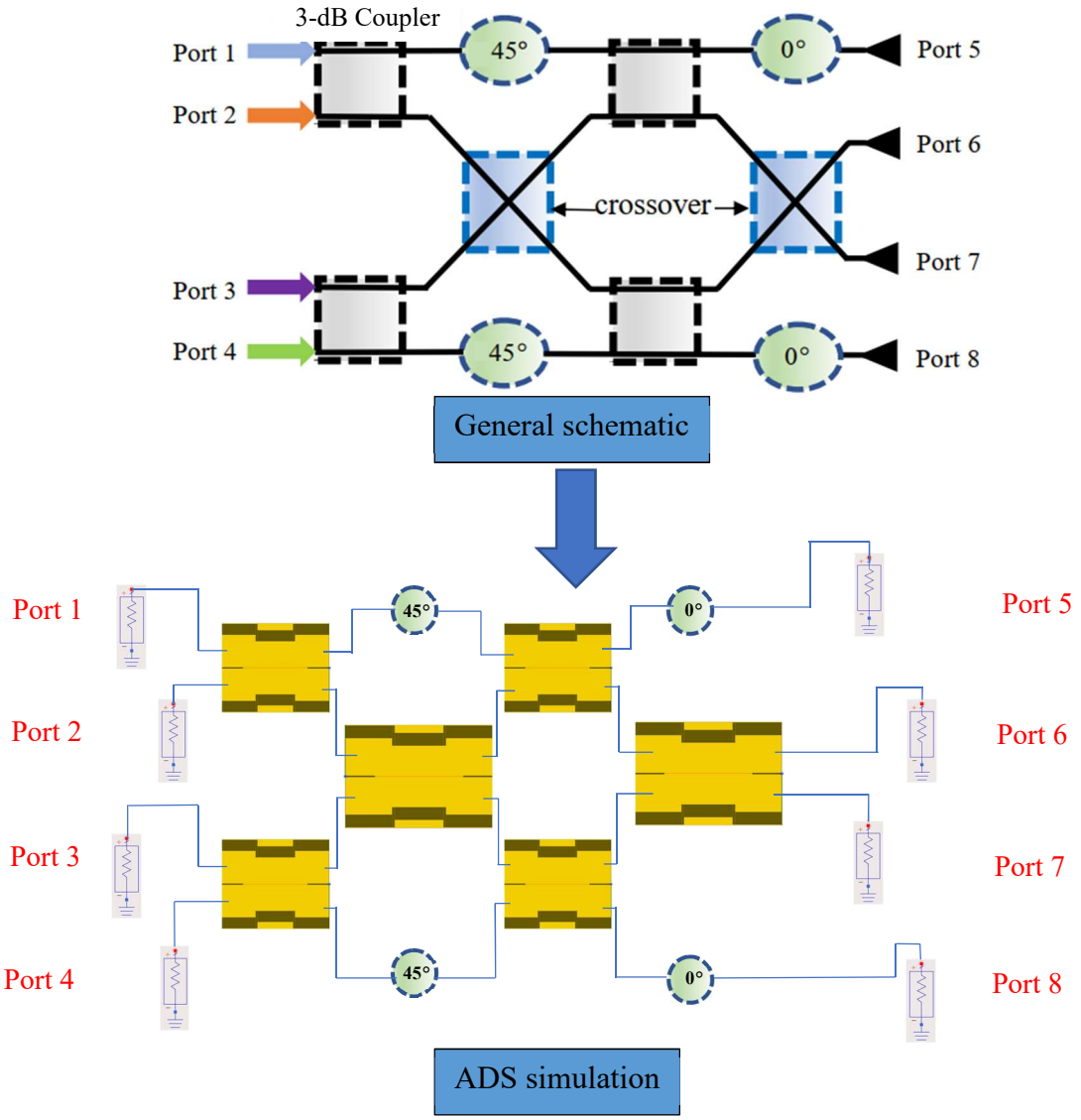

Figure 3-30. Simulation schematic of investigated BM by using Advanced Design System (ADS).

3.7.2 Simulation results

The simulation results of the investigated BM are illustrated in amplitude and phase in Figure 3-31. Due to the symmetry of the BM, only port 1 and port 2 were excited. A matching and an isolation between input ports greater than 15 dB for both excitations can be expected. Focusing on a restricted frequency band from 76 to 86 GHz, the input-output transmission for excitation on port 1 is 6.7±0.7 dB with a maximum phase error of 1.8° while for excitation on port 2 it is 6.4±1.2 dB with a maximum phase error of 3.7°.

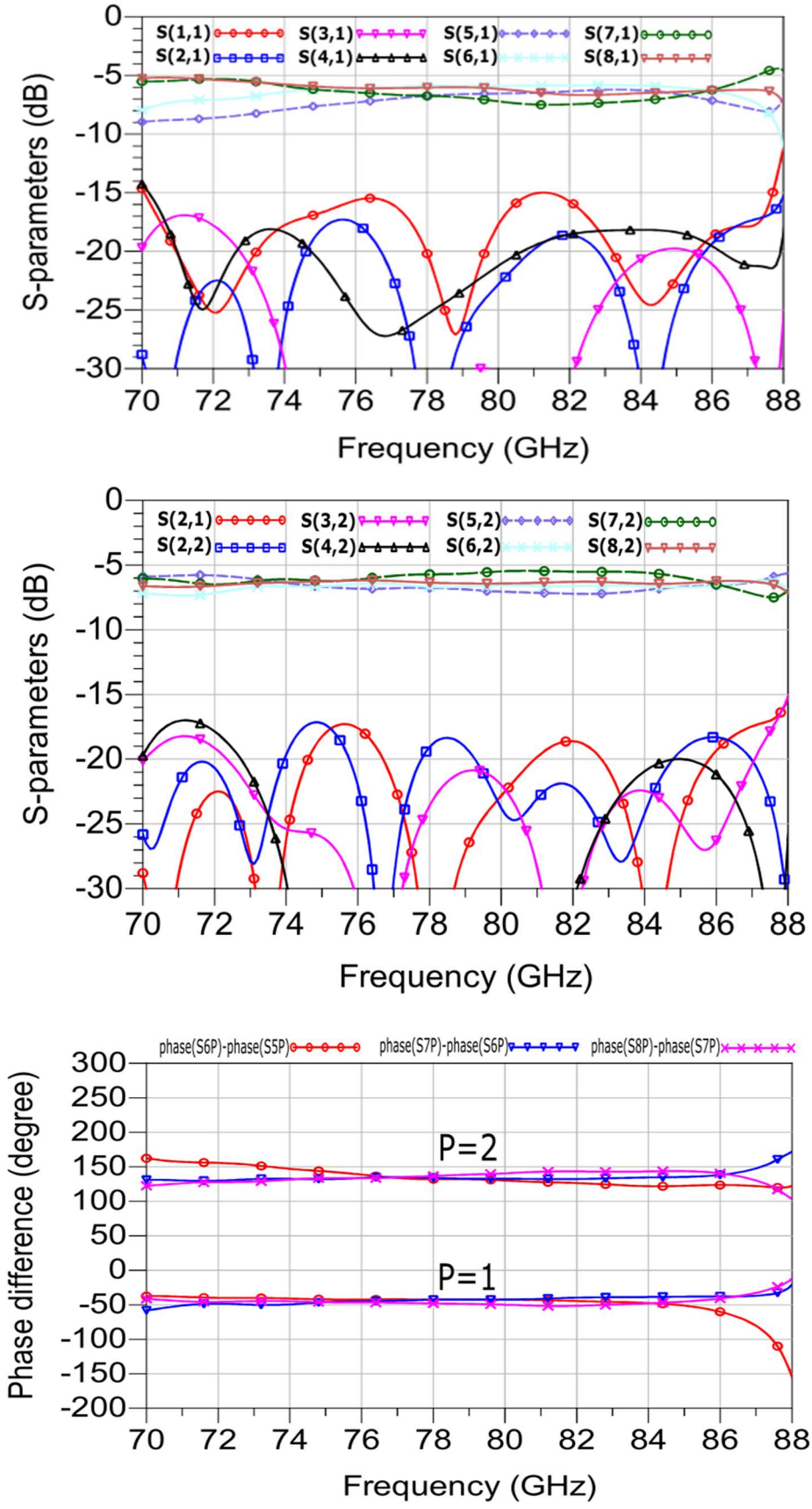

Figure 3-31. Simulated S-parameters in amplitude with (a) excitation on port 1 and (b) excitation on port 2. (c) Phase difference according to the input ports.

3.8 Conclusion

In this chapter, a detailed description of AF-SIW waveguides based on CNT technology was investigated and presented. In order to obtain a good performance, a CPW-to-GCPW-to-SIW transition mainly based on the quarter-wavelength triangle coupling slot was considered for our CNT-based AF-SIW. Indeed, by using this transition, a simulated return loss better than 15 dB in the entire E-band is expected. Meanwhile, the maximum simulated insertion loss is better than 0.5 dB over the E-band. These results allow us to believe in a good transition for our circuits. The detailed design rules of this transition were also introduced in this part. Concerning the expected loss, 0.015 dB/mm of attenuation constant is expected due to the uni-axial conductivity of the CNTs.

Still in terms of simulated devices, the CNT technology used to design the AF-SIW waveguide was also applied to the design of a 0-dB and a 3-dB couplers both based on the short-slot topology. The simulated S-parameters demonstrated that a good performance can be expected for these couplers. In general, the return loss is greater than 15 dB over the 71-86 GHz frequency range for both couplers. At the center frequency of 78.5 GHz, the insertion loss is around 0.1 dB for the 3-dB coupler and 0.05 dB for the crossover, justifying the interest for this low-loss technology. In terms of unbalance for the 3-dB coupler, it is less than 0.63° in phase over the entire E-band and remains less than 1 dB between 73 and 86 GHz in magnitude (1.4 dB at 71 GHz). By combining these couplers with the optimized phase shifter for the design of a Butler matrix in ADS, a simulation was also achieved, leading to an input-output transmission of 6.7±0.7 dB (respectively 6.4±1.2 dB) for excitation on port 1 (respectively, on port 2), with a maximum phase error of 1.8° (respectively, 3.7°). However, the simulation results need to be checked with the future measurement.

Finally, in terms of fabrication and measurements, the fabrication process of the CNT-based AF-SIW circuits developed by CINTRA laboratory was presented in this chapter. Technology constraints are huge. Especially, transferring CNT towards a flexible substrate as the RT Duroid 5880 with a thickness of 0.127 mm is tricky. First results showed some partial delamination of CNT layer from substrate preventing from a good contact with bottom plate and leading to bottom leakage. Technological realization is the challenge for this part of the thesis. And this is unavoidable as AF-SIW excitation assumes energy transfer from substrate to air. Only low-permittivity substrates enable that. And only flexible substrates present such low-permittivity, with more Teflon as a constitutive material. Another excitation, bump feeding, is studied by our XLIM partner in the framework of the TRICOT project. It consists of having a bundle of CNT at the end of a CPW. This assumes to master the contact between the bundle and the cover that is another challenge as well.

In order to benefit from the technological efforts brought to master CNT transfer towards flexible substrates, another idea emerged concerning the possibilities to use CNT as slow-wave material instead of walls. In that case, technological steps should be less compelling. This is the purpose of Chapter 4.

REFERENCES

[1] P. K. Dayalan and B. R. David, “Surface-wave losses of coplanar transmission lines,” pp. 1–4, 1983.

[2] R. J. Collier *et al.*, “A Study of High Frequency Performance of Coplanar Waveguide as a Function of Substrate Thickness,” pp. 1–3, 2000.

[3] R. Kazemi, A. E. Fathy, S. Yang, and R. A. Sadeghzadeh, “Development of an ultra wide band GCPW to SIW transition,” *RWW 2012 - Proc. IEEE Radio Wirel. Symp. RWS 2012*, pp. 171–174, 2012.

[4] H. Grubinger and H. Barth, “An LTCC-based 35-GHz Substrate-Integrated-Waveguide Bandpass Filter,” pp. 1605–1608, 2009.

[5] A. Suntives, S. Member, and R. Abhari, “Transition Structures for 3-D Integration of Substrate Integrated Waveguide Interconnects,” vol. 17, no. 10, pp. 697–699, 2007.

[6] S. Lee, S. Jung, S. Member, and H. Lee, “Ultra-Wideband CPW-to-Substrate Integrated Waveguide Transition Using an Elevated-CPW Section,” vol. 18, no. 11, pp. 746–748, 2008.

[7] D. Deslandes and K. Wu, “Integrated microstrip and rectangular waveguide in planar form,” *IEEE Microw. Wirel. Components Lett.*, vol. 11, no. 2, pp. 68–70, 2001.

[8] D. Deslandes, “Design equations for tapered microstrip-to-Substrate Integrated Waveguide transitions,” *2010 IEEE MTT-S Int. Microw. Symp.*, pp. 704–707, 2010.

[9] D. Deslandes and K. Wu, “Analysis and design of current probe transition from grounded coplanar to substrate integrated rectangular waveguides,” *IEEE Trans. Microw. Theory Tech.*, vol. 53, no. 8, pp. 2487–2494, 2005.

[10] A. Patrovsky, M. Daigle, and K. Wu, “Millimeter-Wave Wideband Transition from CPW to Substrate Integrated Waveguide on Electrically Thick High-Permittivity Substrates,” no. October, pp. 138–141, 2007.

[11] S. Yang, A. Elsherbini, S. Lin, A. E.Fathy, A. Kamel, and H. Elhennawy, “A Highly Efficient Vivaldi Antenna Array Design on Thick Substrate and Fed by SIW Structure with Integrated GCPW Feed,” no. 1, pp. 1985–1988, 2007.

[12] S. Lin, S. Yang, and A. E. Fathy, “Development Of A Novel Uwb Vivaldi An-Tenna Array Using Siw Technology,” pp. 369–384, 2009.

[13] X. P. Chen and K. Wu, “Low-loss ultra-wideband transition between conductor-backed coplanar waveguide and substrate integrated waveguide,” *IEEE MTT-S Int. Microw. Symp. Dig.*, pp. 349–352, 2009.

[14] D. Deslandes and W. Ke, “Integrated transition of coplanar to rectangular waveguides,” *Microw. Symp. Dig. 2001 IEEE MTT-S Int.*, vol. 2, pp. 619–622 vol.2, 2001.

[15] F. Taringou and J. Bornemann, “New Substrate-Integrated to Coplanar Waveguide Transition,” *2011 41st Eur. Microw. Conf.*, no. October, pp. 428–431, 2011.

[16] F. Taringou, J. Bornemann, K. Wu, and C. Engineering, “Inverted Interconnect Between Substrate Integrated Waveguide and Coplanar Waveguide,” pp. 8–10, 2013.

[17] F. Taringoul, J. Bornemannl, K. Wu, and T. Weiland, “Broadband Interconnects Between Coplanar Waveguide and Substrate Integrated Waveguide for Dense Packaging and Integration,” pp. 2–4, 2014.

[18] K. Kim, J. Byun, and H. Lee, “Substrate Integrate Waveguide Quasi Yagi antenna using SIW-to-CPS Transition for Low Mutual Coupling Kyungmin Kim *, Jindo Byun and Hai-Young Lee Department of Electronics Engineering , Design of the SIW quasi-Yagi antenna Conclusion,” *2010 IEEE Antennas Propag. Soc. Int.*

Symp., pp. 1–4, 2010.
[19] F. F. He *et al.*, “A Planar Magic-T Structure Using Substrate Integrated Circuits Concept and Its Mixer Applications,” vol. 59, no. 1, pp. 72–79, 2011.
[20] P. Souzangar and M. Shahabadi, “Numerical Multimode Thru-Line (TL) Calibration Technique for Substrate Integrated Waveguide Circuits,” vol. 5071, 2012.
[21] G. F. ENGEN and C. A. HOER, “Thru-Reflect-Line: An Improved Technique for Calibrating the Dual Six-port Automatic Network Analyzer,” 1979.
[22] C. J. Chen and T. H. Chu, “Design of 60-GHz SIW short-slot couplers,” *APMC 2009 - Asia Pacific Microw. Conf. 2009*, no. c, pp. 2096–2099, 2009.
[23] B. Liu, W. Hong, Y.-Q. Wang, Q.-H. Lai, and K. Wu, “Half Mode Substrate Integrated Waveguide (HMSIW) 3-dB Coupler,” *IEEE Microw. Wirel. COMPONENTS Lett.*, vol. 17, no. 1, pp. 22–24, 2007.
[24] M. Bertrand *et al.*, “A 3-dB Coupler in Slow Wave Substrate Integrated Waveguide Technology,” vol. 29, no. 4, pp. 2019–2021, 2019.
[25] Shin-ichi YAMAMOTO, J. Hirokawa, and M. Ando, “A Half-Sized Post-Wall Short-Slot Directional Coupler with Hollow Special Section on Recent Technologies of Microwave and Millimeter-Wave Devices A Half-Sized Post-Wall Short-Slot Directional Coupler with Hollow Rectangular Holes in a Dielectric Substrate,” *IEICE TRANS. ELECTRON*, vol. E88-C, no. 7, pp. 1387–1394, 2005.
[26] J. X. Chen, W. Hong, Z. C. Hao, H. Li, and K. Wu, “Development of a low cost microwave mixer using a broad-band Substrate Integrated Waveguide (SIW) coupler,” *IEEE Microw. Wirel. Components Lett.*, vol. 16, no. 2, pp. 84–86, 2006.
[27] M. Lee *et al.*, “A Novel 94-GHz MHMET-Based Diode Mixer Using a 3 – dB Tandem Coupler,” vol. 18, no. 9, pp. 626–628, 2008.
[28] C. Lin, S. Chang, and W. Hsiao, “A Full-360° Reflection-Type Phase Shifter With Constant Insertion Loss,” vol. 18, no. 2, pp. 106–108, 2008.
[29] C. Lin, S. Chang, C. Chang, and Y. Shu, “Design of a Reflection-Type Phase Shifter With Wide Relative Phase Shift and Constant Insertion Loss,” vol. 55, no. 9, pp. 1862–1868, 2007.
[30] Q. Yang, Y. Ban, Q. Zhou, M. Li, and A. H. Coupler, “Butler Matrix Beamforming Network Based on Substrate Integrated Technology for 5G Mobile Devices,” pp. 413–414, 2016.
[31] D. Tarek, J. G. F. Nelson, and W. Ke, “Design and Implementation of a Planar 4×4 Butler Matrix in SIW Technology for Wideband Applications,” *Eur. Microw. Conf.*, vol. 24, no. September, 2010.
[32] M. BERTRAND, “Guides à ondes lentes intégrés dans le substrat pour les applications en bandes RF et millimétriques,” 2017.
[33] S. Karamzadeh, V. Rafii, M. Kartal, and B. S. Virdee, “Compact and Broadband 4 x 4 SIW Butler Matrix with Phase and Magnitude Error Reduction,” *IEEE Microw. Wirel. Components Lett.*, vol. 25, no. 12, pp. 772–774, 2015.
[34] A. A. M. Ali, N. J. G. Fonseca, F. Coccetti, and H. Aubert, “Design and implementation of two-layer compact wideband butler matrices in siw technology for ku-band applications,” *IEEE Trans. Antennas Propag.*, vol. 59, no. 2, pp. 503–512, 2011.
[35] C. J. Chen and T. H. Chu, “Design of a 60-GHz substrate integrated waveguide Butler matrix-a systematic approach,” *IEEE Trans. Microw. Theory Tech.*, vol. 58, no. 7 PART 1, pp. 1724–1733, 2010.
[36] W. Che, K. Deng, E. K. N. Yung, and K. Wu, “H-Plane 3-dB hybrid ring of high isolation in substrate-integrated rectangular waveguide (SIRW),” *Microw. Opt.*

Technol. Lett., vol. 48, no. 3, pp. 502–505, 2006.
[37] W. A. TYRRELL, "Hybrid Circuits for Microwaves," *Proc. IRE*, vol. 35, no. 11, pp. 1294–1306, 1947.
[38] H. J. RIBLET, "The Short-Slot Hybrid Junction," *Proc. IRE*, vol. 40, no. 2, pp. 180–184, 1952.
[39] J.-X. Chen, W. Hong, Z.-C. Hao, H. Li, and K. Wu, "Development of a Low Cost Microwave Mixer Using a Broad-band Substrate Integrated Waveguide (SIW) Coupler," *Microw. Wirel. COMPONENTS Lett.*, vol. 16, no. 2, pp. 84–86, 2006.
[40] E. Moldovan, R. G. Bosisio, L. Fellow, and K. Wu, "W -Band Multiport Substrate-Integrated Waveguide Circuits," vol. 54, no. 2, pp. 625–632, 2006.
[41] Z. C. Hao, W. Hong, J. X. Chen, H. X. Zhou, and K. Wu, "Single-layer substrate integrated waveguide directional couplers," vol. 153, no. 5, 2006.
[42] A. Doghri, T. Djera, and A. Ghiotto, "Substrate Integrated Waveguide Directional Couplers for Compact Three-Dimensional Integrated Circuits," vol. 63, no. 1, pp. 209–221, 2015.
[43] F. Parment, S. Member, A. Ghiotto, and S. Member, "Air-Filled Substrate Integrated Waveguide for Low-Loss and High Power-Handling Millimeter-Wave Substrate Integrated Circuits," vol. 63, no. 4, pp. 1228–1238, 2015.
[44] L. W. Hendrick and R. Levy, "Design ofWaveguide Narrow-Wall Short-Slot Couplers," *Trans. Microw. THEORY Tech.*, vol. 48, no. 10, pp. 1771–1774, 2000.
[45] T. Djerafi and K. Wu, "A low-cost wideband 77-ghz planar butler matrix in siw technology," *IEEE Trans. Antennas Propag.*, vol. 60, no. 10, pp. 4949–4954, 2012.
[46] N. Tiwari and T. R. Rao, "A switched beam antenna array with butler matrix network using substrate integrated waveguide technology for 60 GHz communications," *2015 Int. Conf. Adv. Comput. Commun. Informatics, ICACCI 2015*, no. i, pp. 2152–2157, 2015.
[47] Q. L. Yang, Y. L. Ban, K. Kang, C. Y. D. Sim, and G. Wu, "SIW Multibeam Array for 5G Mobile Devices," *IEEE Access*, vol. 4, pp. 2788–2796, 2016.
[48] Q. L. Yang, Y. L. Ban, J. W. Lian, Z. F. Yu, and B. Wu, "SIW Butler Matrix with Modified Hybrid Coupler for Slot Antenna Array," *IEEE Access*, vol. 4, pp. 9561–9569, 2016.
[49] Y. Li and K. M. Luk, "60-GHz Dual-Polarized Two-Dimensional Switch-Beam Wideband Antenna Array of Aperture-Coupled Magneto-Electric Dipoles," *IEEE Trans. Antennas Propag.*, vol. 64, no. 2, pp. 554–563, 2016.
[50] P. Doan *et al.*, "Potentialities of Air-Filled Substrate Integrated Waveguides based on Carbon Nanotubes in E-band," *IEEE MTT-S Int. Conf. Microwaves Intell. Mobil.*, 2020.
[51] T. Djerafi and K. Wu, "60 GHz substrate integrated waveguide crossover structure," *Eur. Microw. Week 2009, EuMW 2009 Sci. Prog. Qual. Radiofreq. Conf. Proc. - 39th Eur. Microw. Conf. EuMC 2009*, no. October, pp. 1014–1017, 2009.

Chapter 4. CNT for slow wave effect in Air-Filled Slow-Wave SIW (AF-SW-SIW) at 28 GHz

In the previous chapter, we have already presented the possibility of using CNT as metallic walls for the design of AF-SIW circuits in E-band. Now, in this chapter, another usage of CNT will be investigated to demonstrate the slow-wave effect, which is applied to existing air-filled SIW topologies at 28 GHz, showing not only interesting miniaturization capabilities but also the ultra-low losses without any change in the principle of operation. The detailed description as well as the design rules of this topology will be introduced completely in this chapter.

4.1 CNT-based AF-SW-SIW waveguide

4.1.1 Design

4.1.1.1 Waveguide structure

Figure 4-1 illustrates the structure of the CNT-based AF-SW-SIW waveguide that was designed and simulated. Table 4-1 summarizes all the dimensions of the waveguide. The latter consists of four layers: layer 1 and layer 3 were made of PCB technology, while layer 2, a special adhesive layer (EM-827), enables to assembly layers 1 and 3 together, thus forming the bottom part of an air-filled SIW waveguide (lateral wall of metallic holes and the metallic bottom). Meanwhile, layer 4 is considered as the metallic top cover for the waveguide. It is made of PCB technology, covered with a CNT forest in the center, which will perform slow-wave effect. Layer 4 can be defined by using the same fabrication process of CNT, which was introduced in the previous chapter with flip-chip technology. Finally, with the help of screws, an AF-SW-SIW could be fabricated. This layer is metallized with 9-µm thin layer of copper and finished with 1-µm thin layer of gold.

The detailed parameters of investigated waveguide are presented in Figure 4-2. The ROGER 4003 substrate with ε_r = 3.55 and $h_{Sub1} = h_{Sub3}$ = 508 µm has been chosen to make the layers 1 and 3 which are metallized by a 17-µm thin layer of copper and finished with 1-µm thin layer of gold. The diameter of metallic holes, d, equals 0.2 mm and the center-to-center distance, s, between two consecutive holes equals 0.4 mm. In order to form the layer 4, the CNT forest could be transferred on the silicon substrate or ROGER substrate depending on the manufacturer. However, with the experiences achieved when fabricating CNT which was presented in chapter 3, the ROGER RT 5880 substrate could be considered for this mission. The height of this substrate does not influence on the waveguide performance. The adhesive layer of EM-827 that was applied to stick layers 1 and 3 together, is about 60-µm thick. An important factor of any slow-wave topology is slow-wave factor, which is, in our case, depending on the height of the CNT forest. In this work, three values of the height of CNT forest (200 µm, 300 µm and 400 µm) were considered to perform the slow-wave effect. The theoretical calculation for the design of this waveguide as well as the simulation and measurement results will be presented in the following parts.

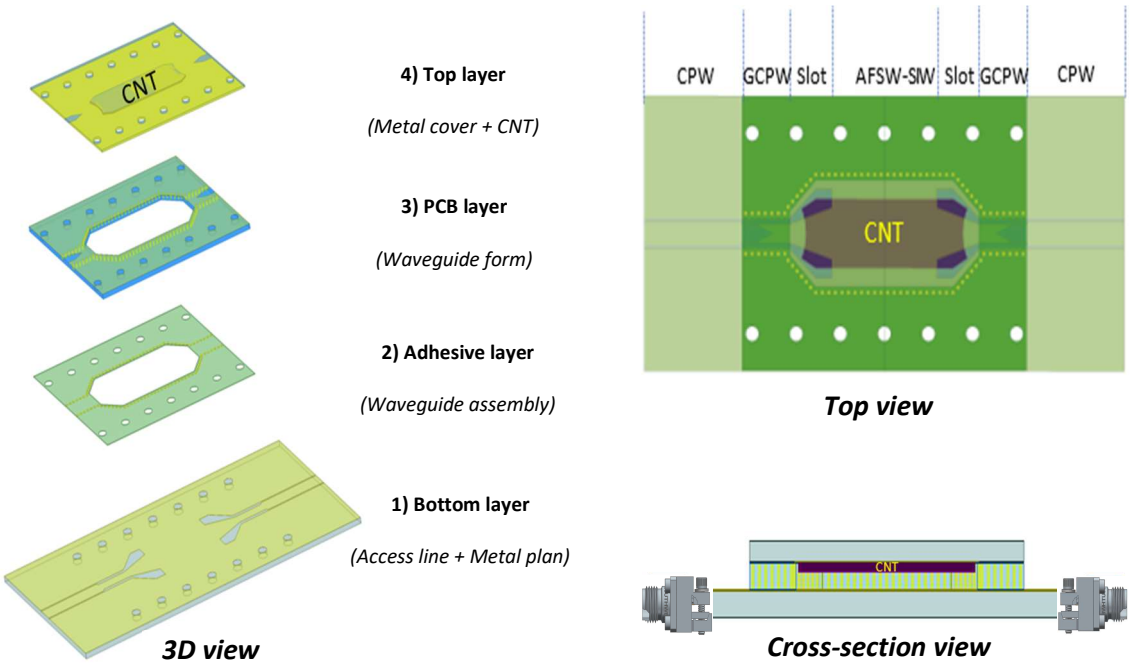

Figure 4-1. Schematic view of the CNT-based AF-SW-SIW in PCB technology.

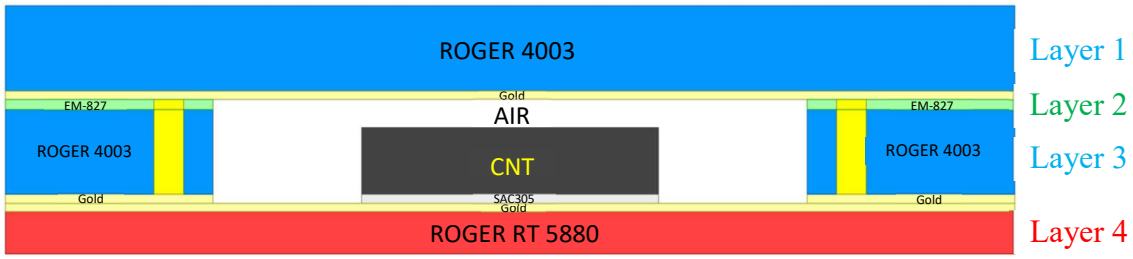

Figure 4-2. Detailed structure of the CNT-based AF-SW-SIW waveguide.

Layer	Substrate	h_{Sub}(µm)	ε_r	$tan\delta$	Metallized Layer
1	ROGER 4003	508	3.55	0.0027	17-µm of copper+1-µm of gold
2	EM-827 (Prepreg)	60	3.6	0.028	No metallized layer
3	ROGER 4003	508	3.55	0.0027	17-µm of copper+1-µm of gold
4	ROGER RT 5880	127	2.2	0.0004	9-µm of copper+1-µm of gold

Table 4-1. CNT-based technology parameters.

4.1.1.2 Slow-wave analysis

As we mentioned previously, three values of CNT forest thicknesses were considered for the slow-wave effect. Thus, in this section, a theoretical calculation of slow-wave factor depending on these values will be presented. Figure 4-3 illustrates the cross-section view of the investigated waveguides with and without CNT forest. The slow-wave factor can be estimated by the following expression [1]:

$$SWF \approx \sqrt{\frac{h_{total}}{h_{total}-h_{CNT}}} \tag{4-1}$$

where h_{total} refers to the total height of the air zone inside the waveguide and can be calculated by $h_{total} = h_{metal3} + h_{Sub3} + h_{Sub2} = 589\ \mu m$ and h_{CNT} is the CNT forest thickness.

In order to compare structures with and without CNT, a simple AF-SIW will be realized as well. For both AF-SW-SIWs and AF-SIW, an operating frequency at 28 GHz will be considered, so that 20 GHz seems to be the good choice as a cut-off frequency. We calculate the width of the reference air-filled waveguide (W_{AF-SIW}) equal to 7.01 mm. As compared to this value, and depending on the height of CNT forest, the width of the AF-SW-SIW ($W_{AF-SW-SIW}$) could be reduced due to the slow-wave effect leading to the efficient miniaturization of the waveguide dimensions. Table 4-2 presents the theoretical calculation of slow-wave factor, based on the approximated formula (4-1), as well as $W_{AF-SW-SIW}$ obtained with three different values of CNT forest thickness. Around 43.5 % reduction in width has been obtained with a 400-µm CNT thickness. As SWF will also impact the desired length of the waveguide with the same percentage, this should enable to save 68% of surface on the PCB at the end.

Due to the fabrication process requirements, the distance between the sidewall of CNT forest and the ROGER substrate (Layer 3) d_c must be at least 1 mm.

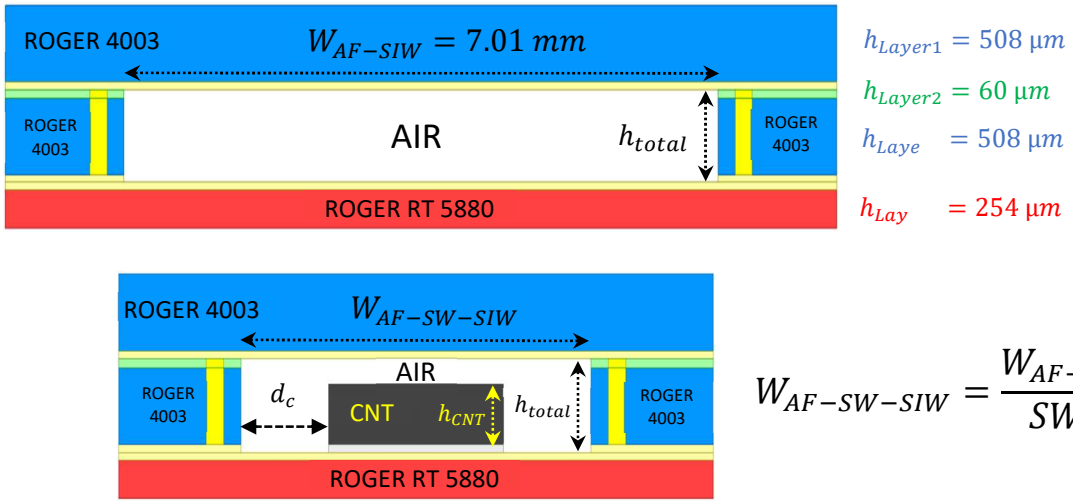

Figure 4-3. Cross-section view of investigated waveguides with and without presence of CNT forest.

h_{CNT} (µm)	w/o	200	300	400
SWF	1	1.23	1.43	1.77
$W_{AF-SW-SIW}$(mm)	7.01	5.69	4.9	3.96

Table 4-2. Slow-wave factor and $W_{AF-SW-SI}$ estimation corresponding to three values of CNT forest thickness. The AF-SIW without CNT is represented as well as an element of comparison.

In order to study the electrical performance of the investigated waveguides, different simulation strategies were adopted. As for most non-TEM waveguides, the relevant parameter is the propagation constant $\gamma = \alpha + j\beta$. An ideal slow-wave structure would be able to increase dramatically the phase constant β while limiting the increase in the attenuation α [1]. Due to its advantages compared to other simulation methods, the eigen-mode solver in HFSS was considered as a straight-forward strategy to explore the propagation constants of these waveguides. As described in [2], [3], closed periodic waveguides can be analyzed through their unit-cell only. In order to obtain the propagation constant, an equivalent resonator is defined with specific boundary condition, as illustrated in Figure 4-4.

More accurately, the propagation term $e^{-j\beta z}$ is replaced by a phase shift $e^{-j\varphi}$ between two opposite faces of the unit-cell. This is imposed by applying "Master" and "Slave" boundaries. Technically, the field on the slave boundary $\boldsymbol{E_s}$ should be a delayed version of that on the master boundary $\boldsymbol{E_m}$. The output data of the solver is a frequency at which the boundary conditions are satisfied, that is for which $\beta = \varphi/s$. Then, by varying φ between 0 and a maximum angle of π, a curve of dispersion $\beta(f)$ can be directly obtained. In reality, the output frequency f' is a complex value, the real part being the physical resonance frequency while the imaginary part expresses dissipation in the resonator (and thus attenuation).

Figure 4-4. Principle of the eigen-mode simulation: a) periodic waveguide and b) equivalent resonant unit-cell [1].

The following equations are implemented to recover the attenuation constant from this complex frequency:

$$f = Re(f') \tag{4-2}$$

$$\alpha = \frac{2\pi Im(f')}{v_g} \tag{4-3}$$

where,

$$v_g = 2\pi \frac{d[Re(f')]}{d\beta} \tag{4-4}$$

is the group velocity.

From (4-3) and (4-4), the attenuation constant α can be described as follows:

$$\alpha = Im(f')\frac{d\beta}{df} \tag{4-5}$$

Figure 4-5 illustrates unit-cell of the investigated waveguide that we used for eigen-mode simulation in this thesis work. The simulation results of the phase constant β, the attenuation constant α, the quality factor Q and the slow-wave factor SWF will be presented in Figure 4-6 corresponding to three different values of CNT forest thickness. The forest model is the same as presented in Chapter 2.

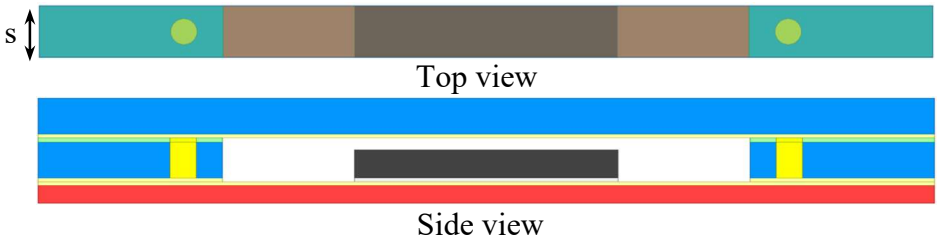

Figure 4-5. Unit-cell of the investigated waveguide.

As we mentioned previously, an efficient slow-wave structure would be able to increase dramatically the phase constant β while limiting the increase in the attenuation

α. It is obviously demonstrated in our investigated waveguides as illustrated in Figure 4-6.a) and b). Be careful however that the attenuation constant values are to be considered with caution (model validity to be confirmed). For examples, at the operating frequency of 28 GHz, the phase constant β equals to 410 rad/m when there is no slow-wave effect and increases to 502 rad/m, 581 rad/m, and 702 rad/m, corresponding to the CNT forest thickness of 200 µm, 300 µm and 400 µm, respectively. This raise in β is accompanied with a slight increase in term of attenuation α, where its value equals to 0.003 dB/mm for non-slow-wave waveguide and grows up to 0.004 dB/mm, 0.0045 dB/mm and 0.0069 dB/mm for 200-µm, 300-µm and 400-µm CNT forest thicknesses, respectively. These values of α indicate the ultra-low loss of CNT, leading to the extremely low loss waveguides. Thanks to the very small value of attenuation α, a high amount of quality factor can be achieved. Indeed, as illustrated in Figure 4-6 (c), a quality factor of 442 is still obtained for a 400-µm CNT forest thickness at operating frequency of 28 GHz. Finally, as presented in Figure 4-6 (d), the simulated slow-wave factors are almost similar to its theoretical values, given by formula (4.1) from [1]. Differences will be justified in next section.

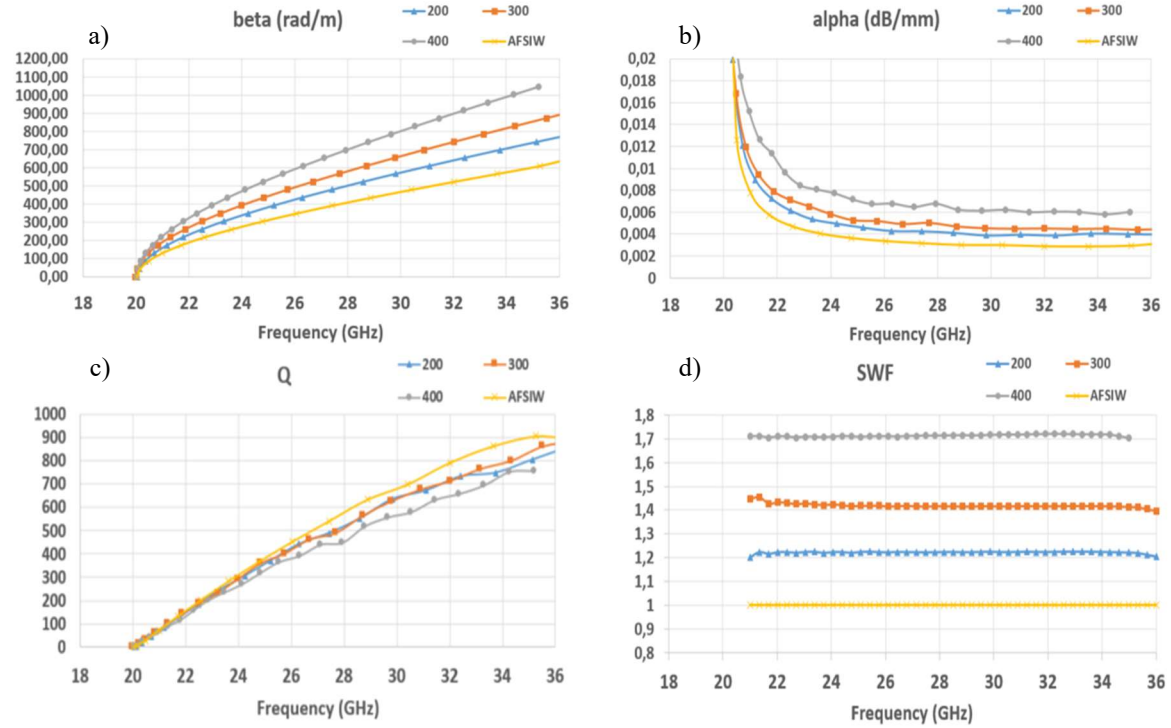

Figure 4-6. Waveguide, simulated through Eigen mode method, performance vs. frequency: a) phase constant, (b) attenuation constant, (c) Q-factor and d) slow-wave factor. Parametric study as a function of CNT forest height.

Table 4-3 summarizes all simulation results obtained by using Eigen-mode solver in terms of the phase constant β, the attenuation constant α, the quality factor Q and the slow-wave factor SWF at operating frequency of 28 GHz. Be careful that attenuation constant is thoughtlessly low and should be comforted by more accurate full-wave simulations leading to more reasonable quality factors. Concerning phase constant and slow-wave factors, results are meaningful.

CNT forest thickness	β (rad/m)	α (dB/mm)	Q	SWF
0 (no slow-wave effect)	410	0.003	593	1
200	502	0.004	545	1.22
300	581	0.0045	560	1.42
400	702	0.0069	442	1.71

Table 4-3. Summary investigated waveguide performance by using Eigen-mode at 28 GHz.

4.1.1.3 Electric and magnetic field distribution

As already known, a separation of electric and magnetic field in a waveguide establishes the slow-wave effect and therefore can slows down its phase velocity. Hence, in this section, a distribution of electric and magnetic fields confined inside the investigated waveguide will be illustrated.

As shown in Figure 4-7, the electrical field is mainly concentrated in the air zone limited by the top of CNT forest and upper metallic layer, meanwhile the magnetic field fills the entire region showing the aforementioned physical separation.

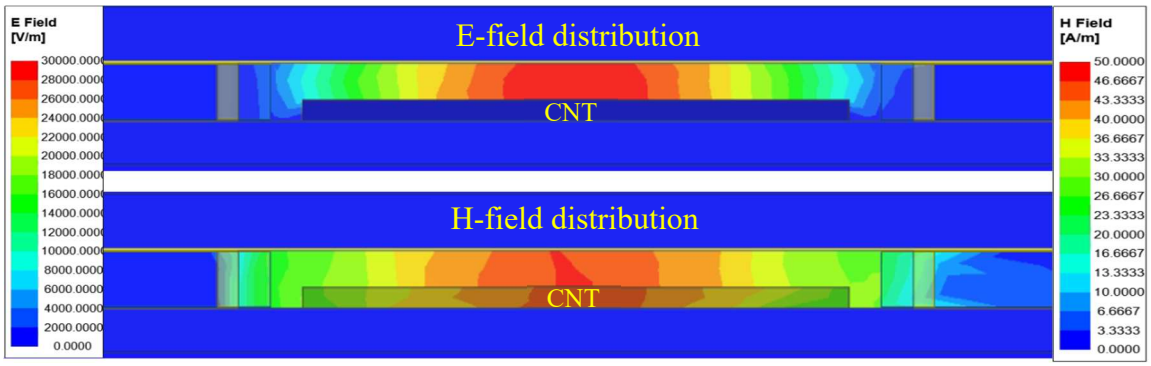

Figure 4-7. Electric and magnetic distribution in AF-SW-SIW waveguide at operating frequency of 28 GHz.

Anyway, even if the E-field is confined inside the defined zone between the CNT forest and top metallic layer, there is still a small amount of electric field going to the zone between the sidewall of CNT forest and ROGER substrate which is define by parameter d_c in Figure 4-3. This leads to a slight decrease in the slow-wave effect and that explains why the simulated slow-wave factor is less than the theoretical one.

4.1.1.4 Feeding structures

Once again, due to its high performance, a GCPW-CPW transition using triangular coupling slot that was presented in section 3.2.3 will be considered as a feeding line for this CNT-based AF-SW-SIW. A detailed view of the proposed transition is presented in Figure 4-8.

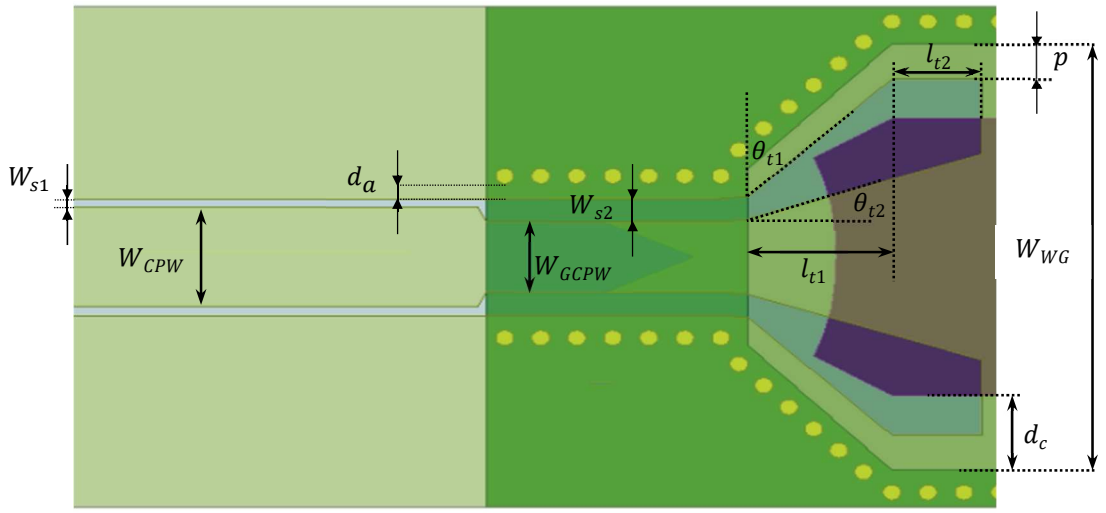

Figure 4-8. Detailed view of the broadband transition for CNT-based PAF-SWSIW.

The broadband transition geometry is established by two angles θ_{t1} and θ_{t2} as well as the taper length l_{t1} and l_{t2}. These dimensions are crucial factors to achieve a very good matching. Also, the distance p between the end of the transition and the lateral wall is also defined. The physical dimension of the CPW and GCPW are also given: W_{CPW}, W_{s1}, d_a, W_{GCPW}, W_{s2}.

For the starting point l_{t1} should be equal to a quarter-wavelength at the center frequency and varies depending on the CNT forest thickness. Then the value of l_{t2}, θ_{t1} and θ_{t2} were optimized to obtain the best waveguide performance. The detailed values of these parameters will be presented in Table 4-4 corresponding to three different values of CNT forest thicknesses.

Concerning the CPW and GCPW dimensions, a 50-Ω characteristic impedance needs to be obtained and these dimensions were also optimized in compliance with the standard of connector End Launch 1492-02A-8 by SouthWest Microwaves for measurements. Thus, the optimized dimensions are given here: $W_{CPW} = 1320\ \mu m$, $W_{s1} = 120\ \mu m$, $d_a = 200\ \mu m$, $W_{GCPW} = 940\ \mu m$, $W_{s2} = 310\ \mu m$.

It is worth reminding that the distance between the side-wall of CNT forest and the ROGER substrate (Layer 3), d_c, must be at least 1 mm due to the manufacture requirements.

CNT forest thickness (μm)	l_{t1} (mm)	l_{t2} (mm)	θ_{t1} (°)	θ_{t2} (°)	$p(\mu m)$	W_{WG} (mm)
200	1.6	1	40	22	0.45	5.69
300	1.6	1	58	15	0.68	5
400	1.5	1	71	5	0.695	4

Table 4-4. Optimized parameters of the broadband transition for CNT-based AF-SW-SIW.

4.1.2 Simulation results

As presented previously in Chapter 3, in this part we considered the same de-embedding algorithm [4] to perform the extraction of the propagation constant which can be used for both simulated and measured results enabling to de-embed the transitions to waveguide. This requires sets of S-parameters for different lengths of waveguides. Ideally,

the extraction should be done using two different waveguides whose electrical length differs from 90° at the center frequency [5]. However, for losses estimation a longer phase difference should be necessary to raise the power loss level that is above the measurement uncertainty. For these reasons, eight different lengths of the investigated waveguides (200 µm, 300 µm and 400 µm of CNT forest height) were implemented following the rule given by (4-6), where L_0 = 0.8 mm stands for the waveguide length of the shorter feature ("Thru") and ΔL is close to a quarter of guided wavelength at center frequency which is depending on the CNT forest height. Therefore, the attenuation constant can be estimated with a better accuracy by comparison of the longest waveguide with the shortest. The simulated results obtained for different lengths of investigated waveguides are illustrated in Figure 4-9, Figure 4-10 and Figure 4-11 for the three heights of CNT forest.

$$L_i = L_0 + i * \Delta L \qquad , 0 \leq i \leq 7 \tag{4-6}$$

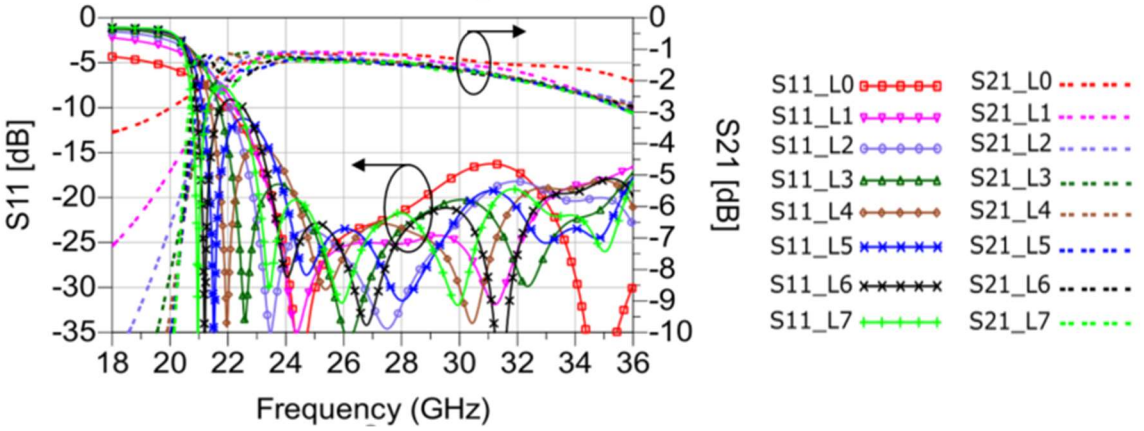

Figure 4-9. Simulated S-parameters of different lengths of waveguides with 200-µm-height CNT forest with its transitions and CPW/GCPW access lines.

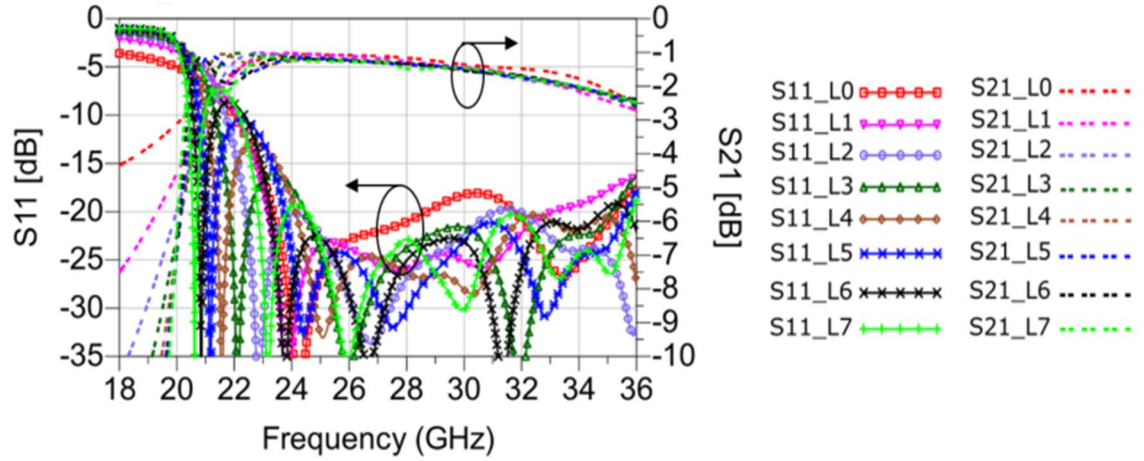

Figure 4-10. Simulated S-parameters of different lengths of waveguides with 300-µm-height CNT forest with its transitions and CPW/GCPW access lines.

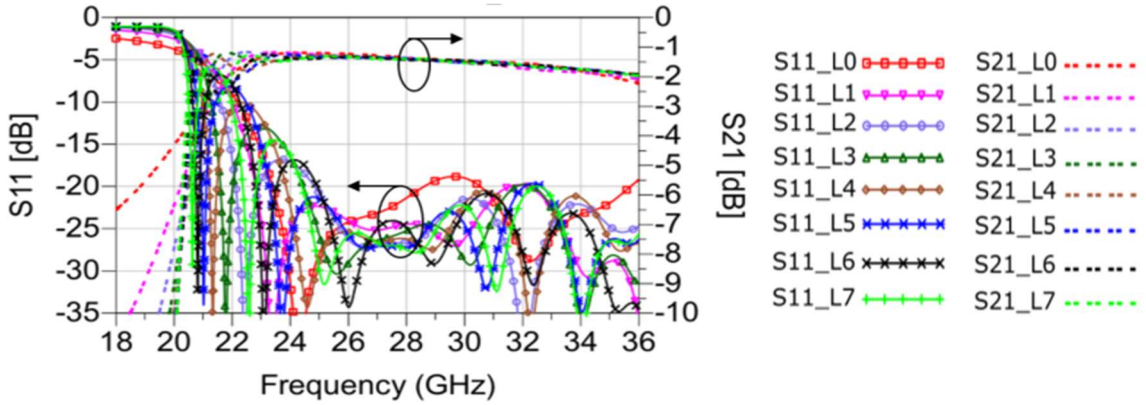

Figure 4-11. Simulated S-parameters of different lengths of waveguides with 400-µm-height CNT forest with its transitions and CPW/GCPW access lines.

In order to remove the effect of the transition loss on the waveguide performance, as aforementioned, the de-embedding method presented in [4] was considered. After applying the method on the shortest and the longest lengths of waveguides, the performance of the waveguide (corresponding to a length L7-L0) has been presented in Figure 4-12, Figure 4-13 and Figure 4-14 for the three heights of CNT forest.

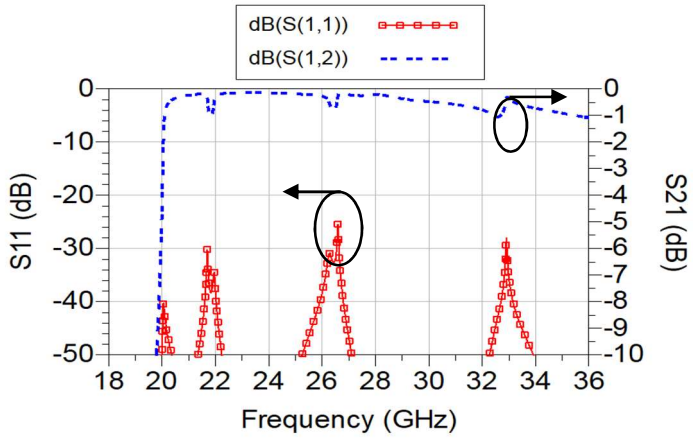

Figure 4-12. Simulated waveguide performance after de-embedding of L7 with L0 for a 200-µm-height of CNT forest.

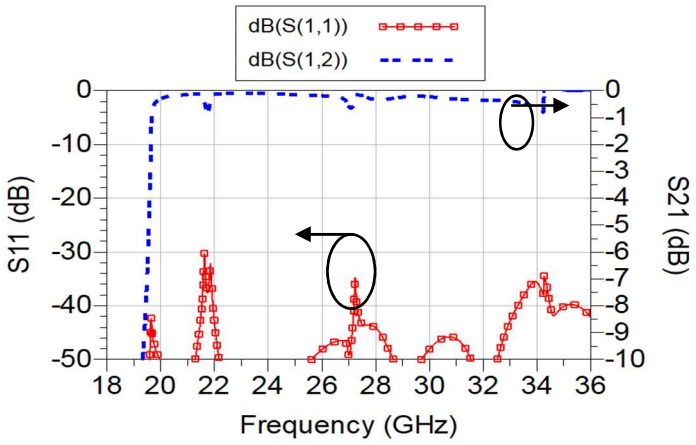

Figure 4-13. Simulated waveguide performance after de-embedding of L7 with L0 for a 300-µm-height of CNT forest.

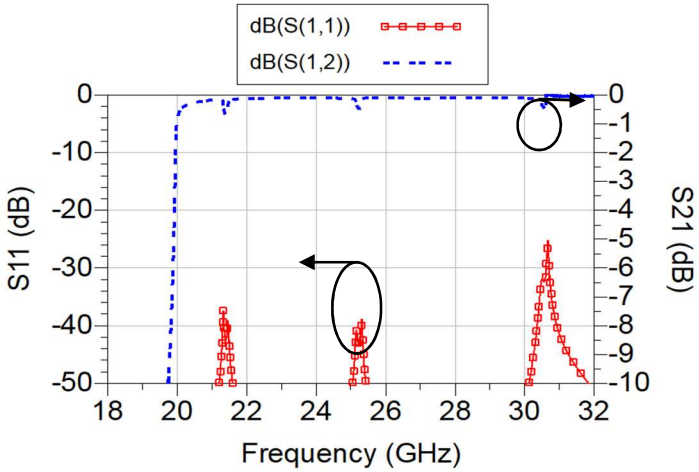

Figure 4-14. Simulated waveguide performance after de-embedding of L7 with L0 for a 400-µm-height of CNT forest.

The results presented so far on Figure 4-12, Figure 4-13 and Figure 4-14, were re-conducted for a couple of waveguides in order to extract the phase and attenuation constants that are presented on Figure 4-15. The expected extremely low value for the attenuation constant requires huge accuracy during simulation with extremely rude conditions for convergence. For time duration reasons, simulations were performed with a ΔS condition of 0.005, no more. In addition, a waveguide of length L_{10} (see equation 4-6) had to be simulated for precision purpose. Shorter waveguides were not enabling enough sensitivity in the simulations results in order to extract an accurate value for the attenuation constant. Remaining error may lead to some uncertainties concerning the value of the attenuation constant because of the precision required.

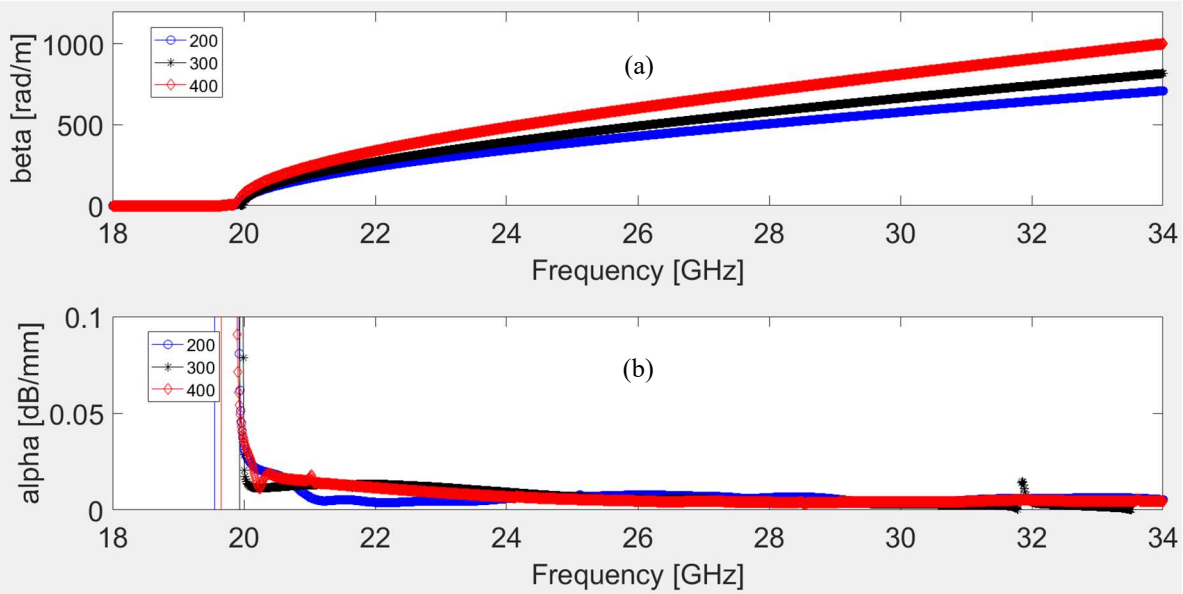

Figure 4-15. Simulated, full-wave, waveguides performance vs. frequency, after transition de-embedding after de-embedding of L10 with L1: a) phase constant, b) attenuation constant. Parametric study as a function of CNT forest height.

Table 4-5 summarizes the waveguide electrical performance at the operating frequency of 28 GHz as a function of CNT forest height. These results allow us to believe in an extremely low-loss waveguide for our applications at 28 GHz. Be careful anyway

that the axial conductivity approximation that enables so low loss has to be validated through the future measurements after CNT transfer.

CNT forest height (µm)	Phase constant (rad/m)	Attenuation constant (dB/mm)	Q-factor
200	506	0.0064	343
300	581	0.0034	742
400	711	0.0040	772

Table 4-5. Simulated waveguide electrical characteristics at 28 GHz, extracted from L7-L0 waveguides. Parametric study as a function of CNT forest height.

4.1.3 Layout and measurement results

4.1.3.1 Masks for PCB and CNT

Figure 4-16 presents the layout of some different lengths of CNT-based AF-SW-SIW waveguides designed with three different values of CNT forest thickness (200 µm, 300 µm and 400 µm). This layout consists of two main parts: the bottom part (see Figure 4-16 (a)), containing layer 1, layer 2 and layer 3 of investigated waveguides, and will be sent and fabricated at CIRLY, Lyon, France. Meanwhile the top part (see Figure 4-16 (b)) will be sent to Singapore on which the CNTs will be transferred by our collaborator: CINTRA laboratory. The process of CNT transfer is identical with the one presented in Chapter 3. The TRL calibration kit was also added in the bottom part.

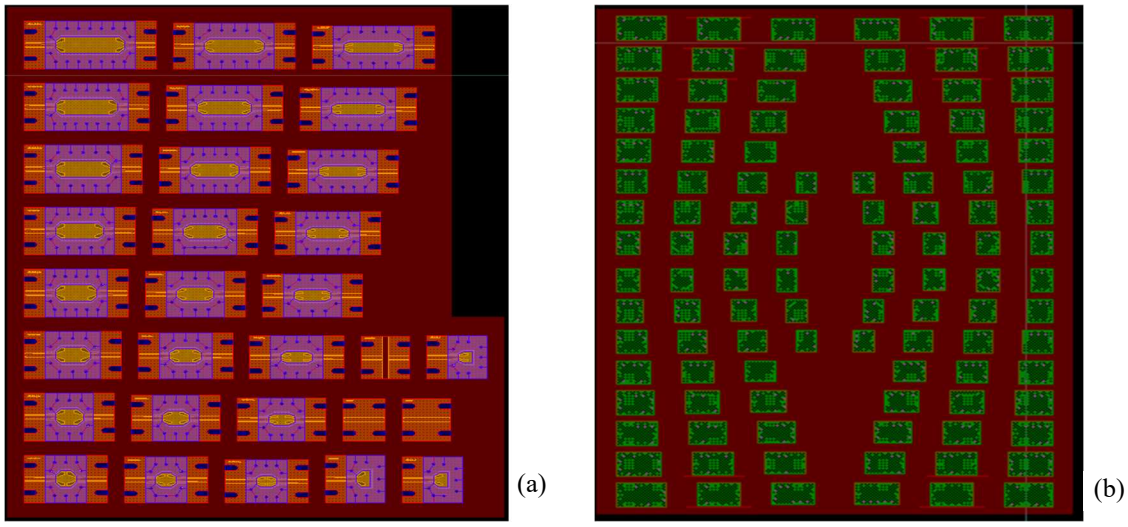

Figure 4-16. Layout sent to PCB provider, CIRLY, Lyon area, France: (a) bottom part, layers 1, 2 and 3. (b) top part to be covered with CNT, layer 4.

4.1.3.2 Measurement results of empty waveguides before CNT transfer

For the future heights of CNTs, empty waveguides were measured in order to validate the fixation process by screwing, and the transition capabilities. The measured S-parameters of "200-µm CNT height" empty waveguides are presented on Figure 4-17 When comparing with Figure 4-9, which were concerning the simulation of the expected final waveguides with CNTs, a deteriorated matching can be observed, as well as a shifted cut-off frequency towards higher frequencies. This is expected as the waveguide is able to work under slow-wave effect and not empty. In addition, insertion losses of about 4.8 dB,

instead of 1.5 dB at 28 GHz, cannot be due to mismatch only but also the contact with connectors inherently deteriorates the transition. The signal-to-ground coupling at the connectors also contributes to the degradation of the insertion losses.

De-embedding technique has been applied and the corresponding electrical parameters for empty waveguides are plotted on Figure 4-18, compared with simulated ones. As a summary, Table 4-6 compares the former measured and simulated empty waveguides electrical performance at the frequency of 30 GHz for the 200-µm transferred CNT forest heights. These results are extremely encouraging in terms of design capabilities before CNT transfer as the cut-off frequency, and phase constant fit very accurately. Attenuation constant is incredibly sensitive to connection repeatability and measurement incertitude. Also incertitude due to VNA only is already as high as 100% with expected losses equal to about 0.05 dB/mm [6], while losses as low as 0.008 dB/mm are simulated. Anyway, very low loss is expected as the attenuation constant varies around 0.01 dB/mm at 28 GHz and 0.05 dB/mm at 32 GHz. CNT transfer is at the present under realization at CINTRA laboratory.

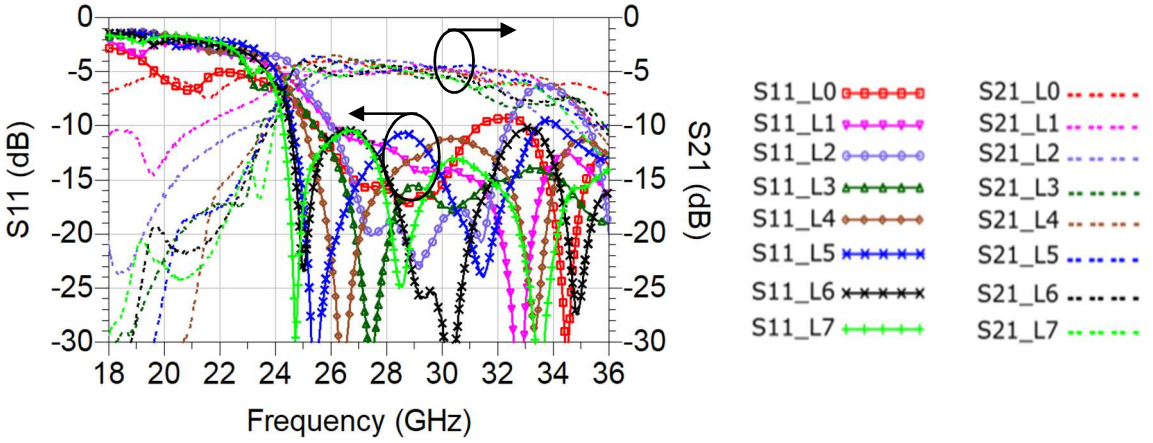

Figure 4-17. Measured S-parameters of different lengths of empty waveguides designed for future 200-µm-height transferred CNT forest with its transitions and CPW/GCPW access lines.

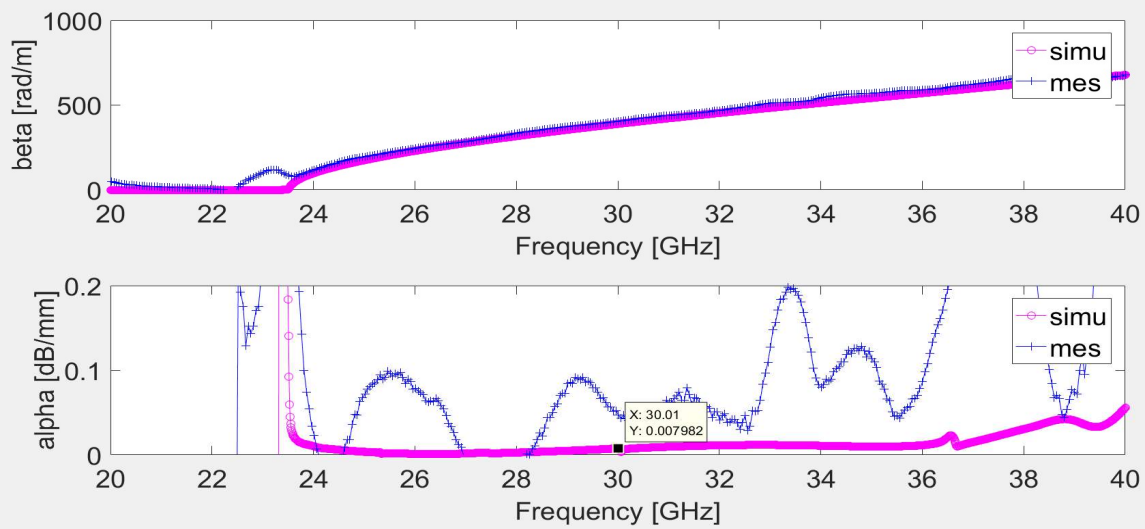

Figure 4-18. Empty waveguides performance vs. frequency. Measurements with transition de-embedding of L7 with L1 compared with simulations with transition de-embedding of L10 with L1. a) phase constant, b) attenuation constant.

Future CNT height (µm)		Phase constant (rad/m)	Attenuation constant (dB/mm)	Q-factor
200	sim	393	0.008	213
	meas	404	0.047	75

Table 4-6. Empty waveguide electrical characteristics at 30 GHz, extracted from L7-L1 waveguides.

4.2 CNT-based AF-SW-SIW 3-dB coupler

In this part, an AF-SW-SIW 3-dB coupler which is based on the short-slot coupler topology and the waveguide structure presented in section 4.1 will be introduced. Only the slow-wave effect performed by a 200-µm height of CNT forest will be studied.

4.2.1 Design

The implementation form of this 3-dB coupler is illustrated in Figure 4-19, the geometric parameters defining this device are denoted as W_a, W, L and L'. W_a is the width of the access waveguide for monomode operation, while W and L are defining the center region size [7]. $W_{CNT} = 1\ mm$ is defined as a gap between the edge of CNT forest and the edge of the ROGER substrate, this gap allows a safety waveguide assembly that prevents an unexpected harm on CNT forest. For 200-μm height of CNT forest, the width of the access waveguide W_a equals 5.69 mm.

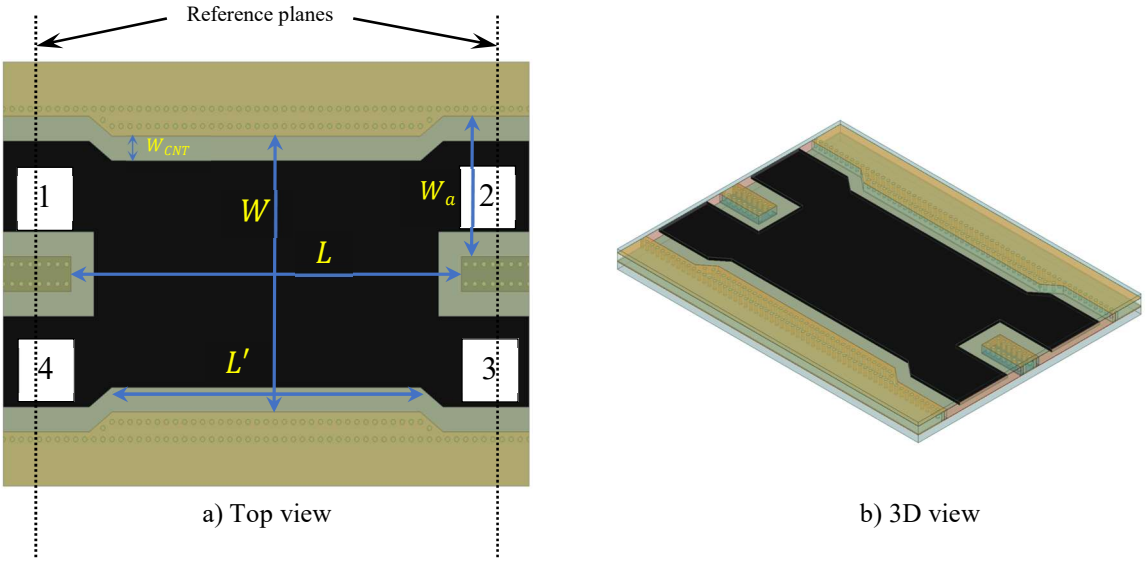

a) Top view b) 3D view

Figure 4-19. 3-dB coupler in CNT-based AF-SW-SIW technology.

The initial dimensions given by design equations were W = 10.85 mm and L = 8.29 mm. After optimization by implementing the coupler in HFSS with full-wave simulation, the optimized dimensions for real structure were obtained and are given in the second row of Table 4-7.

	W (mm)	L (mm)	L' (mm)
Design equations	10.85	8.29	
Optimized real structure	11.26	8.40	4.8

Table 4-7. Optimized dimension for the 3-dB coupler in CNT-based PAF-SWSIW technology.

4.2.2 Simulation results without access lines

Figure 4-20 presents the optimized responses of the investigated 3-dB coupler with the optimized dimensions introduced in the previous part. This coupler was simulated without its access lines in order to evaluate its intrinsic performance in this section. The E-field distributed inside this coupler is also illustrated in Figure 4-21.

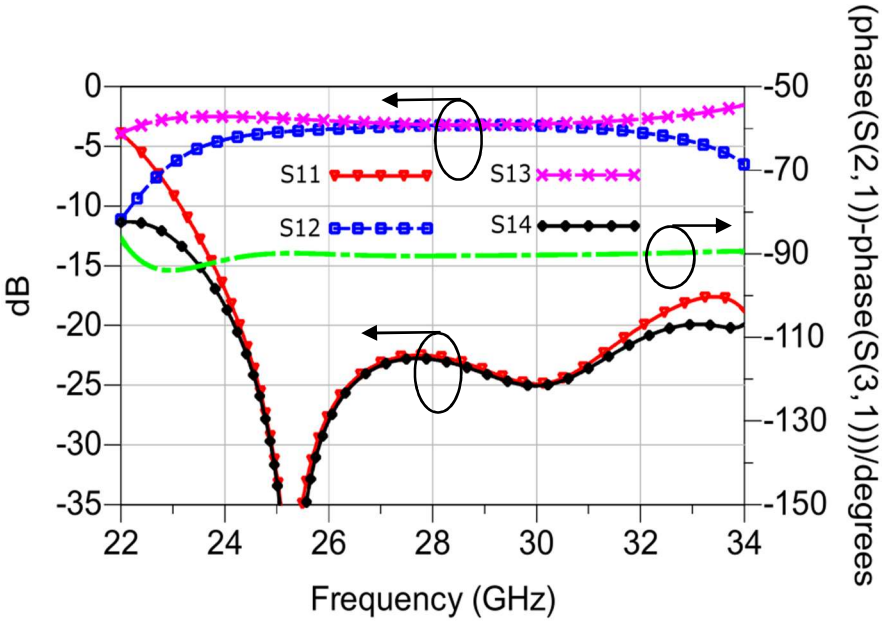

Figure 4-20. Simulated S-parameters of the optimized 3-dB coupler without its access lines in CNT-based AF-SW-SIW technology.

As shown in Figure 4-20, matching as well as isolation are greater than 20 dB over the 24-32 GHz range. At the center frequency of 28 GHz, the insertion losses are around 0.2 dB justifying the interest for this low-loss technology. In terms of unbalance, it is less than 1.5° in phase over the 24-32 GHz and remains less than 1 dB in amplitude between 25.5 and 31.8 GHz (0.08 dB at 28 GHz).

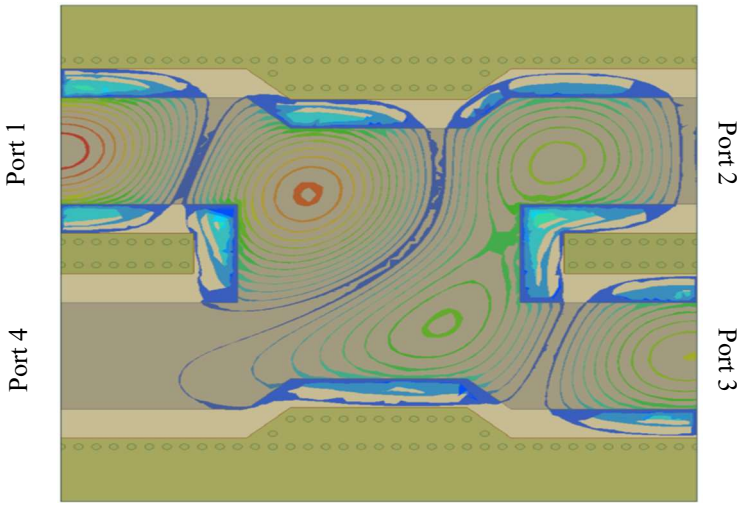

Figure 4-21. E-field distribution inside the 3-dB coupler without its access lines in CNT-based AF-SW-SIW technology.

4.2.3 *Simulation results with access lines*

By assembling the intrinsic structure of the 3-dB coupler presented in section 4.2.2 with the feeding structures introduced in section 4.1.1.4, a complete CNT-based AF-SW-SIW 3-dB coupler can be designed and investigated. The final assembled structure is presented in Figure 4-22 whereas the optimized responses and the E-field distributed inside this coupler are illustrated in Figure 4-23 and Figure 4-24, respectively.

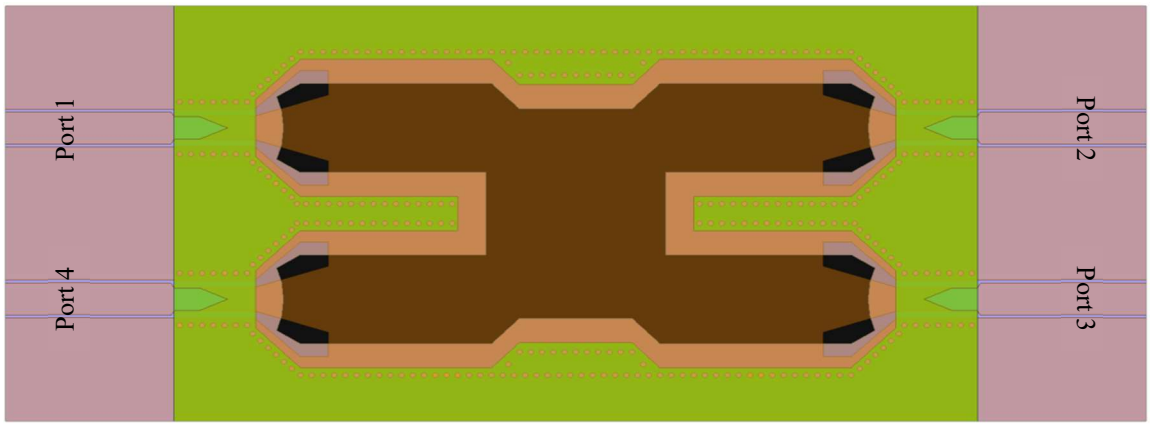

Figure 4-22. 3-dB coupler with its access lines in CNT-based AF-SW-SIW technology.

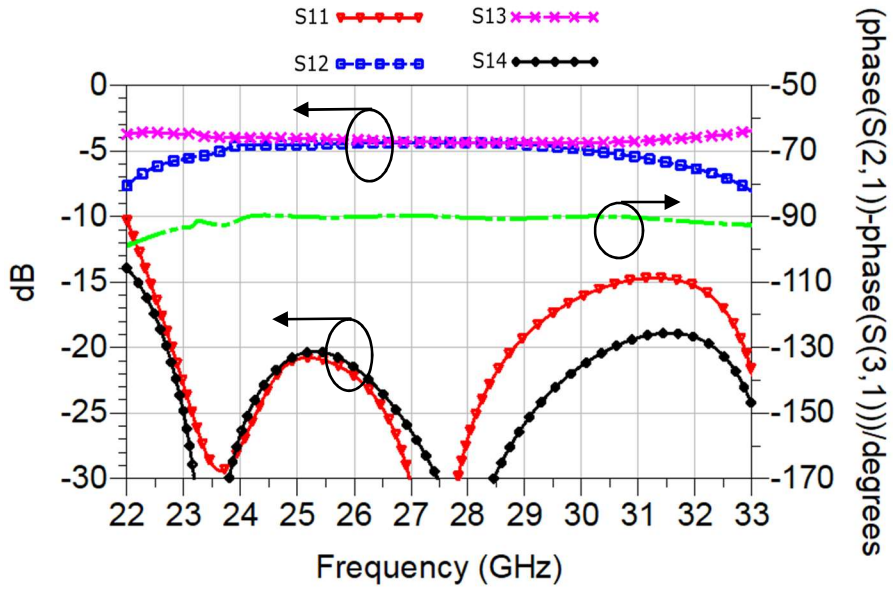

Figure 4-23. Simulated S-parameters of the optimized 3-dB coupler with its access lines in CNT-based AF-SW-SIW technology.

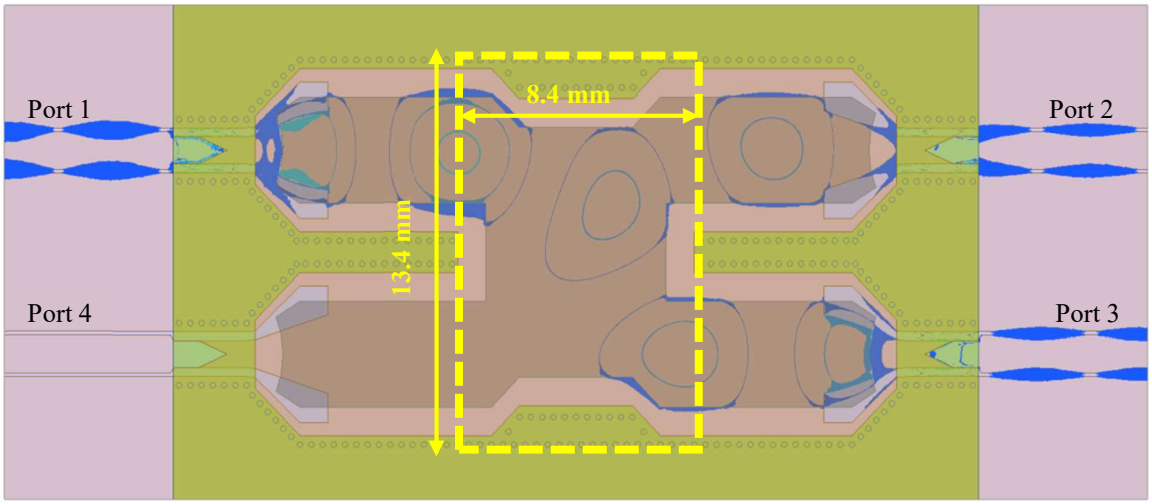

Figure 4-24. E-field distribution inside the 3-dB coupler with its access lines in CNT-based AF-SW-SIW technology.

As shown in Figure 4-23, matching as well as isolation are greater than 15 dB over the 22.5-30.5 GHz range. At the center frequency of 28 GHz, the insertion losses are around 1.35 dB. These losses are due to the transition towards the access lines and the access lines themselves and could be removed further by using the de-embedding technique. In terms of unbalance, it is less than 1° in phase over the 24-31 GHz range and remains less than 1 dB between 23.7 and 30.7 GHz in amplitude (0.02 dB at 28 GHz).

4.2.4 Comparison with SIW 3-dB coupler state-of-the-art in RF frequency band

In order to evaluate our coupler, a comparison in term of electrical performance will be carried out between this investigated coupler and the existing couplers in the literature which were designed for RF applications. This performance summary will be introduced in ****Simulation results***

Table 4-8. The reference, year/type, central frequency, bandwidth, insertion loss, amplitude imbalance, phase imbalance and compactness are compared. The insertion loss, the phase and the amplitude imbalance are taken at the central frequency whereas the relative BW is considered for frequencies where the return loss is better than 10 dB.

Ref	Year/Type	Freq. (GHz)	BW (%) (GHz)	IL (dB)	Amp. Imb. (dB)	Phase Imb. (°)	Surface WxL (λ^2)
[8]	2007/ HM-SIW	12.5	> 40 (10-16)	3.9	0.1	2	0.82x1.33
[9]	2010/cruciform	12.5	36 (10-14.5)	3.25	0.1	5	1.12x1.60
[10]	2011/two-folded	12.5	> 40 (10-16)	3.3	0.15	3	0.73x1.36
[11]	2011/short-slot	24	> 45 (19-30)	3.2	0.1	3	0.81x1.69
[12]*	2014/folded	14.9	1	3.3	0.5	1	0.73x1.88

			(14.82-14.97)				
[13]	2015/short-slot	10	50 (7-12)	3.1	0.1	1	1.06x1.38
[14]	2016/ RHM-SIW	7.5	43 (5-8)	4.28	0.1	1	0.18x1.10
[15]	2017/ SW-HMSIW	14.1	72 (9-19)	3.3	0.5	2.5	0.56x1.61
[16]	2019/short-slot SWSIW	11.15	42 (8.5-13.5)	3.4	0.08	1.5	1.08x1.45
Our work*	2020/short-slot AF-SW-SIW	28	46 (22-35)	3.1	0.08	1	0.97x1.54

Simulation results

Table 4-8. Performance summary of SIW-based couplers for RF applications.

Our short-slot 3-dB coupler results in state-of-the-art insertion loss, amplitude and phase imbalance, equal to 0.1 dB, 0.08 dB and 1°, respectively. The relative bandwidth and phase imbalance remain very competitive with the state-of-the-art while the coupler shows strong compactness with a surface equaling 0.97x1.54 λ^2, where λ is the guided wavelength at working frequency.

4.3 CNT-based AF-SW-SIW crossover

In this part, an AF-SW-SIW crossover which is based on the short-slot coupler topology and the waveguide structure presented in section 4.1 will be introduced. Only the slow-wave effect performed by a 200-µm height of CNT forest will be studied.

4.3.1 Design

The procedure used to design the AF-SW-SIW crossover does not differ so much from that of the 3-dB coupler. The implementation form of this crossover is the same one used for the 3-dB coupler which is illustrated in Figure 4-19. The initial dimensions given by design equations are $W = 10.98$ mm and $L = 16.66$ mm. After optimization by implementing the crossover in HFSS with full-wave simulation, the optimized dimensions for the real structure were obtained and are given in Table 4-9 along with those provided by design equations.

	***W* (mm)**	***L* (mm)**	***L'* (mm)**
Design equations	10.98	16.66	
Optimized real structure	11.78	17.2	14.4

Table 4-9. Optimized dimensions for the crossover in CNT-based AF-SW-SIW technology.

4.3.2 Simulation results without access lines

Figure 4-25 presents the response of the investigated crossover obtained through the optimized dimensions introduced in the previous part. This crossover was first simulated without its access lines in order to evaluate its intrinsic performance. The distributed E-field inside this crossover is also illustrated in Figure 4-26.

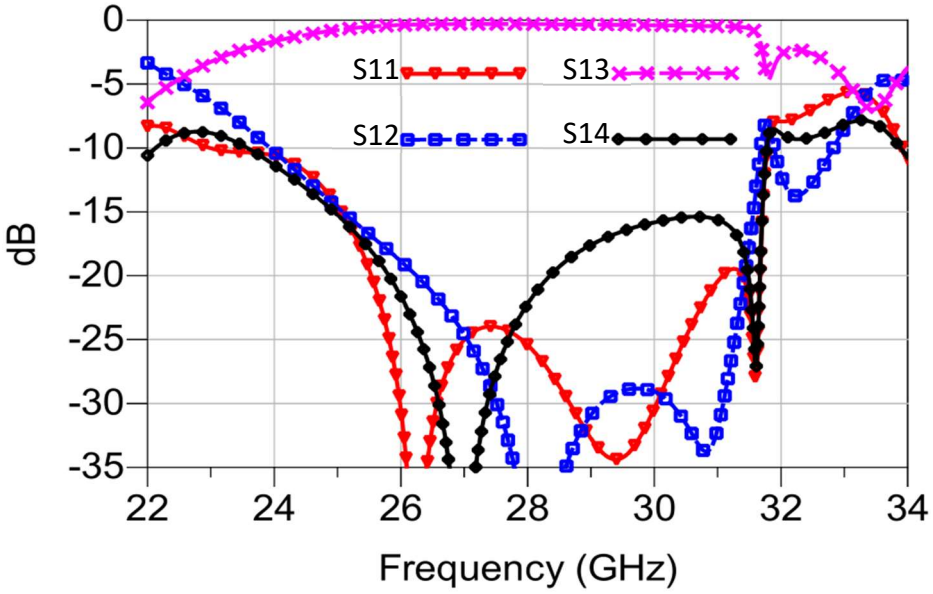

Figure 4-25. Simulated S-parameters of the optimized crossover without its access lines in CNT-based AF-SW-SIW technology.

As shown in Figure 4-25, matching as well as isolation are greater than 15 dB over the 25-31 GHz range. At the center frequency of 28 GHz, the insertion losses are around 0.1 dB justifying the interest for this low-loss technology.

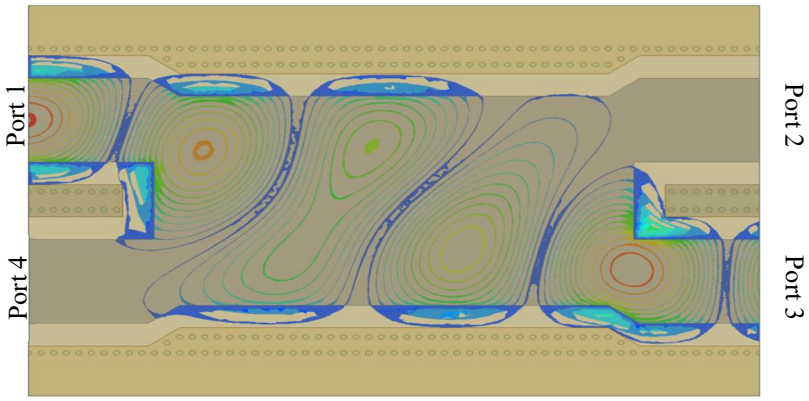

Figure 4-26. E-field distribution inside the crossover without its access lines in CNT-based AF-SW-SIW technology.

4.3.3 Simulation results with access line

Once again, by assembling the intrinsic structure of the crossover, presented in section 4.3.2, with the feeding structures introduced in section 4.1.1.4, a completed CNT-based AF-SW-SIW crossover can be designed and investigated. The final component is presented in Figure 4-27 whereas the optimized responses and the E-field distributed inside this crossover are illustrated in Figure 4-28 and Figure 4-29, respectively.

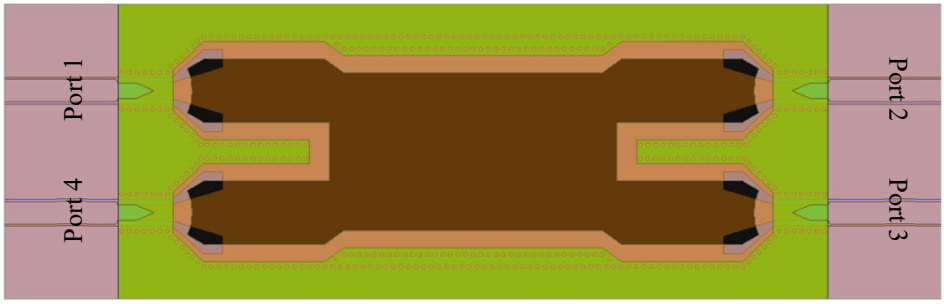

Figure 4-27. Crossover with its access lines in CNT-based AF-SW-SIW technology.

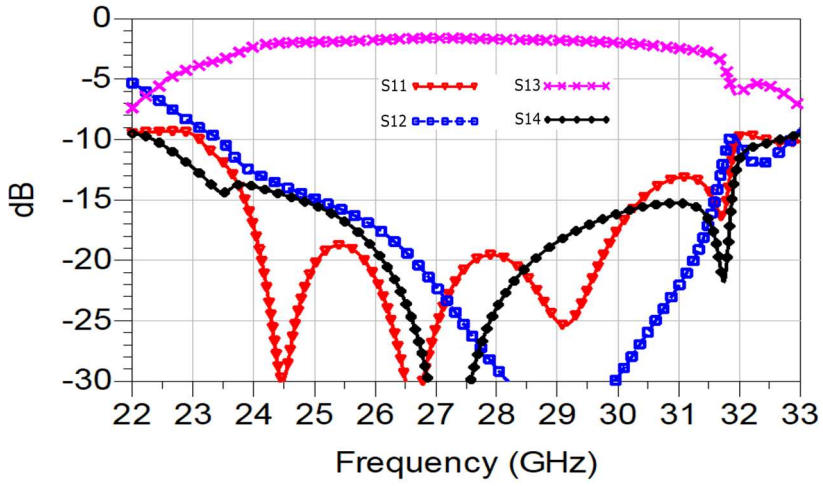

Figure 4-28. Simulated S-parameters of the optimized crossover with its access lines in CNT-based AF-SW-SIW technology.

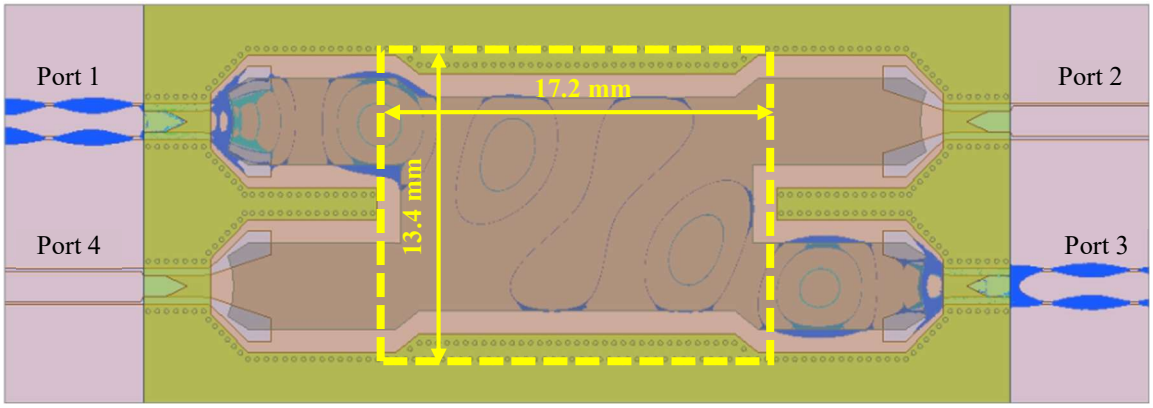

Figure 4-29. E-field distribution inside the crossover with its access lines in CNT-based AF-SW-SIW technology.

As shown in Figure 4-28, matching as well as isolation are greater than 15 dB over the 25-30 GHz range. At the center frequency of 28 GHz, the insertion losses are around 1.34 dB. These losses are due to the reflection that occurs at the transition of the access lines and could be removed further by using the de-embedding technique.

4.3.4 Comparison with SIW crossover state-of-the-art in RF frequency band

In order to evaluate our crossover, a comparison in terms of electrical performance will be carried out between this investigated crossover and the existing ones in the literature which were designed for RF applications. This performance summary will be introduced in ****Simulation results***

Table 4-10. The reference, year/type, central frequency, bandwidth, insertion loss, direct transmission, isolation and compactness are compared. The insertion loss, direct transmission and isolation are taken at the central frequency whereas the relative BW is considered for frequencies where the return loss is better than 10 dB.

Ref	Year/Type	Freq. (GHz)	BW (%) (GHz)	IL (S_{31}) (dB)	Direct trans. (S_{21}) (dB)	Iso. (S_{41}) (dB)	Surface WxL (λ^2)
[9]	2010/ cruciform	12.5	36 (10-14.5)	0.15	20	>20	1.60x3.61
[12]	2014/ folded	14.9	1 (14.82-14.97)	0.13	30.7	39.4	0.73x2.63
[1]	2017/short-slot SW-SIW	11.4	26 (9.8-12.7)	0.58	25	>25	1.45x2.16
Our work*	2020/short-slot AF-SW-SIW	28	28.5 (24-32)	0.1	>35	>20	1.54x1.97

Simulation results

Table 4-10. Performance summary of SIW-based crossovers for RF applications.

Our short-slot CNT-based AF-SW-SIW crossover results in very low loss and high relative bandwidth as compared to the state-of-the-art, while the rest of the parameters comply with the state-of the-art. The crossover shows strong compactness with a surface equaling 1.54x1.97 λ^2, where λ is the guided wavelength at working frequency.

4.4 Conclusion

In this chapter, a detailed description of AF-SW-SIW waveguides based on CNT technology was investigated and presented. An important feature for all slow-wave topologies is the slow-wave factor that is, in our case, depending on the height of the CNT forest. In this work, three heights of CNT forest (200 µm, 300 µm and 400 µm) were considered. Based on the theoretical calculations, the width of the CNT-based AF-SW-SIW waveguides could be reduced due to the slow-wave effect leading to an efficient miniaturization on the waveguide dimensions (around 43.5 % in width, and 43.5 % in length with the 400-µm CNT forest height leading to about 68% of surface reduction).

In order to reach sensitivity in measurements through matched transitions, a CPW-to-GCPW-to-SIW transition, mainly based on the quarter-wavelength triangle coupling slot, was also optimized. Indeed, by using this transition, an adaptation better than 15 dB was obtained over a 24-36 GHz range for all structures, leading to a large relative bandwidth of 43%. The fabricated devices are currently under CNT-transfer process at CINTRA Singapore. Some pre-process measurements on empty waveguides before CNT

transfer were performed showing the expected higher cut-off frequency as well as extremely low-loss. The measurements are extremely sensitive to the VNA remaining incertitude after calibration, and to the repeatability of the contacts. The reached accuracy did not enable us to measure the expected extremely low-loss 0.007 dB/mm; by the way they proved an attenuation below 0.1 dB/mm which is already interesting.

Furthermore, the CNT-based AF-SW-SIW technology was also applied to the design of 0-dB and 3-dB couplers, based on the same concept of the short-slot topology. The simulated S-parameters demonstrated that good performance could be expected for these couplers. In general, the return loss is greater than 15 dB over the 25-31 GHz frequency range for both couplers. At the center frequency of 28 GHz, the insertion loss is around 0.2 dB for the 3-dB coupler and 0.1 dB for the crossover, justifying the interest for this low-loss technology. In terms of unbalance for the 3-dB coupler, it is less than 1.5° in phase over the 24-32 GHz and remains less than 1 dB between 25.5 and 31.8 GHz in magnitude (0.08 dB at 28 GHz).

Finally, a comparison in terms of performance between our couplers and the existing ones that were designed for RF applications was also presented in this chapter, underlying their better compactness while keeping similar electrical performance.

REFERENCES

[1] M. BERTRAND, “Guides à ondes lentes intégrés dans le substrat pour les applications en bandes RF et millimétriques,” 2017.

[2] F. Xu, A. Patrovsky, and K. Wu, “Fast Simulation Of Periodic Guided-Wave Structures Based On Commercial Software,” *Microw. Opt. Technol. Lett.*, vol. 49, no. 9, pp. 2180–2182, 2007.

[3] F. Xu, K. Wu, and W. Hong, “Equivalent resonant cavity model of arbitrary periodic guided-wave structures and its application to finite-difference frequency-domain algorithm,” *IEEE Trans. Microw. Theory Tech.*, vol. 55, no. 4, pp. 697–702, 2007.

[4] P. Souzangar and M. Shahabadi, “Numerical Multimode Thru-Line (TL) Calibration Technique for Substrate Integrated Waveguide Circuits,” vol. 5071, 2012.

[5] G. F. ENGEN and C. A. HOER, “Thru-Reflect-Line: An Improved Technique for Calibrating the Dual Six-port Automatic Network Analyzer,” 1979.

[6] D. A. Oumar, “Développement de méthodes de mesure pour la caractérisation de composants quadripôles passifs intégrés à l ’ impédancemètre,” JEAN MONNET DE SAINT- ÉTIENNE, 2019.

[7] C. J. Chen and T. H. Chu, “Design of 60-GHz SIW short-slot couplers,” *APMC 2009 - Asia Pacific Microw. Conf. 2009*, no. c, pp. 2096–2099, 2009.

[8] B. Liu, W. Hong, Y.-Q. Wang, Q.-H. Lai, and K. Wu, “Half Mode Substrate Integrated Waveguide (HMSIW) 3-dB Coupler,” *IEEE Microw. Wirel. COMPONENTS Lett.*, vol. 17, no. 1, pp. 22–24, 2007.

[9] T. Djerafi, N. J. G. Fonseca, and K. Wu, “Design and implementation of a planar 4 × 4 butler matrix in SIW technology for wide band high power applications,” *40th Eur. Microw. Conf.*, no. 35, pp. 910–913, 2010.

[10] A. A. M. Ali, N. J. G. Fonseca, F. Coccetti, and H. Aubert, “Design and implementation of two-layer compact wideband butler matrices in siw technology for ku-band applications,” *IEEE Trans. Antennas Propag.*, vol. 59, no. 2, pp. 503–512, 2011.

[11] T. Djerafi and K. Wu, “Multilayered Substrate Integrated Waveguide 4 x 4 Butler Matrix,” *Wiley Period. Inc.*, pp. 210–224, 2011.

[12] W. Bhowmik, S. Srivastava, and L. Prasad, “Design of multiple beam forming antenna system using substrate integrated folded waveguide (SIFW) technology,” *Prog. Electromagn. Res. B*, vol. 60, no. 1, pp. 15–34, 2014.

[13] S. Karamzadeh, V. Rafii, M. Kartal, and B. S. Virdee, “Compact and Broadband 4 x 4 SIW Butler Matrix with Phase and Magnitude Error Reduction,” *IEEE Microw. Wirel. Components Lett.*, vol. 25, no. 12, pp. 772–774, 2015.

[14] T. R. Jones and M. Daneshmand, “The Characterization of a Ridged Half-Mode Substrate-Integrated Waveguide and Its Application in Coupler Design,” *IEEE Trans. Microw. Theory Tech.*, vol. 64, no. 11, pp. 3580–3591, 2016.

[15] H. Jin, Y. Zhou, Y. M. Huang, S. Ding, and K. Wu, “Miniaturized Broadband Coupler Made of Slow-Wave Half-Mode Substrate Integrated Waveguide,” *IEEE Microw. Wirel. Components Lett.*, vol. 27, no. 2, pp. 132–134, 2017.

[16] M. Bertrand *et al.*, “A 3-dB Coupler in Slow Wave Substrate Integrated Waveguide Technology,” vol. 29, no. 4, pp. 2019–2021, 2019.

Chapter 5. Partially Air-Filled Slow-Wave SIW (PAF-SW-SIW) in conventional PCB technology at 28 GHz

In this chapter, a Partially Air-Filled Slow-Wave Substrate Integrated Waveguide (PAF-SW-SIW) in conventional PCB technology is introduced for RF applications at the operating frequency of 28 GHz. A compromise between low loss and compactness will be addressed by using respectively, air-filled technology and slow-wave effect. In order to challenge this technology with the one presented in Chapter 4, a comparison between this PCB-based PAF-SW-SIW and the CNT-based AF-SW-SIW will be carried out.

5.1 PCB-based PAF-SW-SIW waveguide

5.1.1 Design

5.1.1.1 Waveguide structure

The detailed structure of the proposed PCB-based PAF-SW-SIW waveguide is illustrated in Figure 5-1. This waveguide is a multi-layer structure made out of three Rogers RO4003 layers (named as Layer 1, Layer 2 and Layer 4) having a relative permittivity ε_r of 3.55 and a loss tangent $tan\delta$ of 0.0027. Layers 2 and 4 are stacked together by an adhesive prepreg layer (named as Layer 3) with a relative permittivity of 3.6 and a loss tangent of 0.028. Meanwhile, in order to ensure a good connection of Layer 1 with the other ones, the use of screws and nuts is necessary. The missions of the three Rogers layers are summarized as follow:

- Layer 1 defines the coplanar access lines and matching slots for feeding the proposed waveguide. The dimensions of these structures are optimized to obtain a good waveguide performance in term of matching and insertion loss.
- Layer 2 defines an air zone for the proposed waveguide, which is formed by engraving the Rogers substrate with a predefined region.
- Layer 4 contains a matrix of internal blind metallized via holes in order to perform the slow-wave effect, which permits to reduce efficiently the device dimensions.

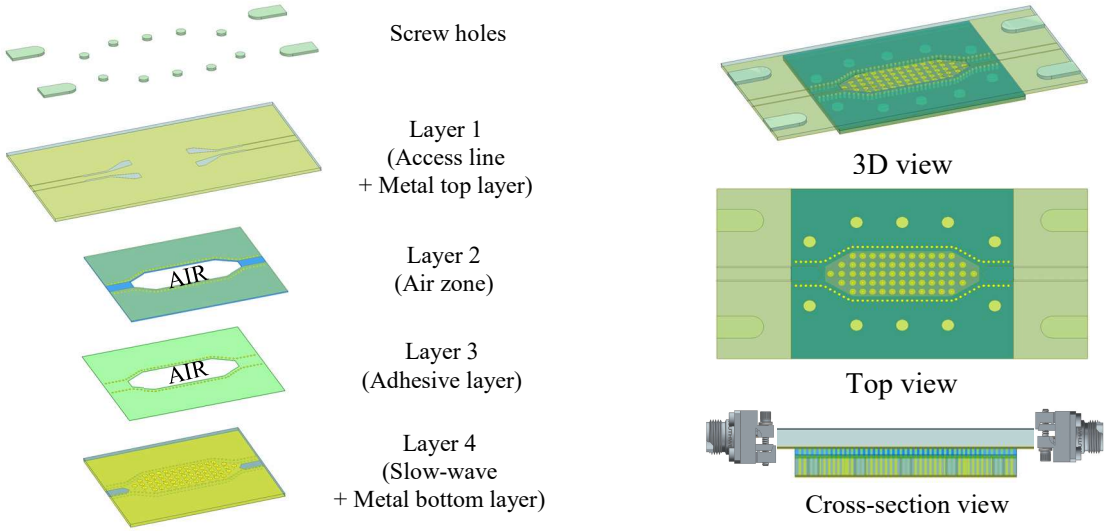

Figure 5-1. Schematic view of the PAF-SW-SIW waveguide in PCB technology.

The detailed parameters of the investigated waveguide are presented in Figure 5-2 and summarized in Table 5-1. Both Layer 1 and Layer 4 have the same thickness of 508 µm while Layer 2 is 203-µm thick in order to obtain a quasi-identical slow-wave factor with the CNT-based AF-SW-SIW presented in Chapter 4. The slow-wave analysis of this investigated waveguide will be introduced in the next section. The adhesive Layer 3 has a thickness of 60 µm. All of the Rogers substrates are metallized by a 17-µm thickness of gold.

As shown in Figure 5-2, the lateral via holes are connected between bottom metal 4 and top metal 1 layers to forms a SIW waveguide. To limit loss leakage of the SIW, the conditions $p \leq 2d_{ext}$ and $d_{ext} < \lambda_g/5$ should be satisfied [1]-[2], where λ_g is the guided wavelength in the SIW, d_{ext} is the diameter of lateral via holes and p is the center-to-center spacing between two consecutive lateral via holes. In this work, d_{ext} and p are set to 0.2 mm and 0.4 mm, respectively. Then, the internal via holes diameter and height are called d_v and h_v, respectively. These internal via holes shall be covered by copper lands due to the fabrication process requirement. The diameter and thickness of these lands are denoted as d_p and h_p, respectively. After optimization, the dimensions of internal via holes and copper lands are as follow: $d_v = 0.15\ mm$, $h_v = 0.508\ mm$, $d_p = 0.54\ mm$ and $h_p = 0.017\ mm$.

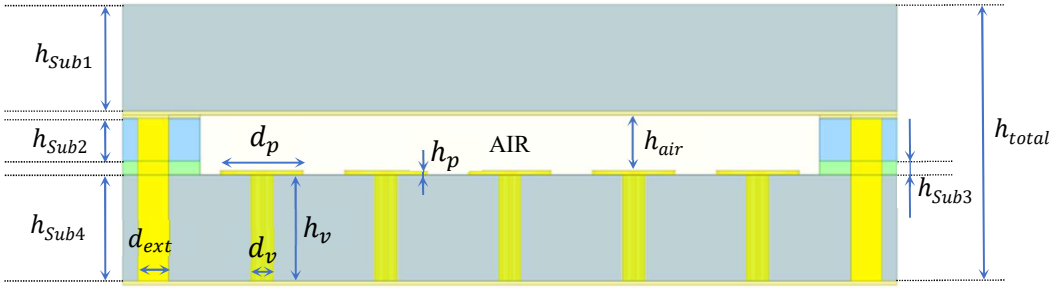

Figure 5-2. Detailed structure of PCB-based PAF-SW-SIW waveguide.

Layer	Substrate	h_{Sub}(µm)	ε_r	$tan\delta$	Metallized Layer
1	ROGER 4003	508	3.55	0.0027	17-µm of gold
2	ROGER 4003	203	3.55	0.0027	17-µm of gold
3	EM-827 (prepreg)	60	3.6	0.028	No metallized layer
4	ROGER 4003	508	3.55	0.0027	17-µm of gold

d_{ext}	d_v	d_p	h_v	h_p
0.2 mm	0.15 mm	0.54 mm	0.508 mm	0.017 mm

Table 5-1. PCB-based technology parameters.

5.1.1.2 Slow-wave analysis

In this section, a theoretical calculation of slow-wave factor corresponding to the waveguide design dimensions introduced in the previous section are presented. Figure 5-3 illustrates the cross-section view of the investigated waveguides with and without the presence of internal via holes. The slow-wave factor can be estimated in a first approximation by the following expression [3]:

$$SWF_{estimate} \approx \sqrt{\frac{h}{h-h_v-h_p}} \quad (5\text{-}1)$$

where h refers to the total height of the air zone inside the waveguide and can be calculated by $h = h_{metal} + h_{Sub2} + h_{Sub3} + h_{Sub4} = 792\ \mu m$, leading to an estimated slow-wave factor ($SWF_{estimate}$) of around 1.72.

As illustrated in Figure 5-3, the lateral dimension of the SW-SIW is then reduced by the SWF ratio as compared to classical SIW counterpart.

For an operating frequency of 28 GHz, a cut-off frequency of 20 GHz can be considered, so we can calculate the width of the waveguide (W_{AF-SIW}) (without slow-wave effect) equal to 7.01 mm. Then, with the presence of internal via holes, this width can be reduced leading to an efficient miniaturization on the transverse waveguide dimension. Around 43.5 % reduction in width has been obtained. As SWF will also impact the desired length of the waveguide with the same percentage, this should enable to save 68% of surface on the PCB at the end, exactly as for the CNTs. It will be shown that the SWF for PCB-based technology will be a little bit higher in practice (1.84 instead of 1.71, leading to higher surface saving by the end (almost 76%).

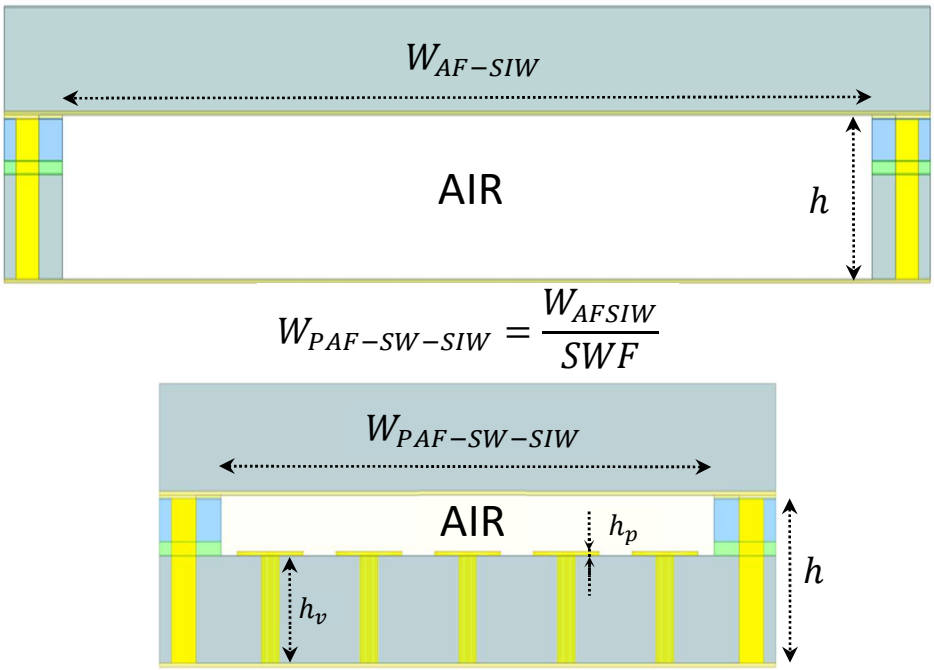

Figure 5-3.Cross-section view of investigated waveguides with and without presence of internal via holes.

In order to study the electrical performance of the investigated waveguides, the Eigen-mode solver in HFSS was considered as a straight-forward strategy to explore the waveguide propagation constants [4], [5]. This method was already introduced in Chapter 4. In order to compare this PCB-based PAF-SW-SIW waveguide with the CNT-based AF-SW-SIW waveguide, the simulation results of the phase constant β, the attenuation constant α, the quality factor Q and the slow-wave factor SWF will be presented in Figure 5-4. In this case, only a 400-µm height of CNT forest is taken into account for the comparison. A width of 4 mm is considered for these two SIWs (PCB and CNT-based ones) presenting roughly the same SWF as compared to their air-filled counterpart.

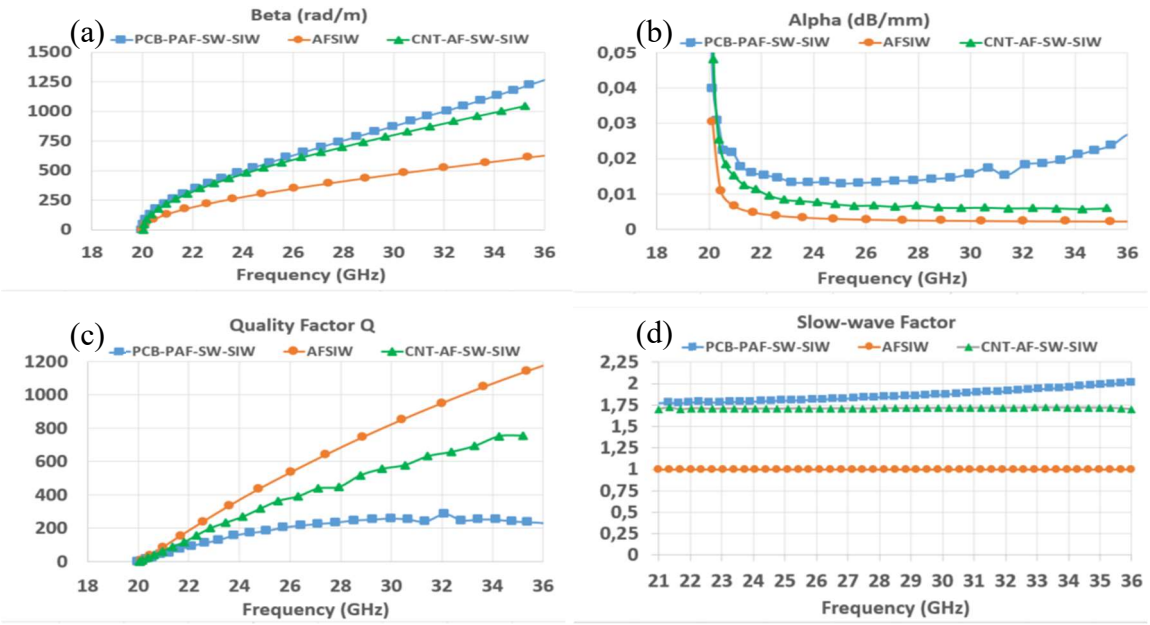

Figure 5-4. Waveguide performance vs. frequency: a) phase constant, (b) attenuation constant, (c) Q-factor and d) slow-wave factor.

As illustrated in Figure 5-4 (b), the higher slow-wave factor, the higher the attenuation constant α. Be careful first that the values for attenuation constant were obtained through Eigen-mode simulation and the following analysis is certainly more qualitative than quantitative. Indeed, whereas α equals 0.003 dB/mm for the non-slow-wave AF-SIW at 28 GHz, it raises up to 0.013 dB/mm when the slow-wave effect is performed by the internal via holes. This attenuation is much larger than the value achieved by using the 400-µm-height of CNT forest to establish the slow-wave effect, which is about 0.0069 dB/mm. It is mainly due to the dielectric losses inside the Rogers substrate and conductive losses distributed inside the internal via holes and in the surface of copper lands. Anyway, let us remember that for the CNT-based SW-AF-SIW an equivalent model of the CNT forest was considered for these simulations; this equivalent model has to be confirmed by future experiments.

The huge difference in attenuation values therefore leads to the huge difference in quality factor. Indeed, while a high amount of quality factor around 442 seems to be obtained with CNT-based AF-SW-SIW, this value is only 251 for the PCB-based PAF-SW-SIW. Table 5-2 summaries all simulation results obtained by using Eigen-mode solver in terms of phase constant β, attenuation constant α, quality factor Q and slow-wave factor SWF at 28 GHz for AF-SIW, PCB-based PAF-SW-SIW and CNT-based AF-SW-SIW.

Waveguide type	β (rad/m)	α (dB/mm)	Q	SWF	Waveguide width (mm)
AFSIW	410	0.003	593	1	7.01
CNT-based AF-SW-SIW	702	0.0069	442	1.71	4.0
PCB-based PAF-SW-SIW	751	0.013	251	1.84	4.0

Table 5-2. Summary of the investigated waveguide performance by using Eigen-mode simulation at 28 GHz.

5.1.1.3 Electric and magnetic field distribution

As already known, a separation of electric and magnetic fields in a waveguide can slow down its phase velocity and therefore establishes the slow-wave effect. Hence, in this section, a distribution of electric and magnetic fields confined inside the PCB-based PAF-SW-SIW waveguide is illustrated. In order to explain the difference in terms of SWF values presented in the previous section, a distribution of electric and magnetic fields enclosed inside the CNT-based AF-SW-SIW are also convened.

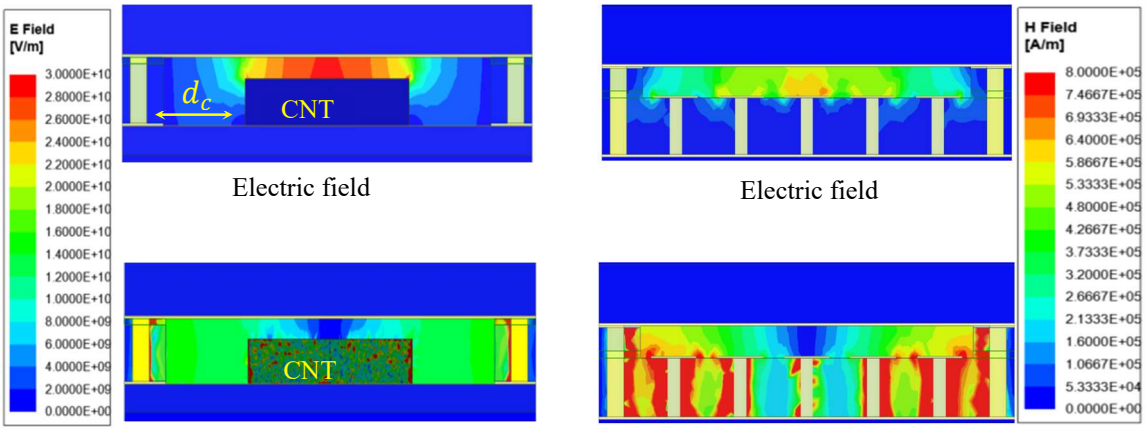

Figure 5-5. Electric and magnetic distribution in (a) AF-SW-SIW and (b) PAF-SW-SIW at 28 GHz.

As discussed previously in Chapter 4, the distance between the sidewall of CNT forest and the ROGER substrate d_c must be at least 1 mm due to the fabrication process requirement. This is a huge value as compared to the waveguide width, which is only 4 mm. Therefore, in the case of CNT-based AF-SW-SIW waveguide, the electric field is not only confined in the air zone limited by the CNT forest and top metal layer but also distributed in the air area defined by d_c as presented in Figure 5-5 (a). Meanwhile, in PCB-based PAF-SW-SIW waveguide, the electric field is mainly concentrated in the air zone between the top metal layer and the top of blind via holes. There is only a small amount of the electric field, which penetrates the dielectric substrate through the space between two blind via holes as presented in Figure 5-5 (b). The electromagnetic field distribution presented in Figure 5-5 also shows that the magnetic field in both cases flows inside the whole waveguide structure. This physical separation of electric and magnetic fields is at the origin of the slow-wave effect [6]. Hence, the difference in the distribution of electric field inside its waveguide explains why PCB-based PAF-SW-SIW finally have a larger amount of SWF than the CNT-based AF-SW-SIW (as indicated in Table 5-2) which could not be expected by the approximated formula (5-1) that was leading to an estimated similar SWF.

5.1.1.4 Feeding structures

Once again, due to its high performance, a GCPW-CPW transition using triangular coupling slot (as presented in section 3.2.3) is considered as a feeding line for this PCB-

based PAF-SW-SIW. A detailed view of the proposed transition is shown in Figure 5-6. The values are summarized in Table 5-3.

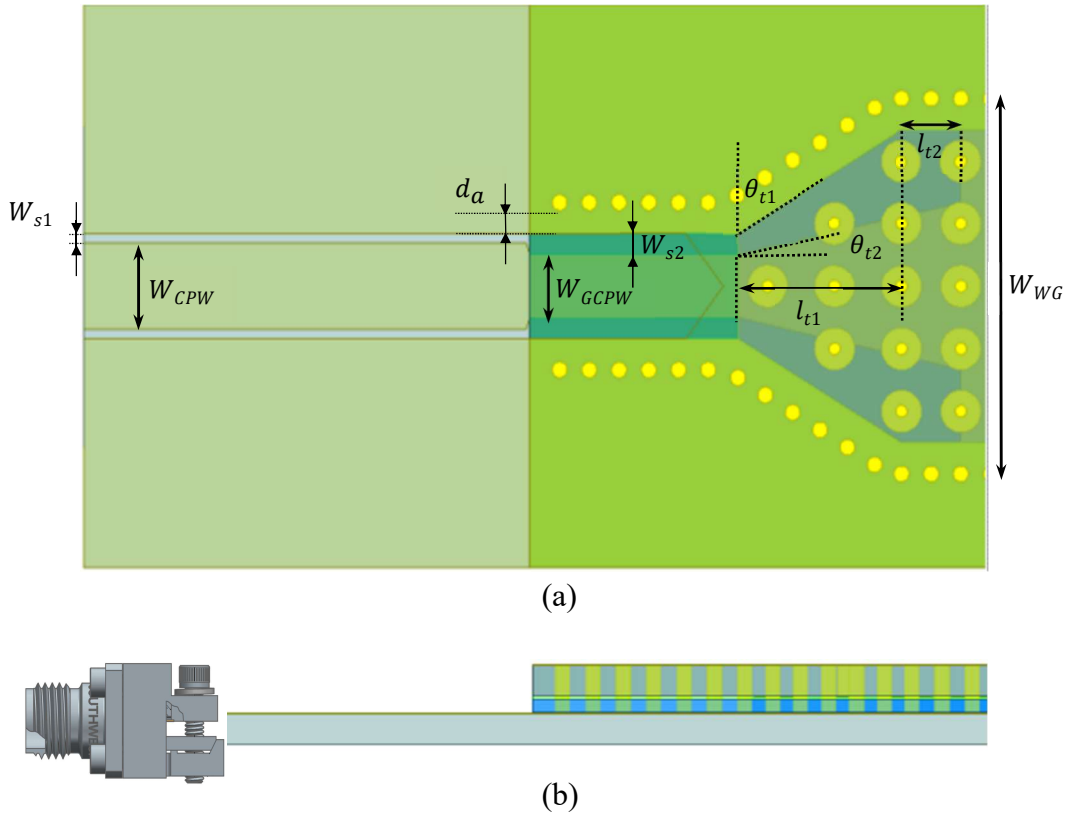

Figure 5-6. Detailed view of the broadband transition for PCB-based PAF-SW-SIW. a) top view, b) side view.

l_{t1} (mm)	l_{t2} (mm)	θ_{t1} (°)	θ_{t2} (°)	W_{CPW} (μm)	W_{s1} (µm)	W_{GCPW} (μm)	W_{s2} (µm)	d_a (µm)
2.2	0.8	60	15	1100	120	800	270	200

Table 5-3. Optimized parameters of the broadband transition for PCB-based AF-SW-SIW.

The broadband transition geometry is established by two angles θ_{t1} and θ_{t2} as well as the taper length l_{t1} and l_{t2}. These dimensions are crucial factors to achieve a very good matching. The physical dimension of the CPW and GCPW are also given: W_{CPW}, W_{s1}, d_a, W_{GCPW}, W_{s2}.

For the starting point, l_{t1} should be equal to a quarter-wavelength at the center frequency of the E-band (2 mm at 28 GHz). It was observed that the outer angle θ_{t1} needs to be around 50°, meanwhile the typical value for θ_{t2} is around 20°. The optimized dimensions of the transitions are as follows: $l_{t1} = 2.2$ mm, $l_{t2} = 0.8$ mm, $\theta_{t1} = 60°$, $\theta_{t2} = 15°$.

Concerning the CPW and GCPW dimensions, a 50−Ω characteristic impedance needs to be obtained and these dimensions must be also optimized in compliance with the standard of connector South-West End Launch 1492-02A-8 for measurements. Thus, the optimized dimensions are given as follows: $W_{CPW} = 1100\ \mu m$, $W_{s1} = 120\ \mu m$, $d_a = 200\ \mu m$, $W_{GCPW} = 800\ \mu m$, $W_{s2} = 270\ \mu m$.

By using this transition, the simulated return loss is better than 15 dB from 21.8 GHz to 37.5 GHz leading to an efficient relative bandwidth of 56%. Meanwhile, the simulated insertion loss is 1.1 dB obtained at 28 GHz. These results allow us to believe in a good access line for our circuits. The detailed simulation results will be introduced in the section 5.1.3.

5.1.2 Equivalent model for PCB-based PAF-SW-SIW circuits

Because of the high complexity of the slow-wave structure, simulations of larger circuits such as 3-dB couplers and crossovers require a large amount of memory, computing power and a lot of time. Hence, an alternative approach needs to be considered to solve this issue. In this section, an equivalent model is introduced for the PCB-based PAF-SW-SIW in order to reduce simulation time while maintaining the same performance accuracy.

5.1.2.1 Methodology for model creation

As introduced in [7], the blind metallized via holes in the waveguide can be removed and their absence can be compensated by an increase in either permittivity or permeability of an equivalent substrate (see Model 1 in Figure 5-7). In practice, let's assume that a certain velocity reduction is achieved by the insertion of a uniform blind via holes distribution. This velocity reduction has to be modelled in the equivalent waveguide by an increase of the product of $\varepsilon_{r_{eff}}$ and $\mu_{r_{eff}}$. In order to retrieve the good phase velocity, the slow-wave factor can be for example absorbed in the permittivity by putting $\varepsilon_{r_{eff}\_1} = SWF^2 * \varepsilon_r$. In the meantime, the permeability remains $\mu_{reff} = 1$.

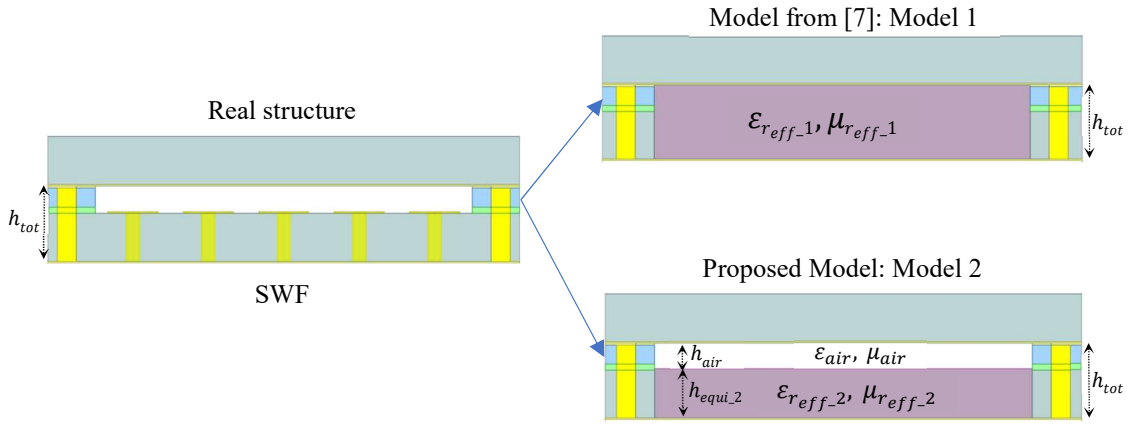

Figure 5-7. From real structure to equivalent model.

However, this equivalent model can be only applied for the homogeneous substrate where there is no presence of the air zone. Hence, in our case, this equivalent model probably will not be correct. In order to check our assumption, a comparison in terms of phase constant β between the real structure and the Model 1 is performed by using Eigen-mode solver in HFSS. With the $SWF = 1.843$ shown in section 5.1.1.2 and $\varepsilon_r = 1$ for air-filled substrate, the equivalent permittivity for Model 1 can be found as $\varepsilon_{r_{eff}\_1} = SWF^2 = 3.396$. After optimization to obtain the same cut-off frequency of 20 GHz, the

value of ε_{reff_1} is around 2.8. Figure 5-8 presents the phase constants β of these two structures.

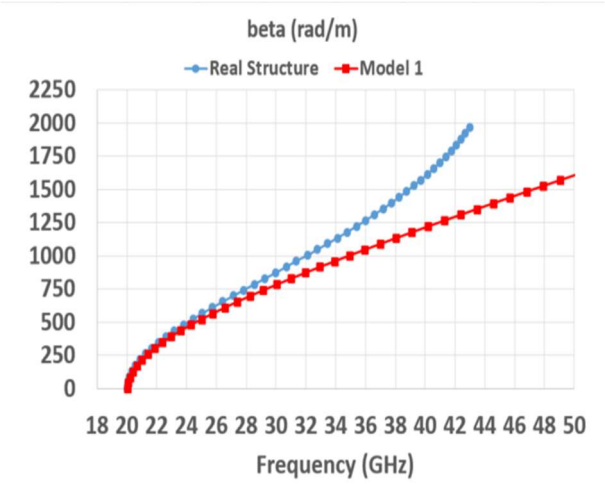

Figure 5-8. Comparison in phase constant β between the real structure and Model 1.

As shown in Figure 5-8, there is a huge difference in shape of phase constant β between the real structure and Model 1, which proves our assumption that the model may not be useable was correct. Therefore, it is necessary to find out another model for our structure, which can provide a similar trend in phase constant curve as compared to the real structure. A proposed model named as Model 2, as presented in Figure 5-7 (c), can be considered as a new equivalent model for our structure. In this model, the presence of internal via holes will be replaced by an equivalent medium having its permittivity and permeability called $\varepsilon_{r_{eff\_2}}$ and $\mu_{r_{eff\_2}}$, respectively. The height of this equivalent medium is the same value with the total height of blind via holes and copper lands. Meanwhile, the air zone inside the real structure is conserved in the proposed model. Now, the question is: "How can we find the value of $\varepsilon_{r_{eff\_2}}$?". Up to now, there is no equation to find this value but we can do it manually with the help of Eigen-mode solver in HFSS. As discussed before, the blind via holes can be removed and their absence can be compensated by an increase in either permittivity or permeability of an equivalent medium. For simplicity, the permeability of equivalent medium is set to 1. Now, we will tune the value of $\varepsilon_{r_{eff\_2}}$ until we find the same cut-off frequency as that of real structure. For example, with the waveguide presented in Figure 5-7 (a) which has a SWF of 1.843, a value of $\varepsilon_{r_{eff\_2}}$ can be found as 13 after optimization. A comparison in term of phase constant β between the real structure and Model 2 with its equivalent permittivity of 13 is presented in Figure 5-9.

As shown in Figure 5-9, a good agreement is obtained in term of phase constant β between the real structure and Model 2. That allows us to have a strong confidence in this model. Let us notice that, by considering this proposed model, the TE-mode cut-off frequency $f_{c_{10}}$ remains unchanged while the dispersive effect can be observed with Model 2, as for the real structure.

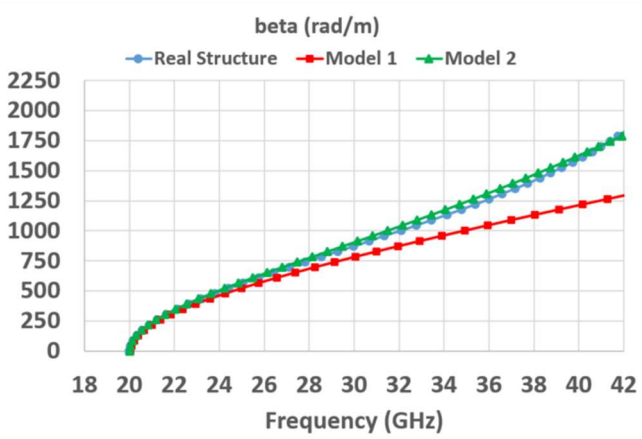

Figure 5-9. Comparison in phase constant β between the real structure and Model 2.

In order to create a relationship between the SWF and the value of $\varepsilon_{r_{eff\_2}}$, several waveguides having different SWFs are considered for this mission. It is worth to notice that these waveguides have the same dimension in the height of air zone and in the total height of blind via holes and copper lands, only the width of waveguide and the diameter of blind via holes and copper lands are changed to obtain the identical cut-off frequency of 20 GHz. The same method was applied to find the optimized value of $\varepsilon_{r_{eff\_2}}$. Table 5-4 summarizes all the parameters of investigated waveguides and the optimized value of $\varepsilon_{r_{eff\_2}}$ corresponding to each waveguide. A comparison in terms of phase constants β between the real structure and Model 2 in each waveguide is also presented in Figure 5-10.

$W_{PAF-SW-SIW}$ (mm)	d_v (mm)	d_p (mm)	SWF (at 28 GHz)	Optimized ε_{reff_2}
4	0.15	0.54	1.843	13
4.11	0.2	0.5	1.735	10.5
4.28	0.4	0.6	1.601	8.05
4.35	0.45	0.6	1.538	7.07
4.4	0.48	0.6	1.506	6.6

Table 5-4. Correspondence between SWF and optimized $\varepsilon_{r_{eff\_2}}$ for investigated waveguides.

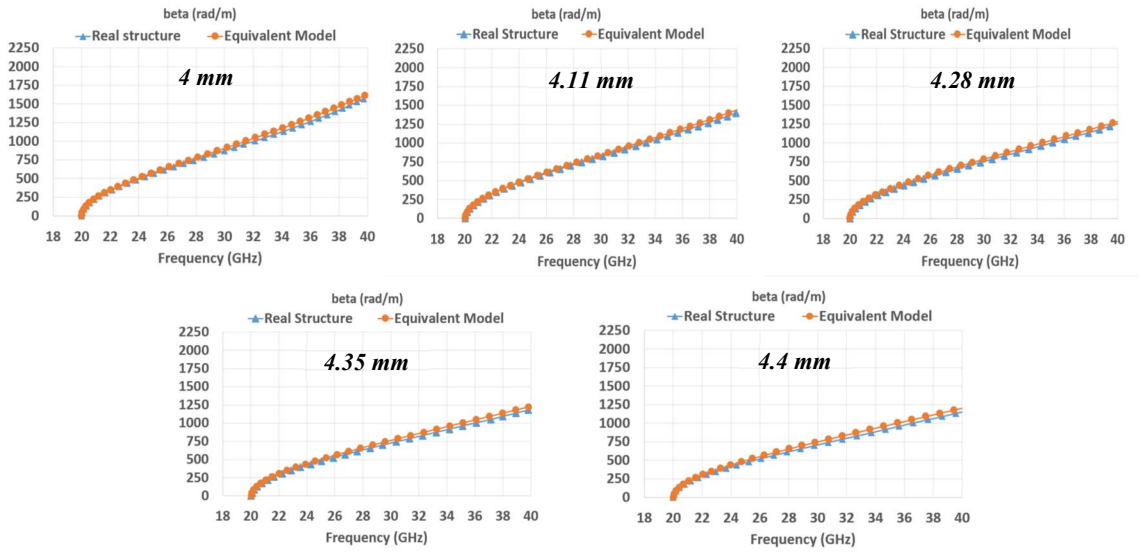

Figure 5-10. Comparison in phase constant β between the real structure and proposed model for each investigated waveguide.

The methodology to create an equivalent model can be illustrated in Figure 5-11.

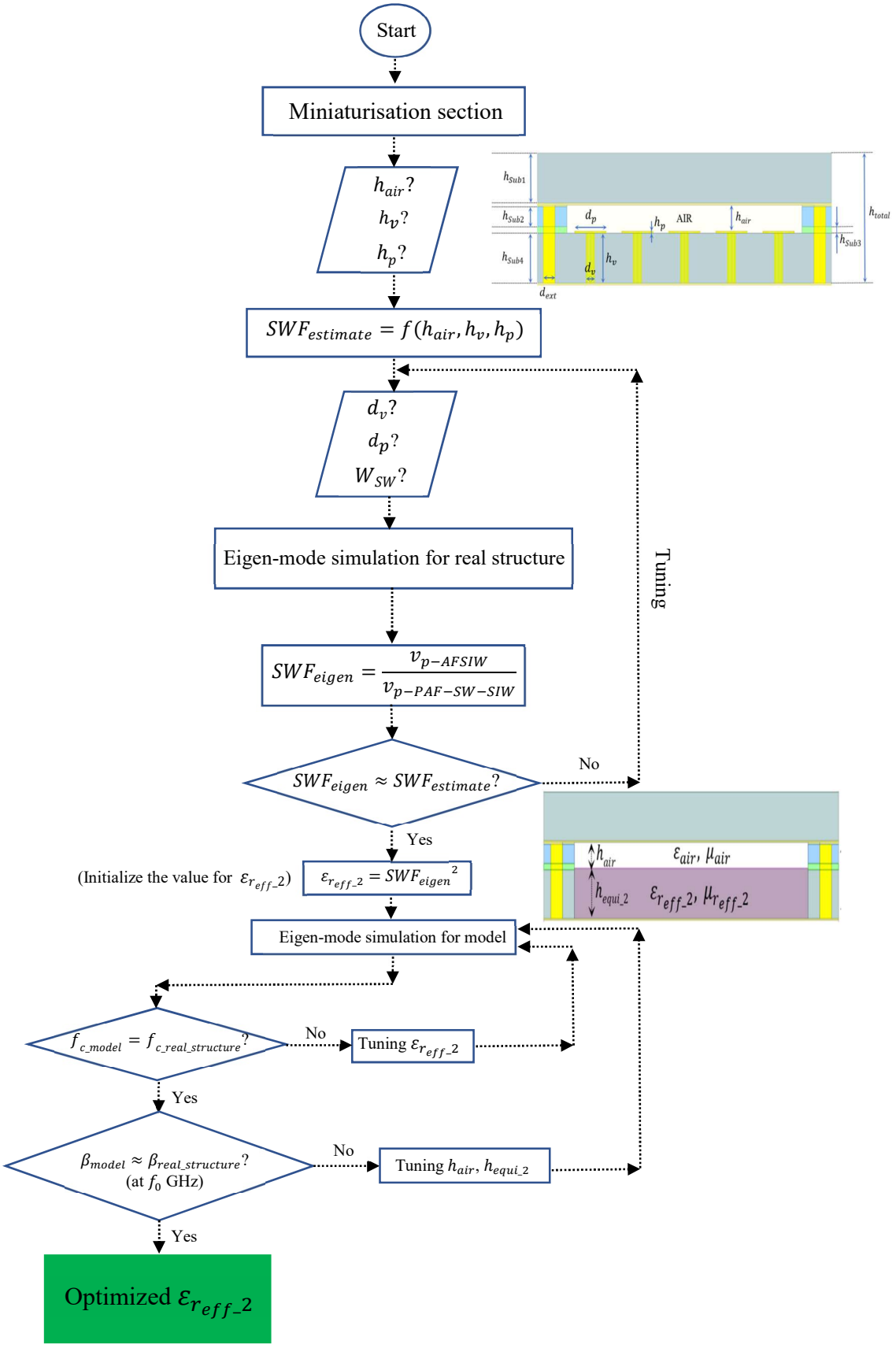

Figure 5-11. Algorithm for equivalent model creation.

5.1.2.2 Model validation

The use of the equivalent model is first validated in the context of a straightforward section of PAF-SW-SIW. For simplicity, a waveguide without the access lines will be considered for the validation. Both waveguides have the same cut-off frequency of 20 GHz and the same length of 7.2 mm as well as the same width of 4 mm. The wave port is chosen to feed these waveguides. Figure 5-12 presents the HFSS full-wave simulation results in terms of S-parameters and the phase of the transmission coefficient $\angle S_{21}$ for both equivalent model and real structure.

As shown in Figure 5-12, a good agreement is obtained between the model and the real structure. They follow a very similar form whether in S-parameters or in phase of the transmission coefficient $\angle S_{21}$. A maximum deviation of 13.8° is observed at 28 GHz over a total electrical length of about 375°. This deviation is mainly due to the dispersion between β_{model} and $\beta_{real\ structure}$ which occurs when building the equivalent model. Anyway, these values of deviation are acceptable for such equivalent model.

As a general rule, because of dispersion, as long as the simulations of the real structure might be performed, the preference will be given to real case. The relevance of this model in coupler and crossover design will be further shown in the next parts.

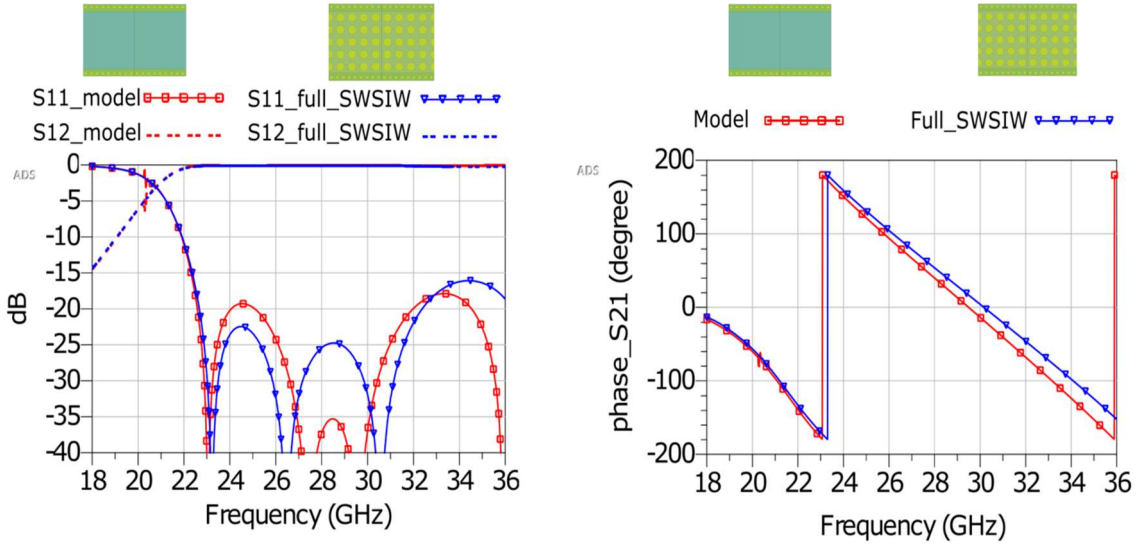

Figure 5-12. Comparison in waveguide performance between equivalent model and real structure.

5.1.3 Simulation results

In this section, the simulation results of several investigated waveguides with its access lines and its transitions are presented. These results are compared with the ones obtained by the equivalent model, which was validated in the previous section. Three lengths of investigated waveguide was chosen for comparison: $\lambda/2$, $3\lambda/4$ and $5\lambda/2$ and its simulation results will be illustrated in Figure 5-13, Figure 5-14 and Figure 5-15, respectively.

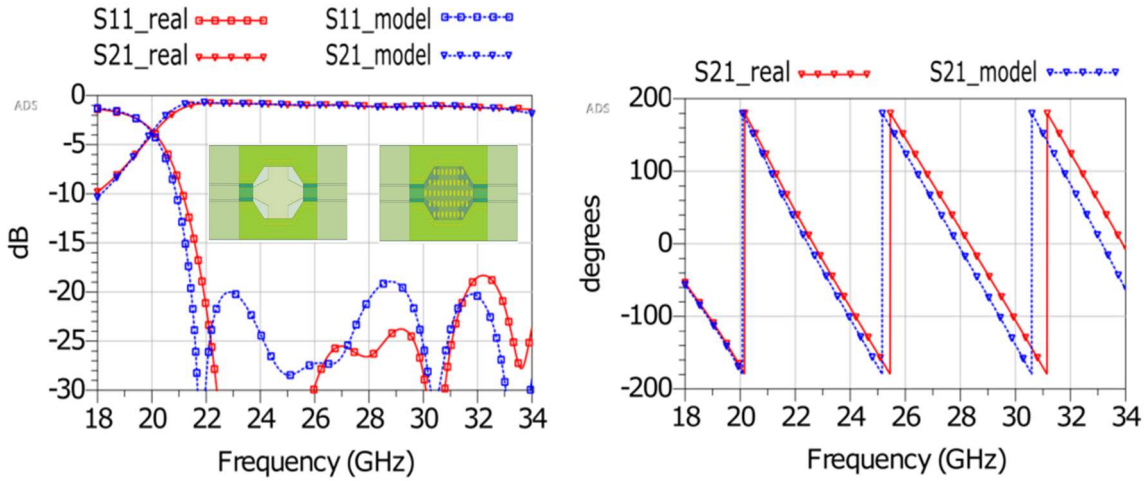

Figure 5-13. Comparison in waveguide performance between the equivalent model and the real structure for investigated waveguide of $\lambda/2$ length.

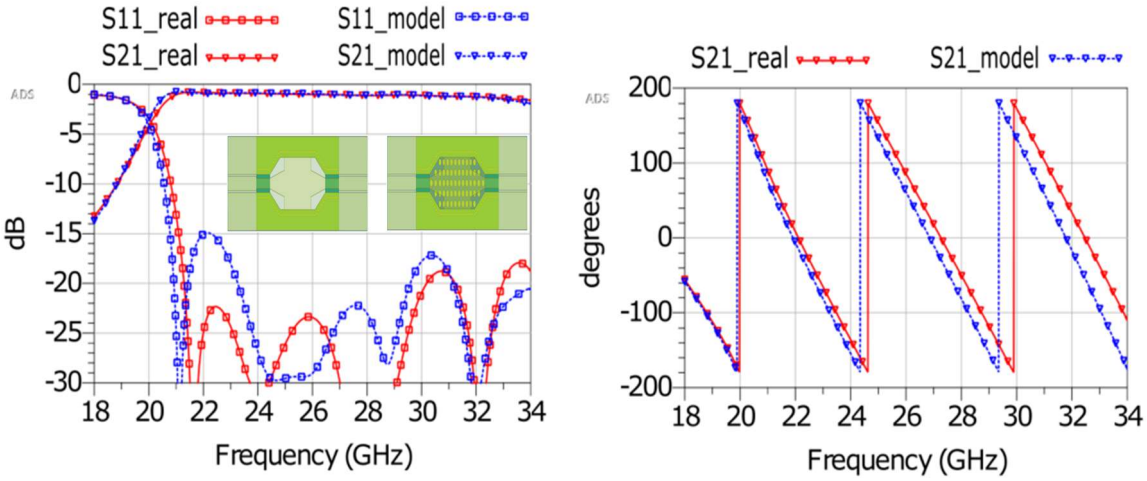

Figure 5-14. Comparison in waveguide performance between the equivalent model and the real structure for investigated waveguide of $3\lambda/4$ length.

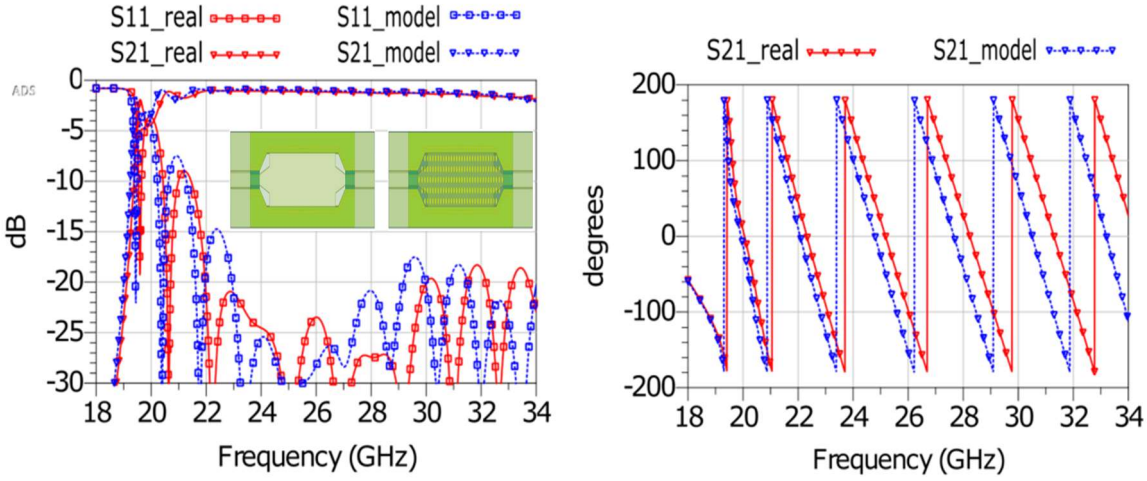

Figure 5-15. Comparison in waveguide performance between the equivalent model and the real structure for investigated waveguide of $5\lambda/2$ length.

Generally, a good agreement is obtained in waveguide performance between the equivalent model and the real structure. They present a very similar form whether in S-

parameters or in transmission coefficient phase $\angle S_{21}$. As shown in Figure 5-13, a deviation of 26.83° is observed at 28 GHz for the $\lambda/2$-length waveguide. Meanwhile, this value is found at 31 06° and 69.69° for the $3\lambda/4$-length waveguide and $5\lambda/2$-length waveguide, respectively. It is clear that these deviation increase along with the increase of waveguide length.

A first comment has to be made at that time: the value of $\varepsilon_{r_{eff\_2}}$ could be re-matched in order to better fit the phase deviation. However, in that case, the cut-off frequency would be modified between real case and model. The choice was made to accept an error in phase, explained by the difficulty to finely model the frequency dispersion, while keeping exactly the same cut-off frequency. For sure, the further from the cut-off frequency, the less accurate will be the results in terms of frequency positioning. This could be improved further by adding dispersion in the model. By the way, this model is already very useful in order to optimize parametric simulations as for the couplers simulations presented later on in this chapter.

In the case of real structure, for the three cases, a return loss greater than 20 dB was obtained over the frequency range of about 9 GHz (22-31 GHz) leading to an efficient relative bandwidth of 32% whereas the maximum insertion loss was found at 1.25 dB for the longest waveguide i.e $5\lambda/2$-length waveguide. It is worth to notice that this insertion loss is composed of the losses occurring in the CPW access line and in the transition. Therefore, in order to remove these effects, the de-embedding method is necessary.

By considering the de-embedding method presented in [8] with two different lengths of waveguides (the shortest $\lambda/2$-length and the longest $5\lambda/2$-length), the phase constant β can be compared for the PAF-SW-SIW real and modeled structures, as shown in Figure 5-16. Concerning the attenuation constants, the comparison between the real simulations and the simulations taking the model into account is not consistent since this model does not integrate adequately the losses. This will have to be added in a future study. Nevertheless, it can be noted that the attenuation constant for the real simulation is lower than 0.015 dB/mm for the PCB-based PAF-SW-SIW.

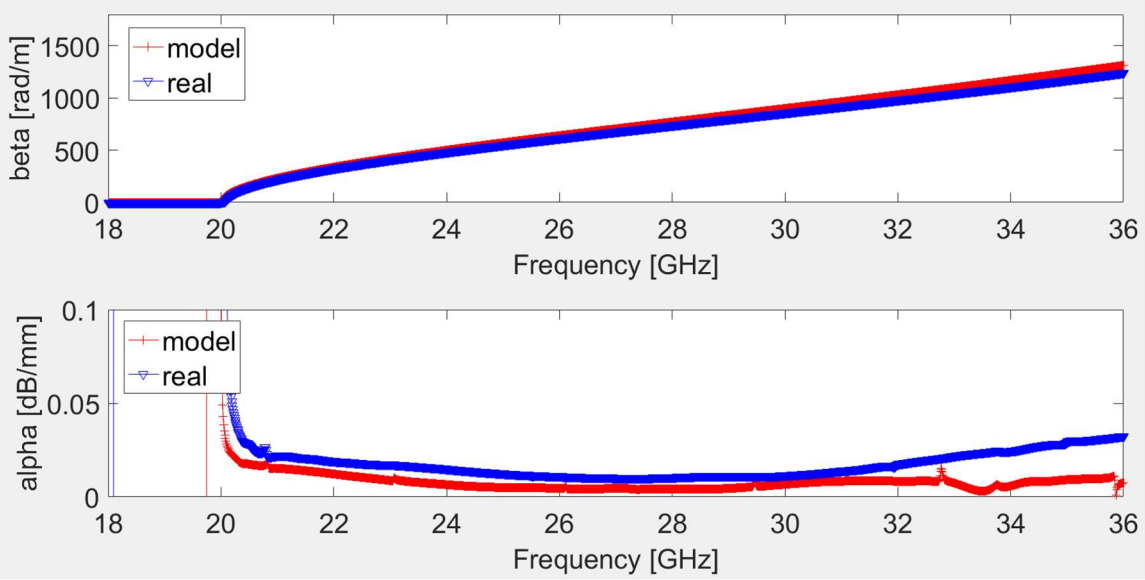

Figure 5-16. Extracted values of propagation constant of real structure and equivalent model after de-embedding technique of $5\lambda/2$-length with $\lambda/2$-length.

In comparison, concerning the CNT-based waveguide, the attenuation constant α is expected to be 0.004 dB/mm at 28 GHz, far lower than the PCB-based waveguide. But let us remember that the CNT-based model must be considered with caution since no validation has been done up to now. The comparison in terms of the phase constant β and the attenuation constant α between CNT-based AF-SW-SIW and PCB-based PAF-SW-SIW is presented in Figure 5-17.

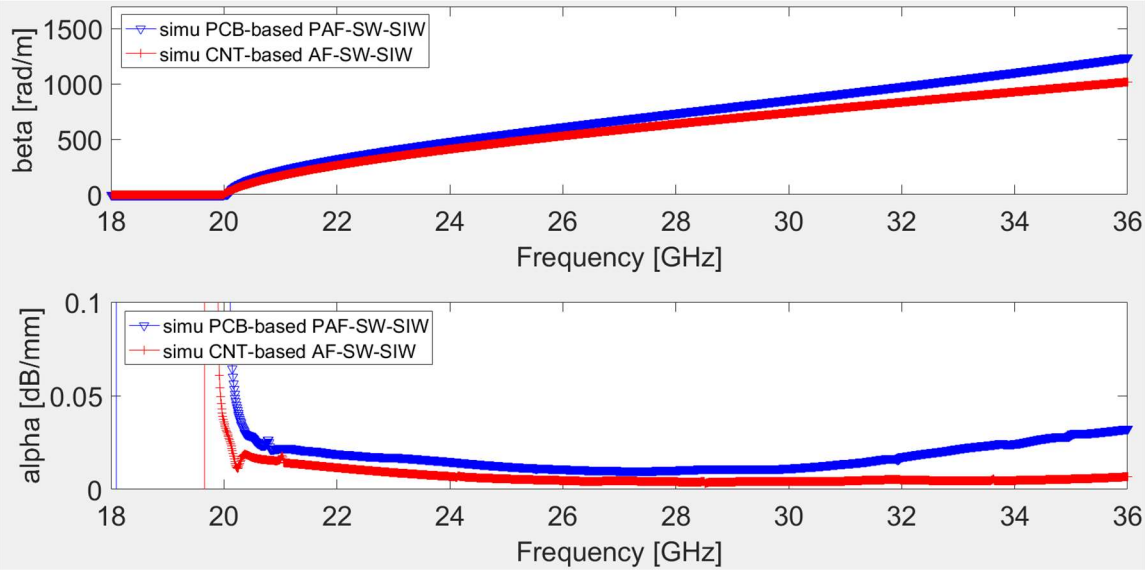

Figure 5-17. Extracted values of propagation constant of PCB-based PAF-SW-SIW and CNT-based AF-SW-SIW after de-embedding technique from MATLAB.

5.2 PCB-based PAF-SW-SIW 3-dB coupler

In this section, a PAF-SW-SIW 3-dB coupler, based on the short-slot coupler topology and the waveguide structure presented in section 5.1.1, is introduced. In order to reduce the simulation time, the equivalent model presented in section 5.1.2 is considered to optimize the coupler parameters. Then, considering technological fabrication constraints, the values are slightly readjusted. A comparison of simulation results between the model (best results after optimization) and the real structure are also illustrated in this section.

5.2.1 Design

The implementation design of this 3-dB coupler is illustrated in Figure 5-18, the geometric parameters defining this device are denoted as W_a, W, L and L', where W_a is the width of the access waveguide for mono-mode operation, while W and L are defining the center region size [9]. For our PCB-based PAF-SW-SIW, the width of the access waveguide W_a equals to 4 mm.

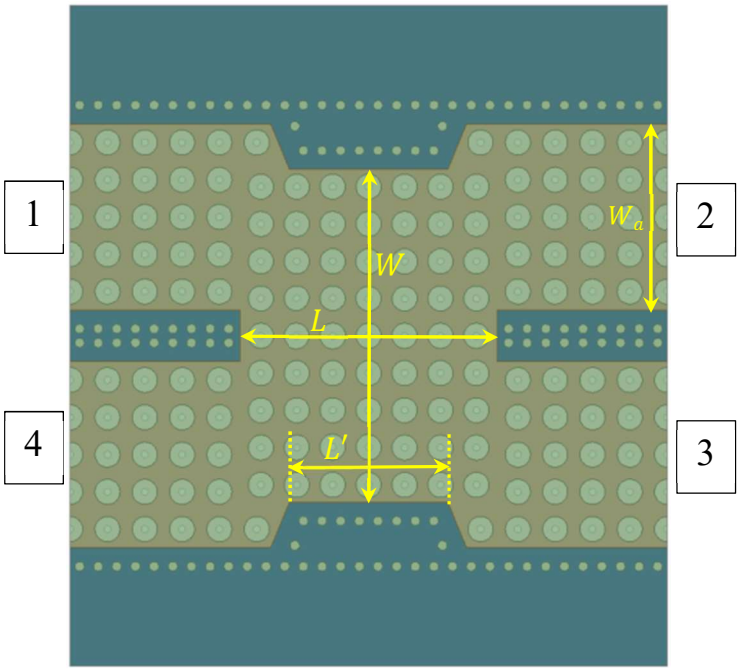

Figure 5-18. Geometrical parameter of the 3-dB coupler in PCB-based PAF-SW-SIW technology.

The initial dimensions were obtained by using the design equations (3-8) and (3-9), leading to $W = 7.35\ mm$ and $L = 4.75\ mm$. The same choice of solution order $n = 1$ was done in SW-SIW. After optimization by implementing the coupler in HFSS with full-wave simulation parametric analysis with model, the dimensions for real structure are given in Table 5-5.

	W (mm)	L (mm)	L' (mm)
Design equations	7.35	4.75	
Model ($\varepsilon_{r_{eff\_2}}$) after optimization	7.82	5.6	3.6
Real structure	7.75	5.6	3.6

Table 5-5. Calculated and optimized dimensions for the 3-dB Coupler in PCB-based PAF-SW-SIW technology.

5.2.2 Simulation results without access lines

Figure 5-19 presents the optimized responses of the investigated 3-dB coupler with the optimized dimensions introduced in the previous part by comparing the EM simulations of the real structure and the one considering the proposed model. This coupler was simulated without access lines in order to evaluate first its intrinsic performance. The E-field distributed inside this coupler is also illustrated in Figure 5-20.

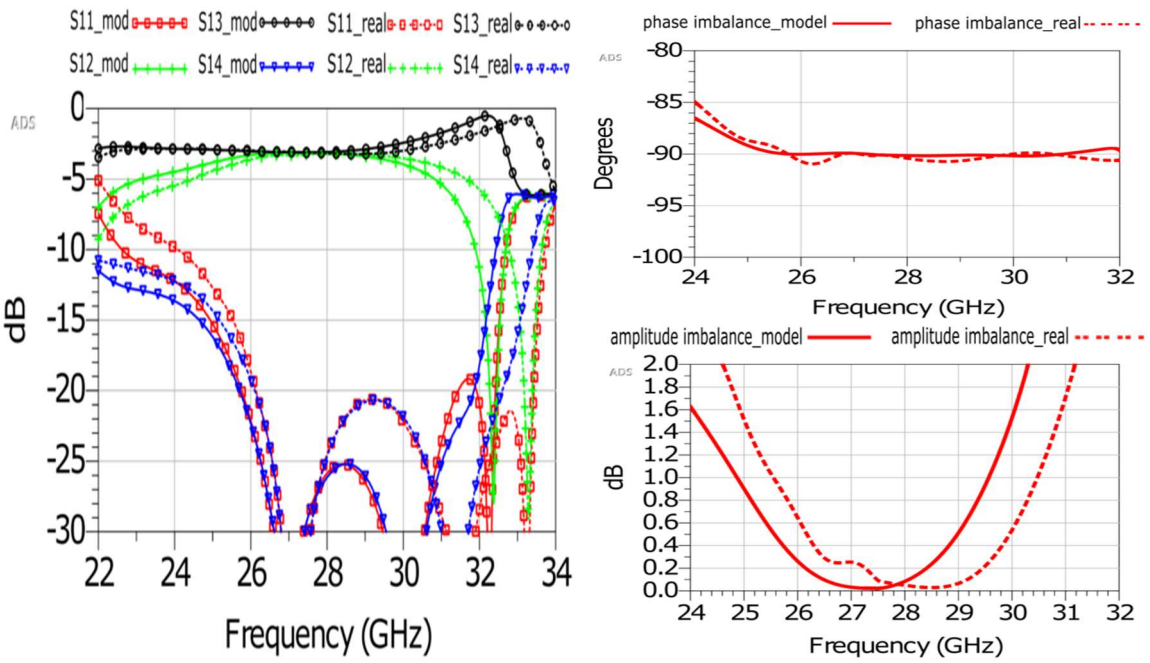

Figure 5-19. Simulated S-parameters of the optimized 3-dB Coupler in PCB-based PAF-SW-SIW technology.

As shown in Figure 5-19, the matching as well as the isolation are greater than 15 dB over the 25.5-32 GHz range. At the center frequency of 28 GHz, the insertion losses is around 0.2 dB justifying the interest for this low-loss technology. In terms of unbalance, it is less than 1.5° in phase over the 24.8-32 GHz and remains less than 1 dB between 25.5 and 30.5 GHz in amplitude (0.05 dB at 28 GHz). A good agreement between the simulation results of real structure and equivalent model is also observed in Figure 5-19. The slight shift in amplitude imbalance is once again due to the deviation between β_{model} and $\beta_{real\ structure}$ which occurs when building the equivalent model.

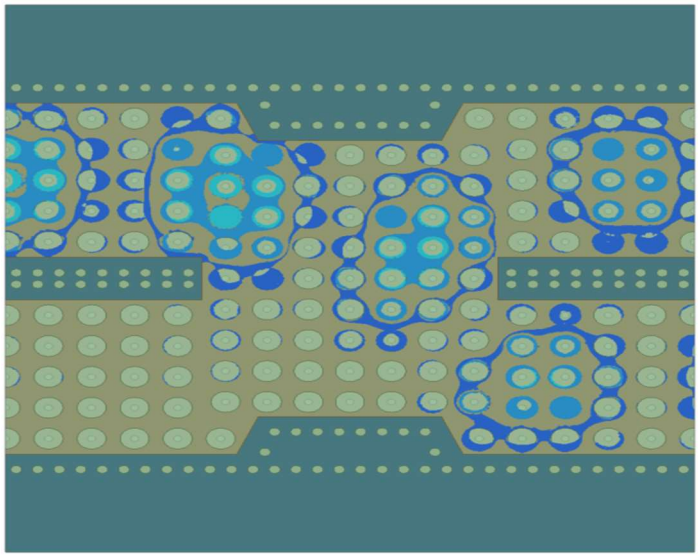

Figure 5-20. E-field distribution inside 3-dB Coupler in PCB-based PAF-SW-SIW technology.

5.2.3 *Simulation results with access line*

By assembling the intrinsic structure of 3-dB coupler presented in section 5.2.2 with the feeding structures introduced in section 5.1.1.4, a completed PCB-based PAF-SW-SIW 3-dB coupler can be designed and investigated. The final assembled structure and the E-field distribution inside this 3-dB coupler are presented in Figure 5-21 whereas the optimized responses are illustrated in Figure 5-22, respectively.

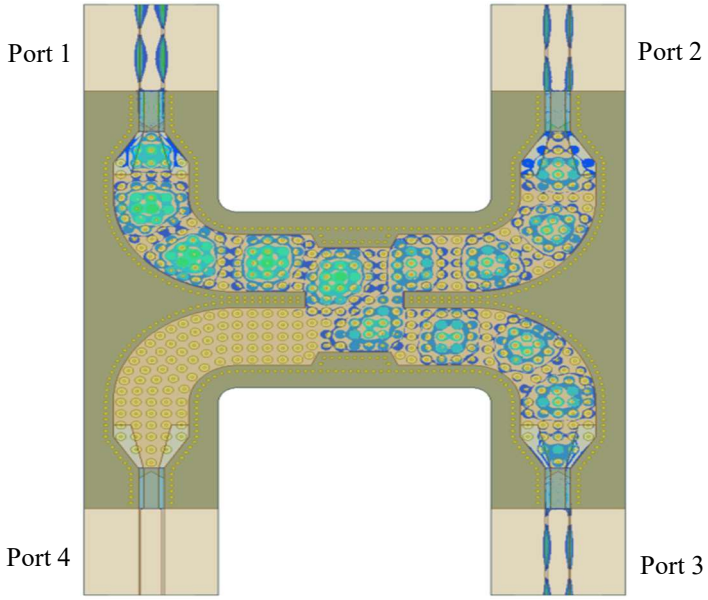

Figure 5-21. PCB-based PAF-SW-SIW 3-dB coupler with its access lines.

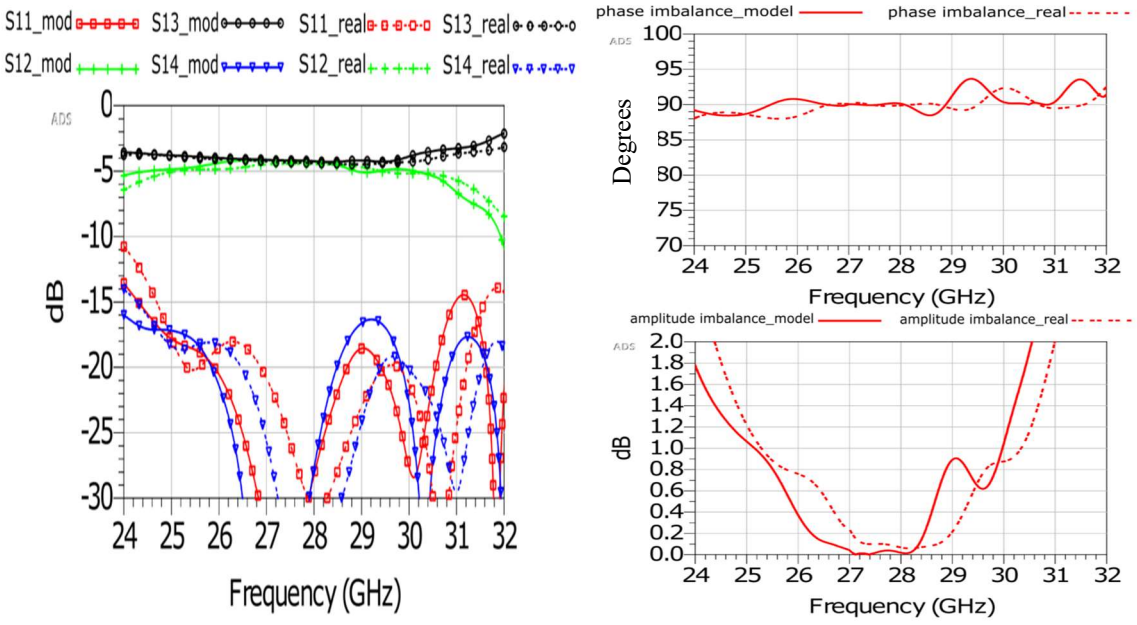

Figure 5-22. Simulated S-parameters of the optimized 3-dB coupler in PCB-based PAF-SW-SIW technology with its access lines.

As shown in Figure 5-22, the matching as well as isolation is greater than 15 dB over the 24.5-31 GHz range giving a relative bandwidth of 23.2%. At the center frequency of 28 GHz, the insertion loss is around 1.4 dB ($|S_{21}|_{dB} = -4.4\ dB$). These losses are due to the transition of the access lines and could be removed by using the de-embedding

technique. In terms of amplitude imbalance, it remains less than 1 dB between 25 and 30 GHz in amplitude (0.05 dB at 28 GHz) leading to a 1-dB amplitude imbalance bandwidth around 17.85%. Meanwhile, the phase variation is limited to $\pm 3°$ in 28% bandwidth (from 24 to 32 GHz).

In order to prove the efficiency of the equivalent model, the simulation times for the design of the 3-dB coupler with and without the use of equivalent model are given in Table 5-6. We do not comment that time the frequency shift observed between real case and model. Same comments as in section 5.1.3 would be considered. Anyway, with complex structures, it may be expected a better accuracy while saving computational time.

	ΔS (%)	Total memory	Parallel task	Total time
Real structure	3*	128.93 Gb	1	32h20
Equivalent model	1	77.71 Gb	1	21h17

** No lower ΔS enabled to finish simulations on the basis of our 128 Gbytes of RAM.*

Table 5-6. Simulation time obtained for the 3-dB coupler with different configurations.

5.2.4 Comparison with SIW 3-dB coupler state-of-the-art in RF frequency band

In order to evaluate our coupler, a comparison in terms of performance is carried out between this investigated coupler and the existing couplers in literature designed for the RF applications. This performance summary is proposed in Table 5-7. The reference, year/type, central frequency, bandwidth, insertion loss, amplitude imbalance and phase imbalance are listed. The insertion loss, the phase and the amplitude imbalance are taken at the central frequency whereas the relative BW is considered for frequencies where the return loss is better than 10 dB.

REF	Year/Type	Freq. (GHz)	BW (%) (GHz)	IL (dB)	Amp. Imb. (dB)	Phase Imb. (°)	Surface WxL (λ^2)
[10]	2007/ HM-SIW	12.5	> 40 (10-16)	3.5	0.1	2	0.82x1.33
[11]	2010/cruciform	12.5	36 (10-14.5)	3.25	0.1	5	1.12x1.60
[12]	2011/two-folded	12.5	> 40 (10-16)	3.3	0.15	3	0.73x1.36
[13]	2011/short-slot	24	> 45 (19-30)	3.2	0.1	3	0.81x1.69
[14]*	2014/folded	14.9	1 (14.82-14.97)	3.3	0.5	1	0.73x1.88
[15]	2015/short-slot	10	50 (7-12)	3.1	0.1	1	1.06x1.38
[16]	2016/ RHM-SIW	7.5	43 (5-8)	4.28	0.1	1	0.18x1.10
[17]	2017/ SW-HMSIW	14.1	72 (9-19)	3.3	0.5	2.5	0.56x1.61
[7]	2019/short-slot SWSIW	11.15	42 (8.5-13.5)	3.4	0.08	1.5	1.08x1.45

Our work*	2020/short-slot AF-SW-SIW (CNT technology)	28	46 (22-35)	3.1	0.08	1	0.97x1.54
Our Work*	2020/short-slot PAF-SW-SIW (PCB technology)	28	35.7 (24-34)	3.2	0.05	0.4	0.96x1.33

**Simulation results*

Table 5-7. Performance summary of SIW-based couplers for RF applications.

Our PCB-based short-slot 3-dB coupler results in lowest phase and amplitude imbalance as compared to the state-of-the-art, equal to 0.4 dB and 0.05 dB, respectively. Meanwhile, the relative bandwidth and insertion loss remain very competitive with the state-of-the-art while the coupler shows strong compactness with a surface equaling 0.96x1.53 λ^2, where λ is the guided wavelength at working frequency. These simulation results have to be confirmed by experimental results.

5.3 PCB-based PAF-SW-SIW crossover

In this part, a PCB-based PAF-SW-SIW crossover, based on the short-slot coupler topology and the waveguide structure presented in section 5.1.1.4, is introduced. In order to reduce the simulation time, the equivalent model presented in section 5.1.2 is also considered to optimize the crossover parameters leading after readjustment to consider technological constraints to the real structure. Finally, a comparison of simulation results between the model dimensions after parametric optimization and the real structure is also proposed.

5.3.1 Design

The procedure used to design the PCB-based PAF-SW-SIW crossover is not much different from that of the 3-dB coupler. The implementation form of this crossover is the same one used for 3-dB coupler, which is illustrated in Figure 5-18. The initial dimensions given by design equations are $W = 7.76\ mm$ and $L = 10.98\ mm$. After optimization by implementing the crossover in HFSS with full-wave simulation, the optimized dimensions for real structure were obtained and are given in Table 5-8 along with those provided by design equations.

	W (mm)	L (mm)	L' (mm)
Design equations	7.76	10.98	
Optimized model ($\varepsilon_{r_{eff\_2}}$)	8.10	11.6	9.2
Optimized real structure	8.10	11.6	9.2

Table 5-8. Calculated and optimized dimensions for the 3-dB crossover in PCB-based PAF-SW-SIW technology.

5.3.2 Simulation results without access lines

Figure 5-23 presents the optimized responses of the investigated crossover with the optimized dimensions introduced in the previous part. This crossover was simulated without its access lines in order to evaluate its intrinsic performance in this section. The E-fields distributed inside this crossover is also illustrated in Figure 5-24.

As shown in Figure 5-23, the matching as well as isolation are greater than 10 dB over the 25-30 GHz range. At the center frequency of 28 GHz, the insertion loss is around 0.28 dB.

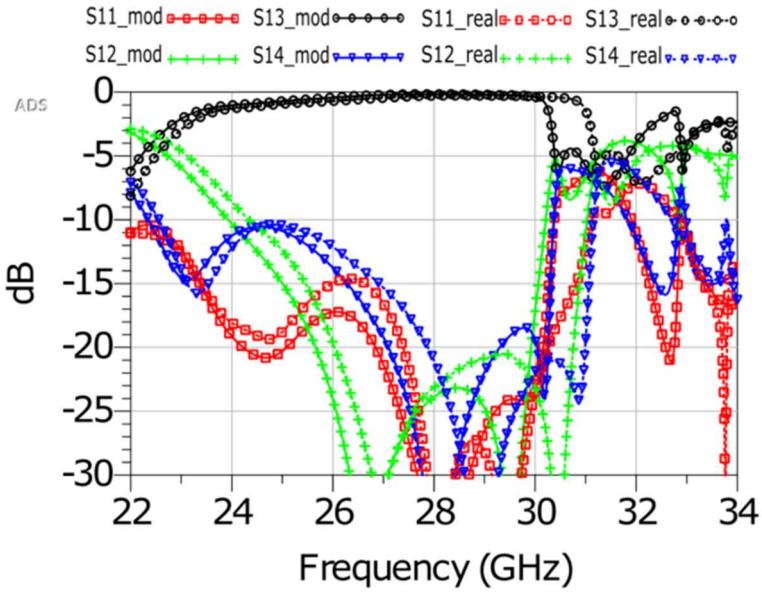

Figure 5-23. Simulated S-parameters of the optimized crossover in PCB-based PAF-SW-SIW technology.

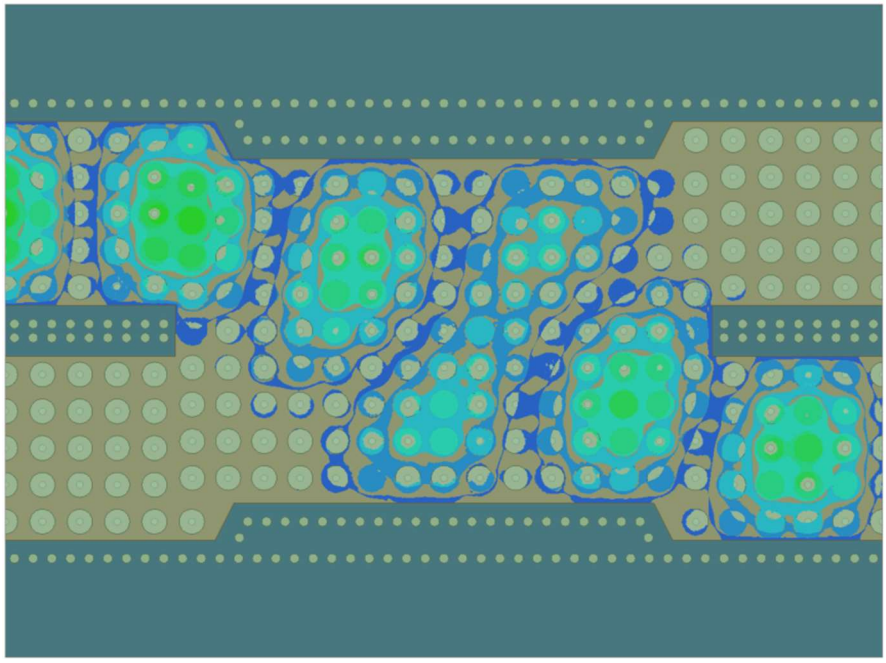

Figure 5-24. E-field distribution inside crossover in PCB-based PAF-SW-SIW technology.

5.3.3 Simulation results with access line

Once again, by assembling the intrinsic structure of crossover presented in section 5.3.2 with the feeding structures introduced in section 5.1.1.4, a completed PCB-based PAF-SW-SIW crossover can be designed and investigated. The final assembled structure and the E-field distribution inside this crossover are presented in Figure 5-25 whereas the optimized responses are illustrated in Figure 5-26, respectively.

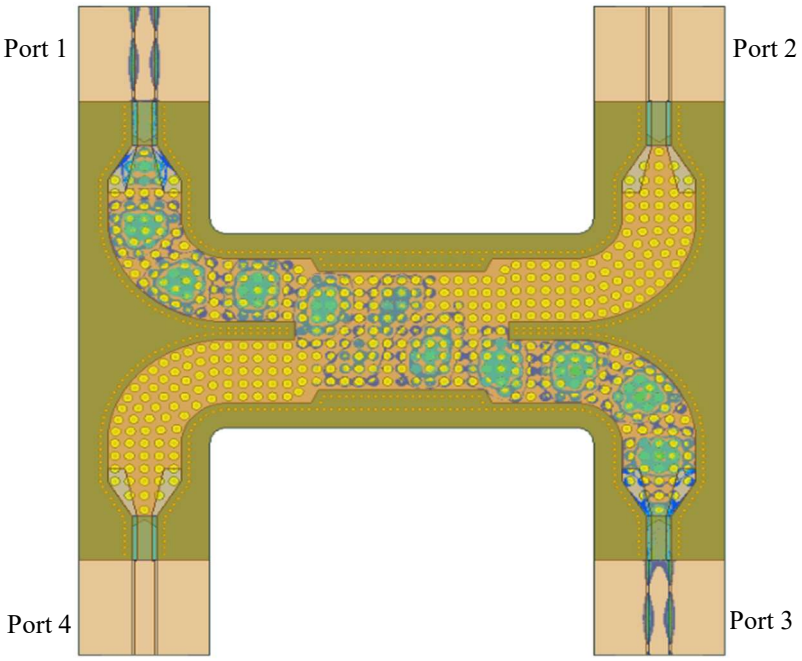

Figure 5-25. PCB-based PAF-SW-SIW crossover with its access lines.

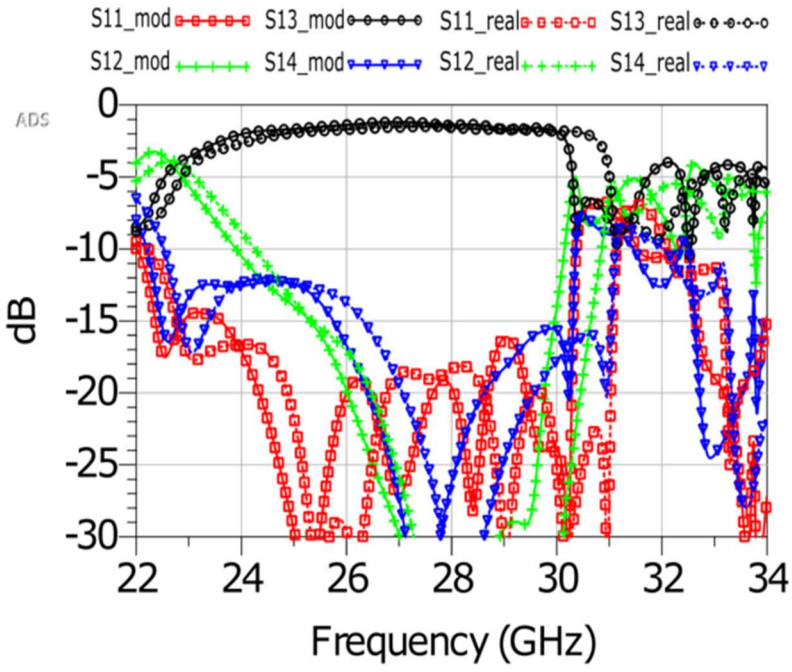

Figure 5-26. Simulated S-parameters of the optimized crossover in PCB-based PAF-SW-SIW technology with its access lines.

As shown in Figure 5-26, the matching (S_{11}) is better than 10 dB over the 22-30.2 GHz range giving a relative bandwidth of 29.3%. Meanwhile, the isolation between port 1 and port 4 (S_{14}) and the direct transmission (S_{12}) are greater than 10 dB from 22 to 30.2 GHz and from 24 to 30 GHz, respectively. At the center frequency of 28 GHz, the insertion loss is around 1.4 dB and is mainly due to the transition of the access lines and will be removed by using the de-embedding technique.

5.3.4 Comparison with SIW crossover state-of-the-art in RF frequency band

In order to evaluate our crossover, a comparison in term of performance is carried out between this investigated crossover and the existing ones in literature which were designed for the RF applications. This performance summary is introduced in Table 5-9. The reference, year/type, central frequency, bandwidth, insertion loss, direct transmission and isolation are listed. The insertion loss, direct transmission and isolation are taken at the central frequency whereas the relative BW is considered for frequencies where the return loss is better than 10 dB.

REF	Year/Type	Freq. (GHz)	BW (%) (GHz)	IL (S_{31}) (dB)	Direct trans. (S_{21}) (dB)	Isolation (S_{41}) (dB)	Surface WxL (λ^2)
[11]	2010/ cruciform	12.5	36 (10-14.5)	0.15	20	>20	1.60x3.61
[14]	2014/ folded	14.9	1 (14.82-14.97)	0.13	30.7	39.4	0.73x2.63
[3]	2017/short-slot SW-SIW	11.4	26 (9.8-12.7)	0.58	25	>25	1.45x2.16
Our work*	2020/short-slot AF-SW-SIW (CNT technology)	28	28.5 (24-32)	0.1	>35	>20	1.54x1.97
Our work*	2020/short-slot PAF-SW-SIW (PCB technology)	28	29.3 (22-30.2)	0.28	>23	>21	1.39x1.95

Simulation results

Table 5-9. Performance summary of SIW-based crossovers for RF applications.

Our short-slot PCB-based PAF-SW-SIW crossover results in very low loss and high relative bandwidth as compared to the state-of-the-art, while the rest of the parameters comply with the state-of the-art. The crossover shows strong compactness with a surface equaling 1.39x1.95 λ^2, where λ is the guided wavelength at working frequency.

5.4 Conclusion

In this chapter, a detailed description of PAF-SW-SIW waveguide based on PCB technology designed at 28 GHz for RF applications was presented. By inserting internal blind via holes inside an air-filled SIW waveguide, a good slow-wave factor and low-loss structure could be obtained. Hence, a compact structure can be reached as compared to the AF-SIW while maintaining a quite low insertion loss. Indeed, the simulations results allow obtaining a slow-wave factor of 1.84 with an expected attenuation constant of 0.01 dB/mm by using this PAF-SW-SIW, leading to almost 76% of surface reduction at the end when associated to the 43.5% of reduction in width. A CPW-to-GCPW-to-SIW transition mainly based on the quarter-wavelength triangle coupling slot was also considered for our PCB-based PAF-SW-SIW structures. Actually, by using this transition, a simulated return loss greater than 20 dB was obtained over the frequency range of about 9 GHz (22-31 GHz) leading to an efficient relative bandwidth of 32.14%. The detailed design rules of this transition were also introduced in this part.

Furthermore, the PCB-based PAF-SW-SIW technology was also applied for the design of 3-dB coupler and crossover based on the short-slot topology with the same concept. The simulated S-parameters demonstrated that a good performance was expected for these couplers. In general, the simulated return loss is better than 15 dB over the 25-30 GHz frequency range for both couplers. At the center frequency of 28 GHz, the insertion loss is around 0.2 dB for the 3-dB coupler and 0.28 dB for the crossover, justifying the interest for this low-loss technology. In terms of unbalance for the 3-dB coupler, it is less than 1.5° in phase over the 24.8-32 GHz and remains less than 1 dB between 25.5 and 30.5 GHz in magnitude (0.05 dB at 28 GHz). A comparison in terms of performance between our couplers and the existing ones which were designed for RF applications was also presented in this chapter.

Finally, in order to reduce the simulation time when simulating the full structure of proposed waveguides or couplers in HFSS, an equivalent model was investigated, leading to a good agreement with real structure in term of simulation results while reducing simulation time efficiently.

REFERENCES

[1] D. Deslandes, “Etude et développement du guide d’ondes intégré au substrat pour la conception de systèmes en ondes millimétriques.”

[2] D. Deslandes and W. Ke, “Accurate modeling, wave mechanisms, and design considerations of a substrate integrated waveguide,” *IEEE Trans. Microw. Theory Tech.*, vol. 54, no. 6, pp. 2516–2526, 2006.

[3] M. BERTRAND, “Guides à ondes lentes intégrés dans le substrat pour les applications en bandes RF et millimétriques,” 2017.

[4] F. Xu, A. Patrovsky, and K. Wu, “Fast Simulation Of Periodic Guided-Wave Structures Based On Commercial Software,” *Microw. Opt. Technol. Lett.*, vol. 49, no. 9, pp. 2180–2182, 2007.

[5] F. Xu, K. Wu, and W. Hong, “Equivalent resonant cavity model of arbitrary periodic guided-wave structures and its application to finite-difference frequency-domain algorithm,” *IEEE Trans. Microw. Theory Tech.*, vol. 55, no. 4, pp. 697–702, 2007.

[6] A. Niembro-Martín *et al.*, “Slow-wave substrate integrated waveguide,” *IEEE Trans. Microw. Theory Tech.*, vol. 62, no. 8, pp. 1625–1633, 2014.

[7] M. Bertrand *et al.*, “A 3-dB Coupler in Slow Wave Substrate Integrated Waveguide Technology,” vol. 29, no. 4, pp. 2019–2021, 2019.

[8] P. Souzangar and M. Shahabadi, “Numerical Multimode Thru-Line (TL) Calibration Technique for Substrate Integrated Waveguide Circuits,” vol. 5071, 2012.

[9] C. J. Chen and T. H. Chu, “Design of 60-GHz SIW short-slot couplers,” *APMC 2009 - Asia Pacific Microw. Conf. 2009*, no. c, pp. 2096–2099, 2009.

[10] B. Liu, W. Hong, Y.-Q. Wang, Q.-H. Lai, and K. Wu, “Half Mode Substrate Integrated Waveguide (HMSIW) 3-dB Coupler,” *IEEE Microw. Wirel. COMPONENTS Lett.*, vol. 17, no. 1, pp. 22–24, 2007.

[11] T. Djerafi, N. J. G. Fonseca, and K. Wu, “Design and implementation of a planar 4 × 4 butler matrix in SIW technology for wide band high power applications,” *40th Eur. Microw. Conf.*, no. 35, pp. 910–913, 2010.

[12] A. A. M. Ali, N. J. G. Fonseca, F. Coccetti, and H. Aubert, “Design and implementation of two-layer compact wideband butler matrices in siw technology for ku-band applications,” *IEEE Trans. Antennas Propag.*, vol. 59, no. 2, pp. 503–512, 2011.

[13] T. Djerafi and K. Wu, “Multilayered Substrate Integrated Waveguide 4 x 4 Butler Matrix,” *Wiley Period. Inc.*, pp. 210–224, 2011.

[14] W. Bhowmik, S. Srivastava, and L. Prasad, “Design of multiple beam forming antenna system using substrate integrated folded waveguide (SIFW) technology,” *Prog. Electromagn. Res. B*, vol. 60, no. 1, pp. 15–34, 2014.

[15] S. Karamzadeh, V. Rafii, M. Kartal, and B. S. Virdee, “Compact and Broadband 4 x 4 SIW Butler Matrix with Phase and Magnitude Error Reduction,” *IEEE Microw. Wirel. Components Lett.*, vol. 25, no. 12, pp. 772–774, 2015.

[16] T. R. Jones and M. Daneshmand, “The Characterization of a Ridged Half-Mode Substrate-Integrated Waveguide and Its Application in Coupler Design,” *IEEE Trans. Microw. Theory Tech.*, vol. 64, no. 11, pp. 3580–3591, 2016.

[17] H. Jin, Y. Zhou, Y. M. Huang, S. Ding, and K. Wu, “Miniaturized Broadband Coupler Made of Slow-Wave Half-Mode Substrate Integrated Waveguide,” *IEEE Microw. Wirel. Components Lett.*, vol. 27, no. 2, pp. 132–134, 2017.

Conclusion

The work introduced in this PhD thesis was mainly concentrated in two directions. The first one involved in considering a CNT technology to design AF-SIW circuits for mm-wave applications in E-band (71-86 GHz). The second direction concerned the utilization of the slow-wave concept for the miniaturization of AF-SIW circuits designed for the RF applications based on both conventional PCB and CNT technologies. In both subjects, the proposed structures were detailed, then theoretical analyses were developed, and simulation and measurement results were presented. The retro-simulations were also realized when needed, which permitted to validate the proposed structures.

In the first chapter, the context for this thesis was introduced, which emphasizes the important role of multi-beam antenna systems for mm-wave applications, especially for 5G mobile communication networks. The beam-forming technique, which has the ability of providing unique patterns for beam switching or steering, has become the core technology in the rapidly development of this antenna system. Therefore, an overview of four common categories of BFNs was also presented. Among them, BM was proved to be particularly attracting. An overview concerning the techniques utilized to design and fabricate BM was also introduced, in RF and mm-wave frequency bands. In fact, the SIW technology has demonstrated its possibility to become a pertinent choice for BM design due to high Q factor, high power capability, low-loss, reduced weight, and no susceptibility to electromagnetic interference or wide instantaneous bandwidth features. Hence, a short description of SIW technology, as well as miniaturization techniques and low-loss air-filled technology were also introduced in this chapter.

The second chapter introduced in detail the physical properties of carbon nanotubes. Some state-of-the-art electronics applications based on CNTs: field effect transistors, antennas, interconnections or promising no-loss waveguides were presented. In particular, waveguides were one of our main goal to study during this PhD thesis. Three main methods to grow CNTs for electronics applications were also described in this chapter: arc discharge, laser ablation, thermal CVD and PECVD method. Thermal CVD and PECVD are the only methods enabling vertical alignments. The choice of thermal CVD in the framework of this PhD work was justified even if a lower CNT purity is obtained with this technique as compared to arc discharge or laser ablation. Also, bundles of single wall CNTs (SWCNTs) grown through thermal CVD present interestingly high densities up to $10^{14-15}m^{-2}$. The analytical and electromagnetic bulk modeling of CNTs performed by XLIM laboratory, Limoges, FR, was also detailed in this chapter. Thanks to the bulk model, the CNT-based devices are designed more easily, and with accuracy. In practice, a bundle of CNTs, or a CNTs forest, is modeled as a bulk material of unique axial conductivity (not so high, about 0.8-1 MS/m, but only vertical, which considerably limits the resistive loss). Hence, the bulk model was then considered for the design and optimization of the electromagnetic circuits in the framework of this PhD in chapters 3 and 4.

The third chapter was then focused on a detailed description of AF-SIW waveguide based on CNT technology. In order to obtain a good performance, a CPW-to-GCPW-to-SIW transition mainly based on the quarter-wavelength triangle coupling slot was considered. Indeed, by using this transition, a simulated return loss better than 15 dB in the entire E-band is expected. Meanwhile, the maximum simulated insertion loss is better than 0.5 dB over the E-band. These results allow us to believe in a good transition for our circuits. The detailed design rules of this transition were also introduced in this part. Furthermore, the CNT technology used to design the AF-SIW waveguide was also applied to the design of 0-dB and 3-dB couplers based on the short-slot topology with the same

concept. The simulated S-parameters demonstrated that a good performance can be expected for these couplers. In general, the return loss is greater than 15 dB over the 71-86 GHz frequency range for both couplers. At the center frequency of 78.5 GHz, the insertion loss is around 0.1 dB for the 3-dB coupler and 0.05 dB for the crossover, justifying the interest for this low-loss technology. In terms of unbalance for the 3-dB coupler, it is less than 0.63° in phase over the entire E-band and remains less than 1 dB between 73 and 86 GHz in magnitude (1.4 dB at 71 GHz). By combining these couplers with the optimized phase shifter for the design of Butler Matrix in ADS, a simulation was also achieved, leading to an input-output transmission of 6.7±0.7 dB (respectively 6.4 ± 1.2 dB) for excitation on port 1 (respectively, on port 2), with a maximum phase error of 1.8° (respectively, 3.7°). In addition, the fabrication process of the CNT-based AF-SIW circuits developed by CINTRA laboratory was also presented in this chapter. First measurements results were also provided showing the existence of the targeted cut-off frequency for waveguides but with 10-dB of insertion loss due to delamination process and bad contact between the CNT wall and the bottom plate of the waveguide. Further investigations are actually made at CINTRA to improve process. It is expected that some solutions concerning delamination can be proposed to overcome the insertion loss issues on CNT-based AF-SIW.

In the fourth chapter, a detailed description of AF-SW-SIW waveguides based on CNT technology designed at 28 GHz for RF applications was investigated and presented. An important feature for all slow-wave topologies is the slow-wave factor that is, in our case, depending on the height of the CNT forest. In this work, three heights of CNT forest (200 µm, 300 µm and 400 µm) were considered. Based on the theoretical calculations, the width of the CNT-based AF-SW-SIW waveguides could be reduced due to the slow-wave effect leading to an efficient miniaturization on the waveguide dimensions (around 43.5 % in width, and 43.5 % in length with the 400-µm CNT forest height leading to about 68% of surface reduction). In order to reach sensitivity in measurements through matched transitions, a CPW-to-GCPW-to-SIW transition, mainly based on the quarter-wavelength triangle coupling slot, was also optimized. Indeed, by using this transition, a matching better than 15 dB was obtained over the 24-36 GHz range for all structures, leading to a large relative bandwidth of 43%. The fabricated devices are currently under CNT-transfer process at CINTRA. Some pre-process measurements on empty waveguides before CNT transfer were performed showing the expected higher cut-off frequency as well as extremely low-loss. The measurements are extremely sensitive to the VNA remaining incertitude after calibration, and to the repeatability of the contacts. The reached accuracy did not enable us to measure the expected extremely low loss; by the way, they proved an attenuation below 0.1 dB/mm, which is already interesting. Furthermore, the CNT-based AF-SW-SIW technology was also applied to the design of 0-dB and 3-dB couplers, based on the same concept of the short-slot topology. The simulated S-parameters demonstrated that good performance could be expected for these couplers. In general, the return loss is better than 15 dB over the 25-31 GHz frequency range for both couplers. At the center frequency of 28 GHz, the insertion loss is around 0.2 dB for the 3-dB coupler and 0.1 dB for the crossover, justifying the interest for this low-loss technology. In terms of unbalance for the 3-dB coupler, it is less than 1.5° in phase over the 24-32 GHz and remains less than 1 dB between 25.5 and 31.8 GHz in magnitude (0.08 dB at 28 GHz). A comparison in terms of performance between these couplers and the existing ones designed for RF applications was also presented in this chapter, underlying their better compactness while keeping similar electrical performance. We hope that some measurements results concerning the CNT-based AF-SW-SIW will be provided soon, proving the expected slow

wave factor and the extremely low loss. CNT transfer should be operative no later than January 2021.

Finally, the last chapter was dedicated to the detailed description of PAF-SW-SIW waveguide based on conventional PCB technology designed at 28 GHz for RF applications. By inserting internal blind via holes inside an air-filled SIW waveguide, a good slow-wave factor and low-loss structure could be obtained. Hence, a compact structure can be obtained as compared to the AFSIW while maintaining a quite low insertion loss. Indeed, the simulation results allow obtaining a slow-wave factor of 1.84 with an expected attenuation constant of 0.01 dB/mm by using this PAF-SW-SIW. A CPW-to-GCPW-to-SIW transition mainly based on the quarter-wavelength triangle coupling slot was also considered for our PCB-based PAF-SW-SIW structures. Actually, by using this transition, a simulated return loss greater than 20 dB was obtained over the frequency range of about 9 GHz (22-31 GHz) leading to an efficient relative bandwidth of 32.14 %. Furthermore, the PCB-based PAF-SW-SIW technology was also applied for the design of 3-dB coupler and crossover based on the short-slot topology with the same concept. The simulated S-parameters demonstrated that a good performance was expected for these couplers. In general, the simulated return loss is better than 15 dB over the 25-30 GHz frequency range for both couplers. At the center frequency of 28 GHz, the insertion loss is around 0.2 dB for the 3-dB coupler and 0.28 dB for the crossover. Even if the lossy substrate surrounding the rows and columns of blind via holes deteriorates slightly the attenuation constant due to a small penetration of electric field, losses are still low, justifying the interest for this slow-wave technology. In terms of unbalance for the 3-dB coupler, it is less than 1.5° in phase over the 24.8-32 GHz and remains less than 1 dB between 25.5 and 30.5 GHz in magnitude (0.05 dB at 28 GHz). A comparison in terms of performance between our couplers and the existing ones which were designed for RF applications was also presented in this chapter. Finally, in order to reduce the simulation time when optimizing the full structure of proposed couplers through parametric analysis in HFSS, an equivalent model was investigated and proposed, leading to a good agreement with real structure in term of simulation results while reducing optimization time efficiently. It is expected that measurement results (concerning waveguides electrical characteristics, 3-dB coupler and crossover de-embedded S-parameters) will be provided by the PhD defense in order to validate the proposed concept.